8-2018

Polysulfide Mitigation at the Electrode-Electrolyte Interface: Experiments in Rechargeable Lithium Sulfur Batteries

Arthur D. Dysart
Purdue University

POLYSULFIDE MITIGATION AT THE ELECTRODE-ELECTROLYTE INTERFACE: EXPERIMENTS IN RECHARGEABLE LITHIUM SULFUR BATTERIES

A Dissertation

Submitted to the Faculty

of

Purdue University

by

Arthur D. Dysart

In Partial Fulfillment of the

Requirements for the Degree

of

Doctor of Philosophy

August 2018

Purdue University

West Lafayette, Indiana

THE PURDUE UNIVERSITY GRADUATE SCHOOL
STATEMENT OF DISSERTATION APPROVAL

Dr. Vilas G. Pol, Chair

School of Chemical Engineering

Dr. James M. Caruthers

School of Chemical Engineering

Dr. Jefferey P. Greeley

School of Chemical Engineering

Dr. Kejie Zhao

School of Mechanical Engineering

Approved by:

Dr. John A. Morgan

Head of the School Graduate Program

For

family, friends,
and

Cristina N. Buensuceso, Elaine D. Dysart, and Prudencio Buensuceso
whose love and legacy continue on.

Thank you.

ACKNOWLEDGMENTS

Thank you to administration, faculty, and staff of Purdue University for their kindness and dedication to the spirit of research.

Thank you to scientists and staff of Argonne National Laboratory for volunteering resources and insight into an unfamiliar discipline.

Thank you to advisory committee Jim Caruthers, Jeffrey Greeley, and Kejie Zhao for their critical guidance and exemplary mentorship.

Thank you to collaborators Aashutosh Mistry, Abdullah Alazemi, Andrea Hicks, Jay Beltz, Neal Cardoza, Xin Li Phuah, and Daniel Abraham for supporting research with dedication and positivity.

Thank you to colleagues Jialiang Tang, Ryan Adams, Joseph Kubal, Pierre Yao, Jungsuk Kim, and William Chin for their enduring confidence and friendship.

Thank you to Vilas Pol for courage through both frustration and fortune.

This work is dedicated to the idea that the academic journey forever continues on. Thank you to loved ones who have made this short adventure a memorable one.

PREFACE

This dissertation comes as the culmination of 5 years of research across Purdue University (West Lafayette, Indiana), Texas A&M University (College Station, Texas), and Argonne National Laboratory (Lemont, Illinois). The original experimental data and results reported within were performed and analyzed by the author Arthur D. Dysart and many research collaborators: Salvador Acuña, Daniel Abraham, Ryan Adams, Abdullah Alazemi, Katsuhiko Ariga, Perla Balbuena, Jay Beltz, Juan Burgos, Neal Cardoza, William Chin, Roberto Esparza, Vinodkumar Etacheri, Chien-Fan Chen, Sean Fronczak, Andrew Chuang, Aaron Cox, Andrea Hicks, Chulgi Hong, Seok–Min Hong, Eunji Jang, Samrudhi Joshi, Dong Hee Kim, Joseph Kubal, Ki Bong Lee, Zhixiao Liu, Aashutosh Mistry, Partha Mukherjee, David Mulqueen, John Okasinski, Xin Li Phuah, Vilas Pol, Farshid Sadeghi, Ram Saraswat, Steven Shaffer, Gregory Shaver, Lok Kumar Shrestha, Lars–Erik Stacke, Jialiang Tang, Candace Tsai, and Pierre Yao. The author gratefully acknowledges the support of these collaborators in various research activities during graduate studies at Purdue University.

TABLE OF CONTENTS

Page

LIST OF TABLES

LIST OF FIGURES

ABSTRACT

Dysart, Arthur D. PhD, Purdue University, August 2018. Polysulfide Mitigation at the Electrode-Electrolyte Interface: Experiments in Rechargeable Lithium Sulfur Batteries. Major Professor: Vilas G. Pol.

In the field of energy storage technology, the lithium sulfur battery is intensely studied in interest of its great theoretical gravimetric capacity (1672 Ah kg^{-1}) and gravimetric density (2600 Wh kg^{-1}). The theoretical performance values satisfy viability thresholds for petroleum–free electric vehicles and other emerging technologies. However, this elusive technology remains in the research sector due to a wealth of challenges resulting from its complex chalcogenide electrochemistry. The most infamous challenge remains the polysulfide redox shuttle, a phenomenon in which lithium polysulfide intermediates are produced as elemental sulfur S_8 is reduced to lithium sulfide Li_2S during the discharge cycle. Because the higher order polysulfides are soluble in organic electrolyte, battery cycling can result in dissolution of the cathode, dendrite formation upon the lithium metal anode, and passivation of electrode surfaces. These problems can ultimately cause rapid capacity fade and unstable Coulombic efficiency.

As lithium sulfur battery research enters its 3rd decade, it is becoming increasingly clear that solutions will be holistic or synergistic; that is, addressing the aforementioned issues by suppressing their source in the polysulfide redox shuttle rather than isolated symptoms of the underlying mechanism. This thesis serves as a summary of research performed to study polysulfide suppression and mitigation through electrode material synthesis, electrolyte design, and in situ characterization. Synthesis techniques include solid state pyrolysis, autogenic synthesis, and ultrasound sonochemistry. Material characterization techniques include isothermal nitrogen sorption; scanning, transmission, and scanning transmission electron microscopy; thermogravi-

metric analysis; energy dispersive X–ray spectroscopy; organic elemental analysis; X–ray diffraction; and Raman spectroscopy. Electrochemical characterization includes galvanostatic battery cycling, differential potentiometric analysis, and electrochemical impedance spectroscopy.

Altogether, this research demonstrates the challenges of polysulfide degradation are not sufficiently addressed by symptomatic approaches. Synthesis pathways for carbon sulfur cathodes that encourage homogeneous sulfur distribution (i.e., autogenic or sonochemical synthesis) improve specific capacity across extended cycling, but show excessive polysulfide production at slow cycling rates. In combination with fluorinated electrolyte, carbon sulfur cathode morphology improves Coulombic efficiency at cycling rates between C/20 — 2 C but at the cost of gravimetric capacity. Synchrotron tomography characterization, developed for Advanced Photon Source Beamline 6–BM–A, evidences that fluorinated electrolytes may also effectively suppress dendrite formation on lithium metal anodes. This suggests more holistic and optimized techniques, or their combinations, may lead to effective polysulfide suppression and successful commercialization of the lithium sulfur battery.

Supplementary research explores broader impact of synthesized carbon applications in lithium sulfur batteries. Pyrolysis synthesis processes are evaluated for health and environment impacts using optical by–product sizing and life cycle analysis, respectively. In the context of pyrolytic synthesis of carbon microsheets, micro and nano-sized carbonaceous particulate by–products released during synthesis must be collected to minimize health exposure risks. The environmental impact of this synthesis process is a function of mode of oxygen deficiency, that is, whether pyrolytic atmosphere is facilitated by vacuum or inert gas stream. Finally, submicron carbon spheres, a carbon morphology produced by pyrolysis of sonochemically-synthesized polymer spheres, demonstrate gravimetric capacity which is a strong function of microstructure (i.e., pore distribution, crystallite size, structural disorder). In turn, microstructural properties are determined by synthesis temperature, a dimension of synthesis pathway.

GRAND CHALLENGE OF ENERGY

Available energy is the main object
at stake in the struggle for existence
and the evolution of the world.

— L. E. Boltzmann, 1905, *Populäre Schriften*

CHAPTER 1: ENERGY STORAGE

Energy independence is the forefront of the 21st century. Calculators, laptops, media players, smartphones: modern technology elevates portability from novelty to prerequisite. Likewise, electric cars dominate consumer markets and popular opinion, rapidly replacing petroleum-reliant vehicles. Inflating demands for technology fuel insatiable appetites for energy; energy grids must keep pace with capability and complexity. Technologic manifest destiny, an international dream for energy independence, has built the lithium sulfur battery — at least, in concept.

This chapter details fundamental concepts for energy storage. This overview begins by answering why energy and its storage are important. Then, the connection between energy and fundamental thermodynamics is explored. Finally, the thermodynamic potential for electric work, as electric voltage, is introduced in context of its mathematic derivation and physical interpretation.

1.1 Energy: A Premier

All things in this world exist and endure through energy. Energy is the ability to do work [1, 2]; a property of things, both living and not, which enables all actions and reactions. Energy is found throughout the natural world in various forms, continually moving and changing. Control of these processes, when thermodynamically permissible, enables energy storage and delivery.

Classifying Energy

Regardless of state or scale, energy is identified according to *how* it is used. Energy can be organized into six primary classes [2]:

- Mechanical energy is associated with all mechanical motion. For instance, displacement of macroscale objects in physical space, both Cartesian (e.g., linear, acoustic) and euclidean (e.g., angular, sinusoidal), results from mechanical energy.

- Electrical energy is associated with the activity of electric fields. An electric field is the region surrounding a charged entity that exerts force on occupying charged objects. Objects of dissimilar charge are attracted, while objects of similar charge are repulsed. Movement of charged entities (e.g., negatively-charged electrons) in an electric field is due to electrical energy.

- Chemical energy is associated with transformation of chemicals. During conversion of one chemical species into another, molecular changes rearrange atomic bonds. Cleavage or formation of chemical bonds is accompanied by release or absorption of chemical energy, respectively.

- Nuclear energy is associated with transformation of atomic nuclei. When an atomic nucleus collides with atomic or subatomic matter (e.g., nucleus, proton, neutron, electron), atomic species called nuclides are formed. Nuclei decomposition is known as fission while their combination is fusion. Depending on participating species, fusion and fission either release or absorb nuclear energy.

- Magnetic energy is associated with the activity of magnetic fields. A magnetic field is the region surrounding a magnetic entity which exerts force on occupying magnetizable objects. Objects of dissimilar polarity are attracted, while objects of dissimilar polarity are repulsed. Movement of polarized entities in a magnetic field is due to magnetic energy.

- Thermal energy is associated with changes in the internal state of an entity. Typically, internal energy is described as Brownian molecular vibrations [3]: vibrations are transferred from high to low (viz., "hot" to "cold") intensity regions. The sum of these vibrations, measured as entity temperature or heat, are due to thermal energy.

Transformation of energy from one class or state to another is known as energy conversion [2]. Typically, a single conversion process converts energy between inactive and active states. Inactive, dormant, or stored energy is potential energy; Active, involved, stimulating energy is kinetic energy. Principle examples of energy conversion include [1, 2, 4, 5]:

- Electrochemical energy is associated with transfer of charged species due to chemical changes. Under an electric driving force, chemical reactions release ionized species (i.e., cations and anions). Typically, electric energy is captured through electron transfer. The transport of ionized species is due to electrochemical energy.

- Electromagnetic energy is associated with the self-propagating motion of radiation waves. Propagating radiation waves (e.g., visible light, X–rays) are comprised of alternating electric and magnetic fields moving through physical space. According to the Maxwell equations [6], changes in magnetic and electric field are periodically complimentary; that is, changes in one field result in changes in the other. The energy of a radiating wave is due to electromagnetic energy.

- Thermochemical energy is associated with latent heat due to chemical changes. Governed by thermodynamic spontaneity, chemical species release or absorb latent heat (i.e., at constant temperature) during phase transitions. The energy as latent heat is due to thermochemical energy.

- Thermoelectric energy is associated with electron transfer due to heat. According to the Seebeck effect [7], charge transfer can be induced by heat at the phase boundary between two connected semiconductors. This results from the contrasting valence electron behavior of different semiconductors during internal energy transfer. Charge transfer, as electric current due to thermally–induced voltage, is due to thermoelectric energy.

- Mechanochemical energy is associated with mechanical motion enabled by chemical changes. Typically observed in biological life, chemical reactions break macromolecules into simpler by–products to release chemical energy. In turn, chemical energy activates motion (e.g., muscle tissue) as mechanochemical energy.

- Thermonuclear energy is associated with the release of nuclear energy by internal energy transfer. High temperature amplifies the energy output of nuclear fission or fusion reactions by inducing greater internal energy into the reaction. The released nuclear energy is passed as heat to a surrounding cooling fluid. The fluid carries thermonuclear energy.

Conversion of energy among classes and states can occur spontaneously, that is, without external intervention. Some conversions are inhibited, requiring initial energy to produce excess energy. Other conversions are improbable, occurring either negligibly or not at all. The likelihood of conversion processes is governed by the laws of thermodynamics.

Controlling Energy

Thermodynamics is the study of energy transfer, analyzing exchanges of energy. Thermodynamics dictates the limits of energy processes and of the systems they act upon. It describes how energy can be traded between a system and its surroundings, and the limits of how efficient these processes can be. It also determines which behaviors are and are not possible in this universe.

All entities in the known universe are subject to the laws of thermodynamics. Systems are continuous, isolable entities within the known universe [2]. They are rigorously segregated from surroundings by continuous boundaries; constructs as rigid as they are imaginary. Ultimately, thermodynamics is a discipline of equilibrium, deducing property changes in systems which must occur from an acting process. Changes in system properties (e.g., temperature, pressure, volume, internal energy, enthalpy, free energy) suggest interaction with surroundings, exchanging energy as work or heat. These state properties are defined as measured or quantifiable values [2]:

- Internal energy measures the bulk energy of an object with macroscopic mass. It quantifies the energy of molecules that exist. It is a specific application of thermal energy which describes the inherent energy of an object; the energy contained within its vibrating molecules that can be reclaimed or repurposed for various property changes or processes. Enthalpy, an extension of internal energy, is an expression representing internal energy and the energy required to maintain its boundaries (viz., boundary work). Enthalpy, in this sense, can be described as the gross system energy: the energy of bulk and border.

- Temperature measures the strength of energy transfer. Temperature represents the average vibrational energy of a system or its subsystems. Changes in temperature require energy: greater temperature suggests greater energy transfer, provided adequate infrastructure is available for system–surrounding interaction. Defined by the third law of thermodynamics, there exists an absolute minimum limit to temperature.

- Volume measures the physical space occupied by a system. Changes in volume require energy: energy consumption can increase volume, while energy release can decrease it. High internal energy systems can be compressed or expanded, able to sustain drastic changes in volume. In contrast, low internal energy systems are incompressible and do not experience significant or measurable volume changes.

- Pressure measures the strength of momentum transfer. Momentum is a measure of inertia, describing the energy used for motion. Changes in pressure require energy: greater pressure suggests greater energy available to move a system or its boundaries. Pressure imbalances will cause motion: immiscible bodies will push or pull, while miscible fluids diffuse and coalesce. Pressure is measured on both absolute and relative scales.

- Entropy measures unavailable energy, energy which must be dedicated to the chaotic tendencies of the universe. It describes the quality of disorder, energy confined and preoccupied to increasing randomness. When combined with temperature, entropy encourages heat exchange across system boundaries.

- Free energy measures the energy which can participate in conversion processes. It is the compliment to entropy, describing available energy which can be manipulated and directed in pursuit of productivity. The two varieties of free energy, Helmholtz and Gibbs energy, describe the maximum energy which can be contributed by or relinquished from systems.

These state properties are discretely related and mathematically interdependent, and are measured to predict or explain energy conversion processes.

The exchange of energy between a system and its surroundings is classified as work or heat. Heat [2] is the exchange of energy across system boundaries, producing temperature changes in either system or surroundings. The minimum limit of heat is dependent upon entropy. In compliment, work [2] is energy transformed: the conversion of energy to another form which is then utilized to perform actions. Work is the exchange of energy across system boundaries that enables action or phenomenon. In effect, useful work enables all transport phenomena, and is classified by the energy conversion process it represents. Rechargeable batteries operate by converting chemical internal energy into electrochemical work, used to transport electrons between electrodes [8].

Ultimately, thermodynamics regulates the behaviors of all energy transformation processes. System changes are quantified by state properties, measurable features that together define the extensive nature of the system. The property of entropy, rigorously defined by postulate, dictates the maximum efficiency of a conversion process. Then, Gibbs free energy, the penultimate thermodynamic descriptor, quantifies the maximum energy available to participate in energy conversion. Thermodynamics defines the ideal energy conversion process as high conversion efficiency with maximized total converted energy. The implementation of this principle has been pursued across history from steam engines, petroleum engines, fuel cells, and modern rechargeable batteries.

Regulating Energy

Energy conversion occurs with or without external energy input. The phenomenon of energy conversion, particularly its properties and transformation, is governed by the four laws of thermodynamics [2]:

(0) The zeroth law states entities must be in thermal equilibrium if all belong to a system in thermal equilibrium. This implies that the temperature of separated entities T_1, T_N must be in equilibrium if both are in equilibrium with temperatures of intermittent entities T_n:

$$T_1 \stackrel{!}{=} T_N \quad \text{if} \quad T_1 = T_n \wedge T_N = T_n \quad \forall \quad n \in (1, N) \tag{1.1}$$

This is the transitive property of internal energy equilibrium, providing a rigorous mathematic definition of temperature.

(1) The first law states the energy of any isolable entity, including the universe itself, must be conserved. In another interpretation, change in energy of the universe ΔU_∞, including changes of interior subsystems ΔU_N and their surroundings $\Delta U_{\widetilde{N}}$, must be equal to zero:

$$\Delta U_\infty = \Delta U_N + \Delta U_{\widetilde{N}} \stackrel{!}{=} 0 \quad \forall \quad N \tag{1.2}$$

The supplementary postulate states energy can only be converted into different varieties: it cannot be created or destroyed. For a given closed system, the change in its energy ΔU_{N} is equal to the energy passing across its boundaries: heat Q, transferred internal energy; and work W, converted energy:

$$\Delta U_{N} = Q + W \tag{1.3}$$

Together, these postulates define the principle of energy conservation.

(2) The second law states the universe is an expression of increasing disorder or entropy ΔS. Energy processes occur to increase entropy of the universe ΔS_{∞} or, equivalently, the entropy sum of any interior subsystem ΔS_{N} with its surroundings $\Delta S_{\tilde{N}}$:

$$\Delta S_{\infty} = \Delta S_{N} + \Delta S_{\tilde{N}} \overset{!}{\geq} 0 \quad \forall \quad N \tag{1.4}$$

The entropy change of the universe cannot decrease. However, entropy change of interior subsystems can change — provided complimentary changes in the surroundings increase universe entropy:

$$\Delta S_{N} < 0 \quad \Longleftrightarrow \quad \Delta S_{\tilde{N}} > \Delta S_{N} \quad \Longrightarrow \quad \Delta S_{\infty} > 0$$

An involuntary or inhibited process, requiring an initial energy input, increases universe entropy. In compliment, a voluntary or spontaneous process causes zero change in universe entropy:

$$\Delta S_{\infty} \geq 0 \quad \text{if possible}$$
$$\Delta S_{\infty} < 0 \quad \text{if impossible}$$

Entropy can be defined as measure of dispersion. Real processes are inherently inefficient, suggesting a limit to the efficiency of any energy conversion process. In addition, entropy implies all ordered systems spontaneously degrade (viz., transition to disorder) provided universe entropy increases.

(3) The third law states entropy is an absolute property: a quantifiable minimum disorder exists for all systems. This postulate, developed by modern statistical thermodynamics, declares that there exist minimum limits for absolute entropy and temperature. Entropy changes are proportional to possible microscale permutations Ω and the Boltzmann constant k_B:

$$\Delta S_{_N} = k_\beta \ln \Omega_{_N} \tag{1.5}$$

$$\lim_{\Omega_{_N} \to 1} \Delta S_{_N} = 0 \quad \Longleftrightarrow \quad \text{ideal crystal} \tag{1.6}$$

The Boltzmann factor k_β is the centerpiece of this postulate. It declares temperature and internal energy of ideal, freely–moving particles are discretely related — bridging microscale behaviors to its macroscale analogues.

The complete thermodynamic description of energy (viz., systems and processes) requires two components: entropy, the measure of stability which quantifies possibility of systems to change; and enthalpy, the measure of value which describes participation of systems during change. Enthalpy represents the sum of internal energy and boundary work, defined herein as work required to sustain or support system boundaries. The change in enthalpy of an entity is the sum of its internal energy $\Delta U_{_N}$ and boundary work $\Delta \left(PV \right)_{_N}$:

$$\Delta H_{_N} = \underbrace{\Delta \left(U \right)_{_N}}_{\text{Internal energy}} + \underbrace{\Delta \left(PV \right)_{_N}}_{\text{Boundary work}} \tag{1.7}$$

In essence, enthalpy describes *constituent* energy of a pressure–bearing system: the energy of bulk and border. Therefore, enthalpy changes describe the transfer of general energy; that is, energy absorbed or released across system boundaries. Enthalpy increases describe energy–absorbing endothermic processes, while decreases describe energy–releasing exothermic processes:

$$\Delta H_{_N} > 0 \quad \text{if endothermic (absorb energy)}$$

$$\Delta H_{_N} = 0 \quad \text{if isenthalpic (zero net change)}$$

$$\Delta H_{_N} < 0 \quad \text{if exothermic (release energy)}$$

The ultimate consequence of thermodynamics is probability of system changes: whether or not a process can occur. Irregardless of rates, processes can occur in the absence of energy transfer (i.e., enthalpy change) or molecular dispersion (i.e., entropy change). Thus, stability and availability (viz., entropy and enthalpy, respectively) must be considered in the probability of a system change. Defined by W. Gibbs [9,10], the system free energy $\Delta G_{_N}$ quantifies probability according to the energy available for isochoric work (viz., non-volume changing):

$$\underset{}{\Delta G_{_N}} = \underset{\text{Available energy}}{\Delta \left(H \right)_{_N}} - \underset{\text{Transferred heat}}{\Delta \left(TS \right)_{_N}} \tag{1.8}$$

Gibbs free energy represents the energy available for work, excluding volume expansion or contraction work. Therefore, spontaneity is directly determined by the direction and magnitudes of enthalpy and entropy (Table 1.1). Free energy decreases describe spontaneous exergonic process, while increases describe non–spontaneous endergonic processes:

$$\begin{aligned} \Delta G_{_N} &< 0 \quad \text{if exergonic (spontaneous)} \\ \Delta G_{_N} &= 0 \quad \text{if equilibrium (zero net change)} \\ \Delta G_{_N} &> 0 \quad \text{if endergonic (non-spontaneous)} \end{aligned}$$

Exergonic processes favor spontaneity toward the final state, while endergonic processes favor spontaneity toward the initial state. Processes at equilibrium experience do not favor either process.

1.2 Defining Free Energy

Free energy is the penultimate property of thermodynamics. Free energy measures usable reserved energy, which is available to participate as work and not heat. For closed systems, free energy change is the difference between system energy change and heat (i.e., energy transferred between system and surroundings) [2]:

$$\underset{\text{Free energy}}{\Delta \Gamma_{_N}} = \underset{\text{System energy}}{\Delta U_{_N}} - \underset{\text{Passed heat}}{Q_{_{N \leftrightarrow \widetilde{N}}}} \tag{1.9}$$

Table 1.1.
Gibbs spontaneity criterion. By definition of Gibbs free energy, spontaneity depends on enthalpy and entropy.

	Endothermic	*Isenthalpic*	*Exothermic*
	$\Delta H > 0$	$\Delta H = 0$	$\Delta H < 0$
Possible	Exergonic	Exergonic	Exergonic
$\Delta S > 0$	if $T\Delta S > \Delta H$	$\Delta G < 0$	$\Delta G < 0$
Isentropic	Endergonic	Equilibrium	Exergonic
$\Delta S = 0$	$\Delta G > 0$	$\Delta G = 0$	$\Delta G < 0$
Impossible	Endergonic	Endergonic	Exergonic
$\Delta S < 0$	$\Delta G > 0$	$\Delta G > 0$	if $\Delta H > T\Delta S$

Free energy is measured in energy per moles of process or reaction, equivalently interpreted as converted energy after $6.022 \cdot 10^{23}$ instances of reaction.

Free energy change is a state property, only dependent on system states at equilibrium (i.e., before and after energy processes). In contrast, work and heat are path properties, inconveniently reliant on both state and process (i.e., *how* systems change). Accounting for this volatility, free energy represents the theoretically available energy after unavoidable losses to the natural world. In this sense, it is the maximum limit of output energy from reversible energy processes — assuming minimal system-surroundings energy transfer:

$$\Delta\Gamma_{N} \coloneqq \lim_{Q \to T\Delta S_{N}} \left(W_{N \leftrightarrow \widetilde{N}} \right) \tag{1.10}$$

Two varieties of free energy are used in thermodynamic description. Helmholtz free energy, proposed in 1882 by H. Helmholtz [11], is the maximum convertible energy available for all work processes. Gibbs free energy, proposed in 1873 by J. W. Gibbs

[10], is the maximum convertible energy available for non-volumetric work processes. Their derivations imply particular restriction: Helmholtz energy change is the limit postulated for reversible isochoric or constant volume processes, and Gibbs energy change is the limit for reversible isopiestic or constant pressure processes.

Electrochemical energy storage favors Gibbs free energy. First, it applies to presently studied energy systems due to its constant pressure condition. Second, Gibbs free energy measures reclaimable energy for non–expansion work: this descriptor is the conceptual basis for voltage. Though, as is the case for many solid battery electrodes, Helmholtz and Gibbs energies converge for incompressible systems.

Interpreting Free Energy

Free energy represents the utility of thermodynamics, describing feasibility of processes. It represents maximum convertible energy relative to available system energy and minimized entropic losses:

$$\underset{\text{Convertible energy}}{\Delta\Gamma_{N}} = \underset{\text{Available energy}}{\Delta U_{N}} \underset{\text{Lost energy}}{- T_{N}\Delta S_{N}} \tag{1.11}$$

- Available energy change ΔU_{N} describes the total available energy of a system that can participate in energy processes. In Helmholtz energy, it is dependent on system internal energy change. In Gibbs energy, it is dependent on enthalpy (Equation 1.29); in turn, dependent upon system internal energy change and boundary work. Note Gibbs energy is exclusive of, yet implicitly dependent on, boundary work (Equation 1.26). Isopiestic enthalpy, combination of internal energy change and boundary work, yields the energy available for non-expansion work.

- Transferred energy change $T_{N}\Delta S_{N}$ describes energy of a system interacting across the system-surroundings interface. There exists a fundamentally trivial, yet shamefully overlooked, implication of the second law: a system is inseparably bonded to its surroundings. To increase entropy of the universe, entropy

changes of surroundings *must* compliment entropy changes of their systems. In effect, energy transfer is an inevitable consequence of symbiosis: resultant energy change quantifies the unbreakable connection between systems with their surroundings.

- Free energy change $\Delta\Gamma_{N}$ describes the greatest possible convertible energy of a system [2]. Identically, it is the limit of non-expansion or non-compression work a system may perform. Helmholtz energy describes changes under constant volume, while Gibbs energy describes changes under constant pressure. It is the remainder of system energy after consideration of entropy: the difference between maximum reclaimable energy of a system and unavoidable energy transfer between system and surroundings.

Extrapolation of free energy, along with the law of energy conservation, defines process efficiency [2]: the maximum extent of energy conversion in energy processes. Process efficiency f is a relative measure, comparing output of energy processes to the theoretical total energy that can participate. Efficiency is reported on a relative scale between zero and unity. It can be expressed as a function of free energy, normalized to the available system energy:

$$f \quad := \quad \frac{\Delta\Gamma_{N}}{\Delta U_{N}} \quad = \quad 1 - \frac{T_{N}\Delta S_{N}}{\Delta U_{N}} \tag{1.12}$$

The mathematic expression of process efficiency has an important consequence: efficiency is dependent upon the negative contribution of entropic effects. Thus, if enthalpic contributions for given energy processes are non-zero, then there will be irresolvable efficiency reductions. This suggests energy losses are inherent and natural: unoptimized processes will always be irreversible, permitting energy exchange between systems and surroundings. Alternatively, this suggests that there is a maximum limit to efficiency of practical processes: inefficiencies will approach this maximum with increasing optimization, but will never reach unity if entropic losses are unaddressed. This conclusion substantiates energy conservation, precluding perpetual motion machines or energy devices which create energy.

The two forms of free energy, Helmholtz energy and Gibbs energy, describe available energy postulated under conservation of certain state properties. Dependence on either constant volume or constant pressure assumptions is due to variability of systems with maximal degrees of freedom.

Isochoric Free Energy

Helmholtz free energy is defined as the total energy available for all reversible work. Helmholtz energy is a function of internal energy U, temperature T, and entropy S:

$$A \coloneqq U - TS \tag{1.13}$$

Helmholtz free energy represents the maximum energy that can be potentially utilized as work in an energy conversion process. Helmholtz free energy ΔA_{N} is confined to the following conditions:

- Total energy available for all work processes.
- Energy change of a system under constant temperature T_{N} and volume V_{N}.

To derive its mathematic definition, begin by defining a closed, macroscopic system at constant temperature and volume. Internal energy change ΔU_{N} of closed systems depends on work W and heat Q interacting with surroundings:

$$\Delta U_{N} = W + Q \quad : \quad \begin{matrix} \Delta V_{N} = 0 \\ \Delta T_{N} = 0 \end{matrix} \tag{1.14}$$

Define heat as reversible. Free energy represents the *maximum energy available* for work — this implies a reversible process in which heat transfer is minimized. Reversible heat, the minimum limit of heat as irreversibility vanishes $Q_{ir} \to 0$, is a function of temperature and entropy:

$$\text{Let } Q = T_{N}\Delta S_{N} \quad \because \quad T_{N}\Delta S_{N} = \lim_{Q_{ir}\to 0}(Q) \quad \text{if reversible process} \tag{1.15}$$

Specify the system (Equation 1.14) with reversible heat (Equation 1.15):

$$\Delta U_{N} = W + \underset{\text{Eq. 1.15}}{T_{N}\Delta S_{N}} \tag{1.16}$$

Isolate total work W from all energy components:

$$W = \Delta U_{N} - T_{N}\Delta S_{N} \tag{1.17}$$

Then, reorganize terms by phase instead of property:

$$\begin{aligned} W = &\quad \left(U_{N} - T_{N}S_{N}\right)_{1} - \left(U_{N} - T_{N}S_{N}\right)_{0} \\ \implies W &= \Delta\left(U_{N} - T_{N}S_{N}\right) \end{aligned} \tag{1.18}$$

Thus, total reversible work under constant temperature and volume is a function of only state variables. This relationship implies the existence of the new property known as Helmholtz free energy. Helmholtz energy change ΔA_{N} is dependent on internal energy, temperature, and entropy:

$$\therefore \Delta A_{N} \coloneqq \Delta U_{N} - T_{N}\Delta S_{N} \quad : \quad \begin{array}{c} \Delta V_{N} = 0 \\ \Delta T_{N} = 0 \\ \text{Reversible} \end{array} \tag{1.19}$$

Isopiestic Free Energy

Gibbs free energy is defined as the total energy available for reversible work — except work of boundary changes. Isopestic work includes all work processes except work of volumetric expansion or compression. Gibbs free energy is a function of enthalpy, temperature, and entropy:

$$G \coloneqq H - TS \tag{1.20}$$

Gibbs free energy represents the maximum energy that can be *effectively* used from energy conversion processes. Gibbs free energy ΔG_{N} is applicable to the following conditions:

- Total energy available for all work that is unrelated to system volume changes.
- Energy change of a closed system under constant temperature T_{N} and pressure P_{N}.

The mathematic form of Gibbs energy can be derived by Socratic reasoning. Begin by defining a closed, macroscopic system at constant temperature and pressure:

$$\Delta U_{N} = W + Q \quad : \quad \begin{matrix} \Delta P_{N} = 0 \\ \Delta T_{N} = 0 \end{matrix} \tag{1.21}$$

Heat and work transfer must be specified. First, recall the definition of work: energy conversion processes between systems and surroundings. The total work occurring between a system and its surroundings is defined as the sum of constituent, independent work processes:

$$W = \sum_{i} W_{i} \quad \forall \quad i \in \{ \text{ expansion, charge transfer, polarization, } \dots \} \tag{1.22}$$

Total work, as is, expresses too many elements as all energy-dependent activities are represented. Thus, work is described as expansion $W_{\Delta V}$ or non–expansion $W_{\widetilde{\Delta V}}$ (viz., isochoric):

$$W = \sum_{i} W_{i} \equiv W_{\Delta V} + W_{\widetilde{\Delta V}} \tag{1.23}$$

Second, define heat as reversible to maximize useful work. Reversible heat, the minimum limit as irreversibility vanishes $Q_{ir} \to 0$, is a function of temperature and entropy:

$$\text{Let } Q = T_{N} \Delta S_{N} \quad \because \quad \text{reversible process} \tag{1.24}$$

Now, specify the system (Equation 1.21) with work (Equation 1.23) and heat (Equation 1.24):

$$\Delta U_{N} = \underset{\text{Eq. 1.23}}{W_{\Delta V} + W_{\widetilde{\Delta V}}} + \underset{\text{Eq. 1.24}}{T_{N} \Delta S_{N}} \tag{1.25}$$

Gibbs free energy is independent of chloric work, so chloric dependence must be eliminated. Recall chloric work describes system volume changes. At constant pressure, expansion work is proportional to surrounding pressure $P_{\tilde{N}}$ and volume change ΔV_N:

$$W_{\Delta V} = -\Delta\left(PV\right)_N = -P_{\tilde{N}}\Delta V_N \quad : \quad \Delta P_N = 0 \tag{1.26}$$

Further specify the system (Equation 1.25) with the definition of expansion work (Equation 1.26):

$$\Delta U_N = T_N \Delta S_N \underbrace{-P_{\tilde{N}}\Delta V_N}_{\text{Eq. 1.26}} + W_{\widetilde{\Delta V}} \quad : \quad \begin{matrix} \Delta P_N = 0 \\ \Delta T_N = 0 \\ \text{Reversible} \end{matrix} \tag{1.27}$$

Then isolate isochoric work $W_{\widetilde{\Delta V}}$ from all energy components:

$$W_{\widetilde{\Delta V}} = \Delta U_N + P_{\tilde{N}}\Delta V_N - T_N \Delta S_N \tag{1.28}$$

This system is simplified by introducing enthalpy, the total available system energy. System enthalpy change ΔH_N is comprised of the available internal energy ΔU_N and work of continuity W_∂. At constant pressure, work of continuity simplifies to chloric work (Equation 1.26):

$$\begin{aligned} &\text{Let } \Delta H_N = \Delta U_N + W_\partial \\ \implies &\Delta H_N = \Delta U_N + P_{\tilde{N}}\Delta V_N \quad \because \quad \Delta P_N = 0 \end{aligned} \tag{1.29}$$

Simplify the system description (Equation 1.28) using the enthalpy definition (Equation 1.29):

$$W_{\widetilde{\Delta V}} = \underbrace{\Delta H_N}_{\text{Eq. 1.29}} - T_N \Delta S_N \quad : \quad \begin{matrix} \Delta P_N = 0 \\ \Delta T_N = 0 \\ \text{Reversible} \end{matrix} \tag{1.30}$$

Then, reorganize terms by phase instead of property:

$$\begin{aligned} W_{\widetilde{\Delta V}} &= \left(H_N - T_N S_N\right)_1 - \left(H_N - T_N S_N\right)_0 \\ \implies W_{\widetilde{\Delta V}} &= \Delta\left(H_N - T_N S_N\right) \end{aligned} \tag{1.31}$$

This relationship implies the existence of a new property called Gibbs free energy. Gibbs free energy change ΔG_N is dependent on enthalpy, temperature, and entropy:

$$\therefore \Delta G_N \coloneqq \Delta H_N - T_N \Delta S_N \quad : \quad \begin{matrix} \Delta P_N = 0 \\ \Delta T_N = 0 \\ \text{Reversible} \end{matrix} \tag{1.32}$$

What happened to the work of expansion? Combining internal energy change ΔU_N and work of continuity W_∂ implicitly eliminates work of expansion. This only occurs under pressure.

Begin by defining the enthalpy change of a system at constant pressure (Equation 1.29):

$$\Delta H_N = \Delta U_N + P_N \Delta V_N \quad : \quad \Delta P_{\widetilde{N}} = 0$$

Internal energy change of a general system is unknown. However, for a closed system, it is always equal to heat and work transferred across the system boundary. Specify the system using this definition of internal energy (Equation 1.21), then the definition of work (Equation 1.23):

$$\Delta H_N = \underset{\text{Eq. 1.21}}{Q} + \underset{\text{Eq. 1.23}}{W_{\Delta V} + W_{\widetilde{\Delta V}}} + P_{\widetilde{N}} \Delta V_N$$

Further specify the system by defining choric work (Equation 1.26):

$$\Delta H_N = Q \underset{\text{Eq. 1.26}}{- P_N \Delta V_N} + W_{\widetilde{\Delta V}} + P_N \Delta V_N \quad : \quad \Delta P_N = 0$$

Expansion work appears with both positive and negative magnitudes, eliminating its dependence:

$$\Delta H_N = Q - \cancel{P_N \Delta V_N} + W_{\widetilde{\Delta V}} + \cancel{P_N \Delta V_N}$$

Thus, enthalpy change of a closed system under constant pressure is independent of expansion work:

$$\therefore \Delta H_N = Q + W_{\widetilde{\Delta V}} \quad \because \quad \Delta P_N = 0 \tag{1.33}$$

Evaluating Free Energy

To declare free energy as a conclusive thermodynamic property is bold, even deceptive. It is pedagogical simplification which, unintentionally, obscures the significance of thermodynamic description: the intricate concert of many state variables at equilibrium. Yet, even then, deception is contextual — for incompressible systems, free energy becomes independent of restriction in the case of vanishing internal energy and entropy. Helmholtz and Gibbs energy changes converge for solid systems, extending the application of these concepts to real electrochemical systems.

Helmholtz and Gibbs energies represent different interpretations of free energy [2]: Helmholtz describes potential for all work at constant volume, while Gibbs describes potential for non-expansion work at constant pressure. These isochoric or isopiestic conditions restrict their practical value. These differences are summarized as follows:

$$\begin{aligned} \Delta A_{N} &= \lim_{Q_{ir}\to 0}\left(W_{\widetilde{\Delta V}} + W_{\partial}\right) &&= \Delta U_{N} && - T_{N}\Delta S_{N} && : \begin{matrix}\Delta V_{N} = 0 \\ \Delta T_{N} = 0\end{matrix} \\ \Delta G_{N} &= \lim_{Q_{ir}\to 0}\left(W_{\widetilde{\Delta V}}\right) &&= \Delta U_{N} - W_{\partial} && - T_{N}\Delta S_{N} && : \begin{matrix}\Delta P_{N} = 0 \\ \Delta T_{N} = 0\end{matrix} \end{aligned}$$

Their difference lies in approach to boundary work W_{∂}, the work of maintaining system boundaries (Equation 1.26). Thus, by comparison, Helmholtz and Gibbs energy change are related by volume and pressure:

$$\Delta G_{N} = \Delta A_{N} + \Delta\left(PV\right)_{N} \tag{1.34}$$

Context determines the relevance of boundary work. Classical thermodynamics was built to explain and predict the behaviors of gases, entities of vast internal energy. Gases can sustain great and irregular volume changes; Helmholtz and Gibbs energies of gases change in proportion. In contrast, the behaviors of liquids and solids are less drastic, even with species considered compressible. This suggests the waning significance of boundary work as system energy decreases.

$$\lim_{U\to\min U}\left(W_{\partial}\right) = 0 \quad \Longrightarrow \quad \Delta G_{N} \simeq \Delta A_{N} \quad \text{if incompressible} \tag{1.35}$$

As internal energy approaches its minimum limit (i.e., for solids, incompressible liquids), Gibbs and Helmholtz energies converge. For solids, the percent difference between these free energies is ca. $< 5\%$ [2]. This is often the case for changing solid electrodes in electrochemical energy storage devices.

1.3 Electric Voltage

Potential difference or voltage E is the grand consequence of free energy. As an interpretation of Gibbs free energy, voltage measures the strength or tendency for electric transport [12]: greater voltage suggests greater available energy to transport charge, and zero voltage suggests no available energy. In electrochemical systems, voltage represents maximum chemical energy for electron transport between source and destination. In this interpretation, the limit of energy extractable from an electrochemical process is given by voltage.

There are three principles underlying voltage [12]:

- Voltage is a representation of the free energy for electrical work. For practical, constant pressure electrochemistry, voltage represents Gibbs free energy:

$$\Delta E_{_N} \propto \Delta G_{_N} \tag{1.36}$$

  Note that this implies two conditions: the constant pressure assumption suggests exclusion of boundary work from consideration because volumetric changes do not contribute to charge transport. Also, this assumes all available energy will contribute solely to electrical work and no other non-expansion work processes.

- As voltage is the measure of energy available for charge transport, it must be expressed as normalized to transported charge. The total transported electron charge, per process, is given by the reaction stoichiometry z and Faraday constant F:

$$E_{_N} \propto \frac{1}{zF} \tag{1.37}$$

Reaction stoichiometry expresses moles of electrons participating per mole of process and Faraday constant expresses charge of one mole of electrons. Their product yields the total charge transported per process.

- Conventions for voltage are defined oppositely for Gibbs free energy. A spontaneous reaction exhibits positive voltage and negative Gibbs energy. Therefore, voltage is related to the negative of Gibbs free energy.

Altogether, these three features describe the principle factors of voltage. Voltage is dependent on the negative of Gibbs free energy, electron stoichiometry, and Faraday constant:

$$E_{_N} \coloneqq -\frac{\Delta G_{_N}}{zF} \tag{1.38}$$

Note this assumes that electric work constitutes the entirety of non-expansion work: that is, all available energy will only contribute to the work of charge transport. This is consistent with the definition of Gibbs free energy, the maximum limit of energy that can be provided by a system in a constant pressure process.

In electrochemical systems, the Boltzmann or thermal voltage E_β [12] is a characteristic property that represents electrostatic behavior due to temperature and internal energy. It is an extension of the voltage concept, equivalently expressed with volt units by dimensional analysis, which describes energy from molecular or thermal motion. The Boltzmann voltage ΔE_β is a function of Boltzmann constant k_β, temperature T, fundamental charge q, valency z:

$$E_\beta = \frac{k_\beta T}{zq} \tag{1.39}$$

Whereas conventional electric voltages measure electrostatic potentials typically from an external impetus, Boltzmann voltage represents electrostatic potentials arising from internal molecular motions. The Boltzmann voltage appears as a characteristic property in kinetics of electrochemical systems.

Summary

Thermodynamics underlies energy quantification for energy storage systems. Various modes of energy can be stores, supplied, or converted using specifically engineered conversion devices or storage technologies. The theoretical framework for electrical energy analysis is based on the fundamental mathematic laws of thermodynamics and the concept of free energy. In particular, the free energy concept established by J.W. Gibbs [10] is the link between fundamental thermodynamics and electric potential measured as voltage.

In its thermodynamic interpretation, voltage represents the maximum energy available for electric work. Voltage also plays a significant role in electrochemical kinetics to describe electrostatic potentials. Chapter 2 describes this relationship in mathematic detail, demonstrating the microscale relationship between charge distribution and electric potential.

CHAPTER 2: CHARGE TRANSPORT

Thermodynamics determines how much energy is stored; kinetics determines how fast energy is delivered. Microscale kinetics control delivery power in rechargeable energy storage devices. In turn, kinetics depends on the individual rates of constituent elementary mechanisms – particularly those which oppose and impede charge transport.

This chapter describes the various mechanisms of lithium transfer, their mathematic representation through the Poisson Nernst Planck equations, and the dimensionless groups which quantify their significance in energy storage systems. Energy and power, visualized with the Ragone diagram, determine the application of energy storage systems. The versatility of the rechargeable lithium-ion battery, in terms of energy and power, drives its dominance in both research and commercial sectors.

2.1 Kinetics of Lithium-ion Batteries

In rechargeable lithium-ion batteries, charging or discharging processes promote lithium ionization and inter-electrode transport [13, 14]. Lithium species travel between electrodes as cations through electrolyte and across electrode-electrolyte boundaries. In compliment, electrons travel between electrodes through an external conductive circuit. Ultimately, the speed of lithium storage controls power, the speed of energy storage. In turn, power is controlled by complex transport pathways with elementary processes dependent on coordinate geometry, spatial position, ionic species, and chemical or material properties [13, 15].

According to the principles of mass conservation [2], the charge associated with a defined system is the linear combination of charge contained within system volume and charge passing across system boundaries. Lithium transported in spatial coordinates is measured by charge flux $\mathbf{J}$, time rate of lithium passage through defined

surface area. Lithium flux depends on mobility b, the ability to pass through the bulk medium, and potential gradient $\nabla\mu$, the thermodynamic impetus for lithium transport. From the Einstein Smoluchowski relation [3, 16], mobility is proportional to chemical diffusion coefficient D, temperature T, concentration c, and Boltzmann factor k_β:

$$b = \frac{D}{k_\beta T} \tag{2.1}$$

Thus, lithium flux $\mathbf{J}$ [14] depends on diffusion coefficient D, concentration c, chemical potential μ, temperature T, and Boltzmann factor k_β:

$$\mathbf{J} = -bc\nabla\mu = Dc\left(\frac{\nabla\mu}{k_\beta T}\right) \tag{2.2}$$

The gradient of charge flux $\nabla \cdot \mathbf{J}$ determines the time rate of lithium concentration change by spatial lithium movement:

$$\frac{\partial c}{\partial t} = -\nabla \cdot \mathbf{J} \tag{2.3}$$

There are various modes or pathways for lithium transport phenomena, classified according to spatial regime: bulk phenomena occur in electrode or electrolyte phases, while surface phenomena occur at the microscale interphase boundary. The mechanisms associated with transport phenomena vary according to their location, mechanism, and associated material factors.

Intraphase Transport Phenomena

In bulk charge transport, there are four principle mechanisms for lithium interaction [13, 14]:

- Diffusion is net particle movement due to chemical potential or concentration gradients. Chemical diffusion is due to Brownian motion or molecular agitation of concentrated chemical species in a bulk region. Lithium species naturally distribute through electrode and electrolyte bulk phases according to chemical potential μ_c, the potential energy for chemical interaction. Relative to reference

state $\mu_{c,0}$, chemical potential μ_c depends on concentration c, temperature T, and Boltzmann factor k_β:

$$\mu_c = \mu_{c,0} + k_\beta T \ln c \tag{2.4}$$

Lithium flux by diffusion depends on chemical diffusion coefficient D and concentration gradient ∇c:

$$\mathbf{J} = -bc\nabla\mu_c = -D\nabla c \tag{2.5}$$

- Migration is particle motion due to applied electric field. According to the applied electric impetus, electric potential gradients give rise to electrochemical migration in a polarizable medium. Electrochemical migration depends on electrostatic potential μ_e, the potential energy from external electric fields. Relative to reference state $\mu_{e,0}$, electrostatic potential depends on applied voltage E, ion valency z, and fundamental charge q:

$$\mu_e = \mu_{e,0} + zqE \tag{2.6}$$

Combining definitions of mobility and electrostatic potential, lithium flux by migration depends on voltage gradient ∇E, chemical diffusion coefficient D, concentration c, and Boltzmann potential E_β:

$$\mathbf{J} = -bc\nabla\mu_e = -\frac{Dc}{E_\beta}\nabla E \tag{2.7}$$

- Advection is passive particle movement due to bulk phase kinematic motion. Particles entrained in moving fluid media (i.e., low viscosity) will transport with the fluid stream. Lithium flux by advection depends on concentration c and fluid velocity v:

$$\mathbf{J} = \mathbf{v}c \tag{2.8}$$

- Conversion is chemical reaction that causes chemical phase or crystal lattice changes. Reaction or binding of lithium with electrode materials coincides with chemical or crystal changes. Rate laws of reaction order n are used to model homogeneous chemical conversion. Concentration change rate for conversion is proportional to rate constant k_n, concentration c, and reaction order n:

$$\frac{dc}{dt} = k_n c^n \tag{2.9}$$

The four mechanisms of bulk lithium transport occur in both electrolyte and electrode bulk phases. The expression of these phenomena are dependent upon the bulk velocity, polarizability, conductivity, and permeability of the medium to lithium ions [13, 15].

Interphase Transport Phenomena

Conventional battery electrodes are semi-polarizable surfaces, supporting both Faradaic and non-Faradaic charge transport. The non-Faradaic phenomenon is the electric double layer [14, 17], a microscale region at the electrolyte-electrode interface characterized by non-isotropic ion accumulation and its steric effects. The Faradaic phenomenon is interfacial charge transfer, spatial translation of charges across the electrolyte-electrode interface. Interfacial charge transfer causes charge flux between the electrolyte and electrode phases.

The non-Faradaic electric double layer (Fig. 2.1) contains non-isotropically distributed charges – including ions stabilized by surrounding solvent molecules – whose steric interactions cause electrochemical (viz., electrostatic and chemical) potential gradients. According to the Stern Gouy Chapman model [18], the Stern compact regime and Gouy Chapman diffuse regime express different electrostatic effects as a function of interface distance. The Stern compact regime [18, 19], adjacent to the electrode surface, is characterized by electrochemical potential gradients due to adsorbed ions and solvent molecules. The Stern compact regime contains two smaller regions [19]: the inner Helmholtz region contains de-solvated species immediately ad-

jacent to the electrode surface, while the outer Helmholtz region contains solvated ions between the inner Helmholtz region and diffuse regime. The normal length of the Helmholtz region is the effective diameter of adsorbed species, while the normal length of the Helmholtz region is the effective diameters of solvated ion species. The Gouy Chapman diffuse regime [20,21], between the Stern regime and bulk electrolyte, is characterized by exponentially–weakening steric effects as distance from the outer Stern plane increases. Debye length [22] represents normal screening length of the Gouy Chapman regime. In low concentration electrolyte [23], Debye length λ_D depends on electrolyte relative permittivity ε_s, free space permittivity ε_0, Boltzmann voltage E_β, valency z, fundamental charge q, and concentration c:

$$\lambda_D = \sqrt{\frac{\varepsilon_s \varepsilon_0 / 2}{q \sum_i \left(zc / E_\beta \right)_i}} \tag{2.10}$$

In ideal (i.e., dilute and monovalent) electrolytes [23], characteristic length is related to charge concentration: the characteristic length of the Stern compact regime is considered negligible relative to that of the Gouy Chapman diffuse regime.

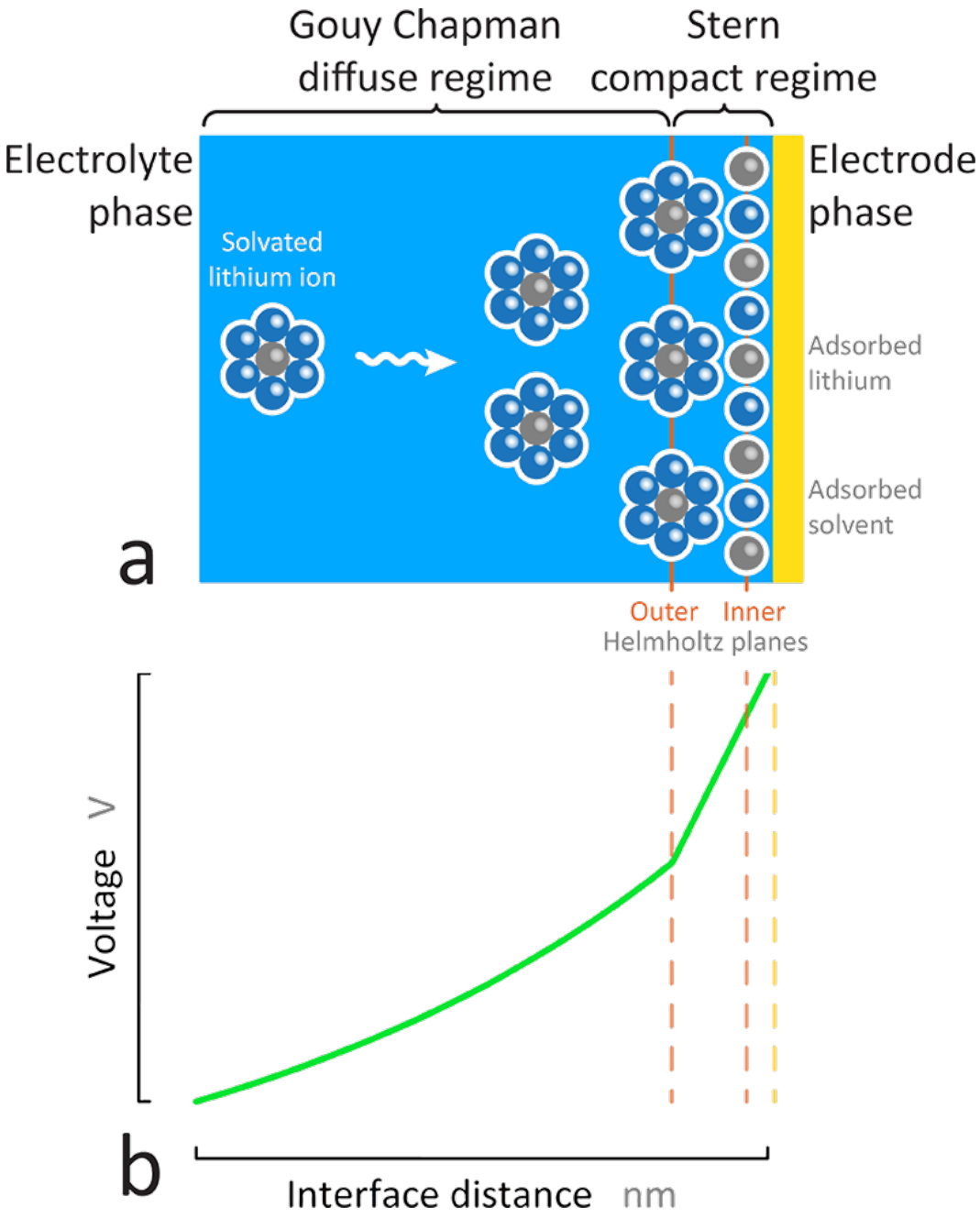

Figure 2.1. *The electric double layer.* (a) In a polarizable electrolyte with applied electric field, steric charge interactions cause concentration polarization near electrode surfaces. (b) Charge accumulation causes different electrostatic effects in the Stern and Gouy Chapman regimes.

Faradaic charge transfer causes lithium flux across the electrode-electrolyte interface (i.e., between inner electrode surface and inner Helmholtz region of Stern compact regime). In classic models, first-order chemical reactions occur within the Stern compact regime of the electric double layer, representing charge transport into electrode and electrolyte phases. Across the electolyte-electrode boundary, electrolyte–bound charge species Li^+ (viz., oxidized species with concentration c_{ox}) binds with an electron to form electrode–bound species Li^0 (viz., reduced species with concentration c_{red}):

$$\mathrm{Li}^{+}_{(\mathrm{l})} + \mathrm{e} \underset{\mathrm{k_A}}{\overset{\mathrm{k_C}}{\rightleftharpoons}} \mathrm{Li}^{0}_{(\mathrm{s})} \tag{2.11}$$

During electrode lithiation, the forward reduction reaction or cathodic reaction occurs with rate constant k_C. Conversely, during electrode delithiation, the reverse oxidation reaction or anodic reaction occurs with rate constant k_A.

In semi-polarizable electrodes, Faradaic interface charge transfer and non-Faradaic double layer electrostatics are intricately convoluted. Kinetic models depend on electrostatic behavior because Faradaic charge transfer occurs within the electric double layer, particularly the Stern compact regime. The Frumkin Butler Volmer model [24], a general model of electrode kinetics, relates interfacial charge flux to electric potential across the Stern compact regime. Stern overpotential η_c, the difference between electrode surface voltage E_e, compact–diffuse regime boundary voltage E_c, and reference voltage $E_{c,0}$:

$$\eta_c = E_e - E_c - E_{c,0} \tag{2.12}$$

In the Frumkin Butler Volmer model [24], net charge flux $\mathbf{J}$ in normal direction n depends on rate constants k_A, k_C; charge concentration c_{ox}, c_{red}; transfer coefficients α_A, α_C; Boltzmann voltage E_β; and Stern overpotential η_c:

$$\mathbf{J} = k_A c_{red} \exp\left(\alpha_A \frac{\eta_c}{E_\beta}\mathbf{n}\right) - k_C c_{ox} \exp\left(-\alpha_C \frac{\eta_c}{E_\beta}\mathbf{n}\right) \tag{2.13}$$

There exist two limiting cases of the Frumkin Butler Volmer model, relating charge flux to different overpotentials depending on significance of the Stern compact regime.

If electrostatic effects from the Stern compact regime are negligible (i.e., Debye length accurately approximates total electric double layer length), the Chang Jaffe kinetic model best describes interfacial charge transport. In the Chang Jaffe model [25], net charge flux $\mathbf{J}$ in normal direction $\mathbf{n}$ depends on rate constants k_A, k_C and charge concentration c_{ox}, c_{red} at the compact–diffuse regime boundary:

$$\mathbf{J} = k_A c_{red}\mathbf{n} - k_C c_{ox}\mathbf{n} \tag{2.14}$$

In the Chang-Jaffe model, charge concentrations are implicitly related to the Stern overpotential [25–27].

If electrostatic effects from the Gouy Chapman regime are negligible (i.e., Debye length does not significantly contribute to total electric double layer length), the Butler Volmer kinetic model best describes interfacial charge transport. The Butler Volmer kinetic model [12, 28] relates interfacial reaction rates to double layer overpotential η_s, the difference between electrode surface voltage E_e, bulk electrolyte voltage E_s, and reference voltage $E_{s,0}$:

$$\eta_s = E_e - E_s - E_{s,0} \tag{2.15}$$

Thus, net charge flux $\mathbf{J}$ in normal direction $\mathbf{n}$ depends on rate constants k_A, k_C; charge concentration c_{ox}, c_{red}; transfer coefficients α_A, α_C; Boltzmann voltage E_β; and double layer overpotential η_s:

$$\mathbf{J} = k_A c_{red} \exp\left(\alpha_A \frac{\eta_s}{E_\beta}\mathbf{n}\right) - k_C c_{ox} \exp\left(-\alpha_C \frac{\eta_s}{E_\beta}\mathbf{n}\right) \tag{2.16}$$

Though developed first [12], Butler Volmer kinetics is a particular solution of more general Frumkin Butler Volmer kinetics expressed in terms of electric potential across the electric double layer.

2.2 Continuity of Lithium Transport

The law of conservation [2] governs spatiotemporal exchange of conserved quantities including mass, momentum, energy, and charge. Applied to charge transport, the law of conservation states charge must remain constant within a system; changes are due to chemical conversion into different species or passage across system boundaries. For any chemical species i in phase N, concentration change depends on flux divergence $\nabla \cdot \mathbf{J}$ and chemical conversion rate r [14]:

$$\frac{\partial c}{\partial t} + \nabla \cdot \mathbf{J} = r \quad \forall \quad i, N \tag{2.17}$$

The continuity equation is a spatiotemporal vector function of geometry (i.e., planar, cylindrical, spherical coordinates), spatial position, and time. In homogeneous and dilute systems (e.g., steric interactions are negligible), chemical conversion rate and concentration change are reasonably independent of spatial position.

During charge or discharge of rechargeable batteries, the complete change transport pathway encompasses three phases: bulk electrolyte N_1, electrolyte-electrode boundary N_s, and bulk electrode N_2. With respect to a reference electrode, the source and destination endpoints for lithium transport are the bulk electrode and electrolyte.

The Poisson Nernst Planck Equations

In rechargeable batteries [14, 29, 30], charge transport includes diffusion, electrostatic, advection, and chemical conversion phenomena. Electrochemical potential μ, the linear combination of electric μ_e and chemical μ_c potentials, is the gross thermodynamic measure of internal and electrostatic energies. Electrochemical potential is a function of concentration c, voltage E, fundamental charge q, valency z, temperature T, and Boltzmann factor k_β:

$$\mu = \mu_c + \mu_e = k_\beta T \ln c + zqE \tag{2.18}$$

Electrochemical charge flux $\mathbf{J}$, change passage across system boundaries, depends on electrochemical potential gradient $\nabla\mu$, charge mobility b, concentration c, and advection velocity $\mathbf{v}$:

$$\mathbf{J} = -bc\nabla\mu + \mathbf{v}c = -D\nabla c - \frac{Dc}{E_\beta}\nabla E + \mathbf{v}c \quad \forall \quad i, N \tag{2.19}$$

By laws of conservation, changes in charge concentration depend on electrochemical charge flux gradient and conversion rate. The Nernst Planck equation [15], the mathematic statement of charge continuity, expresses charge transport as a function of diffusion, electrostatic, advection, and chemical conversion phenomena:

$$\frac{\partial c}{\partial t} = -\nabla \cdot \mathbf{J} + r = \nabla D\nabla c + \nabla\frac{Dc}{E_\beta}\nabla E - \nabla\left(\mathbf{v}c\right) - k_n c^{n-1} \quad \forall \quad i, N \tag{2.20}$$

Across all species i, the Nernst Planck equation comprises an unspecified equation set with one degree of freedom. The Poisson equation addresses the final degree of freedom, relating electric potential to total charge concentration:

$$q\sum_i \left(zc\right)_i = -\nabla\varepsilon\nabla E \quad \forall \quad N \tag{2.21}$$

Together, the Poisson Nernst Planck system of equations [26, 27, 30–32] comprises a specified equation set describing charge transport – including diffusion, advection, migration, and chemical conversion components. The two equations are reciprocative: the Nernst Planck equation describes spatiotemporal charge conservation and the Poisson equation relates total charge density to electrostatic potential.

Dimensionless Groups of Charge Transport

Dimensionless groups [33], the ratio of characteristic properties, compare significance of relevant transport phenomena. Characteristic properties represent the strength of transport mechanisms: for example, diffusion coefficient D characterizes diffusion, bulk velocity $\mathbf{v}$ characterizes advection, and rate constant k_n characterizes bulk reaction. Since charge transport includes various independent phenomena, dimensionless groups serve as quantitative measures of dominant or inhibiting transport mechanisms.

Dimensionless groups are derived from non–dimensionalization of continuity equations [33]. Thus, the dimensionless groups of charge transport appear in the dimensionless Poison Nernst Plank equations. For each species i and phase N, variables x are related to their dimensionless analogues $\widetilde{x}$ by characteristic properties x^*:

$$c = \widetilde{c}\, c^* \qquad t = \widetilde{t}\,\frac{\lambda^{*\,2}}{D^*} \qquad E = \widetilde{E}\, E^*$$

$$D = \widetilde{D}\, D^* \qquad \varepsilon = \widetilde{\varepsilon}\,\varepsilon^* \qquad \eta = \widetilde{\eta}\,\eta^*$$

$$\mathbf{J} = \widetilde{\mathbf{J}}\,\frac{D^* c^*}{\lambda^*} \qquad \nabla = \widetilde{\nabla}\,\frac{1}{\lambda^*} \qquad \mathbf{v} = \widetilde{\mathbf{v}}\, v^*$$

Thus, the dimensionless Nernst Planck Poisson equations [14, 32] yield four types of dimensionless groups:

$$\frac{\partial \widetilde{c}}{\partial \widetilde{t}} = \widetilde{\nabla}\widetilde{D}\widetilde{\nabla}\widetilde{c} + \left[\frac{E^*}{E_\beta}\right]\widetilde{\nabla}\widetilde{D}\widetilde{c}\widetilde{\nabla}\widetilde{E} - \left[\frac{v^*}{D^*/\lambda^*}\right]\widetilde{\nabla}\left(\widetilde{v}\,\widetilde{c}\right) - \left[\frac{k_n c^{*(n-1)}}{D^*/\lambda^{*\,2}}\right]\widetilde{c}^{\,n-1} \tag{2.22}$$

$$\sum_i \widetilde{c}_i = -\left[\frac{E^*}{E_\beta}\right]\widetilde{\nabla}\widetilde{\varepsilon}\widetilde{\nabla}\widetilde{E} \tag{2.23}$$

$$\widetilde{J} = \left[\frac{k_A}{D^*/\lambda^*}\right]\widetilde{c}_{red}\exp\left(\alpha_A\frac{\widetilde{\eta}_c}{E_\beta}\mathbf{n}\right) - \left[\frac{k_C}{D^*/\lambda^*}\right]\widetilde{c}_{ox}\exp\left(-\alpha_C\frac{\widetilde{\eta}_c}{E_\beta}\mathbf{n}\right) \tag{2.24}$$

- The first dimensionless group Π_1, analogous to the Peclet number [34], compares the strength of advection and diffusion phenomena. Advection is characterized by bulk velocity v^* while diffusion is characterized by diffusion coefficient D^* and diffusion length λ^*:

$$\Pi_1 = \frac{v^*}{D^*/\lambda^*} = \frac{\text{advection transport}}{\text{diffusion transport}} \tag{2.25}$$

  The value of this number increases as advection becomes dominant or diffusion becomes negligible. Conversely, the value decreases as advection becomes negligible or diffusion becomes dominant.

- The second dimensionless group Π_2 compares the strength of applied electric potential and thermal electric potential. Applied electric potential is characterized by characteristic voltage E^* while thermal potential is characterized by Boltzmann voltage E_β:

$$\Pi_2 = \frac{E^*}{E_\beta} = \frac{\text{applied voltage}}{\text{thermal voltage}} \tag{2.26}$$

The value of this number increases as applied voltage becomes dominant or thermal voltage becomes negligible.

- The third dimensionless group Π_3, analogous to the second Damköhler number [35], compares the strength of bulk reaction and diffusion phenomena. Bulk reaction is characterized by rate constant k_n, reaction order n, and reactant concentration c^* while bulk diffusion is characterized by diffusion coefficient D^* and diffusion length λ^*:

$$\Pi_3 = \frac{k_n c^{*(n-1)}}{D^*/\lambda^{*\,2}} = \frac{\text{bulk reaction rate}}{\text{bulk diffusion rate}} \tag{2.27}$$

  The value of this number increases as applied voltage becomes dominant or thermal voltage becomes negligible. For first order reaction, this dimensionless group is independent of concentration.

- The fourth dimensionless group Π_4, analogous to the Thiele number [35], compares the strength of interfacial reaction and bulk diffusion phenomena. Interface reaction is characterized by surface rate constant k_s while bulk diffusion is characterized by diffusion coefficient D^* and diffusion length λ^*:

$$\Pi_4 = \frac{k_s}{D^*/\lambda^*} = \frac{\text{interface reaction rate}}{\text{bulk diffusion rate}} \tag{2.28}$$

  The value of this number increases as interface reaction rate becomes dominant or diffusion rate becomes negligible. Unique to charge transport, this dimensionless group compares diffusion within the solid material phase to interfacial reaction at the solid–liquid interface. In comparison, the Thiele number, conventional descriptor of catalytic efficacy [35], compares diffusion within the surrounding liquid phase (viz., within liquid medium in subsurface pore structures) to interfacial reaction.

Evaluated for relevant charged species and spatial regime, these dimensions groups describe dominance and negligibility of charge transport phenomena. In particular, phenomena that significantly limit charge transport are quantifiable; they can be improved by perturbating relevant transport properties.

When applied to practical energy storage systems, simplifications are often employed for pedagogical clarity or analytical simplicity. In classic charge transport models for rechargeable lithium-ion batteries, only lithium transport is considered because electron transport limitations are considerably negligible; across various media, electron mobility is much greater than lithium mobility. In stationary systems, advection effects are also considered negligible (viz., advection velocity $\mathbf{v} = 0$).

2.3 Applications of Energy Storage

Thermodynamics determines the capacity, voltage, and energy limits of energy storage technologies. In compliment, kinetic rates determine the current and power limits of the same systems. Together, thermodynamics and kinetics define viable applications for energy storage systems. For instance, modular transport applications (e.g., electric vehicles, mobile phones, laptop computers) require high power and energy in limited space, suggesting volume and weight constraints are particularly significant. Stationary energy applications are less stringent in volume and weight constraints.

The Ragone diagram summarizes and compares energy and power characteristics for classes of energy storage systems. The abscissa, delivered energy or "range," represents the total energy available, and the ordinate, delivered power or "acceleration," represents the mean energy delivery rate. Diagonal tie lines represent ideal discharge times for given power and energy ratings. Performance values are often expressed on gravimetric or volumetric bases.

There are various classes of energy storage systems. In particular, several energy storage systems are of comparable interest to rechargeable lithium-ion batteries (Fig. 2.2) [36, 37]:

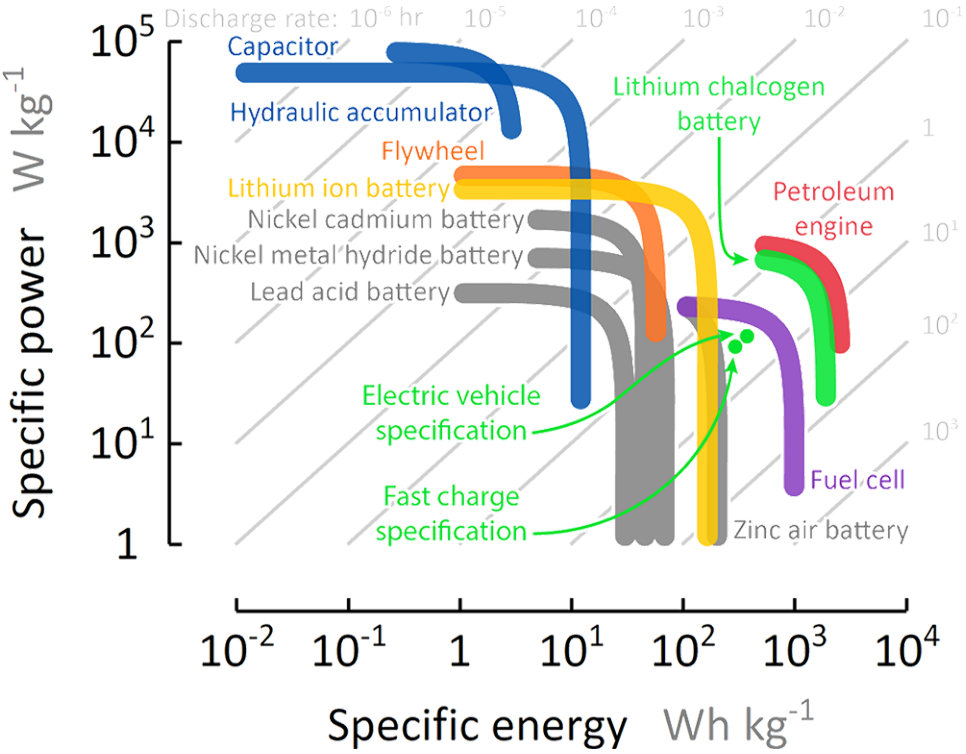

Figure 2.2. *Ragone diagram for lithium-ion and comparable energy storage systems.* Lithium-ion batteries (yellow) meet a broad range of energy and power requirements. Lithium sulfur batteries, a subclass of lithium chalogen electrochemistry (green), are predicted to be viable competitors for electric vehicles. Data extrapolated and adapted from various sources [4, 5, 8, 36–40].

- Rechargeable lithium-ion batteries [8], an electrochemically reversible or secondary energy storage system, operate on the reversible interaction of lithium metal species with electrode materials (e.g., lithium cobalt oxide, graphite). Depending on their constituent electrode materials, lithium-ion batteries can meet a wide range of energy and power requirements. Lithium chalcogen batteries, a subclass of lithium-ion batteries which utilize chalcogen electrodes (e.g., oxygen,

sulfur, selenium, tellurium), enable greater specific energy due to underlying conversion mechanisms.

- Rechargeable batteries [41] that do not utilize reversible lithium interactions include nickel-cadmium, nickel metal hydride, and lead acid batteries. These electrochemical systems, based on reversible redox mechanisms, satisfy less stringent energy and power demands compared to their lithium-containing counterparts. These systems are considered mature technologies and are well commercialized and implemented throughout the world.

- Fuel cells [42] are non-rechargeable or primary electrochemical conversion devices which supply energy through electrocatalytic reactions. In hydrogen fuel cells, hydrogen cations are produced by electrocatalytic oxidation at the anode, migrate through an ionic electrolyte, and react with oxygen to produce water at the cathode. This mechanism produces great energy, however, engineering and safety considerations generally limit fuel cells to stationary applications. Recently, hydrogen fuel cells have been successfully implemented in modular transport vehicles.

- Capacitors [43] are rechargeable energy storage devices which store and supply energy through surface polarization mechanisms. Energy manifests through an electric field maintained between electrodes across a polarizable electrolyte. Liquid electrolyte capacitors satisfy great power demands due to fast polarization rates. Supercapacitors, a subclass of capacitors with great electrochemically-active surface area, can deliver greater energy than traditional capacitor systems at similar power ratings.

- Hydraulic accumulators [41] are mechanical energy storage devices which store and release energy through pressurization and depressurization of a fluid phase. Like capacitors, hydraulic accumulators satisfy great power demands due to fast compression and decompression rates. Hydraulic accumulators are a mature technology featured in modular vehicles.

- Flywheels [39] are mechanical energy storage devices which store and release energy as angular momentum. Due to low friction design, flywheels store energy with great efficiency. Flywheels are a mature technology utilized in stationary storage applications.

Energy storage systems are often compared to the combustion engine [4], the traditional energy conversion system found in electric vehicles and power plants. Petroleum engines convert internal energy of hydrocarbon fuels into usable mechanical or electric energy through combustion processes. The combustion process, however, emits particulates and carbon dioxide pollutants which significantly contribute to global warming. Thus there is a need for sustainable and economical technologies to replace petroleum engines.

The principle impetus for energy storage research is to increase performance — that is, energy and power — for commercially viable and sustainable energy storage technologies. Due to broad applicably, rechargeable lithium ion batteries are viable candidates to be competitive with rechargeable batteries. Thus, rechargeable battery materials are heavily researched to increase energy and power requirements. In particular, lithium sulfur batteries are viable candidates for electric vehicles. The theoretical energy and power for lithium sulfur systems far exceed the US Advanced Battery Consortium (USABC) research goals [44, 45]: ca. $3 \cdot 10^2$ Wh kg^{-1} gravimetric energy and ca. $1 \cdot 10^2$ W kg^{-1} gravimetric power for both electric vehicles or fast charging applications. Bruce et al. [38] predict practical performance values for lithium sulfur batteries to be competitive with those for petroleum engines, suggesting lithium sulfur batteries are likely candidates for non-petroleum electric vehicles.

Summary

Power ratings of energy storage systems are a function of microscale electrochemical kinetics. In turn, kinetic efficacy is determined by the characteristic properties of underlying charge transport phenomena (i.e., diffusion, migration, advection, surface reaction, bulk reaction). Dimensionless groups enable quantitative evaluation of the significance of each phenomenon to the overall transport mechanism.

For a given energy storage system, thermodynamic and kinetic descriptions yield effective energy and power ratings. Together, energy and power determine appropriate applications for given energy storage system. Because of their commercial viability and wide applicability range, rechargeable lithium-ion batteries are among the most heavily researched energy storage technologies. There is much interest in the rechargeable lithium sulfur system due to its theoretical and practical gravimetric energy ratings which can directly compete with those of petroleum engines.

CHAPTER 3: RECHARGEABLE BATTERIES

Rechargeable lithium batteries are the latest frontier in energy storage. Batteries store or supply energy through the manipulation of charged species — a mechanism archetype of fundamental electrochemistry. To improve and innovate performance, modern battery research explores the electrochemical mechanisms of unknown or poorly understood materials. The Lithium sulfur battery is well recognized in this pursuit, actively studied in academic and industrial research since the late 20^{th} century. Nearly four decades later, Lithium sulfur technology remains immature and without viable prototypes progressing beyond research and development.

Building upon Chapter 1 and 2, this chapter introduces the rechargeable battery: its properties and components, and their synergy, are described. The material requirements for rechargeable electrochemistry are then discussed. Finally, the lithium sulfur battery is defined and the challenges inhibiting commercialization are explained.

3.1 Fundamentals of Electrochemistry

Electrochemistry [12] is the science of interfacial redox processes, transforming energy between electricity and chemistry. In rechargeable lithium batteries, potential energy is stored within the interatomic interactions of lithium and its chemical hosts. Interfacial reactions transform this chemical potential energy into kinetic electric energy, supplying energy in the discharge process or absorbing energy in the charge process. In the study of electrochemistry, these phenomena are measured along dimensions of electrical properties.

Measuring Electrochemistry

The extent of electrochemical processes — measured as transported electrons — is quantified by electrical properties of charge, current, and voltage [12]:

- Charge q is the electric property describing sensitivity to electric or charged phenomena. Charge is the fundamental unit of electron transport; it is the electric analog of position and mass, the fundamental units of momentum and mass transport. An entity with greater charge implies greater susceptibility to electron transport. Total charge transported Δq through an electrochemical process is equal to the difference between charge in initial q_0 and final q states:

$$\Delta q = \int dq = q - q_0 \tag{3.1}$$

  Charge is a positive (e.g., polarity: cation, free proton) or negative (e.g., anion, free electron) magnitude measured in Coulombs, a quantity of charged species equivalent in susceptibility to $6.242 \cdot 10^{18}$ protons.

- Current I is the electric property describing the rate of charge transport. In electron transport, electric current exists between electronic endpoints: the source and destination for transported electrons. Greater current implies greater charge transferred per unit time. It is equal to the change in charge Δq with respect to time Δt:

$$I = \frac{dq}{dt} = \frac{\Delta q}{\Delta t} \tag{3.2}$$

  Current is a positive or negative (e.g., polarity) magnitude measured in Amperes, a quantity of current which transports 1 Coulomb in 1 second.

- Voltage E, or potential difference, is the electric property measuring the strength of electron transport. It is a relative measure, describing transport strength of the electron destination relative to the source. Broadly, voltage is the electric variety of transport strength: pressure quantifies the strength of momentum

transport, concentration describes mass transport, temperature describes internal energy transport, and voltage describes electron transport. But voltage, unlike its analogues, must be a relative measurement distinct for a given voltage reference. Voltage references are not universal because voltage only exists between current endpoints which vary among electric systems (therefore, systems with identical voltage references can be compared). Regardless, greater voltage implies greater available energy for electron transport, permitting either faster electron transfer or more transported electrons. Voltage depends upon the available free energy ΔG, electron stoichiometry z, and Faraday constant F:

$$E = -\frac{\Delta G}{zF} \tag{3.3}$$

Voltage is a positive or negative (e.g., polarity) magnitude measured in Volts, a quantity of voltage which imparts 1 Joule on 1 Coulomb. Equivalently, voltage can be defined as Coulombic free energy, the energy acting on unit charge. This definition is derived from electrochemical thermodynamics (Chapter 1).

In an electrochemical system, voltage causes electric current [6]. This implies that, provided adequate infrastructure for charge transfer, voltage can exist without acting current — but current cannot exist without voltage. Together, voltage and current dictate energy and power, the practical performance metrics for rechargeable batteries:

- Energy is a measure of the ability to perform electric work (Chapter 1). The total energy transferred into or out of the battery is the integral sum of voltage E and current I over time t:

$$\Delta U = \int_t IE\,dt \tag{3.4}$$

- Power is rate of electric energy transfer (Chapter 2). Power is the product of voltage E and current I:

$$P = IE \tag{3.5}$$

In rechargeable lithium batteries, the cationic properties are stoichiometrically equivalent in magnitude but of opposite polarity.

Compiling Electrochemistry

A single lithium–ion battery is an electrochemical cell [12], the simplest system that enables electrochemical charge transport. When energy is transferred, lithium atoms are ionized, or separated into positive and negative charges: negative electrons shuttle through the electronic conductor and positive lithium cations shuttle through the ionic conductor. All batteries supply energy through the discharge, or galvanic, process in which charged species are spontaneously transported to the thermodynamically stable electronic endpoint. Rechargeable batteries also store energy through the charge, or electrolytic, process in which charge species are forcibly transported to the thermodynamically unstable electronic endpoint. To support these energy transfer processes, a battery requires four primary components (Fig. 3.1) [8, 12]:

- The positive and negative electrodes are chemical surfaces that interact with electrons and lithium cations. The electrodes are labeled according to the polarity of the battery terminal in direct electrical contact. This distinction is cosmetic, but both electrodes are required as electronic endpoints (viz., electron source and destination) to create electrochemical voltage. During energy transfer, the electrochemical reactions occurring at the positive and negative electrodes are determined by the direction of electron transport (Table 3.1). Electrochemical oxidation occurs at the anode because oxidation state increases as electrons are transported away from this electrode. In compliment, electrochemical reduction occurs at the cathode because oxidation state decreases as electrons are transported to this electrode. Measured relative to a common reference, the voltage of the positive electrode is greater than that of the negative electrode. The magnitude of voltage decreases in the discharge process, and increases in the charge process. The electrode of interest — the subject of elec-

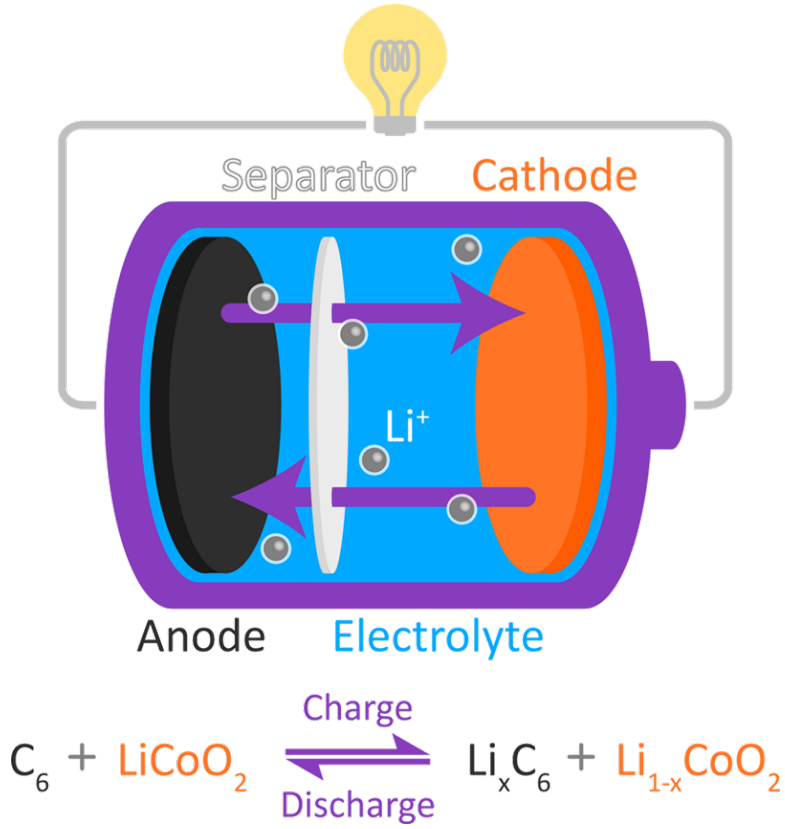

Figure 3.1. *Overview of the rechargeable lithium-ion battery.* The rechargeable lithium-ion battery features two electrodes in an ion-conductive electrolyte separated by an electron-insulating separator. Electrons are forced through an external circuit between electrodes during charge and discharge.

trochemical study — is specified as the working electrode. The appropriately-termed counter electrode serves as the opposite electronic endpoint [12].

- The electrolyte [46] is a physical medium with great ionic conductance and poor electronic conductance. The electrolyte is typically a liquid or solid medium placed between the electrodes to maximize electrode–electrolyte interfacial contact. Because of these properties, the electrolyte serves as an ionic conductor that transports lithium ions between electrodes.

Table 3.1.
Rechargeable battery electrode convention. The definitions of anode and cathode change for the charge and discharge processes.

	Negative electrode	*Positive electrode*
Discharge process	Anode oxidation, delithiation	Cathode reduction, lithiation
Charge process	Cathode reduction, lithiation	Anode oxidation, delithiation

- The separator [47, 48] is a physical separation intended to isolate electrodes from electron transport. Means of separation are determined by the physical construction of the cell. For example, separation is accomplished in rechargeable lithium–ion batteries as an inert porous membrane between the electrodes that does not significantly reduce ionic conduction, and in lead acid batteries as physical distance maintained by rigid electrode placement and support.

Two additional components are required for practical utilization of an electrochemical cell:

- Energy is drawn from the cell by an external electronic conductor that connects the electrodes. Complementary to the electrolyte, the electronic conductor is a great electronic conductor and poor ionic conduction.

- The shell of the electrochemical cell is an inert container designed to isolate the cell components from external mass transfer. Conductive leads or terminals connect the working and counter electrodes to the external circuit without significantly reducing electronic or ionic conductivity. A physically rigid electronic insulator separates the terminals themselves from directly connecting the electrodes without passing through the external load. The requirement of a physical

shell is dependent on the electrochemistry: some electrochemical systems are sensitive to oxygen and moisture in ambient air.

Assembled, the electrochemical cell (Fig. 3.2) contains two active electrodes, connected to the corresponding positive and negative terminals of an external circuit, in optimal, physical separation. The separation is filled with an electrolyte (and if required, a porous membrane) that is a good ionic conductor and poor electronic conductor. When an energy load is applied through the external circuit, voltage between the two electrodes motivates an electric current that transports electrons between electrodes accordingly. Passage of charge from the negative to positive terminal is the discharge process; passage of charge from positive to negative is the inverse charge process.

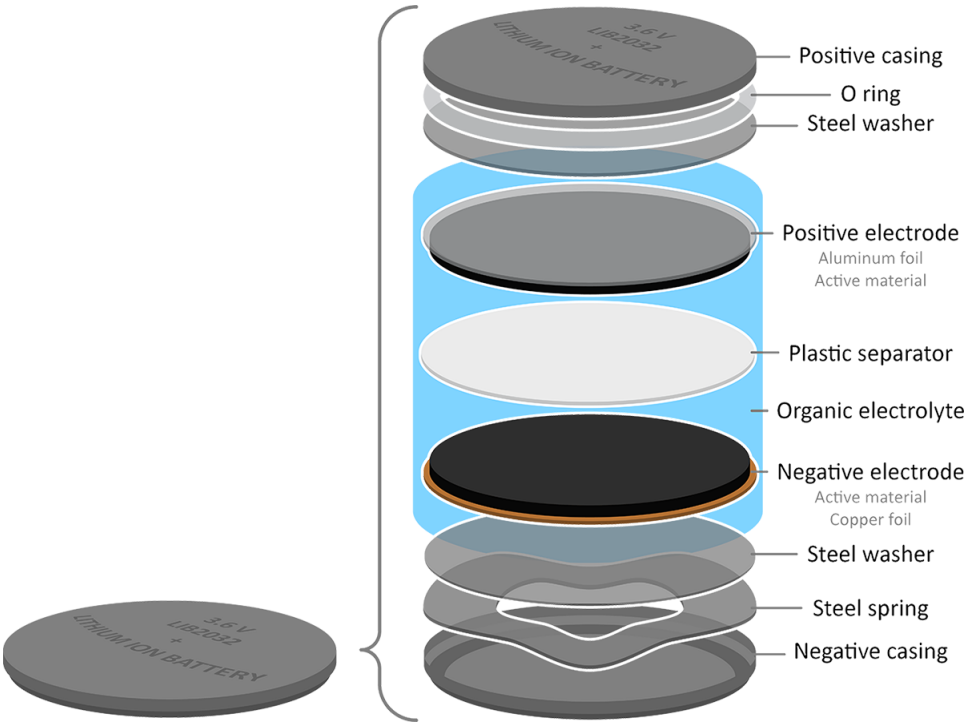

Figure 3.2. *Coin cell configuration for rechargeable batteries.* The CR2032 coin cell configuration for rechargeable batteries consists of an external casing that isolates electrochemically–active electrolyte and electrodes from ambient air.

Altogether, energy and power are practical considerations for rechargeable batteries that determine the most useful application of a particular electrochemistry. An equally important consideration is the lifetime of the energy storage device; that is, how many times can the device be reliably used. This is quantified by the reversibility of the electrochemical mechanism.

3.2 Reversibility of Materials

Mechanisms and materials determine the extent of reversible lithium storage in rechargeable batteries. Rechargeable lithium–ion batteries, available commercially, utilize an electrochemical couple of lithium metal oxide cathode (e.g., lithium cobalt oxide) and graphite anode. Both lithium cobalt oxide and graphite are examples of intercalation materials, in which lithium and the material interact according to physical insertion mechanisms [49]. Elemental sulfur is an an example of a conversion material, in which lithium binds with the material to form different chemical phases (Fig. 3.3) [50].

Intercalation electrodes feature the lithium intercalation mechanism: lithium translation and storage occur in large channels that exist throughout the material [40]. Lithiation or delithiation of intercalation electrodes constitute physical changes to the material crystal lattice; chemical change to the phase of the material does not occur [51]. The extent of intercalation determines capacity storage in the material.

Typical intercalation materials in commercial lithium-ion batteries include lithium cobalt oxide and graphite. At the microscale, lithium cobalt oxide and graphite are layered structures with large interplanar channels which enable lithium to reach active sites throughout the active material [49]. During charge, lithium enters the interplanar spacing of adjacent crystal planes and binds to available active sites. During discharge, intercalated lithium separates from active sites and the host electrode. Lithium cobalt oxide supports intercalation at voltage 3.8 V vs. $Li^{+/0}$ with gravimetric capacity 274 Ah kg^{-1}; however, practical capacity ca. 130 Ah kg^{-1} is reversible due to stability limits of the lithium deficient cobalt oxide structure [49, 52, 53]. Graphite

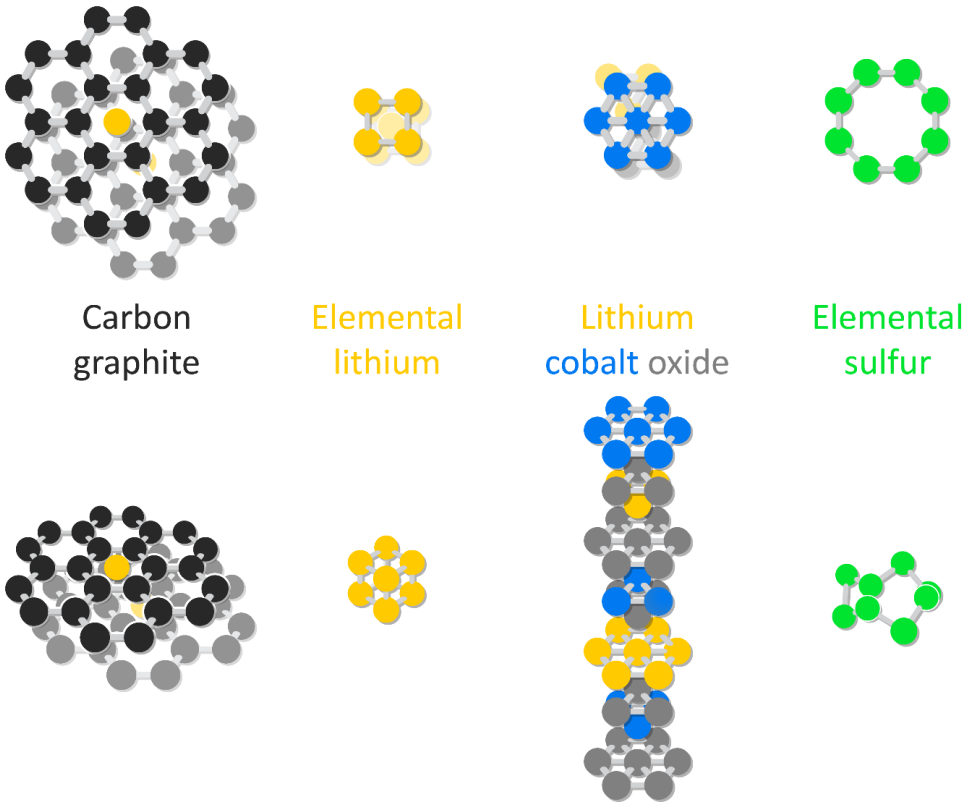

Figure 3.3. *Electrochemically active materials for rechargeable lithium batteries.* Intercalation materials, including graphite and lithium cobalt oxide, support reversible lithium interaction into their crystal structure. Conversion materials, such as elemental sulfur, support reversible lithium interaction which results in multiple electron transfer mechanisms.

supports intercalation at 0 V vs $Li^{+/0}$ with gravimetric capacity 372 Ah kg^{-1} [8,54,55]. Their electrochemical couple produces ca 0.3 V potential loss and practical capacity ca 130 Ah kg^{-1} [49].

Conversion electrodes feature the lithium phase conversion mechanism, in which lithium translation and interaction result in chemical binding and phase transformation [51]. Like intercalation electrodes, conversion electrodes enable microscale lithium ion diffusion through crystal spaces. However, binding of lithium to active sites results in structural and chemical change. The accompanying phase transition enables multiple lithium atoms to interact per mole of active material. Elemental

sulfur supports lithiation reaction at mean voltage 2.2 V vs $Li^{+/0}$ with gravimetric capacity 1672 Ah kg^{-1} [56]. Compared to the intercalation mechanism of lithium cobalt oxide, the conversion mechanism of elemental sulfur enables greater energy storage due to multi–electron transfer (Fig. 3.4).

As advances in traditional intercalation electrodes approach theoretical limits, research in conversion materials has rapidly grown. The principle challenge of conversion materials lies in their structural stability: phase transitions result in excessive volumetric change (e.g., 80 % vol. for elemental sulfur) that accelerates electrode pulverization and degradation. In the case of elemental sulfur, additional challenges arise from polysulfides, parasitic chemical intermediates that dissolve and obstruct sulfur behavior.

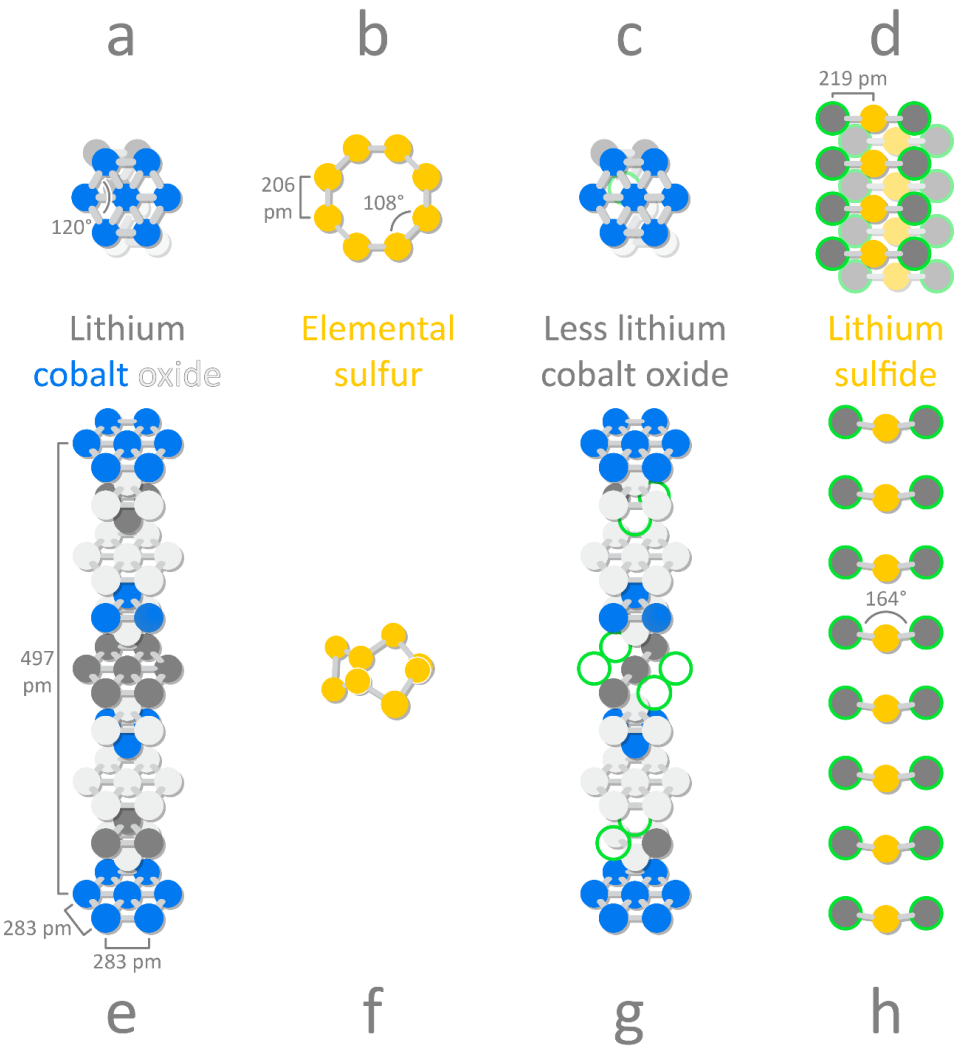

Figure 3.4. *Intercalation and Conversion mechanisms for reversible lithium interaction.* Depending on mechanism, loss or gain of lithium (green) corresponds to changes in binding, crystal structure, or phase. Lithium cobalt oxide in the lithiated state (top view a, side view e) limits lithium contributions to maintain structural stability in the de-lithiated state (c, g). Elemental orthorhombic sulfur in the de-lithiated state (b, f) reorganizes into separate lithium disulfide species in the lithiated state (d, h).

3.3 Lithium Sulfur: The Problem of Polysulfides

Lithium sulfur batteries operate on the reversible storage of lithium via chemical reaction with sulfur (Fig. 3.5). Lithium sulfur electrochemistry enables 1672 Ah kg^{-1} gravimetric capacity at mean voltage ca. 2.2 V vs. $Li^{+/0}$, with mean gravimetric energy ca. 3511 Wh kg^{-1} [50, 56, 57]. Furthermore, sulfur is abundantly available throughout the natural world and a reclaimable by–product of petroleum refining processes. Despite the appealing electrochemistry and sustainability of the Li-S system, it has not yet been realized due to several formidable challenges. The primary material challenge of sulfur and lithium sulfide is their low electrical conductivity on the order of 10^{-17} S cm^{-1}, indicating poor electrical and ionic conductivity that introduce high impedance to the cell.

Physical isolation of sulfur species by electrolyte dissolution unerlies the short life cycle of lithium sulfur batteries [56]. With extended lithiation, sulfur particles experience physical changes and degradation due to chemical and structural rearrangement [57]. Transformation between elemental sulfur S_8 and lithium sulfide Li_2S causes volume change ca. 22 % and induces mechanical strain and weakening of interfacial electrochemical contact [56]. Particularly during lithium sulfide precipitation and polysulfide dissolution, changes in lithiation state lead to active material swelling and pulverization. Cyclic expansion and contraction of sulfur results in eventual separation from the cathode and dissolution into the surrounding organic electrolyte. Loss of electrical contact between active sulfur and cathode substrate precludes low gravimetric capacity and battery failure.

Metallic lithium as counter electrode presents safety hazards for consumer usage. While lithium metal is the ideal anode due to low potential and high specific capacity, its high reactivity results in continual lithum deactivation and irregular interfacial transfer. Repeated lithiation and delithiation cause irregular lithium deposition, encouraging the growth of irregular depositions known as dendrites. Fully–formed dendrites enable direct contact between anode and cathode, causing battery failure and,

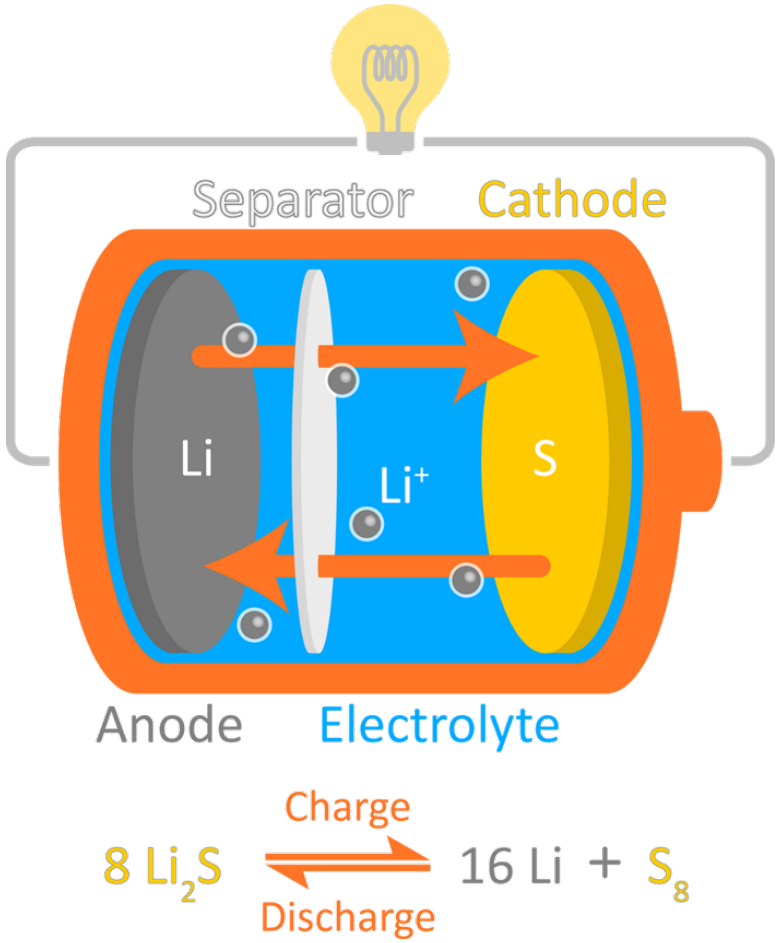

Figure 3.5. *The rechargeable lithium-sulfur battery.* The reversible interaction of lithium and sulfur causes high specific energy. However, chemical intermediates called lithium polysulfides result in premature degradation and rapid capacity fade.

at worst, fires or explosions. In addition, lithiation of native lithium metal prodcues a passivating interfacial film known as a solid electrolyte interlayer (SEI) [8,54]. This amorphous solid film forms due to electrostatic instability of electrolyte components at the voltage of lithium ionization; this results in electrolyte decomposition on the electrode surface that reduces active lithium inventory. Though SEI stabilizes once effective thickness prevents further electron transfer and electrolyte decomposition, irregular interfacial deposition and ionization expose new surfaces to SEI decomposition. Significant lithium loss results in poor efficiency and cycle life.

The technical issues of the lithium sulfur battery manifest due to the polysulfide shuttle mechanism: a phenomenon in which the formation of polysulfide intermediates during cycling inhibits sulfur electrochemistry. With respect to the electrode interface, the polysulfide shuttle mechanism involves dissolved polysulfide species that freely move throughout the battery and are difficult to characterize [56]. During sulfur lithiation, sulfur exists within an orthorhombic crystal lattice as α-sulfur, the stable room temperature sulfur allotrope [58], and proceeds to reversibly oxidize to lithium sulfide Li_2S according to a series of elementary reactions:

$$S_{8(s)} + 2\,Li^+ + 2\,e \rightleftharpoons Li_2S_{8(l)} \tag{3.6}$$

$$3\,Li_2S_{8(l)} + 2\,Li^+ + 2\,e \rightleftharpoons 4\,Li_2S_{6(l)} \tag{3.7}$$

$$2\,Li_2S_{6(l)} + 2\,Li^+ + 2\,e \rightleftharpoons 3\,Li_2S_{4(l)} \tag{3.8}$$

$$Li_2S_{4(l)} + 2\,Li^+ + 2\,e \rightleftharpoons 2\,Li_2S_{2(l)} \tag{3.9}$$

$$Li_2S_{2(l)} + 2\,Li^+ + 2\,e \rightleftharpoons 2\,Li_2S_{(s)} \tag{3.10}$$

In this mechanism, the intermediates are polysulfides of known composition Li_2S_x where x indicates the number of sulfur atoms. Long chain polysulfides (viz., stoichiometry $3 \leq x \leq 8$) are highly soluble in organic electrolytes, but small chain polysulfides (viz., stoichiometry $1 \leq x \leq 2$) are not soluble [56]. The smaller polysulfide chains deposit along the surface of the anode and within insulated regions of the cathode, disqualifying them from further electrochemical participation in the charge and discharge cycle. This uncontrolled, cyclic pattern of dissolution and deposition of active polysulfides results in low sulfur utilization, poor cycle life, low efficiency, and irreversible loss of active material. This phenomenon is observed in electrochemical testing as rapid capacity fade and continuous self–discharge upon storage [56]. The active pathway of sulfur reduction is expected to be a function of supporting electrolyte (Fig. 3.6) [56, 59–61].

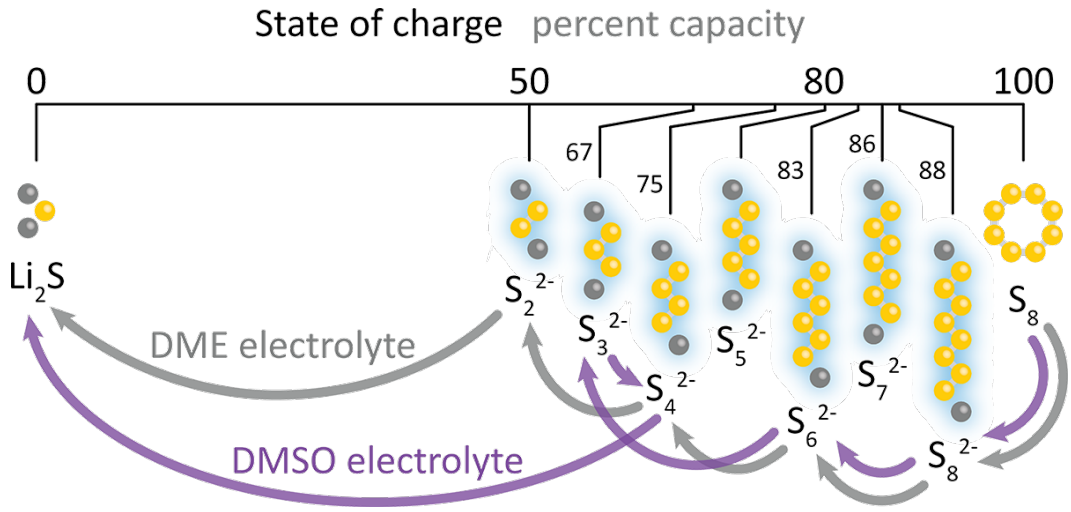

Figure 3.6. *The Polysulfide Shuttle Mechanism.* Polysulfides are chemical intermediates that are soluble in organic electrolyte. Elementary reduction of orthorhombic sulfur to lithium sulfide is non–sequential and dependent on electrolyte properties.

Summary

As a consequence of the polysulfide shuttle mechanism, technical challenges of lithium–sulfur batteries hinder their widespread application and commercialization. Various approaches symptomatically address performance aspects with lithium polysulfides. The morphology approach, discussed in Chapters 4 and 5, emphasizes the significance of microstructure — particularly sulfur distribution and substrate conductivity — in control of impedance reduction and polysulfide dissolution. The electrolyte approach, discussed in Chapter 5, inhibits excessive chemical solvation of polysulfides to reduce degradation effects. Applications of synthesized carbons as sulfur substrates prompts characterization of health and environment risks during synthesis processing in Chapters 6 and 7. Finally, electrochemical applications of amorphous carbon spheres and lithium metal as anode materials are studied in Chapter 8 and 9. An X–ray micro–tomography characterization method is developed in Chapter 9 encompassing experimental characterization and digital image processing.

PART I

POLYSULFIDES & CARBON CATHODES

Energy is liberated matter, matter is
energy waiting to happen.

— B. Bryson, 2003, *A Short History of Nearly Everything*

CHAPTER 4: AUTOGENIC SYNTHESIS OF CARBON SULFUR COMPOSITE CATHODES

In lithium sulfur batteries, morphology approaches enable physical constraint of polysulfides within the microstructure of a conductive substrate or host. Elemental sulfur remains in effective electrochemical contact with the cathode substrate, increasing capacity retention across extended cycles. Effective carbon sulfur cathodes utilze carbon substrates that feature [56]: (1) small pores that inhibit polysulfide solvation and migration, and (2) great bulk conductivity to offset poor conductivity of elemental sulfur. In this context, KETJEN BLACK — a carbon black with high surface area, bimodal porosity, and great conductivity – is the substrate for electrochemically active sulfur. Composites of carbon black and sulfur were synthesized using the pressurized autogenic process to facilitate uniform sulfur deposition.

Carbon sulfur composite synthesis, material characterization, electrochemical testing, and manuscript preparation were performed by Arthur D. Dysart and Neal A. Cardoza. Synchrotron X–ray diffraction was performed by Saul H. Lapidus at Argonne National Laboratory.

Abstract

The role of physically restrained, non–crystalline sulfur species in rechargeable lithium sulfur batteries is examined by electrochemical and high resolution material characterization. Synthesized by the autogenic process, non-crystalline sulfur cathodes demonstrate high specific capacity ca. 1000 Ah kg^{-1} after 100 cycles with gravimetric current 557 A kg^{-1}. Interestingly, this high performance sulfur allotrope lacks long–range structural order: high–resolution X–ray diffraction, performed at the Advanced Photon Source, indicate the lack of crystalline (i.e., orthorhombic or mono-

clinic) sulfur in the nanoscale domain. Electrochemical and material characterization suggest non–crystalline sulfur is a consequence of synthesis, and does not necessarily evidence electrochemical efficacy; high rate capacity depends on sulfur distribution, in turn, controlled by synthesis pathway. At higher sulfur content, the performance of carbon sulfur composites is limited by available surface area in which crystalline sulfur coincides with reduced gravimetric capacity and greater charge transport impedance, suggesting suboptimal sulfur containment.

4.1 The Autogenic Synthesis Method

Advancing electric vehicles and portable electronics necessitate better energy storage. In particular, petroleum–free electric vehicles require gravimetric energy ca. 350 Wh kg^{-1} [56], unachieved by modern commercial batteries operating with lithium cobalt oxide and graphite electrochemistry. In response, there has been increasing interest and research upon the rechargeable lithium sulfur battery, whose theoretical gravimetric energy 2509 Wh kg^{-1} and practical estimate 502 Wh kg^{-1} exceeds viability requirements for electric vehicles [44]. Yet, the lithium sulfur battery remains in the research sector due to inherent challenges of its multistage electrochemistry and inherent resistivity.

The lithium sulfur battery operates on reversible electrochemistry between elemental sulfur and lithium. During discharge, orthorhombic crystalline sulfur S_8 reduces to dilithium sulfide Li_2S through chemical intermediates known as lithium polysulfides [60, 62]. Conventional glyme electrolytes solvate these inorganic species: inadequate long-term performance and battery life result from unrestricted polysulfide dissolution and migration. Recent advances suggest the full redox mechanism is an intricate network of elementary steps dependent on local thermodynamic properties. With this knowledge, reported approaches to polysulfide suppression include morphology control [62], electrolyte control [60], or macroscale inhibition [56, 62].

Morphological control utilize engineered substrates that increase effective cathode conductivity and suppress polysulfide migration away from the cathode. Various morphology approaches have been demonstrated in the literature: the work of Ji et al. [57] demonstrate microporous carbon substrate CMK-3 effectively restrains polysulfide migration, with high gravimetric capacity and long term cycling performance [63]. Similarly, Li et al. [64] demonstrate great gravimetric capacity ca. 800 Ah kg^{-1} using high temperature heating synthesis.

In this context, the autogenic process is applied to synthesize carbon-sulfur composites with non-crystalline sulfur. Autogenic synthesis, studied by Pol et al. [65], enables chemical processes through thermal pressurization of isochoric reactor volumes. Typical applications of the autogenic process include synthesis of inorganic nanoparticles (i.e., vanadium oxide [66]), amorphous carbons (polyethylene–derived carbon nanotubes [67]), and bi–phase composites (i.e., silicon carbide nanospheres [68]). In this work, autogenic heating drives homogeneous distribution of sulfur throughout carbon substrate KETJEN BLACK, a high conductivity and high surface area carbon black. Autogenic carbon sulfur composites demonstrate great gravimetric capacity at high gravimetric current C/3, values almost twice that of their mechanically synthesized counterpart. High-resolution X–ray powder diffraction and scanning transmission electron microscopy of non–crystalline sulfur species suggest electrochemical performance is determined by the efficacy of sulfur distribution throughout the composite, not necessarily the presence of non-crystalline sulfur.

Experimental Methods

Synthesis of Autogenic Carbon Sulfur Composites

Carbon sulfur composites were produced using the autogenic synthesis process (Fig. 4.1) [67]. All autogenic reactor preparation was performed within a high purity glovebox (Nexus II, Vacuum Atmospheres Co.) filled with 99.999 % argon gas (Indiana Oxygen Co.). In given mass ratio, orthorhombic sulfur (Sigma Aldrich Corp.)

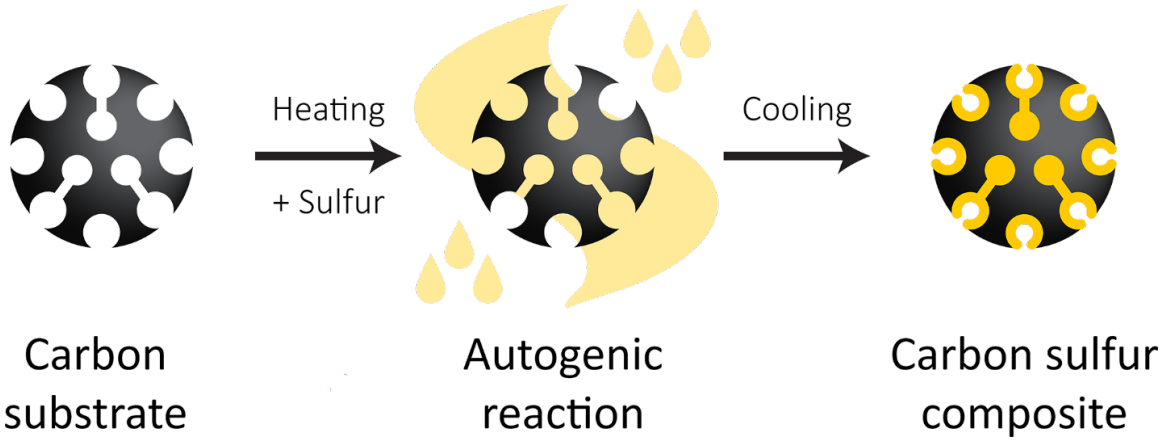

Figure 4.1. *Autogenic synthesis of carbon sulfur composites.* Carbon-sulfur composites are synthesized by controlled deposition of sulfur vapor. Heating carbon and sulfur within the autogenic reactor distributes sulfur vapor throughout the carbon substrate. Upon cooling, solid sulfur deposits on available surface area of the carbon substrate.

and KETJEN BLACK carbon (Akzo Nobel N.V.) precursors were gently homogenized using a mortar and pestle. The stainless steel autogenic reactor (reactor volume ca. 5 mL) was loaded with the carbon-sulfur mixture and sealed under argon atmosphere (Indiana Oxygen Co.). The loaded autogenic reactor was placed within a horizontal steel tube furnace (MTI). The furnace chamber was heated at constant temperature rate 5 C° min^{-1} to specified dwell temperatures then cooled to room temperature at rate ca. –5 C° min^{-1}. Heating profiles included temperatures of 155 or 445 °C for total dwell time of 7 hours. The collected products, termed autogenic carbon sulfur composites, were utilized in the succeeding procedures without further treatment.

Synthesis of Mechanical Carbon Sulfur Composites

Mechanically–synthesized carbon sulfur composites were produced using a vibration ball mill (Quantachrome Instruments). All reactor preparation was performed within a high purity glovebox (Nexus II, Vacuum Atmospheres Co.) filled with 99.999

% argon gas (Indiana Oxygen Co.). In given mass ratio, orthorhombic sulfur (Sigma Aldrich) and carbon KETJEN BLACK carbon (Akzo Nobel) precursors were gently homogenized using a mortar and pestle. The stainless steel milling jar (reactor volume ca. 50 mL) was loaded with the carbon sulfur mixture and stainless steel ball (Quantachrome) then sealed under argon atmosphere (Indiana Oxygen Co.). The loaded milling jar was placed within the vibrating ball mill and processed for 7 hours at vibration frequency 10 Hz. The collected products, termed mechanical carbon sulfur composites, were utilized in the succeeding procedures without further treatment.

Battery Fabrication and Assembly

A viscous mixture of 85 % -wt. carbon-sulfur composite and 15 % -wt. polyvinylpyrrolidone (Sigma Aldrich) was prepared with Type 1 water (Thermo Fisher Corp.). Homogenization was performed in closed polypropylene cups (Flacktec Inc.) with zirconium oxide mixing balls (MTI) agitated using a planetary mixer (Thinky Corp.). The mixture was laminated onto carbon-coated aluminum foil (18 μm thick, battery grade, MTI) using a film applicator (Gardco Inc.) with the assistance of an automatic film coater unit (MTI). The resulting thin film lamination was dried at temperature 30 °C for at least 12 hours. Electrodes were cut from the dried laminate using an arch punch (0.25 in. dia., General Tools Co.) and installed into stainless steel CR2032 (MTI) coin cells. The electrolyte utilized in all cells consists of 1.0 M bis(trifluoromethane)sulfonimide lithium salt (LITFSI, Sigma Aldrich) in a solution of 1,3-dioxolane (DOL) and 1,2-dimethoxyethane (DME). A reference electrode of lithium metal (MTI) and polypropylene separator (Celgard 2500, Celgard LLC) were also utilized. Battery cells were hermetically sealed using a hydraulic pressure of ca. 1000 lb in^{-2} (MTI). All battery assembly and crimping was performed within a high purity glovebox (Nexus II, Vacuum Atmospheres Co.) filled with 99.999 % argon gas (Indiana Oxygen Co.).

Electrochemical Characterization

Following fabrication, battery cells were tested galvanostatically using a multi-channel battery cycler (Arbin Instruments Inc.). Prior to galvanostatic cycling, fabricated cells were left at rest for ca. 12 hr (viz. open circuit configuration) to improve electrode wetting. All cells were tested in the cutoff voltage domain 2.6 - 1.7 V without additional conditioning.

Electrochemical impedance spectroscopy (EIS) was performed using a combination potentiostat and galvanostat with direct digital synthesis circuitry (Reference 600, Gamry Instruments). Potentiostatic impedance spectroscopy was performed in the frequency range of 0.01 - 20,000 Hz. Reported impedances are spatially normalized relative to electrode area A and active material coating thickness λ according to the Pouillet law [69]:

$$Z_{norm} = Z\,\frac{A}{\lambda} \tag{4.1}$$

The definition of the "charge" and "discharge" process is taken with respect to the reference electrode: discharge is defined as lithiation of sulfur (viz., potential approaches 1.7 V), while charge is defined as delithiation of sulfur (viz., potential approaches 2.6 V) [56, 57]. All reported gravimetric variables (i.e., specific capacity, specific current) were determined with basis or reference to the sulfur mass. All voltages or potential differences are reported relative to the ionization potential of lithium metal (viz., versus $Li^{0/+}$).

Characterization of Carbon Sulfur Composites

High resolution X–ray diffraction (XRD) experiments were performed at beamline 11–BM of the Advanced Photon Source (APS). Approximately 2 mg of sample was loaded into polyimide capillaries (Kapton, 3M Corp.) mounted into custom aluminum sample holders. Diffraction patterns were produced using a hard X-ray beam with energy range ca. 15 – 35 keV. Spectral patterns were produced in the $2\,\theta$ scattering range 2 - 50 $^\circ$ at a scanning rate of 0.5 $^\circ$ min^{-1}. Reported spectral patterns are not

smoothed or reduced for background. Control materials (viz., carbon and sulfur) and reference standards (viz., polyimide sample holder, aluminum sample mount, air scattering) were performed or reproduced from beamline 11–BM. Reference standards were not corrected for experiment-specific calibration.

Thermogravimetric Analysis (TGA) was performed using a simultaneous thermal analyzer (Q600, TA Instruments Inc). Approximately 4 mg zinc acetate dehydrate were loaded into a cylindrical aluminum oxide crucible (TA Instruments). The weight of the crucible was tared prior to sample loading. The loaded crucible was placed inside the horizontal furnace chamber under continuous compressed air flow at rate 100 mL min^{-1}. Sample mass was recorded during heating at uniform temperature rate 10 C° min^{-1} to temperature 1000 ° C. Synthesis efficiency $f_{synthesis}$ is calculated as the ratio of the precursor sulfur mass fraction f_0 and product sulfur mass fraction f_f:

$$f_{synthesis} = \frac{f_f}{f_0} \tag{4.2}$$

Scanning Electron Microscopy (SEM) was performed using a scanning electron microscope (Nova 200 DualBeam, FEI Co.). Double-sided carbon tape (3M Corp.) was used to adhere samples to an aluminum sample stage. Approximately 5 mg of sample were evenly dispersed onto the exposed surface of the carbon tape. The loaded sample stage was placed inside the microscope chamber and evacuated to high vacuum (i.e., < 2.6 nbar). Micrographs were recorded at various magnifications after thorough optimization of electron beam alignment, stigmation, focus, brightness, and contrast. Energy dispersive X–ray spectroscopy (EDXS) was performed using an 80 mm^2 area silicon drift detector (Oxford Instruments PLC) at energy level 10 keV. Electron pixel maps were produced using the AZTEC analysis software suite (Oxford Instruments).

Scanning Transmission Electron Microscopy (TEM) was performed using an environmental transmission electron microscope (Titan, FEI). To prepare the sample, approximately 5 mg of sample was dispersed in anhydrous ethanol (Decon Labs). In the presence of a 200-mesh carbon TEM grid (Pelco, Ted Pella Inc.), ethanol solvent

was allowed to evaporate at temperature of 30 °C. The sample-loaded grid was then loaded into the specimen chamber, which was then evacuated to high vacuum (i.e., < 2.6 nbar). Micrographs were recorded at various magnifications after thorough optimization. Electron beam alignment, stigmation, focus, brightness, and contrast were optimized for each magnification.

Nitrogen gas adsorption and desorption isotherms were measured using a surface area and pore size analyzer (Nova 2200e, Quantachrome). Approximately 20 mg of sample were loaded into a dehydrated quartz sample tube cell. The loaded cell was placed into a heating mantle and outgassed at temperature 300 °C for 24 hr in vacuo. The loaded sample cell, cooled by a dewar bath of liquid nitrogen, was subsequently loaded into the gassing chamber for sorption measurements. Measurements were recorded in the relative pressure range 0.005 - 0.999 with minimum equilibration time 60 s. Masses of the quartz sample tube cell, both with and without sample, were measured using an analytical balance (Sartorius).

4.2 The Curious Case of Sulfur State

Influence of Synthesis on Material Properties of Carbon Sulfur Composites

Sulfur distribution and structural order in carbon sulfur composites depend on applied synthesis method. With high porosity carbon substrates at moderate sulfur loading ca. 40 %-wt., autogenic and mechanical synthesis processes produce composites with non-crystalline sulfur. In their composite products, the autogenic and mechanical processes differ according to sulfur mass percentage and physisorption surface area. These differences suggest more homogeneous sulfur distribution in the autogenic composite compared to that in its mechanically produced counterpart (Fig. 4.2).

Autogenic synthesis produces non–crystalline sulfur composites by pressurizing the vapor phase of the heated isochoric reactor. In the first step, carbon and sulfur precursors are heated within the isochoric autogenic reactor under inert atmosphere [64].

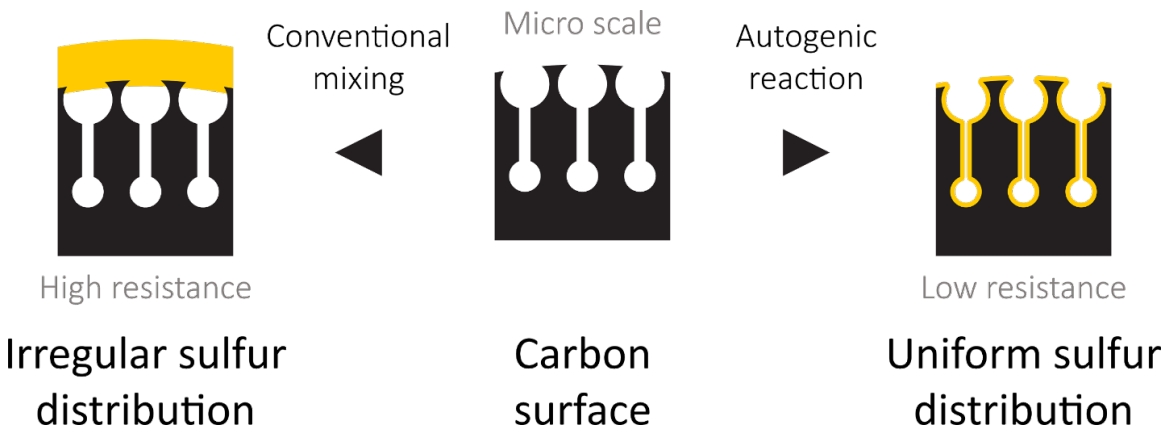

Figure 4.2. *Sulfur distribution in carbon sulfur composites.* Deposition of fluid sulfur phases encourages homogeneous sulfur distribution. In the autogenic process, sulfur vapor can access and deposit onto the large surface area of small carbon micropores. In the mechanical mixing process, solid sulfur species are unable to penetrate or access pores beyond particle surfaces.

During heating, local temperature governs phase transitions of the precursor mixture. At atmospheric pressure, high purity carbon does not experience significant phase transition at temperatures below 4800 K [70]. In contrast, orthorhombic sulfur experiences three phase transitions [58]: orthorhombic-monoclinic solid phase transition at temperature 373 K, monoclinic solid-liquid phase transition at 388 K, and liquid-vapor phase transition at 723 K. The extent of heating at solid-liquid and liquid-vapor transition temperatures control fluid sulfur viscosity and, subsequently, sulfur distribution within carbon substrates. In the second step, sulfur vapor fuses or deposits as solid sulfur upon cooling to room temperature ca. 300.15 K [58]. Within carbon micropores, sulfur deposits or fuses as non-crystalline species. Interestingly, sulfur does not recrystallize after prolonged storage.

Product sulfur mass fraction is sensitive to applied synthesis pathway. Thermogravimetric analysis (Fig. 4.3), heating in an advective inert gas stream, measures composition of carbon-sulfur products. Here, synthesis efficiency measures sulfur mass

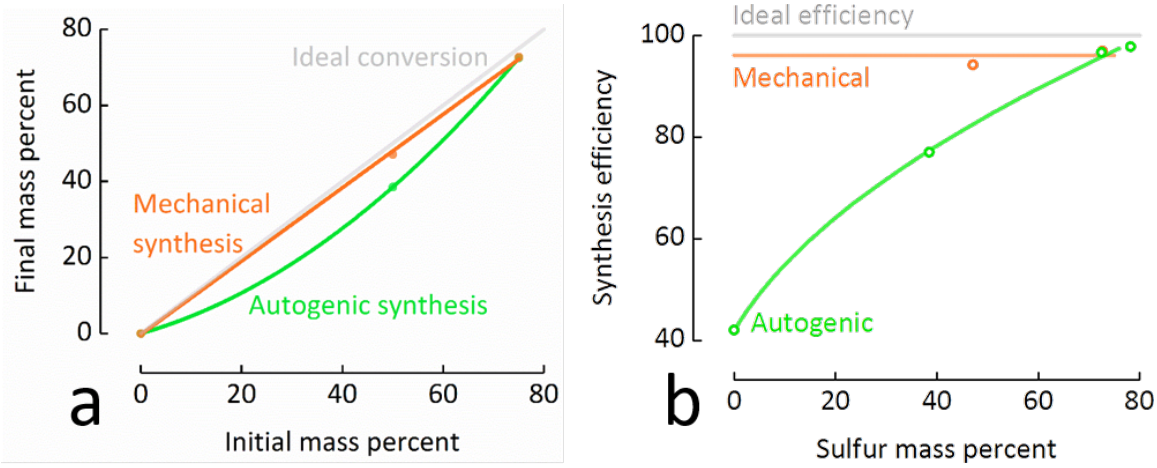

Figure 4.3. *Controlled sulfur loading for autogenic carbon sulfur composites.* (a) As sulfur-carbon precursor ratio increases, the efficiencies of sulfur loading for the autogenic and mechanical mixing processes converge toward unity. (b) While it is constant for mechanical process, synthesis efficiency for the autogenic process is a monotonic function of final sulfur mass percent.

conservation; greater efficiency implies greater sulfur retention through the given synthesis pathway. For the autogenic pathway, synthesis efficiency increases toward unity as sulfur mass faction increases. For the mechanical pathway, synthesis efficiency is constant ca. 96 %-wt. sulfur and generally independent of sulfur mass fraction. Efficiency differences among autogenic and mechanical synthesis are attributed to the underlying pathway mechanism. Autogenic synthesis employs thermal pressurization to mobilize sulfur and homogenize distribution in the composite. With significant vaporization, a fraction of sulfur vapor may remain thermodynamically stable in the vapor phase and not deposit in the composite. In contrast, mechanical synthesis operates on inelastic collisions with stainless steel surfaces to combine precursors. This process does not induce appreciable vaporization, permitting synthesis efficiencies very close to unity.

Structural disorder of the bulk sulfur phase occurs in both the autogenically and mechanically derived composites. Hard X–ray diffraction (Fig. 4.4a), performed at the Advanced Photon Source, enables long penetration depth (i.e., mean X–ray energy ca. 30 keV) and resolution (i.e., differential vector magnitude $2 \cdot 10^{-4}$): ideal facilities for crystallinity measurements at the nanometer scale. Interestingly, carbon sulfur composites exhibit diffractogram features of disordered carbon but not those of crystalline sulfur. For bare carbon, low intensity and significant breadth of diffractogram features suggest short-range structural order as nano–crystallites [71] and long-range disorder. Bare carbon exhibits diffractogram bands [72] at scattering angles ca. 6.38, 11.32, and 19.74 ° corresponding to principle reflections of the 002, 100, and 110 carbon lattice facets, respectively. Crystalline orthorhombic sulfur exhibits several high intensity and narrow diffractogram bands in scattering angle range ca. 3 - 20 °. Rigorous diffractogram accuracy, afforded by high-energy Synchrotron X-rays, confirms long-range disorder in synthesized composites in composites containing ca. 40 %-wt. sulfur and KETJEN BLACK carbon.

Additionally, diffractograms exhibit additional intensity features not associated with carbon or sulfur; these features are caused by experimental artifacts (Fig. 4.4b). Typically, diffractogram features of experimental artifacts are negligible when compared to those of ordered materials (e.g., orthombic sulfur; Fig. 4.4a) [73]. However, artifact features and disordered materials produce diffractogram features of comparable intensity. There are three principle diffraction artifacts observed across the studied materials. In all diffractograms, ambient air produces the diffuse band between 0 - 10 °. This broad feature occurs at low scattering angle due to air molecules [74]. In the autogenic, mechanical, and bare carbon diffractograms, the polyimide capillary produces features between ca. 5 - 9 °. Polyimide films exhibit scattering bands at 5.1 and 6.9 ° corresponding to intrachain polymide reflections, and diffuse bands between 10.9 - 26.8 ° corresponding to interchain reflections [75]. In the mechanical composite, narrow features in scattering range ca. 11.1 - 37 ° are attributed to the aluminum sample mount [76]. The relative intensities of features centered at 10.6, 15.0, 18.5,

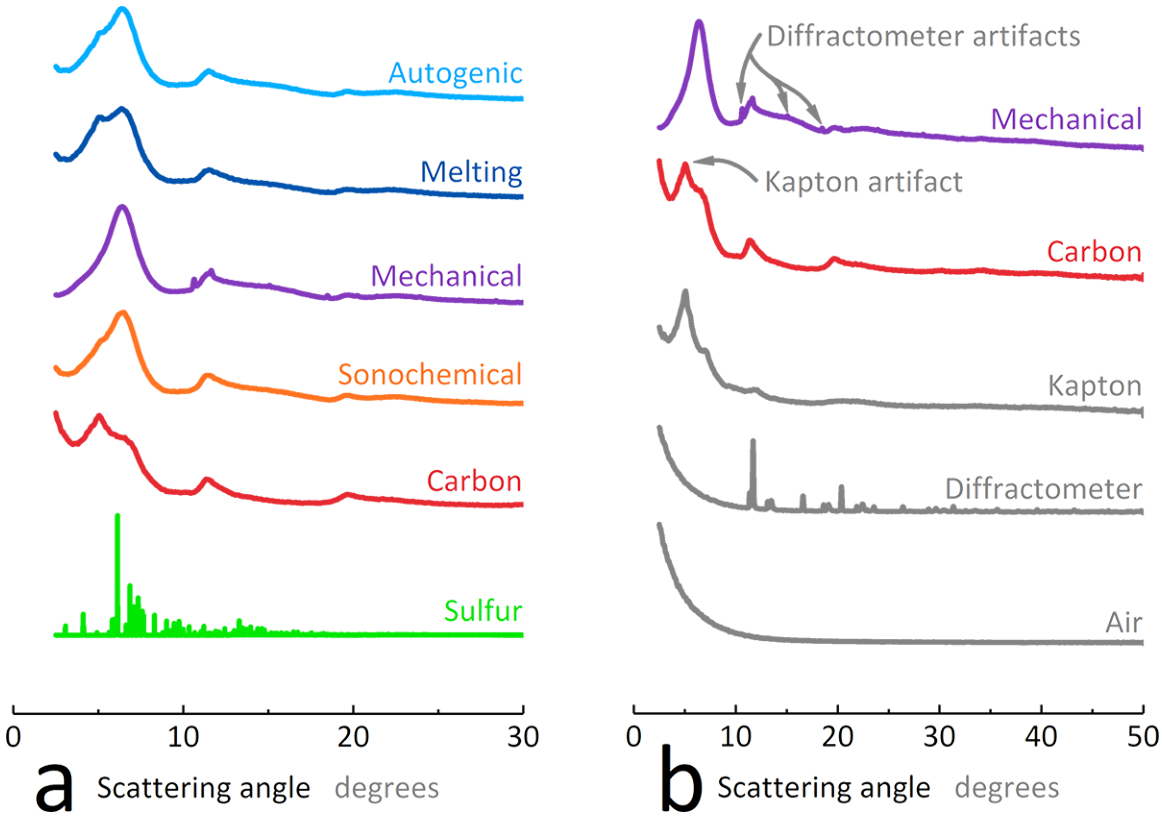

Figure 4.4. *High resolution X-ray powder diffraction of autogenic carbon sulfur composites.* (a) The characteristic diffraction features of orthorhombic sulfur (green) are absent in diffractograms of carbon sulfur composites. (b) Diffractogram features not associated with amorphous carbon are likely attributable to experimental artifacts.

and 28.4 ° match the relative peak intensity profile of the diffractometer reference. Overall, experimental artifacts well describe the appearance of intense diffractograms features unrelated to bare carbon or synthesized composites. Therefore, high resolution hard X–ray diffraction justifies the absence of orthorhombic sulfur in high porosity carbons.

The autogenic method produces more homogeneous carbon sulfur composites than the mechanical method. Following synthesis, change in material surface area quantify sulfur distribution. Isothermal nitrogen sorption (Fig. 4.5) measures physisorption surface area before and after synthesis [77]. Differences in surface area suggest autogenically–deposited sulfur does not greatly obstruct nitrogen sorption while mechanically–deposited sulfur significantly hinders subsurface porosity access. Autogenic synthesis produces composite with gravimetric surface area 263 m^2 g^{-1}, while mechanical synthesis produces composite with gravimetric surface area 10 m^2 g^{-1}. Prior to synthesis, bare carbon black exhibits high gravimetric surface area 1338 m^2 g^{-1}. Modal micropore radiuses, calculated using non-linear density functional theory, of the bare carbon substrate are 3.63 and 1.18 nm; the autogenically-derived composite are 3.79 and 1.23 nm; and the mechanically-derived composite is 4.15 nm. For each material, gravimetric surface area is proportional to differential volume at modal micropore radiuses. Low differential volume and singular modal pore radius in the mechanically-derived composite evidence micropore blockage.

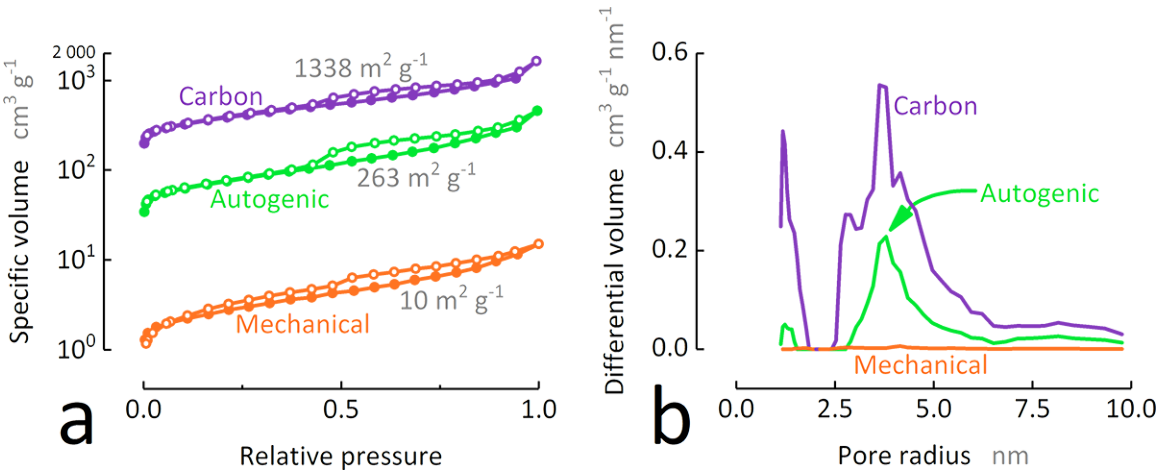

Figure 4.5. *Isothermal nitrogen sorption of autogenic carbon sulfur composites.* (a) The characteristic diffraction features of orthorhombic sulfur (green) are absent in diffractograms of carbon sulfur composites. (b) Diffractogram features not associated with amorphous carbon are likely attributable to experimental artifacts.

Homogeneous sulfur distributions are further supported. Electron microscopy (Fig. 4.6) further suggests homogeneous distribution of sulfur throughout autogenically synthesized carbon-sulfur composites. Scanning electron micrographs show a large sample of autogenically derived carbon sulfur composites show carbon and sulfur distributed throughout the composite. At deeper magnification, scanning transmission electron micrographs (Fig. 4.7) show great morphological similarity of the carbon coated sulfur and bare carbon black. The particle geometry appears branched, without significant change in particle morphology before or after sulfur loading. Even after optimization, the sulfur loaded carbon shows poor contrast, likely attributable to the loaded sulfur.

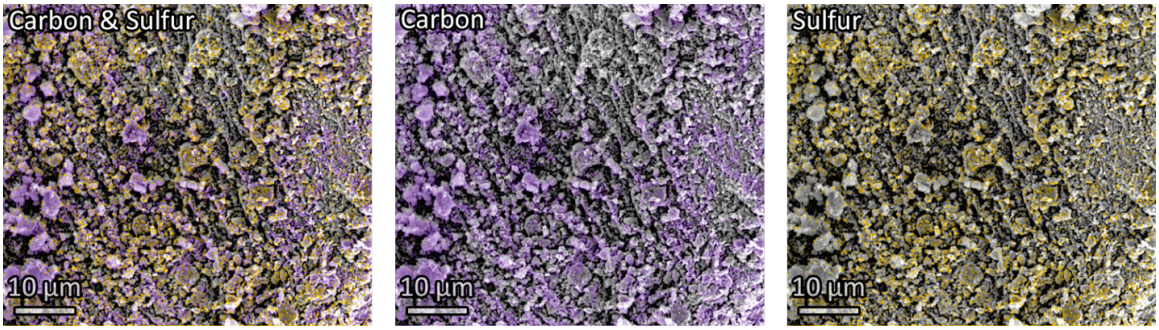

Figure 4.6. *Scanning electron micrographs of autogenic carbon sulfur composites.* Autogenic carbon sulfur composites (left) show carbon (middle) and sulfur (right) species distributed throughout the composite.

In summary, high resolution characterization demonstrates that sulfur lacks long-range order when loaded into microporous carbon. Ultimately, applied synthesis pathway controls sulfur efficiency – that is, the final sulfur mass loading and spatial arrangement. While both synthesis routes produce non-crystalline sulfur, the distribution of sulfur is less obstructive to molecular probes in the autogenic composite. This critical feature has significant implications on rate-dependent gravimetric capacity and effective impedance of these amorphous sulfur-containing composites.

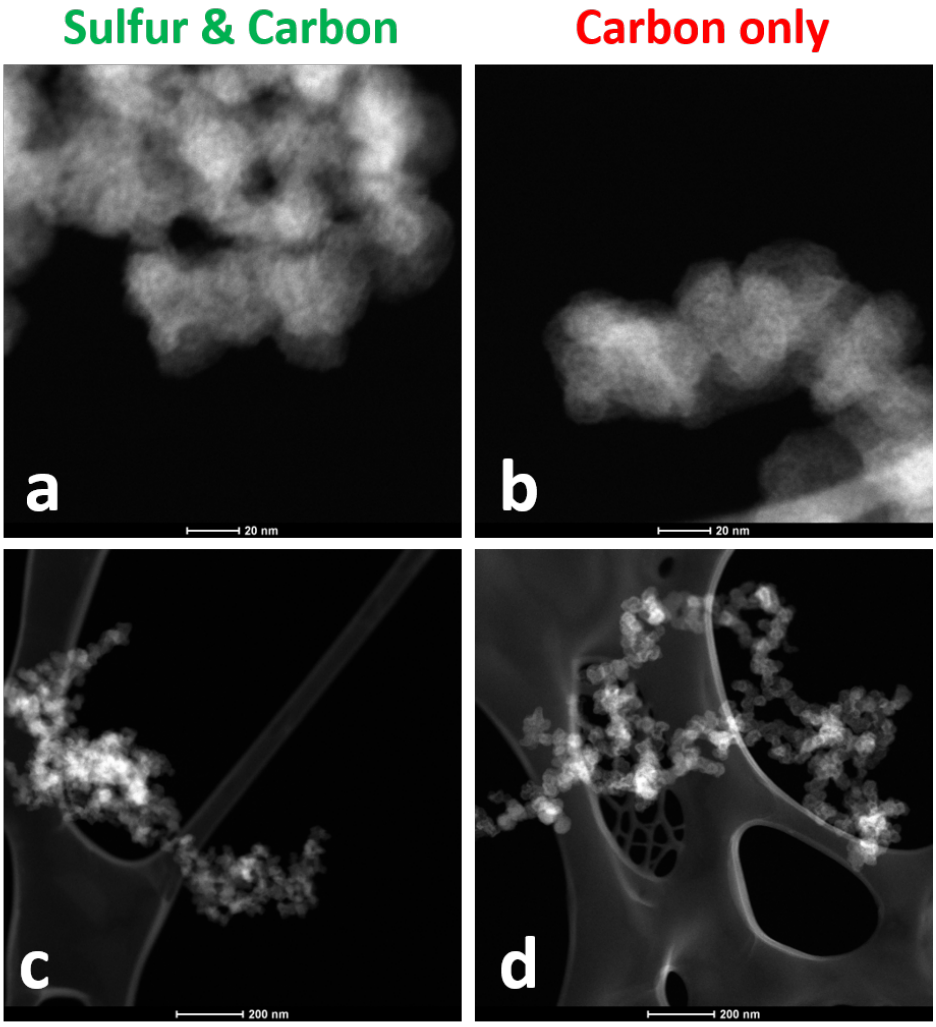

Figure 4.7. *Scanning transmission electron micrographs of autogenic carbon sulfur composites.* Pure carbon (a, c) and autogenic composites (b, d) generally appear the same in scanning transmission microscopy. Lower clarity at low magnification may be due to low conductivity of loaded sulfur.

Influence of Synthesis on Electrochemical Performance of Carbon Sulfur Composites

Material characterization of autogenic and mechanically derived carbon-sulfur composites suggest non-crystalline sulfur allotropes are thermodynamically stable in microporous carbons. The chemical storage of non-orthorhombic sulfur is seemingly independent of synthesis method, producible in carbon sulfur composites synthesized by all studied synthesis methods. Though all materials contain autogenic sulfur, the electrochemical performance of autogenically-derived composites surpasses that of its mechanically-derived counterpart.

Between the autogenic and mechanically derived composites, gravimetric surface area is directly proportional to gravimetric capacity. Gravimetric capacity ca. 1000 Ah kg^{-1} is measured after extended gravimetric cycling of the autogenically-derived carbon sulfur composite with 40 %-wt. sulfur loading (Fig. 4.8). The performance of a conventional sample derived via ball milling is shown for comparison. When cycled at various cycling rates, the autogenically–derived carbon sulfur composite shows greater capacity around 1100 Ah kg^{-1} after extended cycling. However, all materials demonstrate unstable Coulombic efficiency, in which gravimetric capacity decreases to ca. 700 Ah kg^{-1} following 100 cycles at rate C/3. In comparison, the ball milled composite shows much lower capacity ca. 300 Ah kg^{-1} at similar rates. When analyzing the Coulombic efficiency, the autogenic composite demonstrates better uniform efficiency across all rates near unity (ca. 100 %) in comparison to the ball milled composite which shows low efficiencies down ca. 20 % at C/3 rate. Furthermore, the autogenic composite shows efficiencies much more uniformly centered near unity (ca. 100 %) while the ball milled composite shows efficiencies centered far from unity in the same range of cycles.

Following testing at fast 2C and slow C/20 cycling rates, Chronopotentiograms of carbon sulfur composites show improved capacity profiles compared to mechanical mixing (Fig. 4.9). In cycle 130, all autogenic composites show voltage profiles with great specific capacity and less hysteresis than the mechanically mixed com-

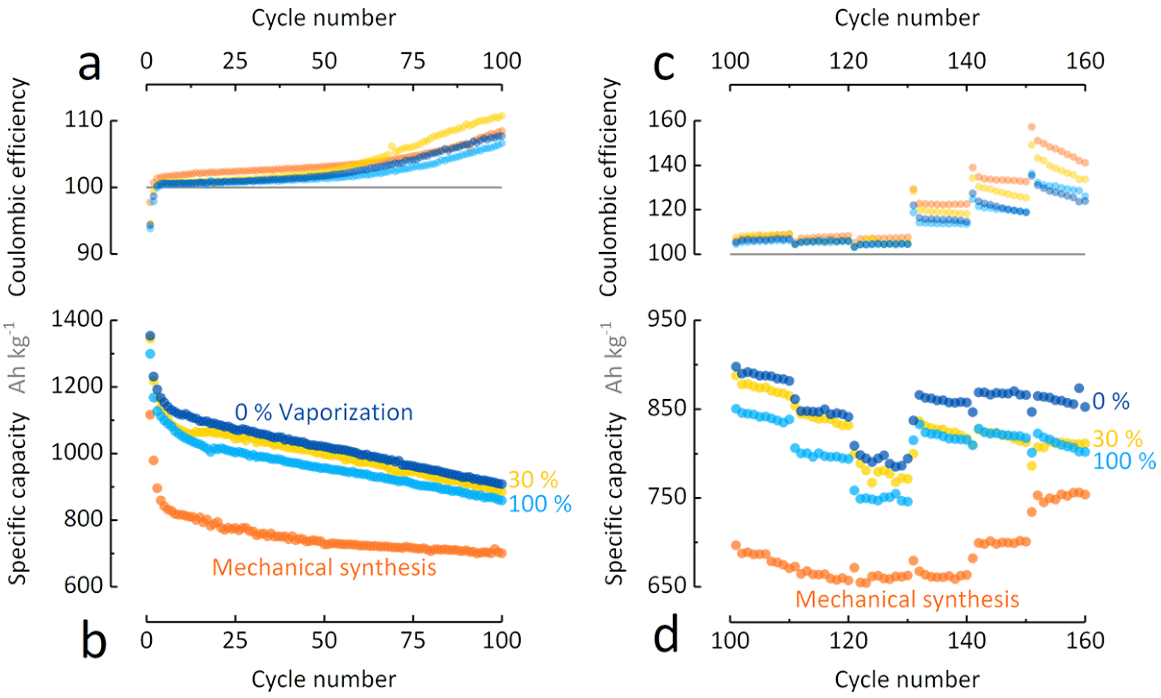

Figure 4.8. *Extended galvanostatic cycling of autogenic carbon sulfur composites.* Autogenic carbon sulfur composites, under various extent of vaporization time at temperature 445 °C, demonstrate high specific capacity compared to mechanical mixing synthesis.

posite. Interestingly, voltage profiles show two characteristic sulfur voltage plateaus: the high voltage plateau near 2.3 V and the low plateau near 2.1 V. The presence of the high voltage plateau during discharge suggests reduction of high order polysulfides to species of form Li_2S_6, which eventually transition to reduction into low order polysulfides and lithium sulfide Li_2S. The sloping transition and activation overpotential observed at approximately 350 Ah kg^{-1} are due to high order polysulfide solvation [50]. Note the overpotential feature which occurs during charging is negligible in the autogenic materials but prevalent in the mechanically–derived composite. This overpotential feature is attributed to activation barriers for lithium sulfuide dissolution [78].

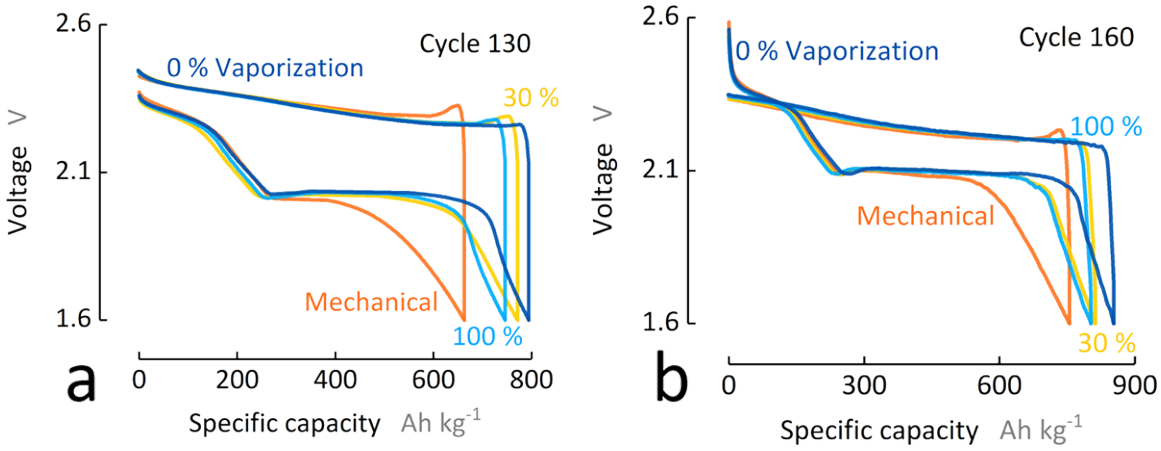

Figure 4.9. *Chronopotentiograms for autogenic carbon sulfur composites.* After cycle 130 at rate 2 C (a) and cycle 160 at rate C/20 (b), autogenic carbon sulfur composites demonstrate high capacity and greater energy efficiency than mechanically synthesized composites.

Electrochemical impedance spectroscopy (Fig. 4.10) suggests autogenic carbon sulfur composites demonstrate less impedances compared than the mechanically–formed composite. The spatially normalized impedance of all autogenic materials show a principle high frequency arc and low frequency diffusion curve. The charge transfer resistance – represented by the diameter of the low frequency arc – is less for all autogenically-derived materials compared to the mechanically milled case. The diffusion tail of the mechanically mixed case also shows lower phase angle than in autogenic cases, suggesting diffusion through the effective sulfur layer has a considerably longer path length than in the autogenically–derived cases. In addition, the physically mixed composite shows a diffuse impedance arc at moderate frequency, that is between the high frequency arc and the low frequency arc. The appearance of this arc is not well characterized for carbon-sulfur composites. In bare carbons, Aurbach et al. [54, 79] attribute the appearance of this feature to heterogeneous material factors including non-uniformity of the superficial electrode surface area, drastic disparity in conductivities of the bulk electrolyte and active material phases, significant poros-

ity. Of these possibilities, significant heterogeneities (1) on the superficial electrode surface and (2) in drastic conductivity differences between the external sulfur layer and bulk electrolyte are probable causes. These impedance differences, consistent with material characterization, suggests an effective sulfur layer much thicker in the mechanically mixed phase relative to the autogenic materials in which this hump is very much absent.

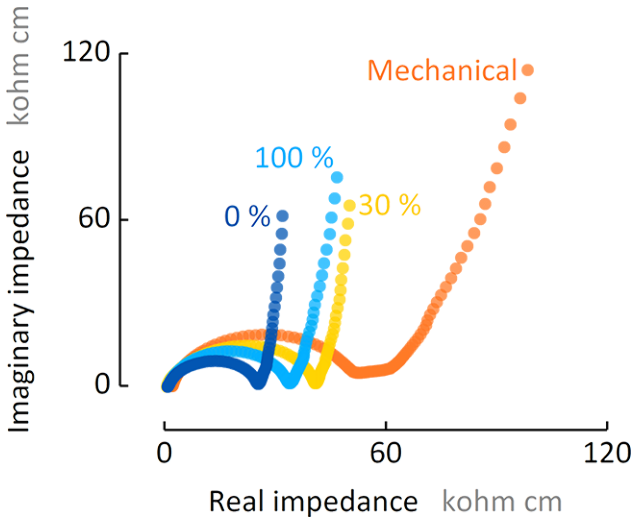

Figure 4.10. *Impedance spectroscopy for autogenic carbon sulfur composites.* After cycle 130 at rate 2 C (a) and cycle 160 at rate C/20, autogenic carbon sulfur composites demonstrate high capacity and greater energy efficiency than mechanically synthesized composites.

4.3 Advantages of Homogeneous Sulfur Composites

Homogeneity of sulfur distribution, within carbon substrates supporting morphological polysulfide control, dictates electrochemical performance and lifetime of carbon sulfur composites. This property is most sensitive to synthesis pathway rather than structural order of the sulfur phase. The effective interfacial surface area (e.g., measured by isothermal nitrogen sorption) of the bare carbon substrate governs the maximum sulfur loading in which morphological polysulfide control can apply. Electrochemical experiments suggest available surface area governs the maximum extent

of constrained sulfur loading, in which high sulfur loading approaches the electrochemical performance of mechanically-synthesized composites with less sulfur.

The pathway of synthesis determines the electrochemical performance of carbon sulfur composite performance. Synthesis methods which encourage homogeneous distribution of sulfur (i.e., with thinner effective sulfur coating thickness) produce composites with better electrochemical performance and less resistance features. In particular, specific capacity and capacity retention was found to increase for composites as homogeneity of sulfur distribution via the production process.

CHAPTER 5: MICROSTRUCTURE, ELECTROLYTE, & MULTISCALE MODELS WITH SULFUR CATHODES

In Chapter 4, autogenic synthesis was shown to produce sulfur and KETJEN BLACK composites with greater gravimetric capacity than its mechanical counterpart. Like synthesis pathway, carbon microstructure or morphology and electrolyte enhance electrochemical performance: sparingly–solvating electrolytes [80] and nanoporous microstructures reduce polysulfide solvation and reduce polysulfide shuttle expression. Both electrolyte and microstructure are studied using the synthesized carbon compartments, produced by pyrolysis of commercial wheat flour.

The original publication of this work appears in the Journal of the Electrochemical Society, volume 163, issue 5, A730 – A741. Compoiste synthesis, material characterization, electrochemical characterization, data analysis, and manuscript preparation was performed by Arthur D. Dysart, Juan C. Burgos, Aashutosh Mistry, , Chien-Fan Chen, and Zhixiao Liu. Modeling work was performed by Juan C. Burgos, Aashutosh Mistry, Chien-Fan Chen, Zhixiao Liu, Prof. Perla B. Balbuena, and Prof. Partha P. Mukherjee.

Abstract

In this work, a heterofunctional porous carbon, termed the carbon compartment (CC), is utilized as a sulfur host within a lithium-sulfur battery cathode. A multi-scale model explores the physics and chemistry of the lithium-sulfur battery cathode. The CCs are synthesized through a rapid, low cost process to improve electrode-electrolyte interfacial contact and accommodate volumetric expansion associated with sulfide formation. The CCs demonstrate controllable sulfur loading and ca. 700 mAh g^{-1} (at 47%-wt. S) reversible capacity with high Coulombic efficiency due to their unique

structures. Density functional theory and ab initio molecular dynamics characterize the interface between the C/S composite and electrolyte during the sulfur reduction mechanism. Stochastic realizations of 3D electrode microstructures are reconstructed based on representative SEM micrographs to study the influence of solid sulfur loading and lithium sulfide precipitation on microstructural and electrochemical properties. A macroscale electrochemical performance model is developed to analyze the performance of lithium-sulfur batteries. The combined multi-scale simulation studies explain key fundamentals of sulfur reduction and its relation to the polysulfide shuttle mechanism: how the process is affected due to the presence of carbon substrate, thermodynamics of lithium sulfide formation and deposition on carbon, and microstructural effects on the overall cell performance.

5.1 Synthesis & Simulation with Amorphous Carbon Compartments

The goal of developing new and efficient renewable energy technologies from intermittent energy sources, such as solar and wind, necessitates the need for effective, economical, and safe energy storage. [81–83] While batteries and supercapacitors have been considered the best options to address this issue, their progress is staggered by both challenging synthesis problems and a continually-developing understanding of their fundamental electrochemistry. [84] Currently, lithium-ion batteries dominate the market for portable electronic devices; however, their cost and relatively low energy density prevents them from being used in electrical vehicle applications at this juncture. [84, 85] Going beyond lithium-ion chemistry, lithium-sulfur and lithium-air are among the most promising battery technologies that can potentially meet the required target of about 1,000 Wh kg^{-1} energy density needed to improve the viability of electrical vehicles.

The appeal of a sulfur-based cathode lies in its high theoretical capacity that is about one order of magnitude higher than current metal oxide-based ones. Sulfur is also cheaper and more environmentally-friendly than commercially available cathode materials. [86] Low density and natural abundancy imply that the manu-

facturing of Li-S batteries from elemental sulfur will be cost effective and have low environmental impact. [87] Thus, Li-S batteries hold significant promise due to their high theoretical specific energy density (2567 Wh kg^{-1}), [57] assuming the complete electrochemical reduction of α sulfur to S^{2-} (i.e., without the formation of lithium polysulfide). Altogether, these properties suggest promising implementations of the Li-S electrochemistry in transportation applications.

However, the Li-S system is known for its complex and highly-interconnected chemistry, [38] which gives rise to various problems throughout the battery. An anode of lithium (Li) metal, due to its extreme reactivity, results in the well-known phenomena of dendrite formation and brings about several safety issues. [38] Similarly, other high energy density anodes compatible with the sulfur cathode afford their own unique challenges. [38] With respect to the electrode interface, the polysulfide shuttle mechanism involves dissolved polysulfide (PS) species that freely move throughout the battery and are very difficult to characterize. [38, 57] Furthermore, these reactions may result in the formation of an insulating lithium sulfide Li_2S or lithium disulfide Li_2S_2 film on the anode surface. [88] The solid sulfur cathode also has specific issues of its own, including low electronic and ionic conductivities and cumulative mechanical damage during cycling that results from volume changes associated with precipitation. Structural changes occur during lithium sulfide precipitation and PS dissolution leading to swelling and pulverization.

Although interesting solutions have been proposed and successfully implemented, such as the use of nanostructured composite sulfur-carbon compounds with reversible capacities up to 1320 Ah kg^{-1}, [60] the development of a Li-S couple into a commercially-viable battery has, however, been hampered by poor reversibility during discharge and subsequent recharge cycles. This is due to the combination of the previously described issues, and the interrelated chemistries that connect the cathode, anode, and electrolyte reactions.

This work demonstrates the first use of carbon compartments (CCs), conductive 3D carbon mesostructures that possess macro and meso-pores that allow high loading of sulfur nanoparticles and enhanced electrolyte-sulfur contact. CCs are fabricated using a scalable, single-step, inexpensive, and solid-state synthesis. The developed 3D carbon architectures provide a conductive backbone for non-conducting sulfur particles and effectively accommodate volume expansion during Li_2S formation. After loading with sulfur, the remaining pore openings in the CCs are sealed by carbon black that is added during electrode preparation. The obtained CC 3D architecture is observed to be filled and/or decorated with functional nanosized sulfur cathode particles. Recently, an ultrasound-mediated [89] aqueous synthetic route was shown to produce a porous carbon-sulfur electrode in one pot synthesis. This procedure is extended to this work for loading of nanosulfur in CCs.

Furthermore, this work reports the synthesis, characterization, electrochemical performance, and modeling of a nanosulfur-loaded compartmented carbon substrate as a novel cathode material for Li-S batteries. This work provides new elucidating microscopic details which are used to explain the observed macroscopic electrochemical performance and discuss potential alternatives. The theoretical analysis uses a combination of density functional theory (DFT), ab initio molecular dynamics (AIMD), and mesoscopic modeling to investigate the role of carbon on sulfur reduction, solubility, and stability of PS products during the discharge reactions. In addition, the influence of sulfur loading and that of the carbon substrate on the microstructure, electrochemical properties, and overall performance are also examined.

Experimental Methods

Solid-state Synthesis of Nanostructured 3D Carbon Compartments

This work reports the first use of CCs, produced by an inexpensive process, to create a 3D carbon mesostructure that serves as a conductive substrate for electrochemic ally-active sulfur. In a typical synthesis, ultrasonic irradiation facilitates

reaction between dilute hydrochloric acid solution and an aqueous sulfur precursor of sodium thiosulfate in the presence of CCs yield a composite of CC carbon with pure nanosized sulfur (CCs/S composite) with a water-soluble byproduct of sodium chloride NaCl. This new process avoids the widely used, less energy efficient "melt-down" approach, which requires heating sulfur to a liquid that permeates non-homogeneously into a porous substrate. The fabricated CCs/S cathode architecture yielded stable cycling performance and high cycling efficiency with a fluorine-containing electrolyte. The Coulombic efficiency in the new DOL/D2/LiTFSI electrolyte is greater than 96% for 100 cycles; a far superior value to those found in existing reports for the numerous known electrolyte formulations. [89]

In our earlier work, commercial-grade mesoporous carbon was used for deposition of sonochemically-synthesized sulfur nanoparticles. [89] The 10 nanometer pore size of the utilized commercial porous carbon is believed to limit the extent of effective sulfur nucleation and loading. Furthermore, this grade of porous carbon is expensive and has been discontinued. Recently, the production of novel micro/meso-porous CCs has been demonstrated with a cost-effective and scalable synthesis. To mediate the previous concern, this work proposes the use of CCs as the conductive carbon substrate and implements CCs to create an industrially-viable and high performance carbon-sulfur (C/S) composite.

The CCs are distinct from todays commercial carbons due to the presence of small and large cavities that enhance electrolyte contact and conductivity of the C/S composite. CCs are synthesized via pyrolytic heat treatment of starch precursors within an inert atmosphere. As a carbohydrate, starch is comprised of long chains of organic glucose monomers. Of particular importance, decomposition of the hydrogen-containing functional groups within the starch are thought to facilitate a reductive atmosphere to encourage reduction into amorphous carbon. Thus, the controlled heating of starch under inert atmosphere facilitates pyrolytic decomposition into a carbonaceous mass due to the presence of intrinsic reducing agents. Post-processing or refining of this carbon substrate is not required. During pyrolysis, the formation

of aerosol byproducts, including water vapor or steam, are observed and assist in the generation of cavities. It is observed that the graphitic nature of CCs is dependent upon the heating profile during pyrolysis: higher carbonization temperatures improve graphitization while lower temperatures yield a more amorphous material.

The synthesis of CC particles is described as follows. Starch precursor was loaded into a covered alumina crucible and placed inside a high-temperature tube furnace (MTI OTF-1200X). The heating chamber was thoroughly purged using high purity argon gas (99.999% purity, Indiana Oxygen Company). Operating under continuous gas flow, the precursor was heated at a rate of 10 °C min^{-1} from room temperature to 900 °C with a dwell time of 120 min and cooling rate of 10 °C min^{-1}. The resulting carbon pellet was then pulverized using a mortar and pestle into a fine powder to create CCs particles. The CCs are characterized for porosity and surface area before implementation into the carbon-sulfur composite.

Characterization of Sulfur Carbon Composite Nanostructures

Scanning Electron Microscopy (SEM) and Energy-Dispersive X-ray Spectroscopy (EDS) were performed using a FEI Nova 200 NanoLab DualBeam SEM/FIB and Oxford Instruments X-Max Silicon Drift Detector, respectively. X-ray diffraction (XRD) was performed using a Rigaku Smartlab X-ray diffraction system with a scan rate of 10 ° min^{-1}. Thermogravimetric analysis (TGA) was performed using a TA Instruments Q500 Thermogravimetric analyzer (TGA). For TGA analysis, the carbon-sulfur composite, after thorough homogenization, is heated under a continuous atmosphere of high purity inert gas (Helium, 99.999%, Indiana Oxygen Company) at a heating rate of 10 °C min^{-1} from 30 °C to 600 °C.

Electrochemical Testing of the Carbon Sulfur Composite

The cathode material is comprised of 70 %-wt. carbon sulfur-composite (45 %-wt. S and 25 %-wt. C), 20 %-wt. carbon black additive (TIMCAL Super P Li), and 10 %-wt. polyvinylidene fluoride (KYNAR HSV900, Arkema Inc.) binder. The cathode was prepared by homogenization of these materials in N-methylpyrrolidone (NMP) using a planetary mixer (THINKY AR-100) at a constant speed of 8500 rpm for 20 minutes. The resulting slurry was coated onto battery-grade aluminum foil using an MTI laminate coater. All materials were tested in CR2032 coin cells (MTI Corp.) assembled in an inert atmosphere glovebox (NEXUS II Vacuum Atmospheres Co.). The working environment was filled with high purity argon gas (99.999%, Indiana Oxygen Company) with moisture and oxygen content both less than 1 ppm. A lithium metal chip (MTI Corp) is used as the anode. The DOL/D2/LiTFSI electrolyte was composed of 50% 1,3-dioxolane (DOL) solvent, 50% 1,1,2,2-tetrafluoro-3-(1,1,2,2-tetrafluoroethoxy)-propane (D2) solvent, and 1 M Lithium bistrifluoromethanesulfonimidate salt (LiTFSI, Sigma Aldrich). The separator was cut from glass fiber filter paper (Whatman). Cells were crimped at a constant pressure of 1000 psi. Electrochemical tests upon the completed CR2032-type coin cells were performed using a BT-2043 Arbin Battery Testing System. All cells were cycled at different current rates in the voltage interval of 1.5 V - 3.0 V. All capacity values were calculated according to the mass of the sulfur active material.

Atomistic Simulations

CCs prepared at 900 °C produce a morphological structure somewhat similar to multilayer graphene. Hence, graphene models were employed to mimic the carbon environment in contact with nanosulfur. The composite material for Li-S cathodes was modeled as graphene flakes with sulfur. [90] The carbon-sulfur interface is modeled as a porous graphitic cathode with two orthorhombic sulfur rings S_8 at the edge of the pore. The pore was built by placing finite graphene layers at the bottom of

an orthorhombic cell, with each layer parallel to both one another and to the z-axis. The free volume was filled with organic solvent (DOL) and 16 Li atoms, which yields a lithium concentration range of 0.007 – 0.013 mol cm^{-3}, with the actual value dependent upon the size of the system (i.e., sulfur percentage). The size of the pore was fixed by placing either one or two graphene layers at the bottom of the cell, which results in pore sizes of 2 nm or 1 nm, respectively. Similarly, the sulfur percentage relative to carbon was fixed by modifying the height of the graphene layers.

Analyses of adsorption energies were carried out with DFT [91,92] within the plane wave basis set approach. [93, 94] The Kohn-Sham equations were solved as implemented in the Vienna ab initio simulation package (VASP). [95,96] Here, electron-ion interactions are described by the projector augmented wave (PAW) method. [97, 98] Additionally, the electron-electron exchange correlation is framed using the generalized gradient approximation (GGA) of the Perdew-Burke-Ernzerhof (PBE) functional. [99] The energy cut-off of the plan wave basis set was set to 400 eV. A 3–by–3 graphene supercell with 16 Å vacuum was used to simulate Li_2S/graphene interaction with the corresponding k-point grid generated by the Monkhorst-Pack technique [100] for the Brillouin zone sampling. Both van der Waals (vdW) vdW-D3 [101] and vdW-D3(BJ) corrections [101, 102] were considered in the present study due to the important role of the van der Waals interaction in these systems. [103]

Ab initio molecular dynamics (AIMD) simulations of CCs/S cathode systems were performed following the Born-Oppenheimer procedure [104] to describe the classical motion of ions as implemented in VASP 5.3.5. The GGA-PBE25 functional was used with a plane wave energy cut-off of 400 eV. The time step was set to 1 femtosecond (fs), and the systems were allowed to run for ca. 3 picoseconds (ps) to adequately allow for a high degree of sulfur reduction to short PS chains, or stabilization of the PS species (i.e., without further reduction). Parrinello-Rahman dynamics [105, 106], at constant parameters of number of particles, pressure, and temperature (NPT), were chosen in order to account for possible volume expansions due to PS reduction. The temperature was set to 330 K using the Langevin thermostat [107, 108], and

all Langevin friction coefficients for relevant atoms present in organic solvents (i.e., carbon, oxygen, hydrogen) were set to 5.0 ps^{-1}. The friction coefficient and the fictitious mass for Parrinello-Rahman lattice degrees of freedom were set at 5.0 ps^{-1} and 20 amu, respectively. The convergence criterion for the electronic self-consistent loop performed for each dynamic step was fixed to 10^{-4}, whereas a 1–by–3–by–1 Monkhorst-Pack grid[26] was used for the Brillouin zone integrations carried out over the system. The partial occupancies were set to each orbital following the Gaussian smearing method[35] with a smearing width of 0.05 eV.

Cathode Microstructure Reconstruction

Chemical reactions (e.g., dissolution, precipitation) alter the cathode microstructure. A simulation method was used to investigate the consequence of microstructural changes in terms of the modified electrochemically active area and effective transport properties. Virtual 3D microstructures were used to investigate the effect of sulfur loading and Li_2S precipitation on electrochemical properties. The current model assumes a uniform film of solid S_8 or Li_2S. The microstructural characteristics are a function of empty (pore) volume and complexity of the pore network. Thus, in the context of uniform film growth, cathode properties can be quantified based on initial carbon structure and film thickness; that is, data for solid S_8 is equally applicable to Li_2S film growth.

Virtual 3D microstructures were utilized to investigate the effect of sulfur loading on the electrochemical properties (e.g., ionic conductivity). The virtual 3D microstructure was reconstructed according to the SEM image of the experimental carbon framework, with primary components in the Li-S cathode microstructure of the carbon substrate and the loaded solid sulfur. [109] The carbon framework substrate, the porous structure that stores solid sulfur and provides pathways for ionic transport, was artificially generated by using a stochastic method. [110–113] During the reconstruction process, the spherical pores were randomly distributed within the carbon substrate, with the actual pore size distribution assigned in accordance with our ex-

perimentally fabricated carbon framework. Here, the spherical pores were permitted to overlap with one another. The solid sulfur was then added at the interface between pore space and carbon substrate. Effective electrochemical properties were calculated by simultaneously solving the concentration gradient inside the microstructure and the Bruggeman relation. [114]

Macroscale Performance Model

Though the cathode and separator are porous components, permitting species to travel through their internal networks of interconnected pores, the mathematical description can be significantly simplified by statistical operations over a sufficient number of pores. This simplification leads to porous electrode theory. The length scale of applicability of this model is much larger than pore dimensions. The microstructure effect is reflected through effective properties like porosity, tortuosity, and effective transport properties (e.g., ionic conductivity).

The mathematical model involves species balances (i.e., Li^+, S_8, ${S_8}^{2-}$, ${S_6}^{2-}$, ${S_4}^{2-}$, ${S_2}^{2-}$, and S^{2-}) to quantify changes in species (both charged and neutral) concentrations and in volume fractions of solid sulfur, solid lithium sulfide salt Li_2S and electrolyte space (i.e., porosity). For slow discharge rates, the species concentration gradients across both the separator and cathode are negligible. Therefore, cell operation non-ideality was attributed to activation overpotential and concentration overpotentials, and transport resistance was treated as negligible. Then, any change in species concentrations and volume fractions is considered a result of chemical reactions (e.g., electrochemical oxidation of lithium metal, reduction of dissolved sulfur to various polysulfide ions, dissolution of solid sulfur, precipitation of lithium sulfide salt). The electrochemical kinetics was described by the Butler-Volmer equation while usual forward-backward reaction kinetics was assumed for the remaining chemical reactions:

$$\frac{d\left(\varepsilon c_i\right)}{dt} = r_i \quad \forall \quad i \in \left\{ Li^+, S_{8(l)}, S^{2-}_{8(l)}, S^{2-}_{6(l)}, S^{2-}_{4(l)}, S^{2-}_{2(l)}, \text{ and } S^{2-}_{(s)} \right\} \tag{5.1}$$

$$\frac{d\varepsilon_k}{dt} = Q_k \quad \forall \quad k \in \left\{ S_{8(l)}, Li_2S_{(s)}, \text{ and electrolyte} \right. \tag{5.2}$$

The resulting set of 7 species equations and 3 volume fraction equations is a set of differential equations. The source terms are related to reaction kinetics.

From these calculations, the terminal cell voltage at each step is computed according to overpotential:

$$\eta_{cell} = E_{cathode} - E_{anode} \tag{5.3}$$

Various sulfide ions (i.e., $S_x{}^{2-}$) can react with lithium ions coming from the anode to produce lithium polysulfides. Our current atomistic analysis indicates that Li_2S is a dominant species. Therefore, only Li_2S precipitation is considered in the electrochemical formulation.

5.2 Electrochemistry and Microscale models

Sonochemical Synthesis of Sulfur Carbon Composites

Sonochemistry is the application of ultrasound waves to produce nano-materials via acoustic cavitation (Fig. 5.1). [115] In sonochemical synthesis, high frequency vibrations are generated by a piezoelectric probe and transferred into an aqueous reaction volume. This action causes diffusion of soluble vapor to create nano-sized vapor pockets that move in high velocity jet-streams. These vapor bubbles have a diameter of 1 nanometer (nm) and a lifetime of 1 nanosecond (ns). Upon implosive collapse, these bubbles release high temperature (4000 K), pressure (1000 atm), and heating rates (1011 K s^{-1}) that encourage accelerated reaction kinetics. [116] Instantaneous kinetics brought about by the short bubble lifetime and high cooling rates prevent the growth of particles larger than a few nanometers. Generally, the resulting sulfur particles are amorphous in the presence of volatile solutes, or crystalline in the presence of non-volatile solutes.

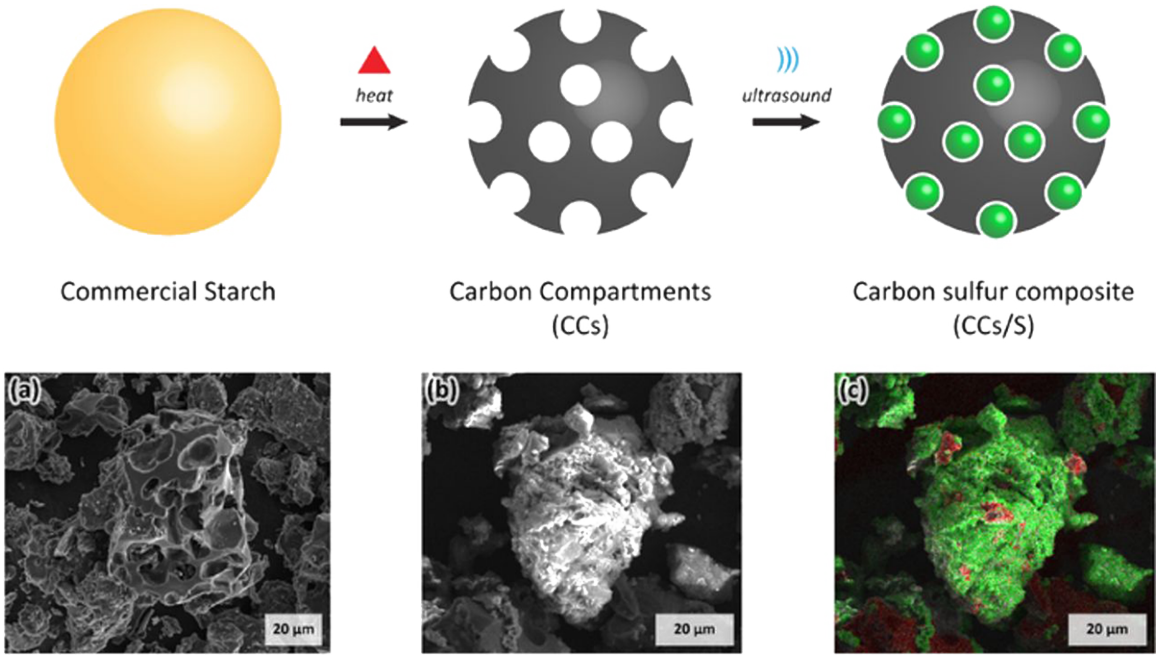

Figure 5.1. *Synthesis of sulfur composites with carbon compartments.* Schematic describing the ultrasonic synthesis of the CCs/S composite. (Top) Graphical representation of the CCs synthesis process and the sonochemical sulfur loading technique. (Bottom) (a) SEM micrograph of a porous CC particle without sulfur. (b) SEM micrograph of the carbon-sulfur composite produced via the sonochemical sulfur deposition process. (c) Elemental mapping of the carbon-sulfur composite by EDS color pixel-mapping. Sulfur is highlighted in green, while carbon is highlighted in red.

In this experiment, 1 gram (g) CCs and 4.9 g sodium thiosulfate (Sigma-Aldrich) were combined in an open-atmosphere vessel containing 100 milliliters (mL) of Type 1 water. The mixture was homogenized using 40 % power ultrasonic irradiation intensity provided by a Sonics Ultrasonic Processor (20 kHz, 750 W) for 1 minute. In a separate container, 10 mL hydrochloric acid (37%, Sigma-Aldrich) is combined with 10 mL Type 1 water. Upon addition of the prepared hydrochloric acid, the carbon-thiosulfate solution was immediately sonicated for up to 15 minutes. The hydrochloric acid solution was added dropwise to the carbon-thiosulfate aqueous slurry across the

duration of sonication. The produced C/S composite was then purified by three centrifuge-assisted washes, two with Type 1 water and one with ethanol, followed by drying in an oven at 100 °C for less than 1 hour.

Before loading sulfur (Fig. 5.1a), the as-prepared CCs exhibit small and large cavities that permit sulfur loading while retaining an intimate electronic pathway. The CCs demonstrated here are synthesized via a separate, single-step pyrolytic heat treatment of a starch precursor. Nitrogen sorption isotherms of CCs only (Fig. 5.2a) demonstrate an appreciable specific surface area of 273.900 m^2 g^{-1} available for sulfur loading, with a modal pore width of 1.289 nm. The specific surface area and average pore size were calculated according to the DFT method. The CCs primarily contain micro and meso-pores according to the isotherm shape as type II according to the suggested IUPAC classification standards [77]. The hysteresis observed between the adsorption and desorption isotherms are characteristic of sorption complications due to microporosity.

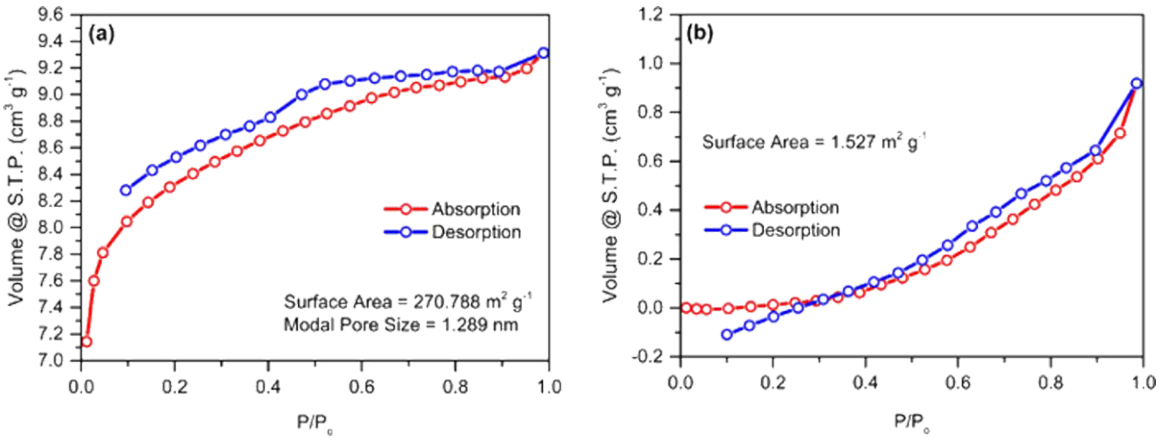

Figure 5.2. *Isothermal nitrogen sorption of sulfur-carbon compartment composites.* Nitrogen sorption isotherms of CCs and the CCs/S composite demonstrate a 269.26 m^2 g^{-1} loading of sulfur on available carbon surfaces. Nitrogen isotherms of CCs alone demonstrate a specific surface area of 270.788 m^2 g^{-1}.

After applying ultrasonic irradiation, the CC particles serve as a conductive substrate for sulfur and create a hybrid composite (Fig. 5.1b). Nano-sulfur is formed via the action of acoustic cavitation in aqueous solution. Nucleated sulfur is loaded into the cavities via sonochemical microjets to produce a homogeneous and conductive CCs/S composite. Elemental pixel mapping (Fig. 5.1c) shows that CCs can accommodate sulfur upon the available compartments. Nitrogen sorption isotherms of the CCs/S composite (Fig. 5.2a) demonstrate a drastic reduction in specific surface area to 1.527 m^2 g^{-1}. In comparison to the isotherms for carbon compartments alone, the isotherms for the CCs/S composite imply that most available carbon surfaces contain deposited sulfur. X-ray powder diffraction (XRD, Fig. 5.3) identifies the crystal structure of the loaded sulfur in CCs as an orthorhombic allotrope of sulfur known as α sulfur, [117] the most stable allotrope at room temperature. The amorphous structure of pristine CCs is further studied by Raman spectroscopy and X-ray diffraction and will be reported in an upcoming publication. Thermogravimetric analysis (TGA, Fig. 5.4) of the CCs/S composite indicated significant mass loss between 100 and 200 °C confirming 47.64%-wt of sulfur loading. Additional experiments have demonstrated up to 65%-wt sulfur loading: the high degree of nano-sulfur loading is manifested through the deposition of sulfur within the pores and micro-size compartments.

Electrochemical Performance of Sulfur Carbon Composites

The electrochemical performance of the novel CCs/S composite electrode vs. Li metal is demonstrated in Fig. 5.5 with the DOL/D2/LiTFSI electrolyte. The hybrid electrode comprising 47%-wt sulfur (0.36 mg cm^{-2}, sulfur per electrode area) shows stable performance during rate studies. Hysteresis is shown to increase as the specific current is increased. The upper voltage plateau in the charge curve is seen to be constant. In the presence of a fluorinated electrolyte containing 1,1,2,2-Tetrafluoroethyl 2,2,3,3-tetrafluoropropyl ether (D2), it is observed that there is a shift in the voltage at which the reduction or oxidation of sulfur compounds occurs. [61, 118] The voltage profiles of the CCs/S composite under different specific currents are shown in

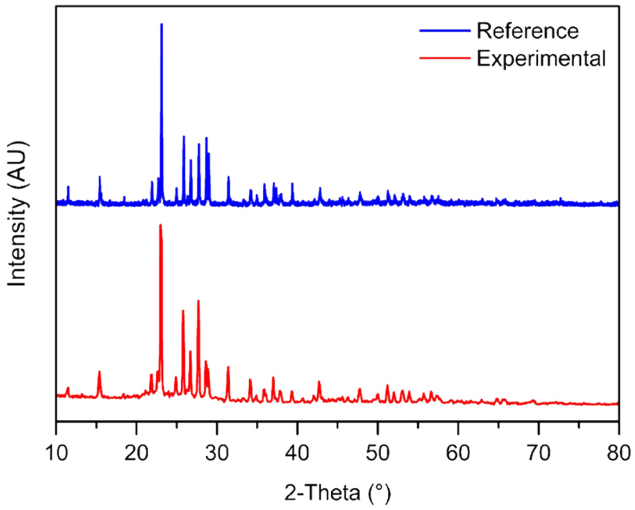

Figure 5.3. *X-ray diffraction of sulfur-carbon compartment composites.* X-Ray Powder Diffraction demonstrates that the CCs/S composite contains nano-size orthorhombic sulfur. The experimental spectrum (red) produced by X-ray treatment of the CCs/S composite shows high similarity to the reference spectrum (blue) for orthorhombic sulfur. The reference spectrum reproduced from Downs and Hall-Wallace. [117]

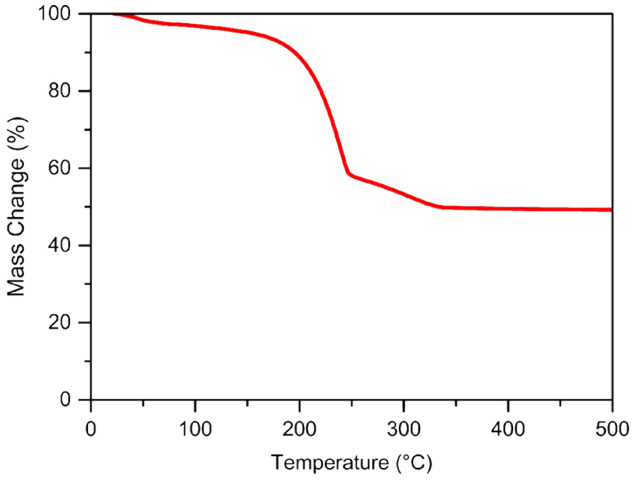

Figure 5.4. *Thermogravimetric analysis of sulfur-carbon compartment composites.* Thermogravimetric Analysis of the CCs/S composite shows significant mass loss of 47.64%-wt attributed to the melting and vaporization of sulfur within an inert gas atmosphere.

Fig. 5.5a. Our current theoretical analysis of the solid-electrolyte interphase (SEI) reactions on the Li metal surface indicates that D2 solvent is highly susceptible to decomposition into lithium fluoride (LiF) and other organic fragments, unlike the greater stability of 1,3-dioxolane (DOL) and dimethoxyethane (DME). The presence of LiF may be responsible for the formation of a more stable and passivating SEI while also stabilizing the rapid PS decomposition. [119] When cycled at a constant specific current of 112 mA g^{-1}, the carbon-sulfur composite demonstrates an average capacity of ca. 650 mAh g^{-1} and minimum 96% Coulombic efficiency. This can be attributed to the effective sulfur accommodation in the CCs/S composite cathode. However, some consistent capacity fade is seen across the 100 cycles.

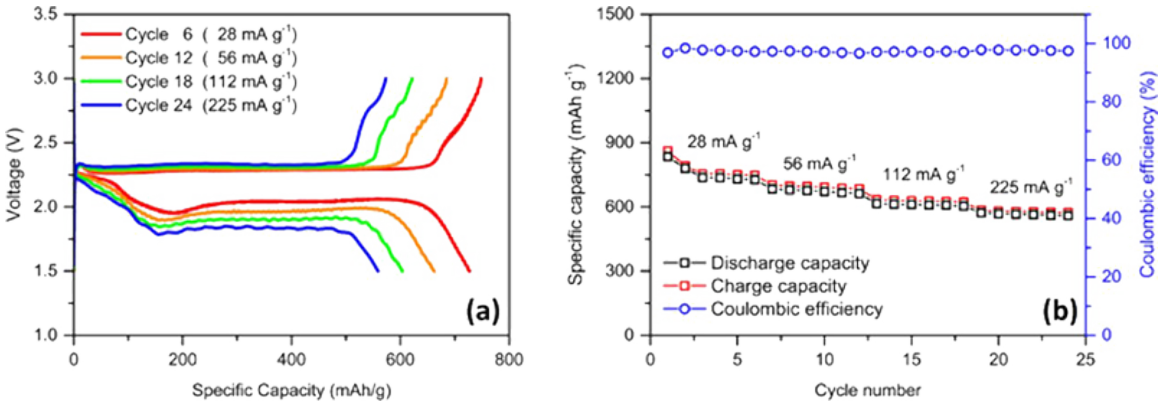

Figure 5.5. *Electrochemical performance of sulfur carbon compartment composite.* With fluorinated electrolyte, there is significant capacity retention at various applied currents. (a) Voltage profile for rate study at four representative specific currents. (b) Rate performance at four representative specific currents.

Cathode & Electrolyte Chemistry

It is important to consider the effect of varying sulfur-to-carbon (S/C) loading ratios upon the overall battery performance. From experimental results, it is observed that the high S/C ratio causes dramatic capacity fade. One possible reason for such

capacity fade is the deposition of Li_2S [120] on both carbon and sulfur surfaces leading to isolation of sulfur particles and subsequent capacity reduction. To test this, a DFT analysis was implemented to investigate the Li_2S deposition on carbon surfaces, and the results were compared to those of Li_2S crystal growth. The Li_2S adsorption structures on a graphene layer and the electronic charge differences upon adsorption are shown in Fig. 5.6.

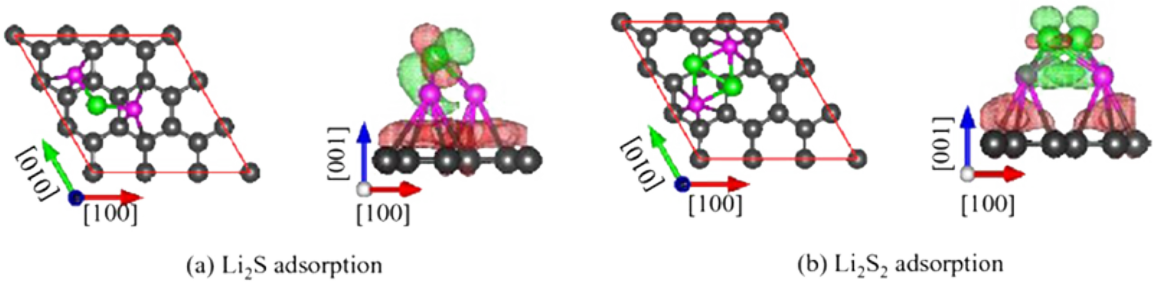

Figure 5.6. *Structure of lithium polysulfide adsorption on graphene.* Atomic structures of (a) Li_2S and (b) Li_2S_2 molecules adsorbed on graphene depend on molecular stability.

Detailed geometric parameters and energies (Table 5.1) describe the strength of graphene-polysulfide adsorption structures. Adsorption energy E_{ads} depends on total energy of graphene-adsorbed polysulfide $E_{Li_2S_x-G}$, energy of isolated graphene monolayers E_G, and energy of isolated polysulfides $E_{Li_2S_x}$:

$$E_{ads} = E_{Li_2S_x-G} - (E_G + E_{Li_2S_x}) \tag{5.4}$$

A slight difference in the adsorption energies favors the adsorption of Li_2S on graphene over that of Li_2S_2; however, the values are comparable. In our earlier work, it was determined that the Li_2S adsorption energy on the Li_2S (111) surface is 1.78 eV without the vdW dispersion correction. [121] However stronger adsorption values of 2.25 eV and 2.40 eV are obtained with the vdW-D3 [101] and vdW(BJ) [102] approaches, respectively. Comparing these values with the adsorption energies on graphene (Table 5.1), molecular adsorption of Li_2S in the absence of electrolyte is almost three times

more favorable on crystalline Li_2S comparted to graphene. Geometric parameters for adsorbed Li_2S (Table 5.1) are very similar to those of the molecular adsorption on the Li_2S (111) surface. [121] Even when the Li-C distance is larger than that of Li atoms adsorbed in graphene, [122] there is an electron transfer from the Li_2S molecule to the substrate C atoms. This results in a region of electron accumulation at the interface (Fig. 5.6) and formation of Li-C bonds.

Beyond molecular adsorption, the formation of molecular films of the Li_2S insoluble polysulfides on carbon surfaces, modeled as a 3–by–3 graphene supercell, was investigated. It was found that the Li_2S film can be arranged in three different structures. In Structure-I, the Li-S bond length (Table 5.2) is 0.27 Å shorter than the Li-S bond in the Li_2S crystal. [121] The length of the short S-S bridge D_{SS} in Structure-I is 0.35 Å shorter than the S-S distance 4.05 Å in typical Li_2S (110) layer. The variation of these geometric parameters is attributed to the lattice parameter differences between graphene and the Li_2S (110) layer. On the other hand, the S atom arrangement in Structure-II is hexagonal, which is similar to that in the Li_2S (111) layer. Each S atom coordinates with four Li atoms, and the S atom at the center of the hexagonal arrangement is not present in the Li_2S (111) surface. Details of these structures will be reported elsewhere. Hence, Structure-II is a defective Li_2S (111) surface with S vacancies. The interaction energies in Table 5.2 demonstrate that Structure-I would be the most favorable adsorption on a graphene layer. Interaction energy E_{int} is a function of total energy of the system $E_{(Li_2S)_n@G}$, energy of substrate E_G, and energy of the Li_2S layer $E_{(Li_2S)_n}$:

$$E_{int} = E_{(Li_2S)_n - G} - (E_G + E_{(Li_2S)_n}) \tag{5.5}$$

When Li_2S coverage θ increases to 1 monolayer (ML), the complete Li_2S (111) layer appears on graphene. This arrangement is named Structure-III. The atomic arrangement is exactly the same as the typical crystalline Li_2S (111) layer with Li atoms outside the S plane. The Li-S bond length in Structure-III (2.54 Å) is closer to that in the Li_2S crystal (2.48 Å). The S-S distance in Structure-III is 0.22 Å longer than that in the Li_2S crystal due to differences in the lattice parameter between graphene

and the Li_2S (111) layer. It is important to note that the distance between the Li_2S layer and graphene in Structure-III is reduced by 0.71 Å under consideration of the vdW-D3 correction. In addition to the energies shown in Table 5.2, this change demonstrates the importance of dispersion interactions within the system.

The process of Li_2S (111) formation on graphene depends on adsorption extent (Fig. 5.7). Although a single Li_2S molecule first adsorbs on graphene with a relatively small adsorption energy, the adsorbed Li_2S molecule interacts with graphene via strong covalent Li-C bonds. When more Li_2S molecules are introduced to pre-adsorbed graphene, Structure-I and Structure-II are observed. The adsorption energy was calculated as:

$$E = E_{(Li_2S)m-G} - E_{(Li_2S)_{m1}-G} - E_{Li_2S} \tag{5.6}$$

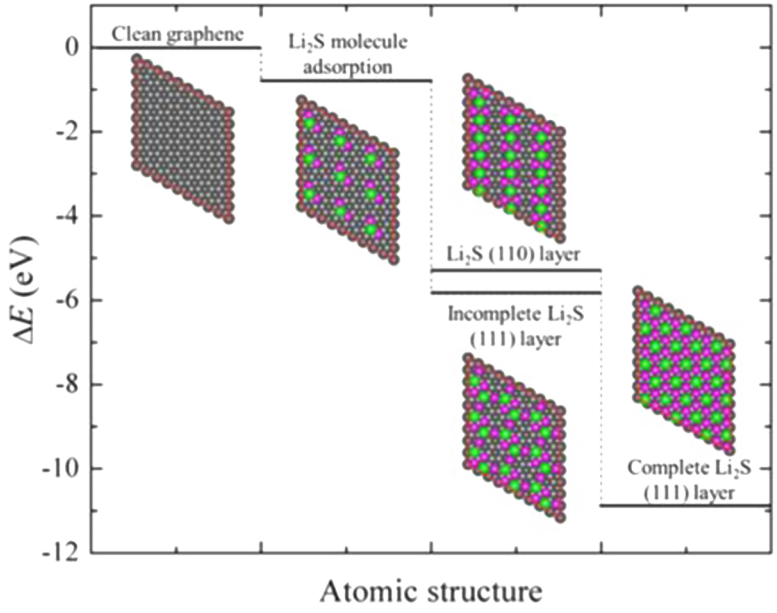

Figure 5.7. *Energy profile of lithium sulfide precipitation on graphene.* Pre-adsorbed single Li_2S molecule is the seed for the formation of Li_2S layer on graphene. When Structure-I is formed, ca. -4 eV is released with respect to the single molecule adsorption, and ca. 0.5 eV more negative for Structure-II, while forming the complete Li_2S layer is a very exothermic process.

Table 5.1.

Geometric and energetic parameters of polysulfide species and graphene. D_{LiS} is Li-S bond length, D_{S-S} is S-S distance of Li_2S_2, Φ is the Li-S-Li bond angle, and θ is the Li-S-S bond angle. D_{LiC} is average bond length between Li atoms and coordinating C atoms. Adsorption energy E_{ads} includes van der Waals corrections determined by DFT vdW-D3 [101] and vdWD3(BJ) [102] methods. Values in brackets are calculated by the latter approach.

	$D_{\text{Li-S}}$	$D_{\text{S-S}}$	Φ	θ	D_{LiC}	E_{ads}
	Å	Å	degrees	degrees	Å	eV
Isolated Li_2S	2.11 (2.11)	None	115.7 (115.7)	None	None	None
Li_2S on graphene	2.18 (2.17)	None	94.4 (96.8)	None	2.63 (2.79)	0.80 (0.85)
Isolated Li_2S_2	2.24 (2.24)	2.19 (2.19)	95.9 (95.9)	60.7 (60.7)	None	None
Li_2S_2 on graphene	2.28 (2.28)	2.11 (2.11)	86.2 (92.9)	62.5 (62.1)	2.68 (2.78)	0.76 (0.80)

Table 5.2.

Geometric parameters of lithium sulfide on graphene. D_{Li-S} is Li-S bond length, D_{S-S} is distance between adjacent S atoms, H is separation between graphene and Li_2S. Adsorption energies $E_{\widetilde{vdW}}$, E_{vdW} and all structures determined with the DFT vdW-D3 and vdW-D3(BJ) methods, with values in parentheses calculated by the latter approach.

Configuration	D_{Li-S}	D_{S-S}	H	$E_{\widetilde{vdW}}$	E_{vdW}
	Å	Å	Å	eV	eV
Structure-I	2.22 (2.22)	3.70 (3.70)	3.49 (3.37)	0.03	0.52 (0.58)
Structure-II	2.25 (2.24)	4.28 (4.28)	3.53 (3.50)	0.03	0.49 (0.53)
Structure-III	2.53 (2.53)	4.27 (4.27)	3.70 (3.63)	0.04	0.66 (0.73)

In discussing Li_2S formation, it is important to consider the initial nucleation of the Li_2S species in the real environment: the electrolyte solution surrounding the C/S cathode. The AIMD simulations reveal that stable Li_2S molecules can be formed at the very initial stages of S_8 reduction in the electrolyte phase (Fig. 5.8) or close to the carbon pore of nano-size dimensions. According to Table 5.1, the calculated Li_2S bond length is 2.11 Å. Once this length is reached, stability is maintained in the DOL electrolyte phase. Li_2S molecules can also form near the C pore edges due to the affinity of Li ions to the edges, resulting in chemical reduction. This phenomenon is illustrated in Fig. 5.9.

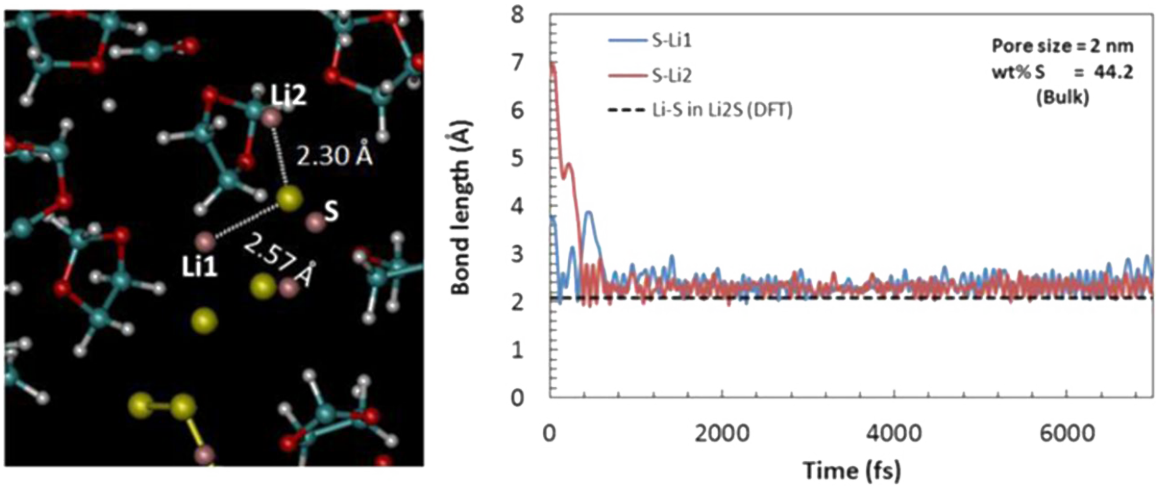

Figure 5.8. *Simulation of polysulfide formation in electrolyte.* Li-S bond distances, during formation of a Li_2S molecule from reduction of a S_8 ring, determine the stability of Li-S bonds as a function of time.

By following the time evolution of the Li ion locations relative to the electrolyte phase and the carbon pore, it was found that most of the Li ions -- and their corresponding S anions -- are located in the vicinity of the nano-size C pore edges (Fig. 5.10). Such locations would favor the nucleation of the solid Li_2S on the carbon surfaces and on the Li_2S crystals.

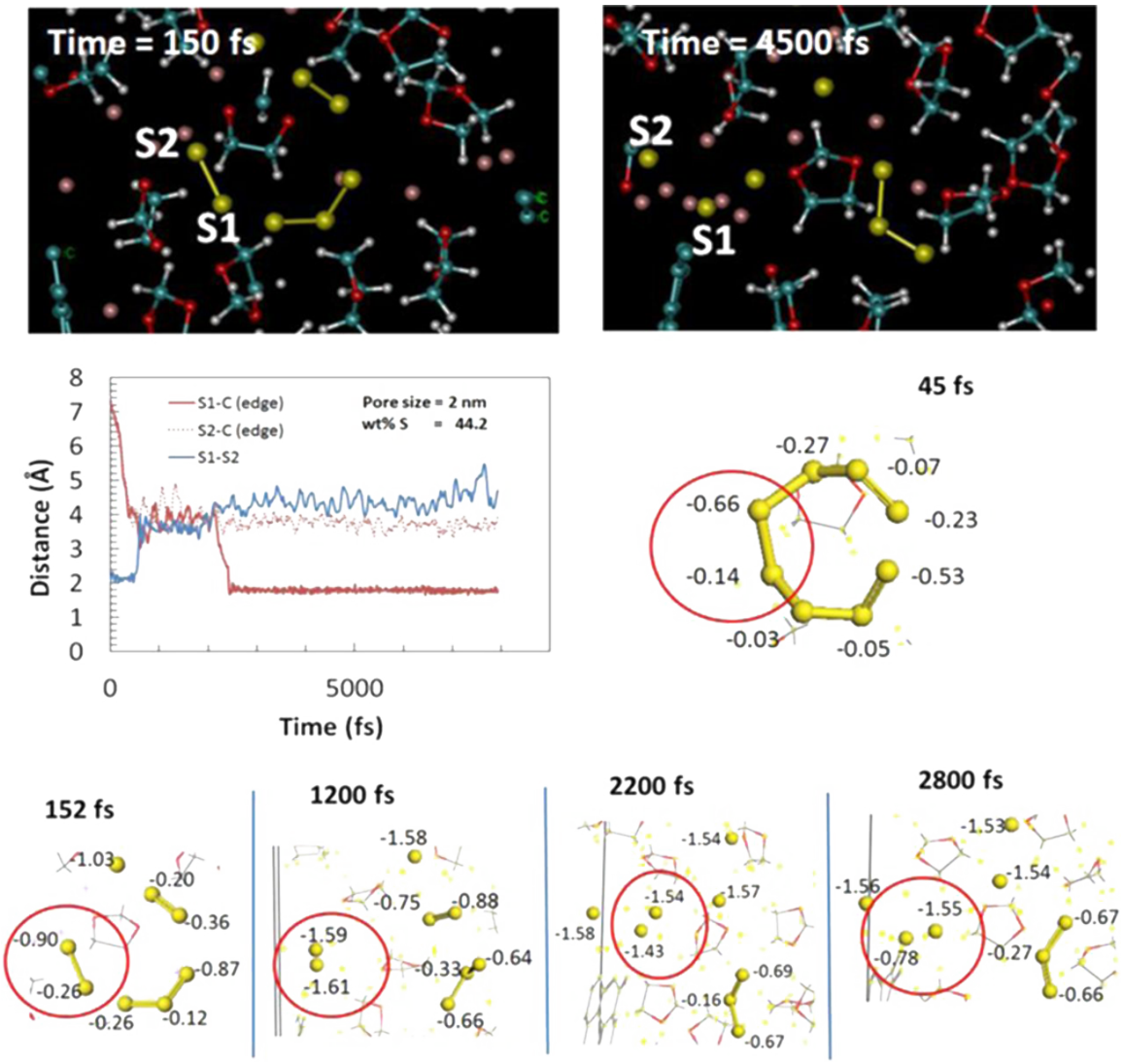

Figure 5.9. *Simulation of sulfur dissolution in electrolyte near pore defect sites.* (Top) Snapshots at 150 and 4,500 fs illustrating the initial and final fragmentation of a S_8 ring. At 4,500 fs, the S_3^{2-} is still intact. The other S dianions are paired with Li ions forming short-chain PS species. (Bottom) Time evolution of the S-S and S-C distance of a S_2 radical anion. Sulfur is shown as the color yellow, lithium as pink, carbon as blue, oxygen as red, and hydrogen as gray.

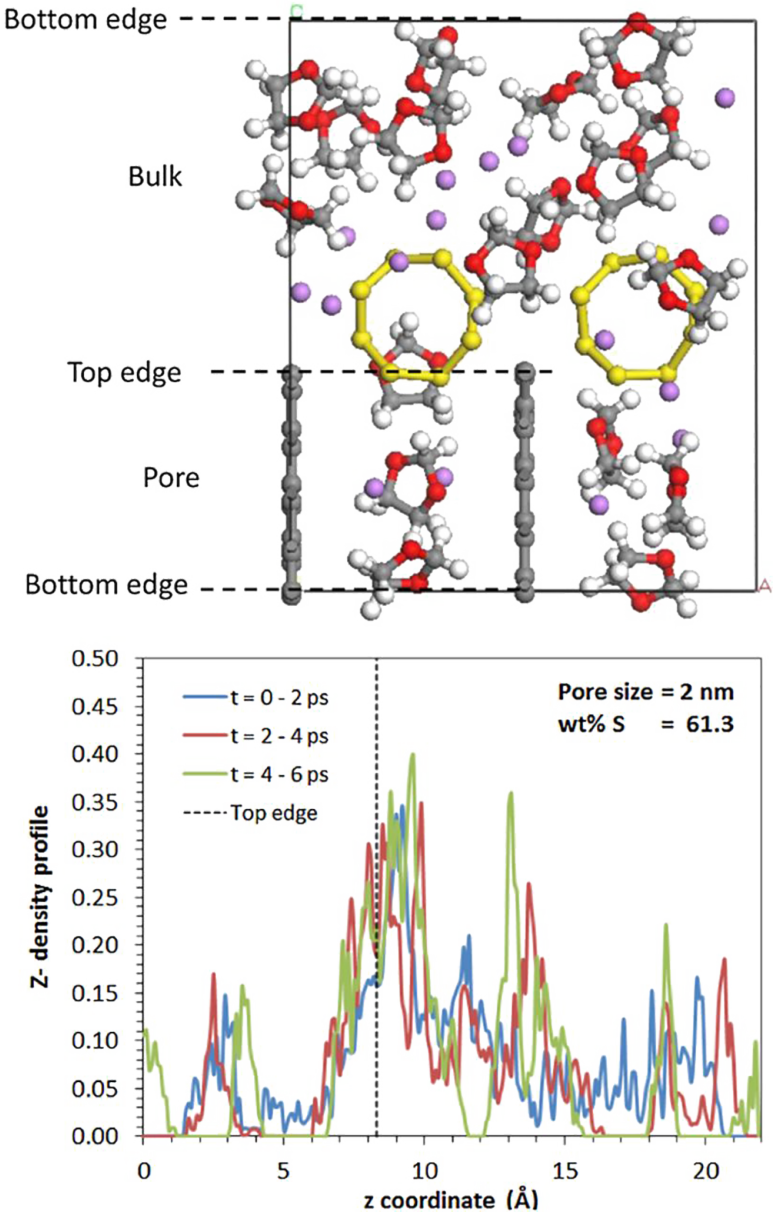

Figure 5.10. *Simulation of electrolyte-carbon pore interface.* (Top) Initial configuration of the system showing the S rings, Li ions, and electrolyte phase as well as a carbon pore defined by two graphene parallel layers. (Bottom) Location of Li ions in the system. It is observed that the Li ions accumulate near the pore edges at top and bottom. A large bulk space is in electrolyte volume in bulk is seen without Li ions after 4 ps.

Effect of Microstructure on Electrochemical Properties

As previously discussed, the porous carbon substrate is artificially generated using a stochastic method, [110–113] with solid sulfur added to the interface between pore space and carbon substrate. The purpose of stochastic modeling is to understand the effect of sulfur loading on the transport properties of the composite material. During discharge, Li_2S is formed as sulfur dissolves in the electrolyte. DFT and AIMD studies have demonstrated that Li_2S will deposit on the carbon substrate to form a solid Li_2S film. Changes in film thickness translate into microstructure evolution, an effect identical to that of sulfur loading on microstructural properties. The macroscale model presented in the next section uses these effective properties to simulate species evolution and cell discharge as a function of time.

Fig. 5.11 illustrates various stages of microstructure reconstruction. The pores assigned to the carbon substrate form cavities similarly observed in the corresponding SEM micrograph. Although increased sulfur loading does increase the capacity of the lithium sulfur battery, the resulting changes to the cathode microstructure affect the ionic transport and the subsequent cell performance.

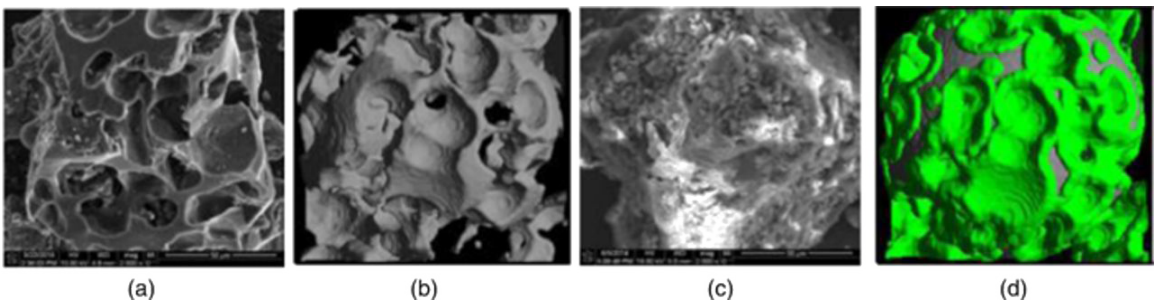

Figure 5.11. *Stochastic reconstruction of sulfur-carbon compartment microstructure.* (a) SEM micrograph of carbon microstructure without sulfur loading. (b) Stochastic regeneration of carbon microstructure. (c) SEM micrograph with sulfur loading. (d) Stochastic reconstruction of microstructure with sulfur loading.

Fig. 5.12 shows the influence of sulfur loading on the microstructure and electrochemical properties. As shown in Fig. 5.12a, when the volume fraction of solid sulfur is increased, the loaded sulfur fills the pore spaces of the carbon substrate or framework. Due to the loading of solid sulfur, the pore space in the cathode microstructure decreases as shown in 5.12b. In addition, since the pathways for ionic transport (i.e., transport of Li^+ and ${S_x}^{2-}$) are partially blocked by sulfur loading, the loading of sulfur decreases the ionic transport pathway inside the electrode.

Moreover, the blocking of ionic transport pathways causes the ionic transport to seek different routes. This is manifested as an increase in tortuosity. The variation of tortuosity under different sulfur loadings is shown in Fig. 5.12b. High tortuosity corresponds to a longer ionic transport path. According to the Bruggeman relation, a decrease in porosity and increase in tortuosity result in a lower effective ionic conductivity due to the fewer number and longer length of ionic transport pathways. Fig. 5.12c shows the decrease of ionic conductivity due to increased sulfur loading. Decreased ionic conductivity increases the internal transport resistance in the lithium sulfur battery, which in turn affects cell performance, especially during the earliest discharge stages. Additionally, increasing cell resistance due to low ionic conductivity also increases the voltage drop across the cell during early stages.

Similar to the extent of sulfur loading, the carbon microstructure framework exerts influence upon the electrochemical properties. Fig. 5.13 shows the cathode microstructure with the same sulfur loading of 22%-vol at different volume fractions of carbon substrate. From these microstructures, it is apparent that, for a constant sulfur loading, a decrease in the volume fraction of substrate carbon increases the porosity. That is, for the same volume fraction of sulfur loading, a decrease in the volume fraction of carbon substrate can increase the ionic transport path inside the porous electrode, and hence maintain the transport properties. As shown in Fig. 5.13a, larger pore volume fractions also decrease the tortuosity in the electrode. Furthermore, the positive tortuosity change decreases as sulfur loading is increased at low volume fractions of carbon substrate. This slow tortuosity increase is explained

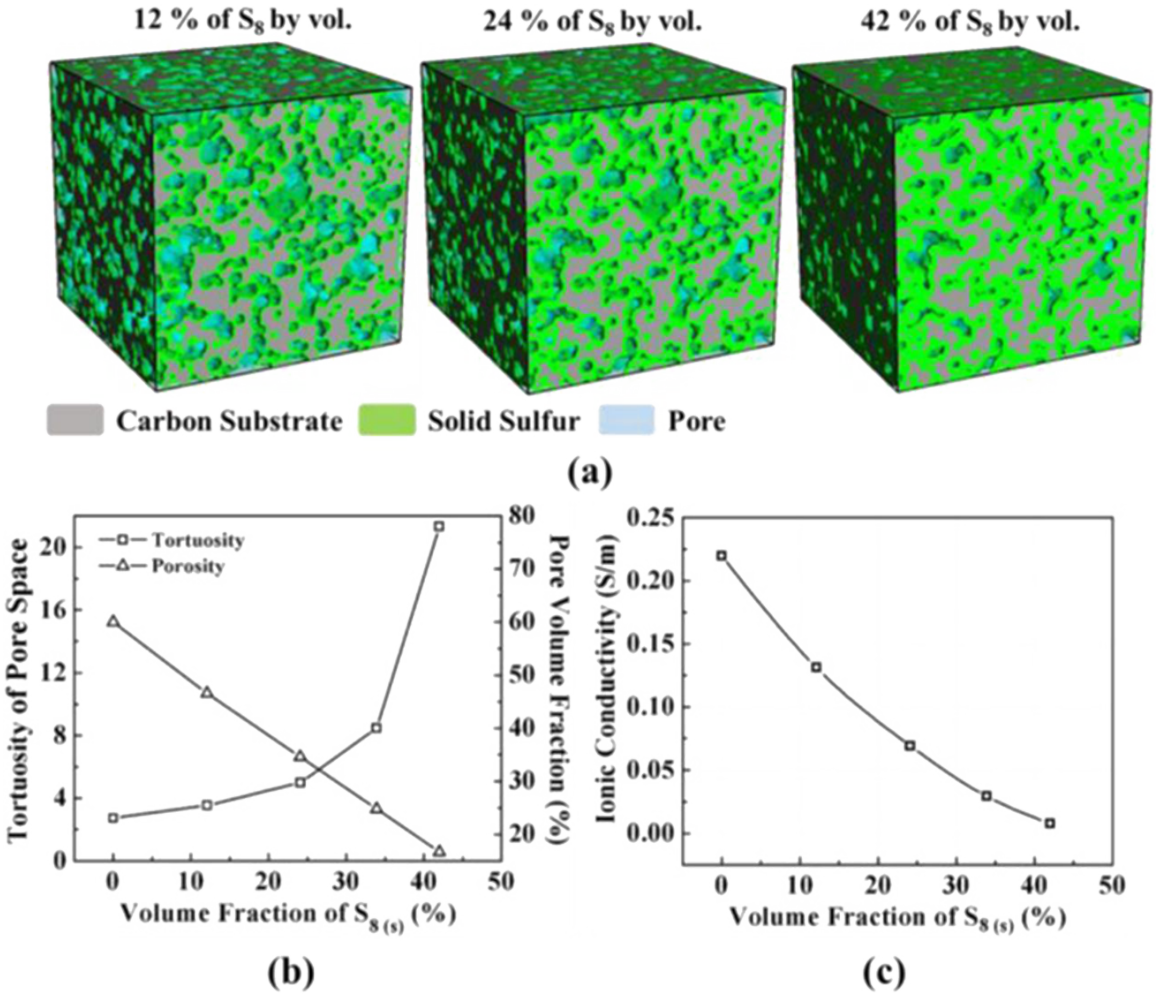

Figure 5.12. *Electrode properties with carbon compartments substrate.* (a) Representative electrode microstructure with 12%, 24%, and 42% of solid sulfur by volume. (b) Effect of sulfur loading on tortuosity and volume fraction of pore space. (c) Effect of sulfur loading on the ionic conductivity. The porosity (volume fraction of pore space) of the carbon substrate without sulfur loading is 0.6. The surface area of carbon substrate is 1,471 cm^2 g^{-1} (i.e., $4.60 \cdot 10^4$ cm^2 in 50–by–50–by–50 μm^{-3} control volume).

by the availability of transport pathways. The microstructure with 20% carbon substrate, for instance, has more pathways for ionic transport compared to the other two microstructures; though the sulfur partially blocks some pathways, the microstruc-

ture still has many alternative pathways for ionic transport. In contrast, since the microstructure with 40% carbon substrate has less alternative pathways due to blockage by the loaded sulfur, the constrained ionic transport causes a significant increase in tortuosity. Due to differences in tortuosity and porosity, the microstructures with different carbon content have different effective ionic conductivities, as shown in Fig. 5.13c. From these results, decreasing the volume fraction of carbon substrate can alleviate the effect of loading sulfur on the electrochemical properties, and hence the internal resistance in the cell can be effectively controlled.

Numerical Simulation of Cell Performance

The following macroscale performance calculation results are used to explain the observed trends in experimental measurements. At the start of discharge, it is assumed that no lithium sulfide Li_2S is present. Thus, the initial state is determined by the initial porosity and initial sulfur loading. Since sulfur is the limiting reactant, the time of discharge is a strong function of initial sulfur loading. This suggests that the major input parameters for the lumped performance model are initial sulfur loading, initial porosity, and rate of discharge. Simulations were performed for (i) three discharge rates: C/10, C/25, and C/50; (ii) three sulfur loadings: 10%, 15%, and 20% by volume; and (iii) three initial porosities: 65%, 75%, and 85%. It should be emphasized that these porosity values describe the initial carbon substrate (i.e., before the solid sulfur is impregnated in the matrix). For example, at 15%-vol sulfur loading, the volume fractions available for electrolyte become 50%, 60%, and 70%. This agrees with the experimental quantification of the resulting microstructures. The baseline case was determined with input parameters of 15% sulfur loading, 75% initial porosity, and C/25 discharge rate.

The results for the baseline simulation are presented below. The terminal voltage exhibits two different discharge stages: (i) the initial voltage reduction stage, and (ii) the constant voltage discharge stage. These two stages are joined by a transition stage. During the first stage, the porosity increases due to sulfur dissolution.

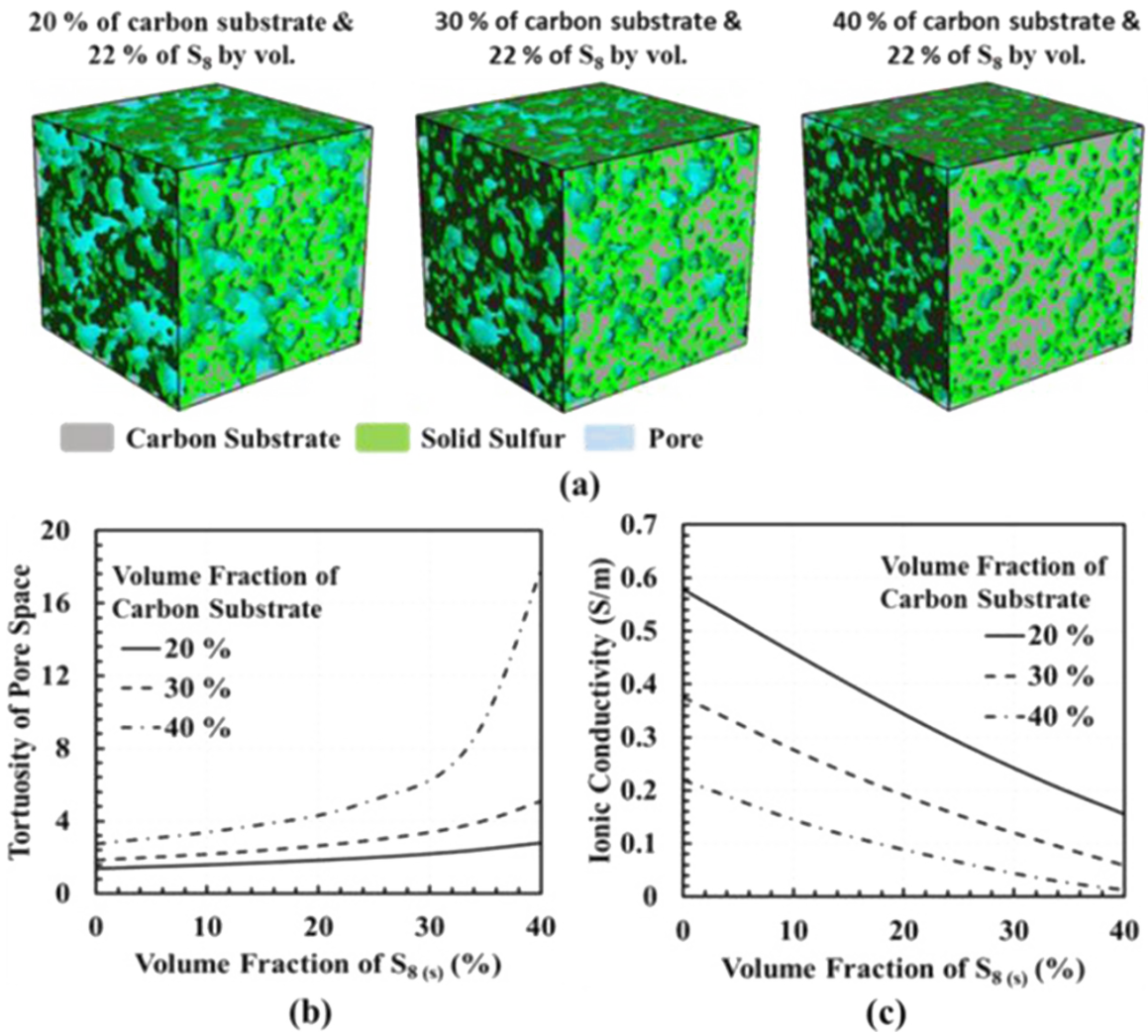

Figure 5.13. *Charge transport properties with carbon compartments substrate.* (a) Representative electrode microstructure with 22% solid sulfur by volume. (b) Effect of sulfur loading on tortuosity with different volume fractions of carbon substrate. (c) Effect of sulfur loading on ionic conductivity in the cathode.

During both stages, there is a continuous reduction of dissolved sulfur into sulfide ions by electrochemical reaction. The trends for electrode porosity change agree with those described in these two discharge stages. Once the solid sulfur is completely dissolved, the electrode porosity cannot increase further. During this first discharge

stage, the concentration of S^{2-} ions increases and the ionic product $[Li^+]_2[S^{2-}]$ exceeds the solubility product of Li_2S salt, which in turn leads to precipitation of Li_2S. This establishes a quasi-steady state in terms of S^2 ion concentration: the generation of S^2 ions: the generation of S^{2-} due to electrochemical reaction is roughly balanced by precipitation of S^{2-} in the form of Li_2S. This precipitation of solid product obstructs pathways in the microstructure and reduces electrode porosity. Since the electrochemically active area is an increasing function of electrode porosity, it follows this trend in porosity change. As demonstrated in Fig. 5.14, the simulation results produce a discharge capacity very close to the theoretical capacity. This indicates a lack of capacity fade, particularly due to side reactions (i.e., consumption of higher order sulfide ions) or sulfur isolation (i.e., pore clogging and transport limitations at low discharge rates). The experimental results qualitatively confirm the presence of two discharge states.

The effect of discharge rate on cell performance is displayed in Fig. 5.15a. The activation losses are reduced as the rate of discharge is decreased, leading to better discharge performance at lower current operation. This fact is apparent from the simulation results, and are also present in the experimental data. At these different C-rates, the two discharge stages are still present.

By increasing the sulfur loading, more active material is available. This will lead to more cell capacity for the same cell dimensions. For a given C-rate, increasing sulfur loading increases specific current upon discharge, in turn proportional to the rate of electrochemical reaction. Since increasing the rate of reaction leads to greater kinetic losses, the discharge performance decreases. This feature is due to the fact that cells with different capacities are discharged in the same time (Fig. 5.15b).

Electrode microstructure plays a decisive role in transport, however, transport limitations are not present at low C-rates (that is, as used in the present simulations). However, the electrochemically active area, or the effective cathode area over which electrochemical reactions take place, changes with the electrolyte volume fraction. A smaller electrolyte porosity corresponds to less active area and thus higher activation

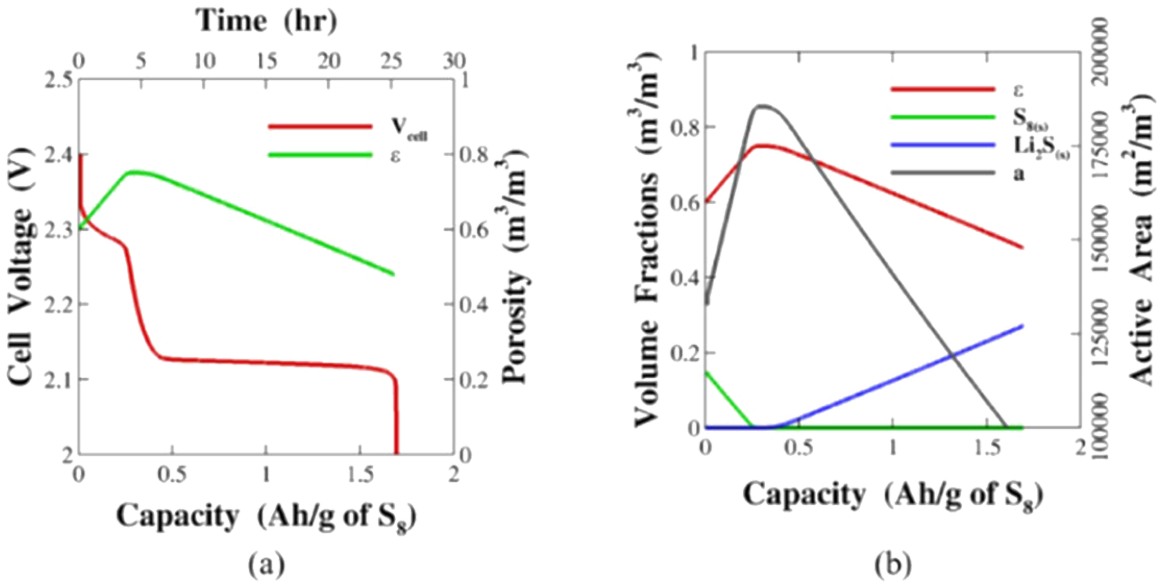

Figure 5.14. *Electrochemistry simulation with carbon compartments substrate.* At C/25 rate with 15% by volume sulfur loading and 75% initial porosity, (a) terminal cell voltage, as a function of discharge capacity, shows two distinct regimes during discharge. (b) Changes in cathode porosity, volumes fractions of solid species (i.e., S_8 and Li_2S), and electrochemically active area exhibit two different regimes.

losses for the same discharge rate. In turn, this leads to inferior performance. This explains why the discharge plateau voltage decreases with initial porosity for the same sulfur loading. As it turns out, the dependence is not as strong as that of C-rate and sulfur loading.

5.3 Microstructure Controls Sulfur Performance

The present work demonstrates a novel, low-cost carbon compartment synthesis technique which is subsequently used to manufacture cathodes for Li-S cells. These cathodes are evaluated for their morphological and structural characterization along with their electrochemical performance. A multiscale simulation framework is proposed to explain the experimental results and answer various fundamental questions,

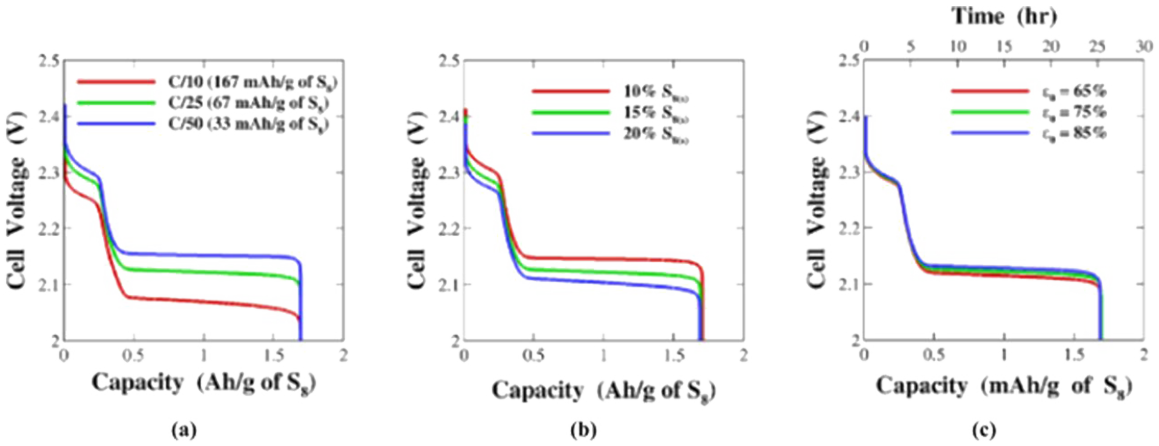

Figure 5.15. *Chronopotentiogram simulation with carbon compartments substrate*. (a) Cell discharge curve for three different C-rates, for 15% initial sulfur loading and 60% electrolyte volume fraction (or 75% porosity of initial carbon substrate). (b) Effect of sulfur loading on discharge behavior for the same discharge rate of C/25 and initial cell porosity of 75% (before sulfur loading). (c) Influence of porosity of unloaded carbon substrate for the same discharge rate of C/25 and 15% by volume sulfur loading.

including the influence of carbon upon cell reactions. It is found that the presence of low-coordinated sites at the edges or defects in the carbon structure facilitate nucleation of Li_2S, which may develop on a well adsorbed (111) Li_2S layer on a basal carbon (graphene-like) plane. Li ions accumulate at the C pore openings where it reduces dissolved S to a rich variety of S_x^{2-} species. Dissolution of initially loaded sulfur and Li_2S film formation alters cathode microstructure in time, which is quantitatively correlated to effective transport properties at microstructural scale. Eventually, an electrochemical model is developed at a macroscale (much larger than pore size) to correlate cell performance to constant current discharge. This model qualitatively explains the trends in experimental studies.

Electric properties and microstructure are significant considerations in substrate selection for carbon sulfur composites. Sonochemical synthesis produces carbon sulfur composites with moderate electrochemical performance, even with greater internal resistance carbon substrates. Autogenic synthesis, studied in Chapter 1, produces carbons-sulfur composites with poor capacity performance when non-HOPG carbonaceous substrates are used. This is correlated to significant low-frequency internal resistance of materials of the carbons themselves. Therefore, internal resistance is important to consider alongside interfacial surface area when evaluating carbon substrates for carbon-sulfur materials. Experimental results suggest fluorinated electrolytes improve Coulombic efficiency relative to conventional glyme electrolytes; further effects on lithium metal are explored in Chapter 9.

PART II

CONSIDERATIONS IN CARBON SYNTHESIS

Man cannot discover new oceans unless he
has the courage to lose sight of the shore.

— André Gide, 1925, *Les Faux–Monnayeurs*

CHAPTER 6: CHARACTERIZATION OF BY–PRODUCTS FROM CARBON SYNTHESIS

In Chapters 4 and 5, electrochemical and material characterization suggest synthesized carbons are viable cathode substrates in lithium sulfur batteries. To better understand industrial implementation of carbonaceous material synthesis, the health risks of pyrolysis were characterized according to downstream particulate by-products. Real–time optical sizing measurements identify aerosol particulates in the micro and nano-scale domains.

The original publication of this work appears in Environmental Science & Technology, volume 50, issue 5, 2627 - 2634. Experimental design, apparatus assembly, material characterization were performed by Arthur D. Dysart and Jay H. Beltz. Manuscript preparation was preformed by Arthur D. Dysart, Jay H. Beltz, and Candace Su-Jung Tsai.

Abstract

A scalable, solid-state elevated temperature process was developed to produce high capacity carbonaceous electrode materials for energy storage devices via decomposition of starch-based precursor in an inert atmosphere. The fabricated carbon-based architectures are useful as an excellent electrode material for Lithium-ion, Sodium-ion and Lithium-sulfur batteries. This article focuses on the study and analysis of the formed nanosized byproducts during the lab-scale production of carbonaceous electrode materials through the process design. The complete material production process was studied operando; namely during heating, holding reaction at elevated temperature followed by cooling. The unknown downstream particulates of the process exhaust were collected and characterized via aerosol and liquid suspensions, and

they were quantified using direct-reading instruments for number and mass concentrations. Such airborne emissions were collected on polycarbonate filters and TEM grids using Tsai diffusion sampler (TDS) for characterization and further analysis. Released byproduct aerosols collected in deionized (DI) water trap were analyzed using Nanosight real time nanoparticle characterization system and the aerosols emitted post water suspension were collected and characterized. Individual particles in the nanometer size range were found in exhaust aerosols, however, crystal structured aggregates were formed on sampling substrate after a long-term sampling of emitted exhaust. After characterizing those released aerosol byproducts, we found ways to mitigate their exposure to human health and environment upon the industrial implementation of such process.

6.1 Consequences of Industrial Scale

There has been increasing interest in solid-state chemistry, particularly synthetic techniques, due to its growing implementation in industry and manufacturing to create engineered particles in the micrometer to nanometer-size range. Within the past decade alone, various synthesis techniques exploiting solid-state methods have been developed to produce a wide variety of advanced and valuable materials including metal-oxide nanoparticles (e.g., zinc oxide nanorods, [123] ZnO_2; titania nanowires, [124] TiO_2) and intercalation electrode materials (lithium iron phosphate, [125] $LiFePO_4$; lithium manganese phosphate, [125] $LiMnPO_4$). One such technique is solution processing, such as the solvent-based hydrothermal synthesis in which high temperature and pressure encourage heterogeneous reaction of dissolved species. [126] Similarly, sol-gel processing promotes the growth of polymeric networks or gels from colloidal solutions of solid monomer. [127] Finally, heat treatment, perhaps the most conventional solid-state process, facilitates extensive reaction through the controlled heating of solids at elevated temperatures. Countless publications validate the versatility and applicability of these and more processes in production of hundreds of different nanomaterials. [126, 127] As the potential for solid-state science continues to

grow, it is important to understand the potential environmental and human health impacts of its industrial implementation. With this in mind, the focus of this study is the characterization of emissions from a novel solid-state controlled pyrolysis technique, developed for the production of bimodal-porosity amorphous carbon.

Classified as a specialization of heat treatment, pyrolysis is defined as the thermal decomposition of a given precursor within an oxygen-deficient atmosphere at elevated temperatures. [128, 129] When a biomass precursor is utilized, up to three phases are produced: solid, liquid, and vapor. In solid-state applications, the desired product is the solid phase and termed char. [130, 131] The yield of char is determined by the type of pyrolysis (e.g., slow, intermediate, fast, or flash), in turn determined by the conditions of reaction time, temperature, and heating rate. [129, 130] Slow pyrolysis, also known as carbonization in the case of biomass precursors, is the preferred char-producing technique because it produces the greatest solid yield, with typical values reported in the range of 25 - 35%. [130] Typical properties of slow pyrolysis include low heating rates (10 - 30 °C min^{-1}), long residence times (up to hours), and low temperatures (300 - 650 °C), but many exceptions have been reported. [128–131] Significant work has been done to characterize slow pyrolytic reaction of a variety of biomass precursors. Unfortunately, less effort has been dedicated to the emissions from pyrolysis processes; specifically, the unusable vapor and liquid by-products that can be directly released or lost to the environment. A major concern has been raised regarding exposure and toxicity associated with the release of materials from furnace synthesis due to the unknown characteristics of such particles.

The number of studies investigating toxicological effects of engineered nanomaterials has increased greatly in recent years for a greater understanding of biological end points. Various synthesis methods have been developed for producing advanced materials; however, the investigation of by-product emissions or loss during synthesis has been limited to managing by-product release and further enhancing the synthesis production yield. Few studies have reported the analysis of furnace synthesis emissions, [132, 133] and nanotube production has been studied showing the release of

particles in the nanometer size range. [132, 133] Novel synthesis methods will produce different emissions of unknown composition, and characterization of these unknown substances is critical before commercialization. The proliferation of new applications in nanotechnology has highlighted the need to minimize the harm to the environment and to humans. The risk of potential harm to the environment and humans from selected nanomaterials has been studied, and concerns have been raised. [132, 134–137] For example, exposure to carbon and metal oxide NPs has been found to induce an inflammatory response in human cells that could be associated with various potential health effects. [138–142] The synthesis process studied in this work has demonstrated carbonaceous nanometer-sized by-products during large-scale production with susceptibility to air suspension, which raises concerns of possible biological and environmental health effects upon exposure.

The carbon product, termed carbon compartments, is produced from a chemical precursor of commercial wheat flour in a scalable, single-step furnace process within a high-temperature inert gas atmosphere. Wheat flour [143–146] is a mixture primarily composed of hydrocarbons, primarily gluten and various saccharides or sugars, derived from cereal grains belonging to the Triticum genus. The upcoming report explains that a wheat-flour precursor was chosen over other biomass materials due to its sustainability and cost effectiveness. The purpose of the furnace is to provide a high-temperature environment to facilitate pyrolysis and reduce the organic compound to a porous, carbonaceous structure. Various biomass-derived amorphous carbons have demonstrated utility in a variety of applications, [147–151] including CO_2 adsorption, catalyst supports, supercapacitor applications, and novel electrode materials for rechargeable batteries.

The developed process has shown that the precursor experiences a mass loss of approximately 80% upon pyrolysis into a porous carbon. Although mass loss was primarily attributed to the production and subsequent discharge of water vapor, some solid and gaseous by-products were observed. In the laboratory, the solid and gas by-products can be collected upon exhaust using a laboratory-hood ventilation system

or liquid-suspension trap. Due to the variety of promising industrial applications of carbon compartments, the authors motivation is to characterize the released particles and plan the study to understand their potential health and environmental effects. In particular, the aim of this study is to perform a quantitative analysis on the primary and agglomerated nanoparticles that are released from the furnace process as aerosols and within the liquid suspension. This thorough analysis provides a basis for appropriate controls to be utilized both in the laboratory and when the process is scaled up to the industrial level.

Experimental Methods

The furnace synthesis process was methodically monitored throughout the entire heating procedure. The three stages of the full process include: (1) heating of the furnace reaction chamber to an elevated temperature, (2) dwell time holding at a constant elevated temperature, and (3) cooling and purging of the furnace chamber. Exhaust particles were monitored at the exhaust as suspensions in the continuous gas stream and in the water trap. The particles in the gas stream were directly analyzed inline using aerosol particle-size analyzers for concentration and observed offline using microscopy techniques upon collection onto sampling grids. The particles in the liquid suspension were analyzed using real-time analysis equipment. The detailed methods of synthesis and measurement are described below.

Synthesis Process for Amorphous Carbon

The synthesis of carbon compartments utilizes an organic precursor derived from a sustainable biomass material. A certain mass of this precursor is loaded into an inert aluminum oxide Al_2O_3 crucible and placed within an insulated high-temperature quartz-tube furnace (MTI Corp.). The crucible is used only to contain precursor and does not contribute to the reaction. The volume of the heating chamber is then purged using a continuous argon gas stream at the inlet to the furnace. The replacement of

humid air with argon gas within the furnace chamber creates an oxidizer-deficient environment promoting chemical reduction of biomass into a high-purity carbonaceous mass upon heating. Under a continuous inert inlet stream, the precursor is heated from ambient temperature to 900 °C at a heating rate of 10 °C min^{-1}. Heat treatment at 900 °C was sustained at a dwell time of approximately 2 h. After constant-temperature heating, the furnace was cooled to room temperature at a rate of approximately -10 °C min^{-1}. At the end of the process, the biomass precursor decomposed into amorphous carbon compartments. This multifunctional product does not require further processing before utilization in various applications.

Because the elemental composition, size, and the possible environmental and health effects of the by-products in the furnace exhaust had yet to be characterized, precautionary and protective measures were employed during this process. All experiments were performed in a well-enclosed constant velocity fume hood, and protective equipment such as N100 disposable respirators and gloves were used when conducting any activities related to this furnace and its exhaust. The furnace setup is illustrated in Fig. 6.1.

Aerosol Concentration Measurement

Real time direct-reading instruments (DRI) were used to record aerosol concentration during each minute of the sampling process. The DRIs used were the NanoScan Scanning Mobility Particle Spectrometer (NanoScan SMPS) (TSI, Shoreview, MN, model 3910), Optical Particle Sizer (OPS) (TSI, Shoreview, MN, model 3330), and DustTrak II Aerosol Monitor (TSI, Shoreview, MN, model 8533). The TSI NanoScan SMPS measures the particle number concentration for particle mobility diameters from 10 to 420 nm and operates at an air flow rate of 0.9 L min^{-1} (Fig. 6.1). The OPS measures particle number concentration for particle mobility diameters from 300 to 10,000 nm and operates at an air flow rate of 0.9 L min^{-1}. The DustTrak measures mass concentration for particles with aerodynamic diameters from 0.3 to 10 μm for the detecting mass concentration in the 0.001 - 400 mg m^{-3} range and operates at an

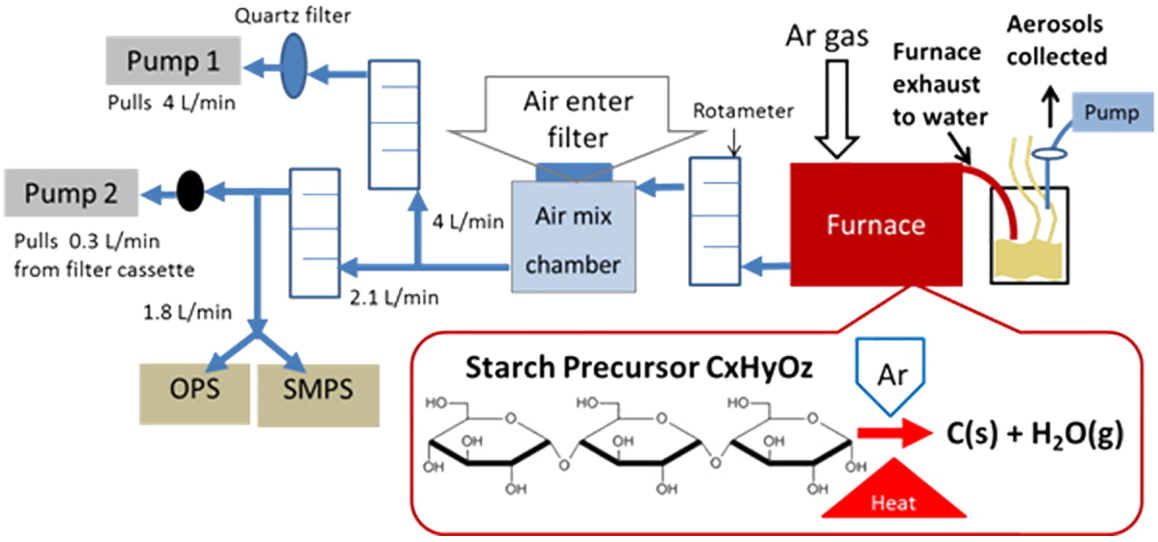

Figure 6.1. *Experiment apparatus for particle sizing characterization.* Process by-products are sampled from diluted output stream using micro and nanoscale optical measurement devices.

air flow rate of 3 L min^{-1}. When implemented to study aerosol exhaust, each instrument was operated during the full three-stage heating process. Other devices used include a dilution chamber with filter air inlet and multiple rotameters to monitor the gas flow.

Aerosol Sampling and Material Analysis

Particles suspended in both the gas stream and liquid suspension were collected during furnace operation. Aerosol samples were collected using 25 mm sampling cassettes with polycarbonate filters (pore diameter of 0.2 μm) affixed with a transmission electron microscopy (TEM) grid (copper 400 mesh with SiO_2 film) [135] at three different time periods of the furnace operation. Each TEM grid was attached to a polycarbonate filter on the area facing the oncoming gas stream. Each sampling cassette was connected to a suction pump with a flow rate of 0.3 L min^{-1}. Particles deposited on both the filter and grid were utilized in further analysis procedures.

Analysis methods applied to aerosol particles on filters, grids, and synthesized carbon compartments include scanning electron microscopy (SEM), TEM, and X-ray energy-dispersive spectroscopy (XEDS). The SEM and TEM techniques enable the observation of the particle shape and size. The XEDS technique allows elemental composition analysis of the reactant, product, and by-product particles. The wheat-flour precursor particles and polymeric filters were coated with a thin gold-palladium (Au-Pd) alloy film using a SPI sputter-coater module prior to SEM analysis to increase surface conductivity and increase the micrograph quality. SEM (FEI Nova 200 SEM/FIB) was operated at 10 kV and 2.1 nA. Elemental composition was analyzed using XEDS detector (Oxford XMAX with Oxford Aztec). A FEI Technai G2 20 TEM equipped with an Oxford INCA 250 X-MAX 80 silicon-drift XEDS system was operated at 200 kV to perform image and elemental composition analysis.

Collection and Analysis of Solvated Aerosol Particulates

Furnace operation was repeated with the same operating conditions as the aerosol measurement and collection process. Instead of collecting emitted aerosols directly, air/argon-suspended particles were collected by passing the furnace exhaust (ca. 2 L min^{-1}) through a DI water bath. Particles suspended in the water and particles passing through the liquid trap were subsequently analyzed. Sampling was performed for the entire duration of the furnace operation. Particles captured in the water trap were analyzed for particle-number concentration and mobility particle diameter using the nanoparticle tracking analysis (NTA) technique provided by the Nanosight Nanoparticle Characterization System (Malvern Instrument Ltd., Worcestershire, UK, model LM10). As shown in Fig. 6.1, the aerosols emitted after the water trap were collected using the same aerosol sampling technique already described. The aerosol samples collected after the water trap on filters, and TEM grids were analyzed using TEM, SEM, and XEDS to investigate the emitted particles.

Normalized particle number concentrations of aerosols from the NanoScan and OPS were analyzed individually, with data merged using TSI multi-instrument manager software to obtain the fitted concentration distribution of 10 nm to 10 μm. Background concentration was averaged as the baseline to be compared to the concentration change during synthesis. Concentrations measured using the Nanosight system were analyzed to obtain the average number concentrations of particles suspended in the liquid samples.

Furnace Operation and Product Characterization

Before performing particulate sampling and analysis experiments, preliminary tests were conducted to characterize the major process variables and mechanisms for this process. Thermogravimetric analysis (TGA) was performed using a TA Instruments Simultaneous TGA/Differential Scanning Calorimeter (SDT) Q600 (TA Instruments, New Castle, DE) to characterize the temperature-dependent transformation of the wheat-flour precursor into carbon compartments (Fig. 6.2). In this test, a predetermined amount of wheat flour precursor is loaded into the device and heated uniformly at rate of 10 °C min^{-1} from 30 to 1000 °C under a continuously flowing atmosphere of inert helium (He) gas. The thermal behavior under inert atmosphere indicates that the primary mass loss around 300 °C is indicative of biomass decomposition.

Prior to installation of the by-product sampling and sizing apparatus (Fig. 6.1), preliminary testing was performed to characterize the flow and temperature properties of the furnace process. To ensure the accurate operating conditions of all devices connecting to the furnace exhaust, a temperature profile of the furnace outlet was developed as a function of the lateral distance from the outlet flange. During the constant temperature heating stage at 900 °C, the maximum temperature of the downstream exhaust immediately exiting the furnace was measured to be approximately 27 °C at a length of 13 cm (5 in.) from the furnace outlet flange. No appreciable difference was found between the downstream temperature and the measured ambi-

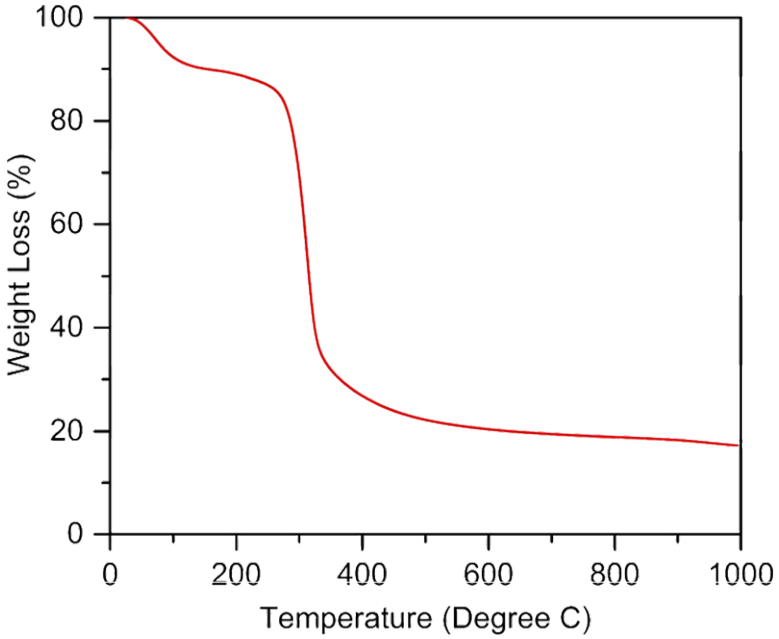

Figure 6.2. *Thermogravimetric analysis of carbon compartments precursor.* The two principle mass losses correspond to moisture vaporization ca. 100 °C and pyrolytic decomposition ca. 300 °C.

ent temperature (25 °C) at distances greater than 13 cm (5 in.). Due to this initial observation, all aerosol measurements were taken at least 15 cm away from the outlet flange. An additional test determined the flow-rate properties of the furnace exhaust. In the presence of a downstream rotameter, furnace operation demonstrated an increase in exhaust flow rate to approximately 2 L min^{-1} when the furnace reached 350 °C. This flow rate remained constant until the end of the cooling step.

Upon operation of the furnace, an opaque and smoke-like gaseous product was observed in the furnace exhaust in the temperature range of approximately 350 to 900 °C. Furthermore, a severe reduction in the intensity of this gaseous product was observed at approximately 600 °C during the cooling process, at which point decomposition of the reactant is considered complete. From the TGA and background-setup observations, it is likely that the gaseous product is composed of high concentrations of aerosol by-products and is the cause of the flow-rate increase observed at onset of the pyrolysis reaction.

As previously discussed, carbon compartments are synthesized via pyrolytic heat treatment of a commercial wheat flour. The carbon particles collected after pyrolysis demonstrate diameters in the range of 50 - 100 μm. These particles are uniquely distinguished by the presence of micrometer-sized compartments or cavities. The formation of these cavities is attributed to the mechanism of pyrolytic heat treatment in which the release of organic by-products, including heated water vapor, promotes the generation of micrometer-sized pores. These cavities facilitate moderate surface area that allow various applications for the carbon compartments. Additional smaller-sized carbon particles can be observed on the carbon compartment surface as shown in Fig. 6.3 (examples are marked with arrows).

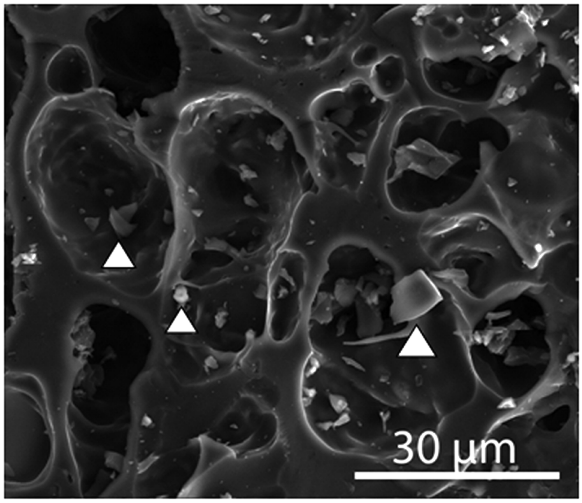

Figure 6.3. *Scanning electron micrograph of carbon compartments.* SEM micrograph depicting a representative micro-sized carbon compartment particle synthesized via thermal decomposition of wheat flour.

6.2 Analysis of Carbon Product & Aerosol By–Products

Material Characterization of Synthesized Carbon

Multiple synthesis trials were performed under identical operating conditions for various measurements and sample collection. Aerosol number concentrations at the exhaust for the entire synthesis process were monitored, and aerosol particles were simultaneously collected using TDS techniques. The mass concentration was monitored for the entire process in a separate trial. The aerosol sampling downstream to the liquid particle suspension was also collected in a separate trial.

For number concentration measurements, aerosol concentrations were diluted with high-efficiency particulate air (HEPA) filtered air within an air mixing or dilution chamber (air-mix chamber, Fig. 6.1). The air-mixing chamber was installed in series to the furnace exhaust and before the particle spectrometer equipment to ensure the particle-number concentration of the gas stream did not exceed the upper detection limit for each instrument. The measured particle number concentrations were corrected to account for a dilution factor of 3, determined from the ambient laboratory particle concentration. The resulting aerosol concentrations are presented in Fig. 6.6a, showing the particle total-number concentration change throughout the entire duration of the synthesis process. The left ordinate axis reports the particle concentration for smaller particles in the diameter range of 10 - 420 nm (NanoScan), while the right ordinate axis reports the particle concentration for larger particles in the diameter range of 0.3 - 10 μm (OPS). The particle number concentrations during the first heating stage (heating from room temperature to 900 °C) and second stage (constant pyrolysis temperature of 900 °C) were greater than 10^5 and 10^4 particles cm^{-3} for the particle diameter ranges of 10 - 420 nm (NanoScan) and 0.3 - 10 μm (OPS), respectively. The number concentration profile shows a rapid increase to a peak value near 30 and 90 min of furnace operation for the particle diameter ranges of 10 - 420 nm and 0.3 - 10 μm, respectively. The concentrations then increased as the temperature was held at 900 °C for 2 h, as seen in the red correlated temperature

profile shown in Fig. 6.6a. The concentration reached its maximum after 3 h and decreased as the furnace entered the cooling phase.

The maximum peak total particle concentration reported by the NanoScan (particle diameter range of 10 - 420 nm) was approximately $7.0 \cdot 10^5$ particles cm^{-3} near 35 min, and the second highest peak was approximately $6.0 \cdot 10^5$ particles cm^{-3} and occurred approximately 200 min toward the end of the 2 h hold time at 900 °C. The total background particle concentration of the laboratory space was approximately 1000 and 30 - 600 particles cm^{-3} as measured by the NanoScan and OPS, respectively. The maximum total particle concentration read by the OPS was approximately $2.8 \cdot 10^4$ particles cm^{-3} at 197 min, which correlates to the end of the constant temperature heating step at 900 °C. At this time, the concentration of larger particles reported by the OPS is identical to that reported by the NanoScan. At 81 and 121 min, both DRIs reported a peak concentration of approximately $2.3 \cdot 10^4$ particles cm^{-3}.

Particle mass concentrations, measured using the DustTrak, as a function of the furnace operation time are shown in Fig. 6.4. In this graph, the right ordinate axis shows the correlated temperature profile. The horizontal plateau observed between 35 and 120 min for the mass concentration profile indicates that the DustTrak maximum mass concentration limit of 400 mg m^{-3} was exceeded. It is noteworthy that the rapid increase to the maximum limit at 35 min coincides with the emergence of a visible opaque, gaseous fume at the dilution-chamber inlet. This gaseous product is identical in appearance to that observed in the standalone furnace operation previously discussed. After the opaque fume vanished, the mass concentration remained at its maximum detection limit for over 1.5 h until the furnace temperature reached 900 °C. The concentration then started to decline after 120 min, while the temperature remained in the 900 °C hold. Because the instrument limitations were exceeded, the mass concentration during the relevant time domain are possibly larger than the reported value of 400 mg m^{-3}. The increase in mass concentration appeared around the same time, when the visible gaseous fume was emitted from the furnace

exhaust at a temperature of 350 °C. This temperature correlates well to the biomass decomposition temperature observed in thermogravimetric analysis (Fig. 6.2).

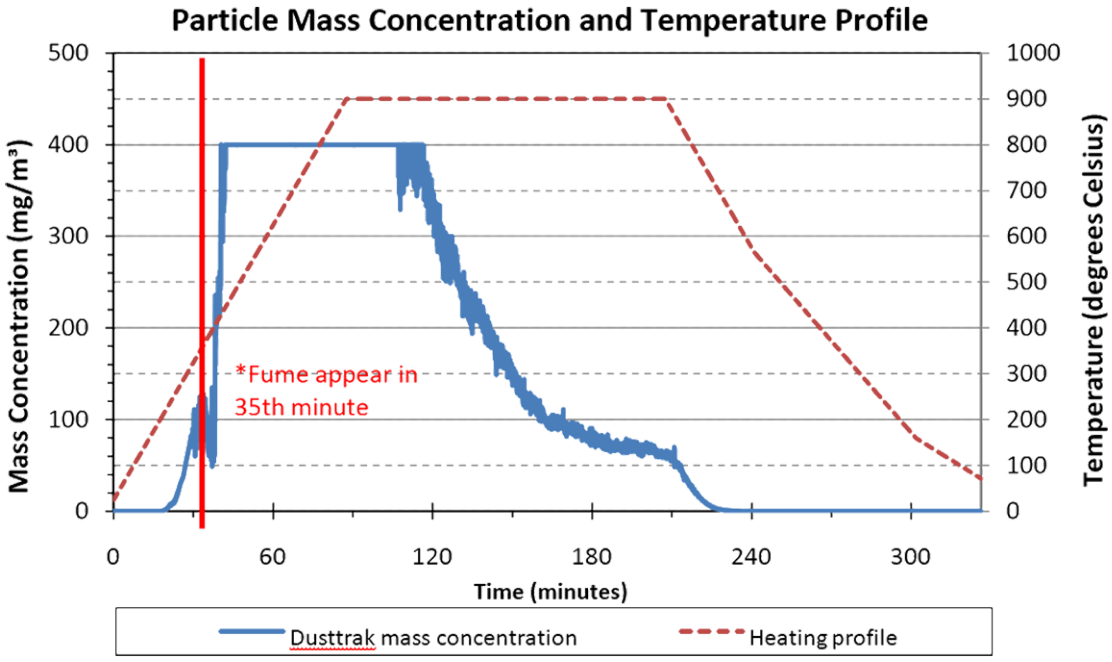

Figure 6.4. *Temperature profile and mass concentration of process exhaust.* (a) Particle-number concentration change over the entire process for particle diameters from 10 – 420 nm (left axis) and 0.3 - 10 μm (right axis). (b) Exhaust-gas particle-number concentration versus diameter over a size range of 10 - 420 nm.

The particle-size profile of emitted particles in the OPS size range of 0.3 - 10 μm shown in Fig. 6.5 reports the mean, median, and mode for the particle size. This size profile and the particle-mass concentration profile (Fig. 6.4) show similar trends. The particle size profile shows a similar increasing trend to that in the mass concentration profile because the overall mass is affected more strongly by large particles than small ones. The trend in the particle size profile differs to that in the particle number concentration profile because a large number of nanoparticles contribute minimally to the overall mass.

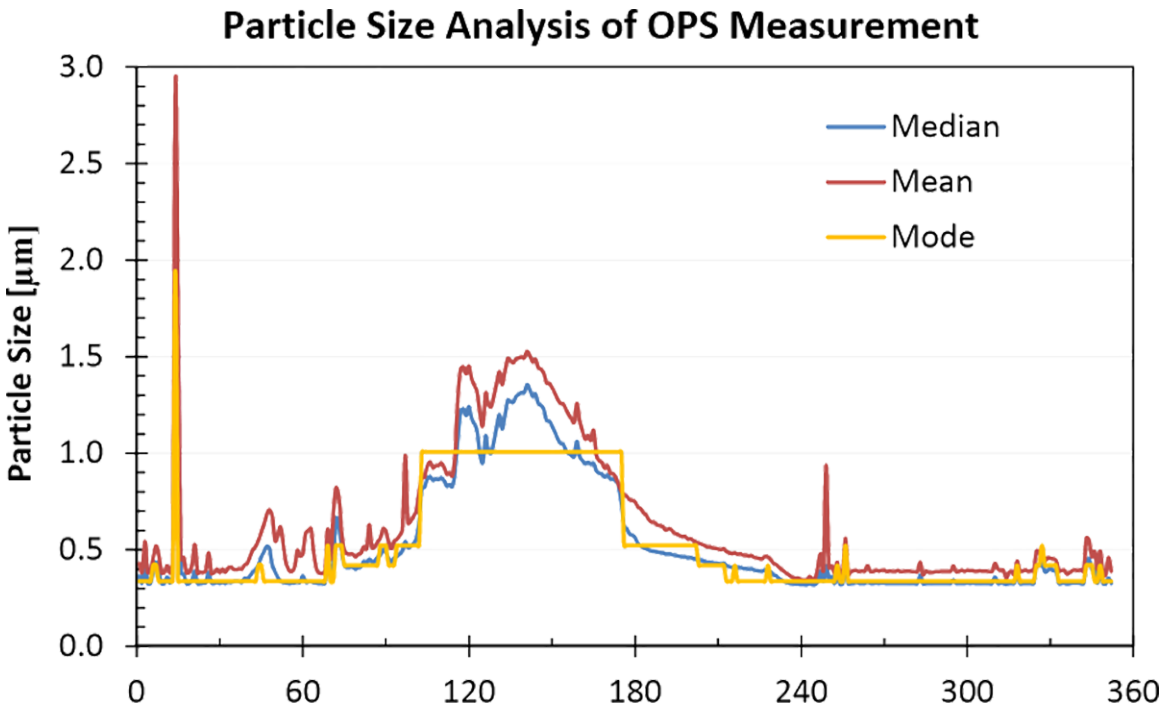

Figure 6.5. *Particle size analysis of process exhaust.* Particle size (i.e., median, mean, and mode) profiles of emitted particles are in the range of 0.3 – 10 μm.

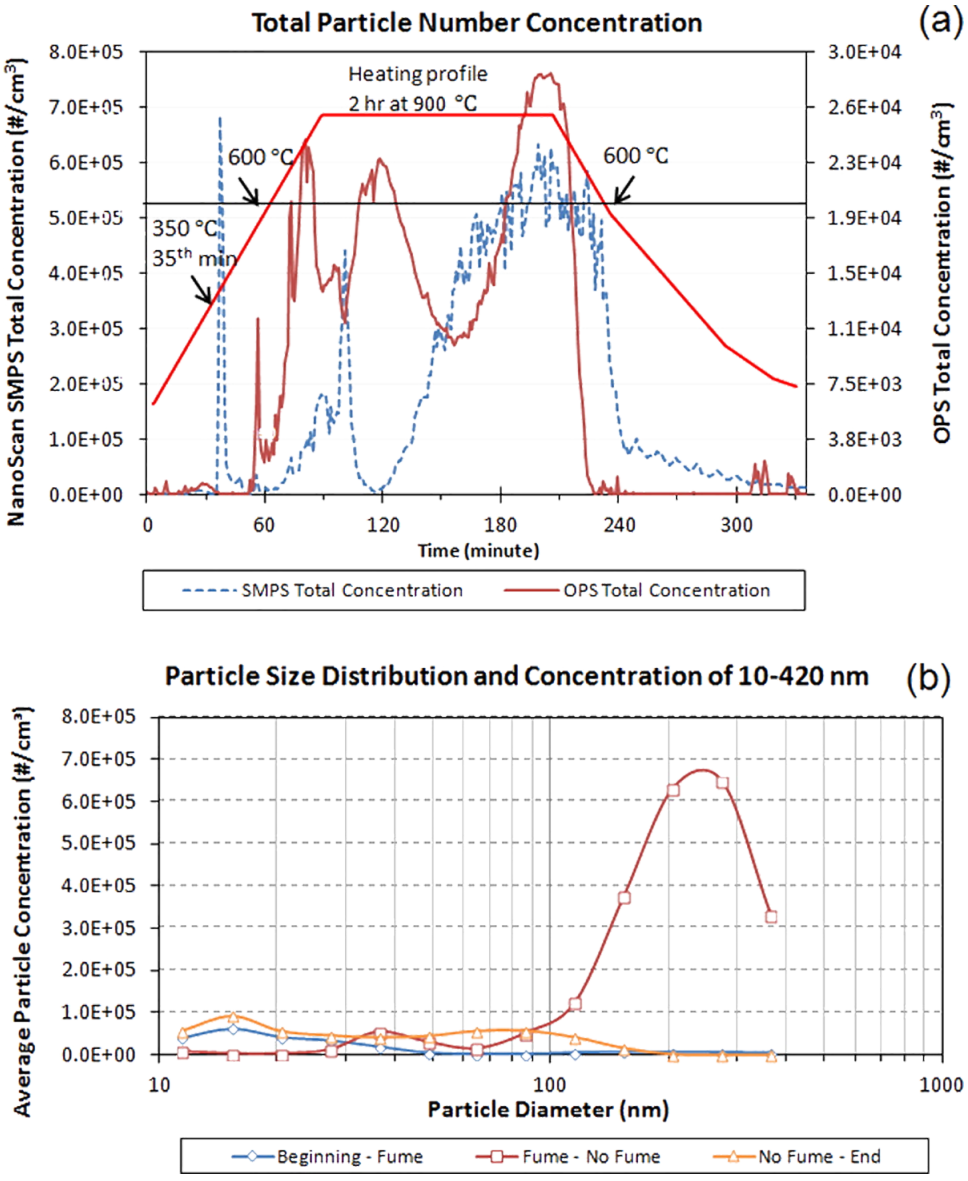

Figure 6.6. *Particle concentration distributions of process exhaust.* (a) Particle number concentration change over the entire process for particle diameters from 10 to 420 nm (left axis) and 0.3 - 10 μm (right axis). (b) Exhaust gas particle number concentration versus diameter over a size range of 10 - 420 nm.

The particle number concentration profiles collected by the OPS and Nanoscan show differing trends in concentration change: the increase was seen earlier and higher during 60 - 120 min for larger particles (0.3 - 10 m) than small particles (10 - 420 nm) when the temperature reached 600 °C (Fig. 6.6). Smaller particles were observed to show a delayed concentration increase.

Aerosol Concentration Profile

Particle size distributions were analyzed using DRI data for the Nanoscan diameter range 10 - 420 nm and OPS diameter range 0.3 - 10 m as shown in Fig. 6.5 and Fig. 6.7, respectively. Because the visible fume appeared during the heating cycle and vanished during the cooling cycle, the corresponding temperatures of 350 and 600 °C were identified as points of comparison. Thus, the analysis of the particle sizes was categorized according to three different time periods of the furnace process: the first stage, defined between the start of furnace operation to the initial appearance of the fume ("beginning to fume," or 25 to 350 °C of the heating step); the second stage, defined between the initial appearance of the fume to the disappearance of the fume ("fume to no fume," or 350 °C of the heating step to 600 °C of the cooling step); and the third stage, defined between the disappearance of the fume to the end of furnace operation ("no fume to end," or 600 °C of the cooling step to 25 °C).

When comparing the total concentration and particle size measurements for particles smaller than 420 nm, it was found that the highest average particle concentration was approximately $6.5 \cdot 10^5$ particles cm^{-3} (Fig. 6.6b) and occurred between 350 °C in the heating step to 600 °C in the cooling step. The mode for this first concentration peak was approximately 250 nm, while the mode for the second concentration peak occurred in the nanoparticle size range with a mode of approximately 40 nm. Nanoparticles were found during the heating period with a mode smaller than 20 nm and almost all particles were smaller than 50 nm. During the cooling period, almost all particles were smaller than 200 nm, with a majority of particles smaller than 100 nm and a similar mode to the heating period. For diameters smaller than 50 nm,

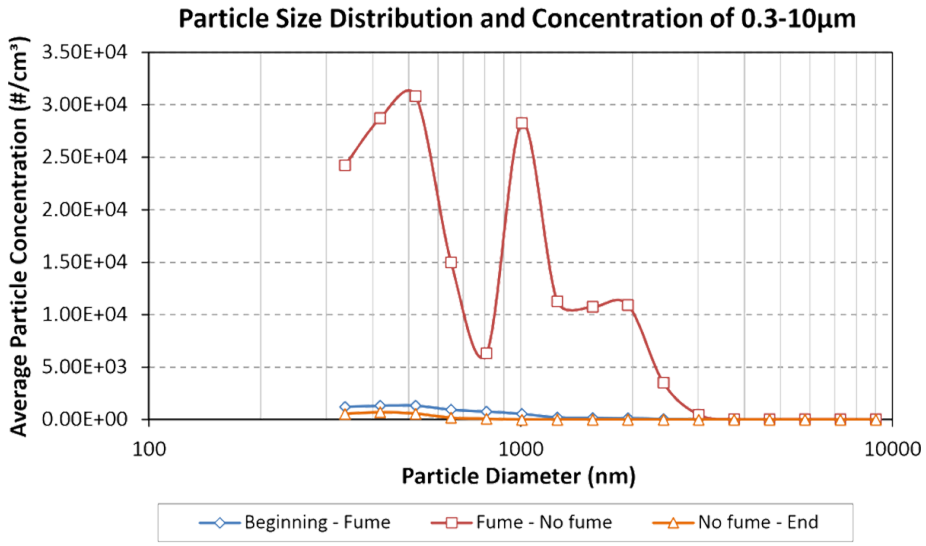

Figure 6.7. *Particle size distribution in microscale range.* Particle size distribution of exhaust gas over a size range of 0.3-10 μm.

the distributions were similar in the heating and cooling periods; however, the ending cooling period released more particles in the 50 - 150 nm range.

For the larger particles in the 0.3 - 10 μm size range (Fig. 6.7), the highest concentration appeared during the visible fume emission with multiple peaks, indicating that a combination of various particle sizes were emitted. The highest peak occurred at a diameter of approximately 0.5 μm, followed by 1 and 2 μm. When comparing the total concentration and particle size measurements, the highest average concentrations were approximately $3.2 \cdot 10^4$ particles cm^{-3} for a diameter of 500 nm and approximately $2.8 \cdot 10^4$ particles cm^{-3} for a diameter of 1 μm. The particle concentrations in the beginning and ending periods were very low and had similar size distributions. It appears that a large quantity of micrometer and submicrometer-sized particles were emitted in the period defined between 350 °C in the heating step and 600 °C in the cooling step. In contrast, the nanoparticles were produced during both the beginning and ending periods. It is thought that the continuous flow of argon gas could serve as a driving force for particle aerosolization. The overall particle size distribution,

combining the distribution data from the OPS and Nanoscan size ranges, is presented in Fig. 6.8.

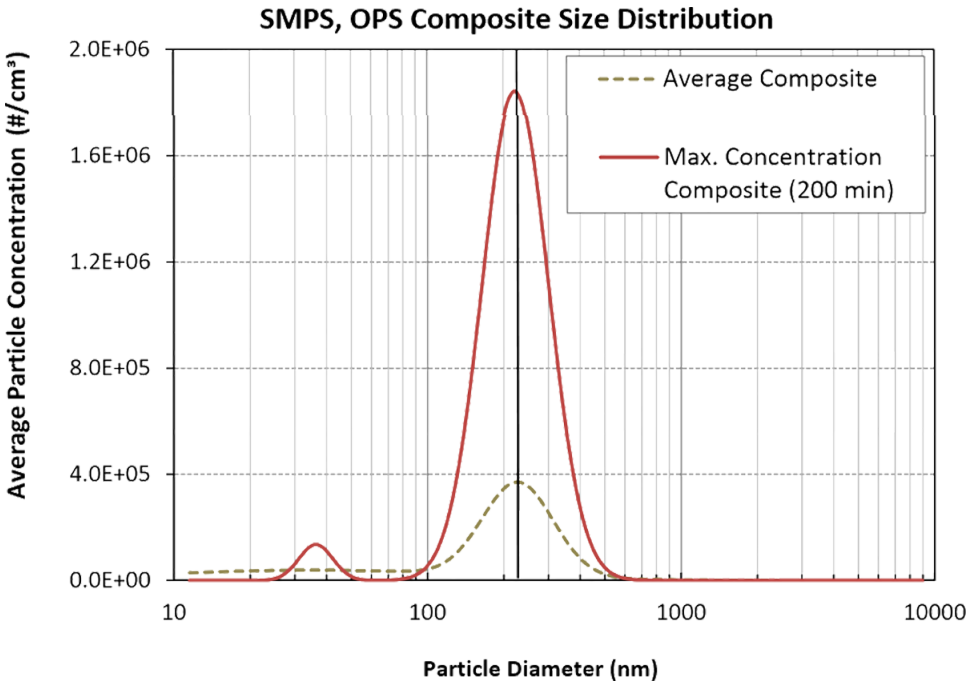

Figure 6.8. *Total particle size distribution for process exhaust.* Emitted particles in the size range of 10 nm to 10 μm exhibit two modal diameters at ca. 35 and 225 nm.

Particle Size of Exhaust Aerosols

Aerosol particles in the exhaust gas were collected using the Tsai Diffusion Sampler (TDS), a sampler designed to primarily collect micrometer-sized particles on the filter and nanoparticles on the grid. Particles in the exhaust directly released from the furnace are shown in Fig. 6.9a,b for short-term and long-term sampling, respectively. The short-term sampling period lasted for 30 min and demonstrated individual particles with particle diameters less than 200 nm collected on the TEM grid (Fig. 6.9a). This observation is consistent with the particle-size range measured using the DRIs. The long-term sampling period lasted for 5 h, permitting the collection of aerosols during the entire duration of the furnace process. In this period, particle

accumulation was found to form agglomerates in layered structures on both the grids and filters. The accumulated particles formed a coating-like layer covering the pores of the polycarbonate filter as seen in the SEM image of Fig. 6.9b. As indicated in the figure, the unblocked pores appear as dark holes (emphasized with arrows), and the covered pores are seen as a layer of material (emphasized in the boxed area). Additional larger-sized particles, found on the filter after long-term sampling, are possibly trace particles from residues in the furnace and exhaust tubing. The size of agglomerates also corresponds with the DRI results in the micrometer size range.

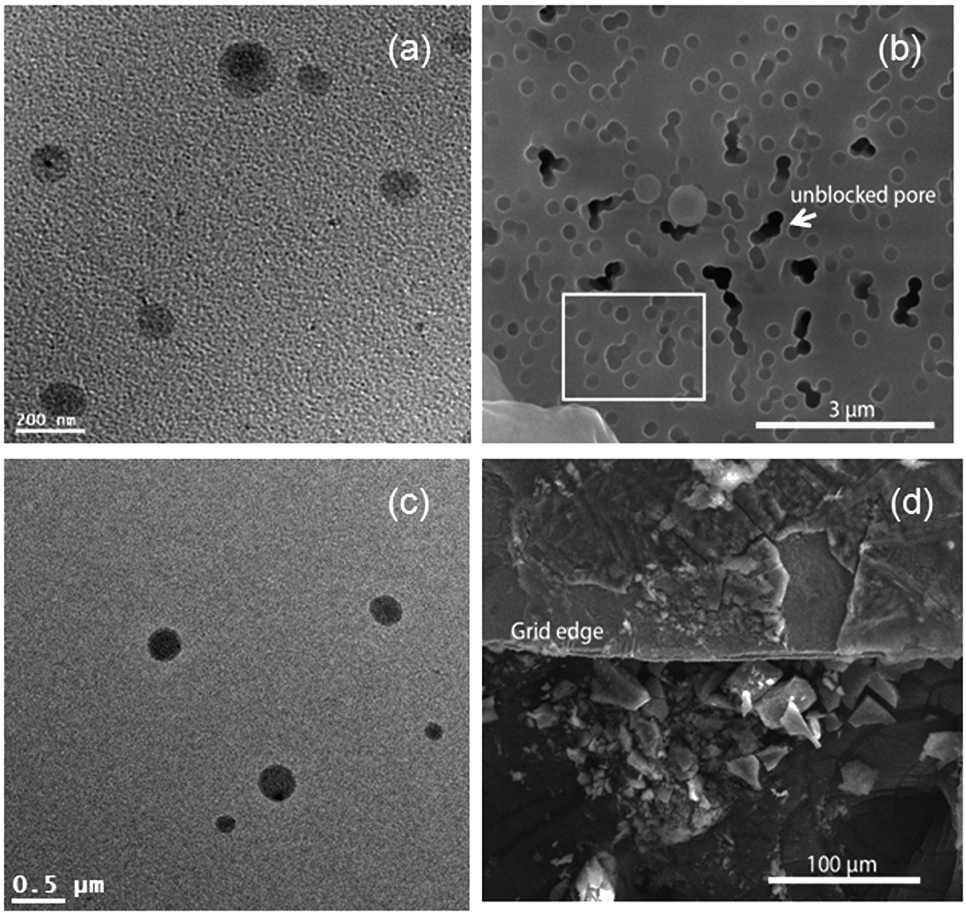

Figure 6.9. *Transmission electron microscopy of emitted particles.* Particles were collected from the exhaust gas for a duration of (a) 30 min and (b) 5 h. Similarly, particles were collected from exhaust gas, downstream of the water bath, for (c) 30 min and (d) 5 h.

Understanding Synthesis Process Characterization

Solvated byproduct particles, emitted post-water trap, were collected using the TDS. Particles collected during the short sampling period (30 min) and the long sampling period (5 h) are shown Fig. 6.9c and d, respectively. A consistent result was observed for short-term sampling in that individual particles were collected on the TEM grid (Fig. 6.9c). Particles (Fig. 6.9c) were similar in size to the aerosols directly collected at the exhaust (Fig. 6.9a). The long-term sample resulted in a visible dark brown stain appearing uniformly on the TEM grid and filter. This color change was also seen on the grid and filter from direct aerosol sampling. On the grid, particles were found to form agglomerates with a layered structure. Fig. 6.9d is an SEM image of the grid after long-term sampling, showing layered agglomerates on the grid edge (top portion) and pieces of agglomerates separated from the grid on the copper tape of the SEM substrate (bottom portion).

Consequences of Particulate Size

To provide insight into (1) the thermal pattern responsible for the transformation of the starch into a carbonaceous product and (2) the correlated emission observations, thermogravimetric analysis was performed. The controlled heating of the carbon compartments precursor under inert atmosphere demonstrates principle sources of weight loss. The produced TGA curve (Fig. 6.2) demonstrates two primary stages at which mass was released. The first stage occurs at approximately 100 °C, when absorbed moisture is released from the precursor in the form of steam that generates the aforementioned cavities or compartments. The second stage occurs at approximately 300 °C, when reductive pyrolysis facilitates the transformation of the starch-based carbohydrate into a carbonaceous product. At this temperature, thermal degradation of starch occurs and results in the release of nanoparticles and a produced pressure. This suggested decomposition temperature for wheat flour is similar to that observed in other biomasses. [128, 130, 152–154] As shown in the observations of this controlled

heating experiment, it is during this second heating stage at which the nanoproducts released throughout the heating in this studied furnace process. From room temperature, the first principle mass loss of approximately 10% is observed near 100 °C and is associated with the vaporization of hygroscopic water content. The second principle mass loss of approximately 70% begins at 300 °C and is associated with the pyrolytic decomposition of the biomass into amorphous carbon and simultaneous emission of particulate by-products.

This synthesis process produced high particle concentrations in the exhaust gas during synthesis, reaching $6.0 \cdot 10^5$ particles cm^{-3}. Particles produced by the furnace were found to be largely in the 200 - 300 nm size range in an airborne medium and around 100 - 150 nm in a liquid medium. The furnace exhaust also contained very high mass concentrations when the temperature reached approximately 300 °C. A closed-loop system is being considered for the next stage of this research to redirect a large amount of the released incomplete hydrocarbon substances back into the furnace during synthesis. These reactive hydrocarbons could interact with the precursor and minimize the release of free particles into the exhaust. A closed-loop system will also avoid the continuous flow of inert gas, minimizing the airborne particle concentration due to flow effects and ultimately reduce process costs. A short-term release of particles was of concern because individual primary particles were emitted, and most of the particles were less than 200 nm. However, agglomerated particles were larger, and the resuspension of nanoparticles from the agglomerate will unlikely occur. In current practice, the water trap used for cleaning exhaust gas was found to collect some particles in the nanometer size range; however, some particles were found to escape the water and become airborne. This finding is important evidence that, in the water suspension, nanoparticles can possibly pass the water media and enter the surrounding headspace. Using liquid water as a collection media requires further study to determine the collection efficiency, including dispersed bubble size and saturation content in water.

Until the current system is modified to incorporate recirculation, it is recommended that the process equipment be located in a ventilated enclosure to prevent human and environmental exposure. For the control of the exhaust gas before release to the surrounding environment, an air filtration unit such as a quartz filter or other high-efficiency filter material [155] is highly recommended to be installed downstream of the liquid bath.

The production process that was evaluated in this experiment is an abbreviated version: the complete carbon compartment process can run up to 16 h. It is possible that the concentration and size distribution of released particles could be different for longer processes; however, it is expected that most characteristics of the exhaust material will remain the same.

The released by-products were found to be carbonaceous particles: such substances have not been studied for their potential to harm humans and the environment. Future experiments could utilize the collected released carbonaceous substance with human-cell culturing to investigate the biological response, including viability, toxicity, and possible mutation to predict human health effects associated with exposure to such substances exhausted from this production process. Additional future experiments will study the effective capture and recycling of the carbonaceous by-products. After effectively trapping carbonaceous by-products of this process, the saturated water can be centrifuged, and the captured carbon nanoparticles can be used for various applications including energy storage, optical devices, and color dying.

Emitted aerosols from the synthesis of the carbon compartment particles were found in nanometer and micrometer size ranges, and most emitted nanoparticles were both spherical in shape and primarily carbon in composition. Such carbonaceous spherical nanoparticles will interact quicker than micrometer-sized particles with biological entities. Identifying the chemical formulation of the emissions substance and biological responses such as cytotoxicity are our next steps of project. Long-term collection of emitted particles on the sampling media was found to form

layer-structured agglomerates primarily consisting of carbon (on an elemental basis). Aerosols trapped in the water medium suspension were mostly nanometer in size, while the particles escaping from the water bath formed agglomerates similar to aerosols directly collected from exhaust gas. The water medium trapped a large quantity of nanoparticles emitted from the furnace; however, some particles we observed to penetrate the water trap. Process recirculation is suggested as a modification for the next step in process development, and emitted particles will be further characterized after process modification. Filtration was suggested as an interim control to capture emitted particles to avoid exposure.

6.3 Particulate Remediation Recommendations

Emitted aerosols from the synthesis of carbon compartments were found in nanometer and micrometer size ranges, most nanoparticles emitted were in spherical shapes containing carbon. Long term collection of emitted particles was found to form crystal structured agglomerates on the sampling media containing mostly carbon element. Aerosols trapped in water media were shown mostly in nanometer size and such particles escaped from water formed agglomerates similar to aerosols directly collected from exhaust gas. Water media trapped high quantity of nanoparticles emitted from the furnace, however particles were also found to release from the water. Process recirculation was the suggested modification for the next step of process development and emitted particles will be further characterized after process modification. Filtration was suggested a current control to capture emitted particles before the effects of exposure can be concluded.

CHAPTER 7: LIFE CYCLE ANALYSIS OF CARBON SYNTHESIS

Environmental impact, alongside by-product exposure risk, is a significant consideration for industrial pyrolysis processes. In this study, environmental impact is assessed for the synthesis of carbon microsheets, a carbon morphology produced by pyrolysis of waste packing peanuts. Through life cycle analysis, environmental impact is evaluated along various TRACI categories including acidification, carcinogenics, eco–toxicity, eutrophication, fossil fuel depletion, global warming, ozone depletion, respiratory risks, and smog. Like material characterization, environmental impact is a strong function of synthesis pathway: here, the mode of oxygen deficiency (viz., vacuum or inert gas) influences environmental impact profile.

The original publication of this work appears in Environmental Science: Nano (2018), volume 5, 1237 – 1250. Electrochemical testing and material characterization was performed by Arthur D. Dysart. Life cycle analysis was performed by Andrea Hicks. Manuscript preparation was performed by Arthur D. Dysart and Andrea Hicks.

Abstract

For rechargeable lithium ion batteries, natural and synthetic graphite anodes come with great economic and environmental costs. Carbon microsheets, developed from used starch packing peanuts, are a carbonaceous alternative with great electrochemical performance and quantifiable environmental footprint. This work investigates how synthesis route (e.g., ambient inert gas or vacuum) influences microsheet electrochemistry and environmental impact. Carbon microsheets show gravimetric capacity greater than conventional graphite, with argon-derived microsheets demonstrating gravimetric capacity up to ca. 30% greater than vacuum-derived ones. Life cycle

assessment (LCA) is used to examine the environmental impact of synthesis routes across standard midpoint TRACI categories (viz., ozone depletion, global warming, smog, acidification, eutrophication, carcinogenics, non-carcinogenics, respiratory effects, eco-toxicity, and fossil fuel depletion). Midpoint LCA illustrates that the impact of the vacuum process is sensitive to the origin of utilized energy. For instance, with respect to ozone depletion, vacuum pyrolysis produces less emission equivalents than its argon analog – assuming conventional domestic energy profile. In this sense, the context of energy should be considered alongside environmental impact in evaluation of process sustainability.

Battery storage is critical to advancing alternative energy technologies. Conventional rechargeable lithium ion batteries use battery grade graphite. This work presents an alternative graphitic anode produced from starch packing peanuts using two synthesis methods (viz., inert gas and vacuum) with superior performance to conventional graphite. Life cycle assessment analyzes the environmental impact of the synthesis routes and identifies significant contributors. Electrochemical testing shows battery components generated from waste materials may perform better than conventional graphite. Ultimately, this work demonstrates new environmental avenues for waste materials as raw materials: an increasingly critical area of research.

7.1 Analysis of Environmental Impact

Innovations in alternative energy technologies (e.g., wind and solar [156–159]) require more cost-effective energy storage. Rechargeable lithium-ion (Li-ion) batteries demonstrate sufficient energy and power density, yet modern Li-ion systems struggle to meet ever-increasing demands from energy grids and electric vehicles. [160–162] While many works present excellent materials with better battery performance or smaller form factors, few have explored the practicality and sustainability of their materials. In parallel, existing battery sustainability and life cycle assessment (LCA) literature has focused on outlets of electric and hybrid vehicle technology [162–166] and lithium or production constraints. [164, 166]

There is a deficiency of environmental impact studies investigating synthesis pathways for graphitic anodes. LCA studies on batteries [163, 167] typically employ graphite inventory data from the 1980 study of Hittman Associates Inc. [168] Hittman and associates' work quantifies the energy required for each life cycle stage, demonstrating an overall energy demand 11,090 British thermal units per pound of battery produced (BTU lb^{-1}) assuming inventory with 13.8 %-wt. graphite. Though pioneering at the time, the study does not consider the influence of synthesis route to overall impact. Similarly, other studies utilizing different battery-grade graphite inventories [166] disregard synthesis pathway, such as choice of inert gas (i.e., argon, nitrogen) [167, 169–174]. In representative cases, Rydh et al. [175] and Notter et al. [166] both neglect the choice of inert gas during the graphite synthesis process, potentially leading to a significant underestimation in the environmental impact of graphite and subsequent battery production. Interestingly, Rydh et al. estimated battery energy requirements to be greater than those of Notter et al. This overlooked yet critical parameter makes it challenging to compare conventional techniques with innovations in graphite synthesis – particularly methods utilizing waste precursors.

This work explores the transformation of waste packing peanuts into semi-graphitic anode materials. Packing peanuts are common packaging filler used in transportation of goods. In 1996, 50 million pounds (22.68 million kilograms) of packing peanuts were used, valuing the entire packing peanut industry at over 500 million U.S. dollars [176]. Though reusable, packing peanuts are typically disposed after only a single use as landfill waste. Alternatively, oxygen-deficient heat treatment transforms packing peanuts into carbon microsheets, a disordered carbon morphology with bimodal porosity. This carbon morphology performs with gravimetric capacity greater than that of conventional graphite at comparable cycling rates.

The relationship between synthesis and product capability is an objective measure for evaluations of sustainability and commercial viability. Thus, this work investigates effects of inert gas or vacuum synthesis routes of carbon microsheet anodes for rechargeable Li-ion batteries. Both processes produce carbon microsheets with

similar material properties and electrochemical performance (e.g., gravimetric capacity difference of 15%). The environmental impact of both processes is studied using LCA according to functional unit and life cycle stage, demonstrating that the impact of the vacuum process is dependent on energy source. Two functional units (viz., mass yield and gravimetric capacity) are employed to account for functionality of the semi-graphitic anode material through synthesis and application. Finally, the broader impact of carbon microsheets as rechargeable Li-ion battery anodes is assessed. This work suggests LCA is a significant tool in evaluation of battery materials, emerging today at an ever-increasing rate.

Experimental Methods

This work is a comprehensive assessment of the carbon microsheet as a viable alternative to graphite for rechargeable Li-ion batteries. From the materials perspective, material properties and electrochemical performance are studied as a function of synthesis route. From the sustainability perspective, cradle-to-gate life cycle assessment compares the environmental impact of carbon microsheets as a function of synthesis route. The scope encompasses raw material acquisition, in which packing peanuts are designated as waste materials; and manufacturing, in which packing peanuts are transformed into carbon microsheets. In the manufacturing stage, particulate emissions are modeled according to the downstream aerosol characterization performed by Tsai et al. [177]. Environmental impact reduction is explicitly considered as avoided impact: impacts avoided by eliminating packing peanuts instead of disposing as landfill waste. Impacts avoided are represented as the percent decrease of overall environmental impact (Fig. 7.9). Due to deficiency of life cycle inventory literature on graphite synthesis, quantitative comparison with conventional synthesis techniques is not included in this work.

Carbon Microsheet Synthesis

In 2015, Etacheri et al. [178] first reported synthesis and Li-ion battery anode application of carbon microsheets. The modified procedure used in this work introduces inert gas or vacuum evacuation for pyrolysis atmosphere (Fig. 7.1). An aluminum oxide crucible was loaded with waste starch packing peanuts and placed within a high temperature tube furnace. The continuous oxygen-free atmosphere required for pyrolytic decomposition was enabled by (1) inert gas purge at rate ca. 2 mL min^{-1} or (2) rotary vacuum pump evacuation to gauge pressure below 0.1 mPa. An organic trap was implemented downstream of the furnace exhaust to collect aerosol contaminants [177]. After atmosphere facilitation, packing peanuts were heated from 27 °C to the specified dwell temperature at rate 10 C° min^{-1}. The furnace was maintained at dwell temperature for 2 hours, and then cooled to room temperature at rate ca. –10 C° min^{-1}. The dwell temperatures studied in this work are 600 and 900 °C. Resultant carbon microsheets were utilized without further treatment (e.g., acid or base), separation, and purification.

The original and modified procedure differ along three principle features. The primary difference is ambient atmosphere during heating. In the original procedure, oxygen-free atmosphere is enabled by continuous purging with high purity argon gas before and during heating. In the modified procedure, oxygen-free atmosphere is enabled by continuous pump evacuation. The second difference is the dwell temperature. Dwell temperatures 600 and 900 °C are studied in this work. The third difference is the implemented organic trap. The original procedure collects organics using a water bath, while the modified procedure collects organics using a liquid nitrogen-cooled condenser. Among these differences, the most significant influence is expected from the ambient atmosphere (viz., inert gas or vacuum) and synthesis dwell temperature.

The total energy consumed in this process was calculated using a precursor mass of 273.81 mg and a specific heat 0.71 kJ kg^{-1} K^{-1}. The specific heat was modeled as graphitic carbon due to unavailability of packing peanut specific heat measurements.

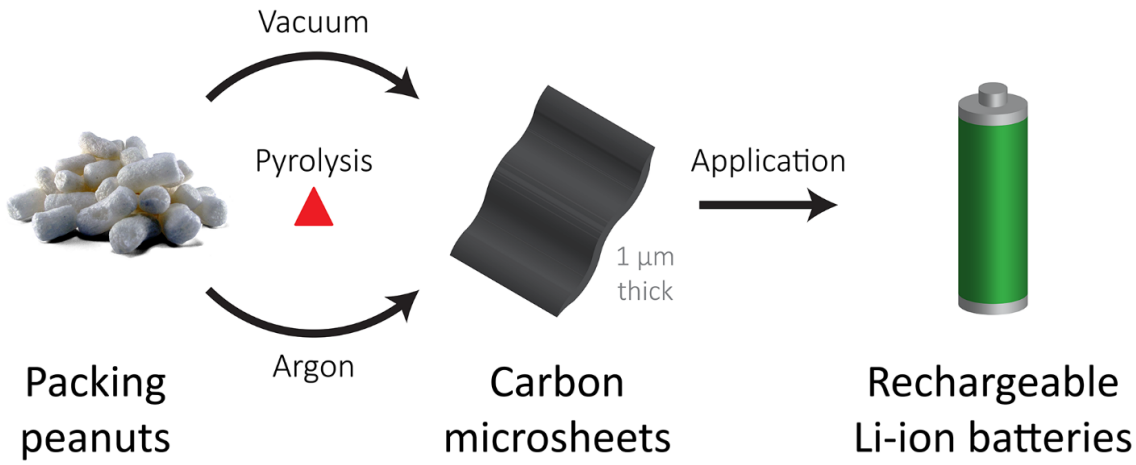

Figure 7.1. *Synthesis of amorphous carbon microsheets.* Carbon microsheets are synthesized by pyrolytic heating of packing peanuts in an oxygen-free atmosphere. Non-oxidizing atmosphere is enabled by continuous argon gas purge or vacuum evacuation. After pyrolysis, micron-sized carbon microsheets are used in rechargeable battery anodes without further chemical separation or purification.

Calculation of consumed energy assumes required energy for the constant temperature step is 10 % of that for the constant heating rate step. Energy consumption of the vacuum pump at 1/3 horsepower was calculated according to manufacturer specification [179].

Mass lost as particulate matter is determined according to by-product characterization performed by Tsai et al. [177]. Inert gas pyrolysis is modeled as two-step decomposition with overall mass loss ca. 70 %-wt. of initial packing peanut mass. The first mass loss of ca. 40 %-wt. occurs near 100 °C due to vaporization of hygroscopic moisture. The second mass loss of ca. 60 %-wt. occurs near 300 °C due to chemical and morphological changes. The modal particulate diameter is less than 2.5 μm as characterized from the downstream water bath.

Software and Impact Metrics

The Sima Pro (version 8.1) LCA software tool was used to produce data inventories for each studied synthesis method. TRACI (Tool for Reduction and Assessment of Chemicals and Other Environmental Impacts, version 2.1) environmental impact methods were used to assess impact data. TRACI, developed by the United States Environmental Protection Agency (EPA) for particular application to North American models, includes ten impact categories: ozone depletion, global warming, smog, acidification, eutrophication, carcinogenics, non-carcinogenics, respiratory effects, eco-toxicity, and fossil fuel depletion. TRACI was selected as the midpoint analysis method for multiple reasons: (1) the method was developed to be relevant to North America, the location of the study, (2) this method utilizes multiple midpoint impact categories, which allows for the evaluation of tradeoffs, and (3) finally it produces and unweighted suite of midpoint values instead of fewer weighted endpoint values. The LCA utilizes various databases including US Life Cycle Inventory (US LCI) [180], ecoinvent 3 [181], and European Life Cycle Database 3 (ELCD), as there was no single database that housed all of the necessary data for the work [182]. Where applicable, the following conventional energy mix for the United States was assumed: 53 % coal, 20 % nuclear, 16 % natural gas, 7 % hydropower, 3 % fuel oil, 1 % biomass, 1 % other fossil fuel, and less than 1 % each of wind, photovoltaic, and geothermal. The influence of energy source is analyzed independently of overall LCA analysis.

Functional Units

Modern rechargeable batteries contain four primary components: the anode, cathode, electrolyte, and separator. The anode and cathode, collectively known as electrodes, create the impetus for energy storage known as voltage or potential difference. During charge and discharge, net potential difference drives lithium cation and electron transfer between electrodes. Lithium cations pass between electrodes through the

electrolyte, a solid or liquid medium which is ionically-conductive typically through dissolution of alkali metal salts. The two electrodes remain separated by the separator, an insulating porous membrane that reinforces external electron transfer as electric current. From the life cycle perspective, environmental impact of rechargeable batteries is a function of the individual impact of these constituents.

This work quantifies the environmental impact of carbon microsheets as an alternative to graphite in rechargeable battery anodes. Two different functional units are utilized to normalize impact: mass and functionality (i.e., specific or gravimetric capacity). The mass functional unit is defined as environmental impact per kilogram of graphitic anode material. The mass unit accounts for synthesis process yield. The capacity functional unit accounts for practical or useful ability of graphitic anode material. The gravimetric capacity unit is defined as environmental impact per amp-hour per kilogram of graphitic anode material, accounting for electron storage ability of battery grade graphitic material. Impacts per specific capacity unit are normalized to gravimetric capacity 372 Ah kg^{-1} of graphitic anode material.

Material Characterization

Scanning electron microscopy (SEM) was performed using a Nova 200 DualBeam scanning electron microscope (FEI Co.). Double-sided carbon tape (3M Corp.) was used to adhere carbon microsheet samples to an aluminum sample stage. Approximately 1 mg of sample was evenly dispersed onto the exposed surface of carbon tape. The microscope chamber was loaded with the sample stage and evacuated to high vacuum (i.e., < 2.6 nbar). Micrographs were recorded at various magnifications after thorough optimization of electron beam alignment, stigmation, focus, brightness, and contrast.

Organic elemental analysis (OEA) was performed using an autosampling combustion pyrolysis furnace with a tungsten conductivity sensor (CE440, Exeter Analytical Inc.). Approximately 2 mg carbon microsheets were placed within a nickel combustion capsule (Exeter Analytical) and loaded into the combustion chamber. Dynamic

flash combustion was enabled by controlled oxygen (99.997%, Praxair Inc.) injection within a continuous helium atmosphere (99.997%, Indiana Oxygen), permitting direct measurement of carbon, hydrogen, and nitrogen content. Oxygen content was determined by difference from unity. Reported values for elemental composition are the average of at least 3 separate trials.

X-ray powder diffraction (XRD) was performed using a Smartlab I X-ray diffractometer (Rigaku Corp.) with a cross-beam optic system. Approximately 20 mg carbon microsheets were loaded into the cavity of borosilicate sample holders mounted into the theta-theta goniometer. Monochromatic Cu-Kα radiation was produced with a 9 kW rotating anode X-ray source, and collected with a sodium iodide scintillation detector. Spectral patterns were produced in X-ray scattering domain (i.e., 2θ) 2 - 150 $^\circ$ at scanning rate 0.5 $^\circ$ min^{-1}. Reported spectral patterns are smoothed for clarity of interpretation, but not reduced for background.

Raman spectroscopy was performed using a DXR Raman microscope (Thermo-Fisher Scientific). The apparatus was calibrated using a polystyrene calibration standard (Thermo-Fisher). Carbon microsheet samples were evenly dispersed across a borosilicate microscope slide (Fisher), and then loaded into the microscope chamber. Spectral patterns were produced using an aperatured green laser with wavelength 532 nm, beam diameter 25 μm, and power 8 mW. A single spectral pattern is the average of at least 3 exposures, with collection time 20 seconds per exposure. Reported spectral patterns are reduced for background and smoothed for clarity of interpretation.

Electrochemical Measurements

The battery fabrication and galvanostatic cycling procedure was performed as follows. Electrodes were fabricated using an automatic constant-speed doctor blade technique. The electrode components of 80 %-wt. vacuum-synthesized carbon microsheet material, 10 %-wt. Super P Li conductive additive (TIMCAL Ltd.), and 10 %-wt. polyvinylidene fluoride (Arkema Inc.), were homogeneously mixed to a viscous mixture with N-Methyl-2-pyrrolidone (MTI Corp.). Mixing was performed

using a polypropylene mixing cup and alumina mixing balls (MTI, 4x 6 mm. dia., 2x 10 mm dia.) within a planetary mixer (THINKY Inc.) at constant speed 8000 rpm for ca. 15 minutes. After mixing, the mixture was coated onto a substrate of aluminum foil (MTI, 15 m thick.) at gap thickness 8 mil using an automatic film applicator (MTI). The resulting thin-film lamination was subsequently dried in a vacuum oven (MTI) at temperature 80 °C and gauge pressure -0.1 mPa for at least 12 hours. Electrodes were cut using a 0.5 in. diameter arch punch (General tools) and assembled into CR2032 battery cells using stainless steel parts (MTI). Batteries were constructed within a high-purity inert atmosphere glovebox (Vacuum Atmospheres Co.). The electrolyte (MTI) is composed of co-solvents ethylene carbonate (EC; 40 %-vol.), dimethyl carbonate (DMC; 20 %-vol.), and diethyl carbonate (DEC; 40 %-vol.); lithium salt lithium hexafluorophosphate (LiPF6, 1.0 M conc.); and additive vinylene carbonate (VC; < 5 %-vol.). All batteries contain porous polypropylene membrane separator (CELGARD; 25 μm thick.) and lithium metal counter electrode (MTI). Batteries were electrochemically tested by galvanostatic cycling at gravimetric currents (i.e., 25, 50, 125, 250, and 500 A kg^{-1}) corresponding to conventional cycling rates (C/10, C/5, C/2, C, and C/10) in the voltage range 0.005 - 3.0 V. Formation cycling was performed at cycling rate 25 A kg^{-1}. Applied gravimetric currents were estimated according to theoretical gravimetric capacity 372 Ah kg^{-1}. Mean areal carbon microsheets per electrode was 1.17 mg cm^{-2}.

Electrochemical impedance spectroscopy (EIS) was performed using a potentiostat with direct digital synthesis circuitry (Reference 600, Gamry Instruments). Following fabrication, a LIB cell was loaded into the potentiostat and cycled in voltage domain 0.01 - 2.0 V for 100 cycles. At conditioned voltage 0.01 V, potentiostatic impedance spectroscopy was performed in the frequency range of 0.01 - 20,000 Hz.

7.2 Electrochemical & Environmental Considerations of Synthesis

Electrochemical cycling illustrates that gravimetric capacity of packing peanut-derived carbon microsheets is weakly dependent on synthesis method. Instead, the two synthesis methods differ by their respective environmental impact, with each method offering unique sustainability advantages. Each synthesis method is characterized by the features of their products, including material properties, electrochemical performance, and LCA along TRACI impact categories (presented on bases of mass and gravimetric capacity) at overall and midpoint life cycle stages.

Material Properties

Carbon microsheets synthesized by vacuum and inert gas pyrolysis share morphological and material properties. The following observations made for inert gas-derived carbon microsheets are comparable to those for the previously reported process [178]. This suggests that the heating profile (i.e., intensity and duration) has the strongest influence upon material character of pyrolytic materials. However, material characterization suggests minute differences in the degree of crystallinity strongly influence the electrochemical ability of the synthesized carbon microsheet materials.

Scanning electron micrographs (Fig. 7.2) show the thin, sheet-like morphology of carbon microsheets is generally independent of synthesis method. Sampled across 20 different particles, carbon microsheets demonstrate mean thickness $1.09 \pm 0.62 \mu m$ independent of synthesis method. Carbon microsheets also show irregular particle shape and texture: vacuum-derived carbon microsheets exhibit asymmetrical and bulging surface protrusions. In comparison, inert gas-derived carbon microsheets exhibit similar size and thickness, with coarser particle geometries.

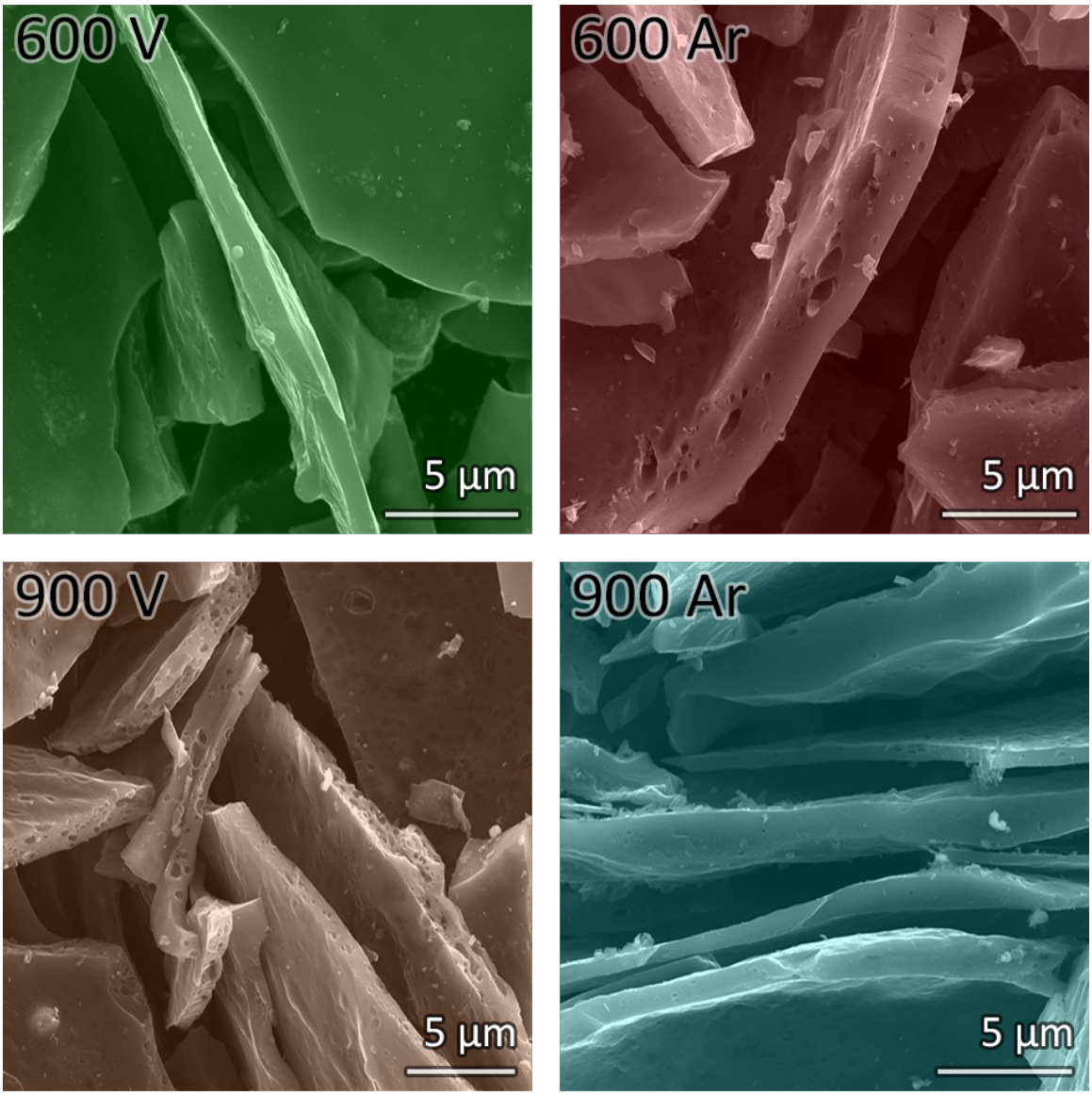

Figure 7.2. *Scanning electron microscopy of carbon microsheets.* Carbon microsheets are synthesized by pyrolytic heating of packing peanuts in an oxygen-free atmosphere. Non-oxidizing atmosphere is enabled by continuous argon gas purge or vacuum evacuation. After pyrolysis, micron-sized carbon microsheets are used in rechargeable battery anodes without further chemical separation or purification.

Organic elemental analysis shows that the chemical composition of carbon microsheets is weakly dependent on synthesis method (Fig. 7.3). However, compositional changes are subtle; composition is more strongly a function of synthesis atmosphere than temperature. At 600 °C synthesis temperature, inert gas-derived carbon microsheets exhibit 4.97 %-wt. greater carbon and 4.60 %-wt. less oxygen content than vacuum-derived microsheets. Similarly, at 900 °C, inert gas-derived carbon microsheets show 2.41 %-wt. greater carbon and 1.77 %-wt. less oxygen content than vacuum-derived microsheets. Synthesis temperature better influences hydrogen composition: in vacuum and inert gas synthesis, hydrogen content is 0.58 and 1.32 %-wt. greater at lower temperature, respectively.

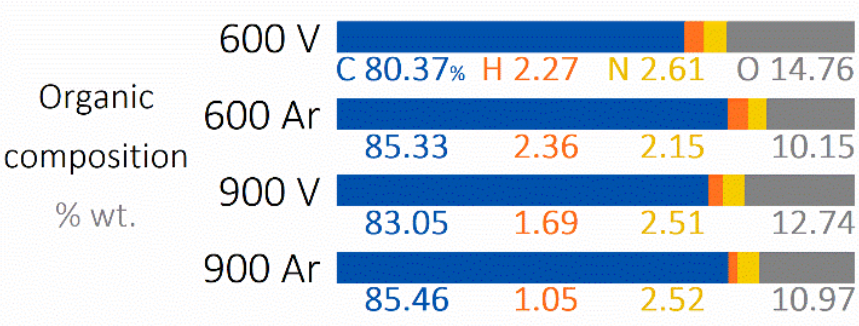

Figure 7.3. *Organic elemental composition of carbon microsheets.* Though generally similar among the studied synthesis procedures, final carbon content is more strongly influenced by synthesis atmosphere than temperature. At either 600 or 900 °C, carbon microsheets synthesized under vacuum demonstrate less carbon and greater oxygen content than those synthesized under inert gas. Note oxygen content is calculated as the residual from unity.

Nanoscale organization of carbon microsheets is characteristically amorphous irrespective of synthesis method. At 600 and 900 °C, X-ray powder diffractograms (XRD, Fig. 7.4a) of vacuum-derived carbon microsheets demonstrate two principle intensity features in scattering domain (viz., 2-theta) 0 - 80 °. These features indicate nanoscale crystalline regions, called crystallites, within carbon microsheet particles. Specifically, the two diffraction peaks occurring near 26 and 42 ° and represent the

(002) and (100) crystal planes, respectively [183]. The (002) plane represents the mean width of nano-crystallites, while the (100) plane represents the mean layer separation of microsheet crystallites. The wide breadth of observed diffraction peaks is characteristic of disordered or non-crystalline phases within carbon microsheets. Similarly, inert gas-derived microsheets demonstrate spectral features of a principle amorphous carbon phase [178]. At constant synthesis temperature, vacuum-derived carbon microsheets demonstrate sharper or more defined diffraction peaks compared to their inert gas-derived counterparts. Furthermore, definition increases with increasing pyrolysis temperature: diffractograms exhibit a less refined (100) peak, suggesting less overall crystalline organization. Similarly, with increasing temperature, decreasing definition of the low-intensity diffraction peak near 6 ° suggests this peak depends on heteroatom content.

Raman spectrograms of carbon microsheets further evidence non-crystalline order (Fig. 7.4b). Two principle Raman features are observed in the frequency range 1000 - 2000 cm^{-1}: The intensity peaks at frequencies 1350 and 1580 cm^{-1} are known as the D and G vibration modes, respectively [184]. The D mode corresponds to the vibrational mode of sp^3 hybridized carbon atoms, while the G mode corresponds to sp^2 hybridized carbon. Carbon with sp^2 hybTidization is typical of planar arrangement or aromatic bonding, and thus measures graphitic crystallinity. Carbon with sp^3 hybridization is typical of three-dimensional bonding structures, and thus measures disordered or aliphatic carbon content. Three additional peaks (i.e., I, D', and D") are overtone vibrations of the D and G modes. The I peak is characteristic of amorphous carbon [185]. As observed for the diffraction peaks of the x-ray diffractograms, the breadths of these Raman features are characteristic of significant disorder within the microsheet particles. Again, inert gas-derived microsheets also demonstrate these same spectral features. At a given synthesis temperature, the areal intensity of the D mode is greater than that of the G mode. With increasing temperature, the areal intensity ratio of these vibrational modes also increases.

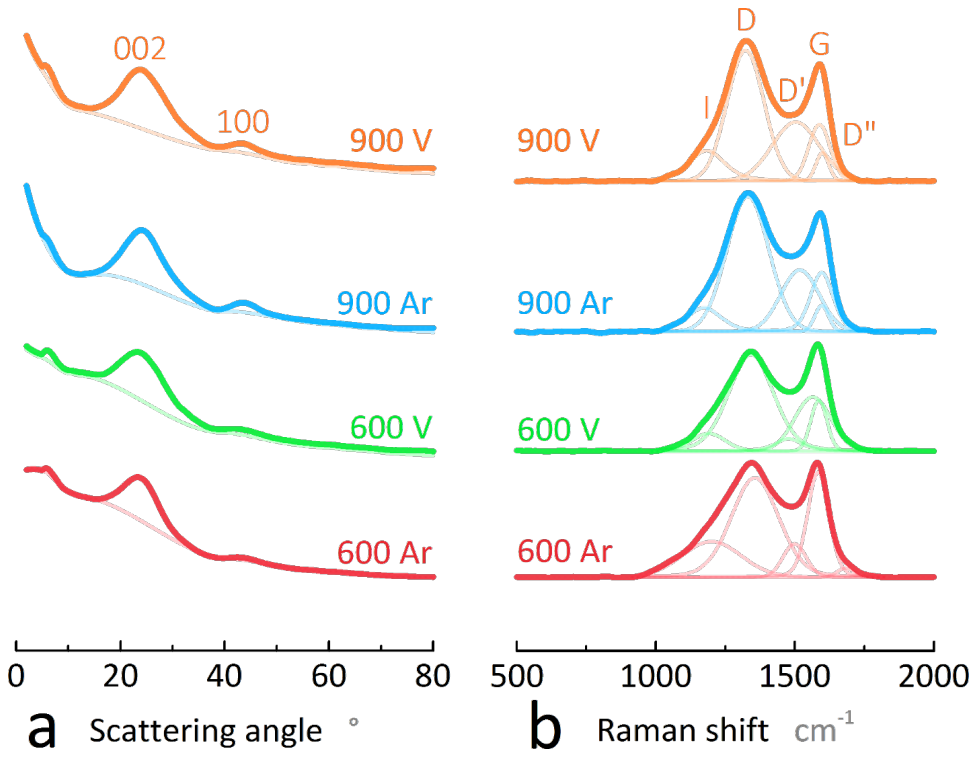

Figure 7.4. *Material characterization of carbon microsheets.* Carbon microsheets synthesized under inert gas and vacuum demonstrate great disorder typical of low temperature pyrolytic carbons. (a) X-ray powder diffractograms demonstrate diffuse (002) and (100) peaks that characterize nano-crystallites within a dominant disordered phase. (b) Raman spectrograms show diffuse peaks including the D and G fundamental vibration modes, and the I, D, and D overtone modes that echo the great degree of material disorder.

The crystalline parameters of the synthesized carbon microsheets suggest that vacuum-derived microsheets are more disordered with smaller crystallite sizes compared to inert gas-derived microsheets (Fig. 7.5). These relationships are also conserved with higher synthesis temperature. This is explained by the effective size of crystallites in carbon microsheets, where asymmetrical Raman vibrations from crystallite edge sites impart greater intensity than symmetric vibrations from the bulk crystallite phase [184].

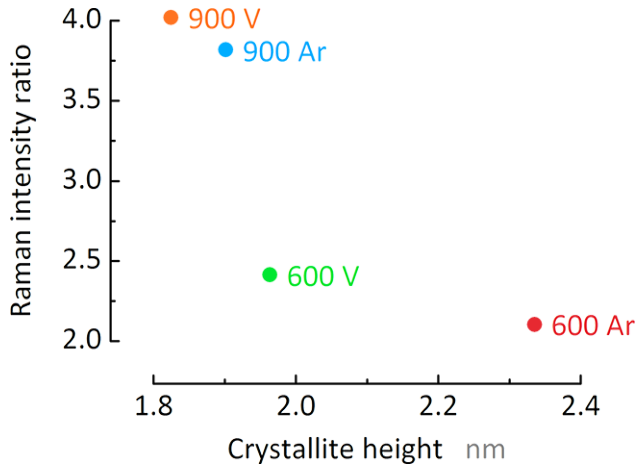

Figure 7.5. *Crystallite parameters of carbon microsheets.* As synthesis temperature increases, the crystallite height decreases while the areal intensity ratio of the D and G vibration modes increases. At a given synthesis temperature, vacuum-derived carbon microsheets demonstrate larger intensity ratios and smaller crystallite size compared to inert gas-derived microsheets.

Electrochemical Performance

Electrochemical performance of vacuum-derived carbon microsheets is similar to that of inert gas-derived microsheets [178], particularly under comparable currents and synthesis temperature (Fig. 7.6b). But, at either synthesis temperature, extended cycling gravimetric capacity is greater for inert gas synthesis. With synthesis temperature 900 °C, inert gas and vacuum-derived carbon microsheets demonstrate mean gravimetric capacity 200 Ah kg^{-1} in cycle 10 (gravimetric current 25 A kg^{-1}) – a similar capacity rating to that of synthetic graphite. [178] In cycle 60 (25 A kg^{-1}), gravimetric capacity increases to 250 Ah kg^{-1} with inert gas synthesis, but remains ca. 200 Ah kg^{-1} with vacuum synthesis. Similarly, with synthesis temperature 600 °C, inert gas and vacuum-derived carbon microsheets demonstrate mean gravimetric capacity 325 Ah kg^{-1} in cycle 10 (25 Ah kg^{-1}).

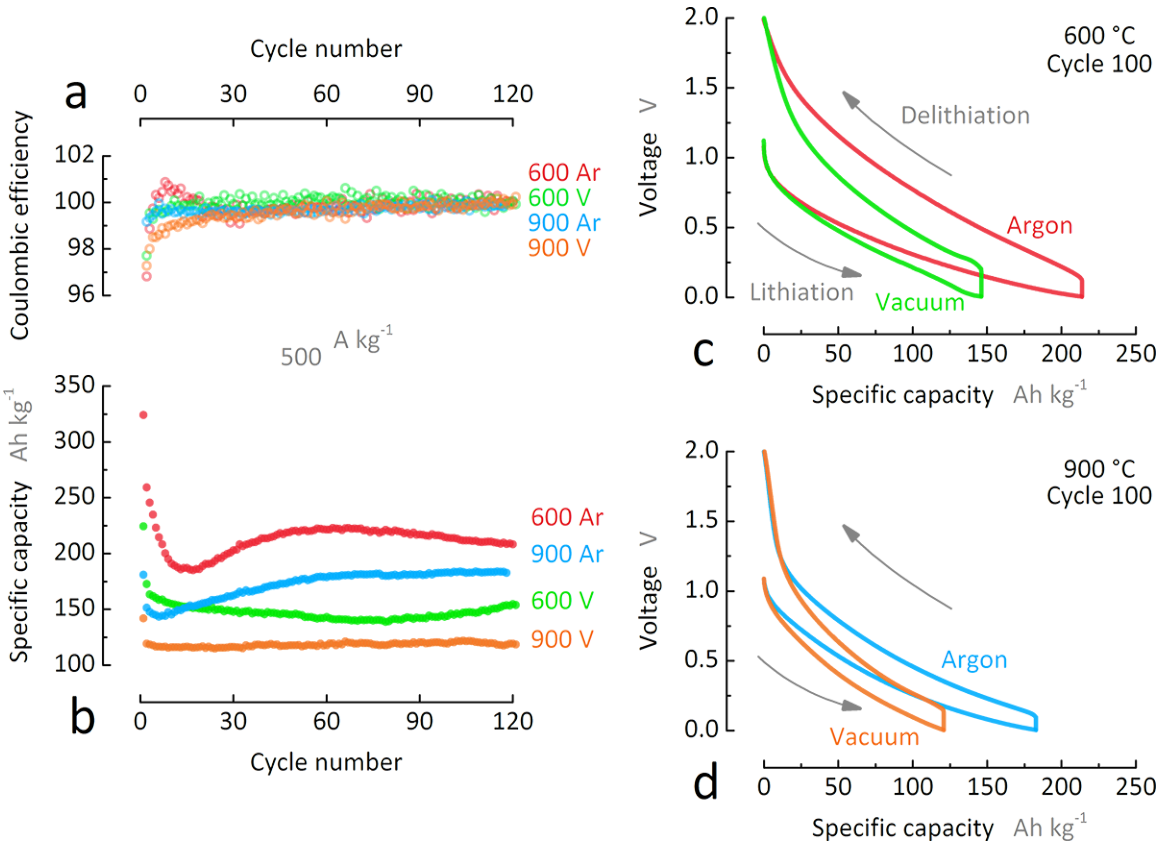

Figure 7.6. *Rate-dependent electrochemistry of carbon microsheets.* As a Li-ion battery anode, each carbon microsheet sample demonstrates large reversible specific capacities and short-term stability. (a) Across all materials, the Coulombic efficiency approaches unity under increasing applied specific current. (b) The specific capacity of carbon microsheets is equivalent or better than that of commercial graphite, especially at fast rates. The cycle 60 chronopotentiogram, corresponding to current 25 A kg^{-1}, shows greater capacities with larger energy inefficiencies at (c) 600 °C compared to (d) 900 °C. Solid (•) and open (○) symbols represent discharge capacity and Coulombic efficiency, respectively. Symbols and chronopotentiographs of the same color correspond to the same data set.

Chronopotentiograms of inert gas and vacuum-derived carbon microsheets suggest greater capacity occurs with higher energy inefficiency (Figs. 7.6c,d). Energy inefficiency is measured as hysteresis, disparity between charge and discharge chronopotentiograms. Carbon microsheets synthesized at 600 °C demonstrate less energy inefficiency than those synthesized at 900 °C. Greater hysteresis in microsheets synthesized at lower temperature suggests higher capacity consequentially occurs with lower energy efficiency. Overall, vacuum-derived carbon microsheets demonstrate gravimetric capacities ca. 15 % less than that of inert gas-derived microsheets, but with better energy efficiency.

Over extended galvanostatic cycling at high applied current 250 Ah kg^{-1}, vacuum-derived carbon microsheets demonstrate more stable gravimetric capacity (Fig. 7.7). With synthesis temperature 900 °C at cycle 100, inert gas-derived microsheets demonstrate greater gravimetric capacity than vacuum-derived microsheets. However, inert gas-derived microsheets demonstrate unstable charge accumulation between cycles ca. 2 - 50 before reaching the steady capacity value of 175 Ah kg^{-1}. This trend also occurs with synthesis temperature 900 °C, but with instability between cycles ca. 2 - 50. As concluded from rate-dependent cycling, the minimally decreased capacity occurring with vacuum synthesis is accompanied by greater energy efficiency (i.e., lower voltage hysteresis) compared to its counterpart with argon synthesis (Fig. 7.7c,d).

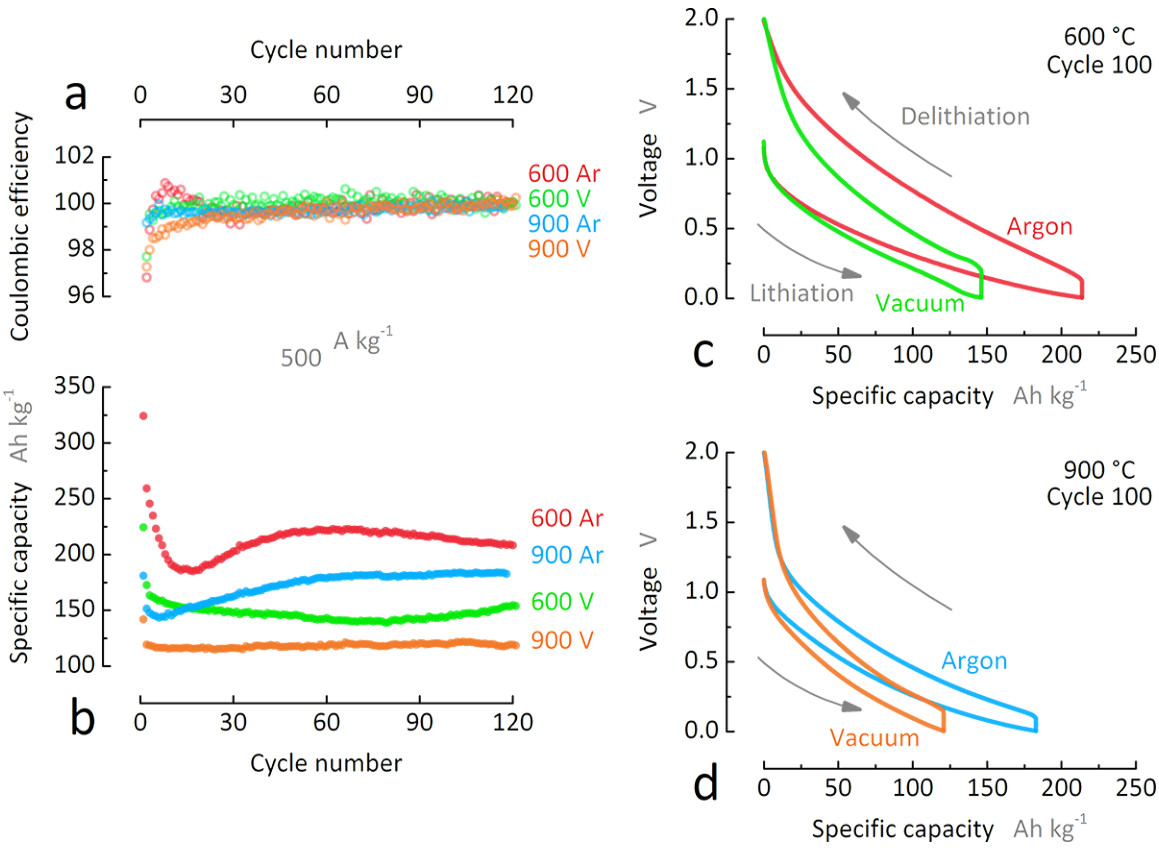

Figure 7.7. *Extended cycling of carbon microsheets.* Under specific current 500 Ah kg^{-1} at similar synthesis temperature, vacuum-derived carbon microsheets demonstrate better cycling stability compared to inert gas-derived ones. (a) Across all materials, the Coulombic efficiency approaches unity with increased cycling. (b) The specific capacity of inert gas-derived microsheets is higher than that of vacuum-derived microsheets. The cycle 100 chronopotentiogram shows greater energy inefficiency accompanies higher capacity at (c) 600 °C compared to (d) 900 °C. Solid (•) and open (○) symbols represent discharge capacity and Coulombic efficiency, respectively. Symbols and chronopotentiographs of the same color correspond to the same data set.

After high current cycling, greater gravimetric capacity and unstable coulombic efficiency (e.g., greater than unity) are attributed to accelerated aging mechanisms. Great applied currents induce high overpotentials which accelerate material changes – though the specific nature of these changes are not well understood [186, 187]. One explanation is morphology change within the active material, where solid-state diffusion of lithium ions creates small channels within microsheets morphology [178]. This phenomenon reveals new sites for lithium storage (e.g., surface charge storage) within increasing cycle number. Another possible explanation is instability at the electrode-electrolyte interface, where morphological and compositional changes occur with increasing cycle number or increasing applied current.

Electrochemical impedance spectroscopy shows vacuum-derived carbon microsheets have less high frequency impedance and greater low frequency impedance compared to inert gas-derived microsheets (Fig. 7.8). From high to low frequency, the complex impedance spectra for each carbon microsheet sample demonstrates four principle features [188] (Fig. 7.8c): (1) high frequency arc, corresponding to solid electrolyte interphase (viz., electrode passivation) impedance; (2) moderate frequency arc, corresponding to heterogeneous or intrinsic material impedance; (3) low frequency arc, corresponding to charge transfer impedance; and (4) low frequency line, corresponding to solid diffusion impedance. All materials demonstrate appreciable solid state impedance. The combined resistance (i.e., SEI, microsheet material, and charge transfer sources), represented in each spectrum as the projection of the cumulative arc onto the abscissa, is less for the inert gas-derived materials compared to the vacuum-derived materials. Lower capacity in the vacuum-derived material can be attributed to their higher impedance.

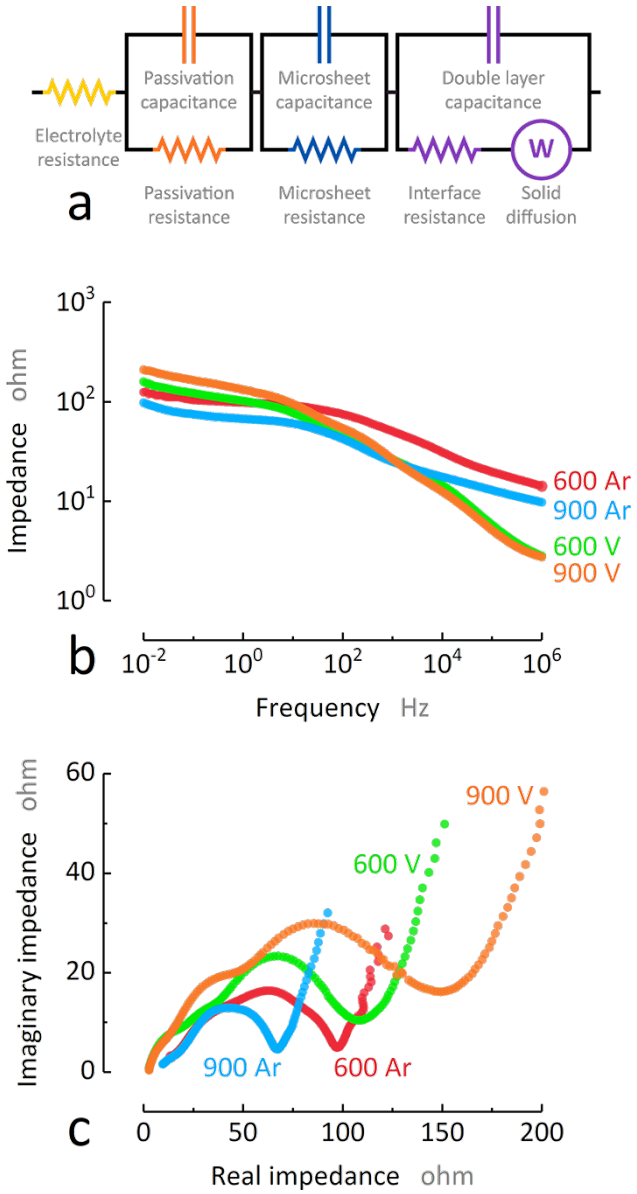

Figure 7.8. *Impedance spectroscopy of carbon microsheets.* Vacuum-derived carbon microsheets demonstrate lower impedance at high frequency, but higher impedance at low frequency, compared to inert gas-derived ones. (a) The impedance spectrum for carbon microsheets can be modeled with four separate impedance sources: electrolyte, solid electrolyte interphase, bulk microsheet phase, and electrode interface. (b) The Bode impedance diagram shows several capacitance and resistance features occurring between 1 - 106 Hz for all carbon microsheet samples. (c) The Nyquist complex impedance diagram shows overlapping Randles features at low to high frequency and a distinct Warburg feature at low frequency for all carbon microsheet samples.

Mass-based Life Cycle Assessment

Midpoint life cycle assessment (LCA) is performed to understand the broader impact of large scale carbon microsheet manufacture. Results of LCA are compared for the processes of ambient vacuum at synthesis temperature 900 °C or inert gas at 600 °C. The environmental impact of carbon microsheets is analyzed using the TRACI impact categories (Fig. 7.9). Overall environmental impacts are reported on a constant mass basis (functional unit) of 1 kg of graphitic material.

Along dimensions of TRACI categories, both synthesis methods have different advantages. The inert gas process demonstrates less impact in the categories of acidification, smog, respiratory effects, global warming, and fossil fuel depletion; except in respiratory effects, environmental impact improves by at most 1 order of magnitude. In comparison, the vacuum process demonstrates less impact in carcinogenics, ecotoxicity, eutrophication, non-carcinogenics, and ozone depletion. In these categories, impact increases by 1 - 4 orders of magnitude.

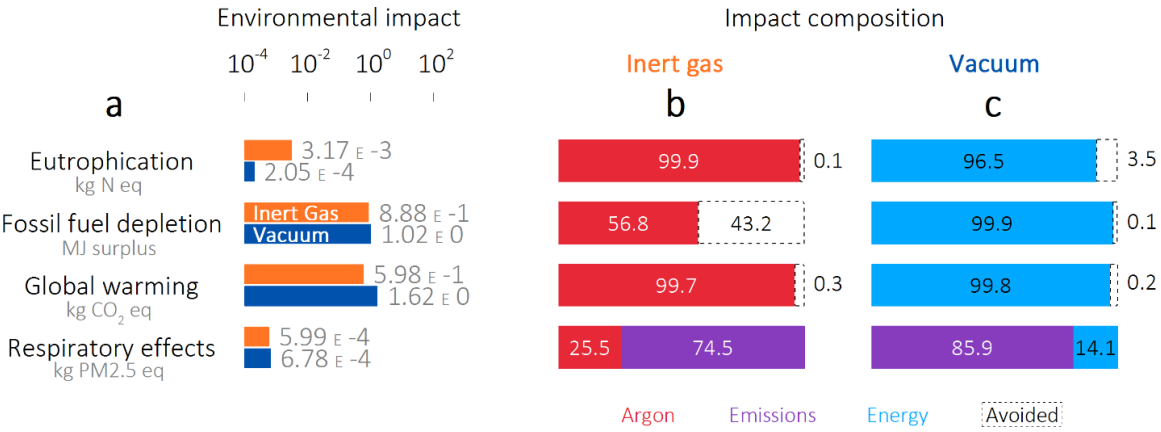

Figure 7.9. *Midpoint environmental impact of carbon microsheets.* (a) At mid-life cycle, environment impact of the vacuum process (c) is generally greater than that of the inert gas process (b), though by at most one order of magnitude. In the inert gas process, a significant landfill impact is avoided in preventing fossil fuel depletion. Midpoint impacts are normalized to specific capacity 372 Ah kg^{-1}.

In all categories, inert gas contributions dominate environmental impact of inert gas synthesis while continuous vacuum contributions dominate that of vacuum synthesis. Continuous inert gas atmospheres utilize great quantities of manufactured gas: increased gas production implies increased energy costs. In consequence, more energy for gas production increases pollutant equivalents: particularly, equivalents of CO_2 and CFC-11. With respect to global warming and ozone depletion, increasing gas production underlies overall greater impact in the inert gas process. Finally, energy requirements comprise ca. 4 % impact due to fossil fuel depletion. Overall impact of the vacuum process is proportional to energy consumption which, in turn, is a function of the applied energy mix.

In both processes, air emissions dominate respiratory effects (Fig. 7.9). Pyrolysis reactions are thermal decompositions: high-temperature heating breaks organic precursors into phases of solid carbon and aerosol hydrocarbons [189]. Hydrocarbon by-products are respiratory risks because of their small average particle diameter [177]. As suggested by Tsai et al. [177], possible by-product mitigation techniques include advanced HVAC filtration and stream recycling.

Both processes demonstrate avoided landfill impact, the effective reduction in environmental impact by preventing packing peanuts from becoming landfill waste. In the inert gas process, fossil fuel depletion decreases by ca. 40% of the maximum predicted impact. In the vacuum process, ozone depletion and eutrophication decrease by ca. 40% and 5%, respectively.

Broader Impact of Carbon Processes

Carbon microsheets are inherently amorphous: phase disorder enables unique electrochemical performance, including specific capacities greater than conventional graphite. This behavior results from large mean interlayer spacing – greater than that of crystalline graphite [190]. As observed through XRD, broad diffraction peaks are characteristic of carbonaceous pyrolysis products with low crystallinity. In pyrolytic carbons, low crystalline order is inversely related to intensity of heat treatment.

For example, disordered carbon microsheets are subject to low intensity heating at less than 1000 °C for moderate synthesis time. In comparison, crystalline synthetic graphite is subject to excessive temperatures (e.g., 2800 °C) for sufficient synthesis time, encouraging development of ordered phases.

Li-ion anode performance of inert gas-derived carbon microsheets has been previously reported by Etacheri et. al. [8]. Vacuum-derived carbon microsheets are reported for the first time in this work. Gravimetric capacity, measuring electrochemical charge storage ability, is weakly dependent on synthesis atmosphere. At cycling rate C/10, carbon microsheets demonstrate mean gravimetric capacity 420 Ah kg^{-1}; in contrast, conventional graphite exhibits less gravimetric capacity at comparable rate (with maximum theoretical limit 372 Ah kg^{-1}) [8]. Greater gravimetric capacity suggests carbon microsheet anodes can enable batteries with greater energy storage. Several electrochemical challenges, particularly voltage hysteresis and energy efficiency, should be addressed to improve microsheet applicability as alternative anodes in rechargeable Li-ion batteries.

Across all of the environmental impact categories considered, the vacuum process is consistently dependent upon energy and its context. In particular, the vacuum process was determined with mixed energy sources assumed representative of the United States (viz., US conventional energy mixture; an itemized breakdown is shown in Table 3). This mixture is comprised of energy from various sources proportioned by prominence. The LCA suggests energy context is as significant to environmental impact as energy itself: the origin of utilized energy significantly effects environmental impact of the vacuum-synthesis method (Table 7.1). Replacement of the mixed energy source with renewable technologies of wind, nuclear, and hydropower decrease impact across several categories. In contrast, energy from only natural gas increases environmental impact in carcinogenics, eco-toxicity, fossil fuel depletion, and non-carcinogenics; and weakly reduces impact in eutrophication potential, ozone depletion, and smog. Energy derived from combustion materials (i.e., biomass, anthracite, bituminous, lignite, oil fuel) generally increases impact, but least environmental im-

pact is observed from biomass sources. Specifically, biomass energy sources reduce acidification, eutrophication potential, and ozone depletion; however, smog increases by over 300 %.

Overall, energy context is significantly influential to environmental impact of the vacuum process. Between different energy sources and combustion sources, greatest decreased impact is observed in ozone depletion by using renewable technologies (i.e., wind, hydropower, nuclear) or biomass and anthracite combustion; and in non-carcinogenics by biomass combustion. The greatest increased impact is more divisive: excessive environmental impact occurs in fossil fuel depletion by using natural gas; in ozone depletion, eutrophication, and ecotoxicity by using photovoltaic technologies; in global warming, acidification, and respiratory effects by anthracite combustion; in smog by biomass combustion; and carcinogenics and non-carcinogenics by fuel oil combustion.

Table 7.1.

Percent change in environmental impact due to selected energy sources. The origin of energy utilized in the vacuum process has a significant influence upon environmental impact. If the energy consumed by the vacuum process is generated solely by renewable energy technologies, particularly nuclear and wind, the overall environmental impact decreases radically. Negative values indicate decreased environmental impact.

Category	Conversion processes				
	Hydropower	Natural gas	Nuclear	Photovoltaic	Wind
Acidification	- 99.9 %	- 8.8	- 95.9	- 93.8	- 99.6
Carcinogenics	- 95.9	108.5	- 97.8	515.7	- 71.1
Eco-toxicity	- 99.4	216.5	- 83.7	833.9	- 98.4
Eutrophication	- 102.5	- 38.6	- 99.6	333.5	- 101.7
Fossil fuel depletion	- 99.8	283.5	- 98.0	- 88.0	- 98.9
Global warming	- 97.1	- 7.5	- 98.7	- 92.5	- 99.4
Non-carcinogenics	- 99.3	57.0	- 93.8	76.9	- 98.2
Ozone depletion	2,223.0	- 395.6	- 214.3	365,223.5	- 410.5
Respiratory effects	- 14.1	1.6	- 13.5	- 11.4	- 14.0
Smog	- 99.8	- 70.9	- 96.7	- 92.9	- 99.6

7.3 Sustainability Recommendations for Carbon Synthesis

The environmental impact of Li-ion batteries has been studied in exhaustive detail, but a complete battery-grade synthetic graphite inventory has yet to be produced, which includes a comprehensive analysis of different synthesis processes. Hittman et al. [168] reported overall energy consumption 177,169 BTU kg^{-1} of carbon produced in the synthetic graphite process. Natural graphite performs with theoretical capacity 372 Ah kg^{-1} and practical capacity ca. 250 Ah kg^{-1} at moderate cycling rates [191]. In comparison, inert gas-synthesized carbon microsheets perform with similar practical capacity but with quantifiable environmental impact, accounting for non-negligible influence of synthesis pathway. This work calculated cumulative energy demand for inert gas and vacuum pyrolysis pathways as 10,700,000 and 24,500,000 BTU kg^{-1} of carbon produced, respectively. The calculated energy demands for carbon microsheets are 2 orders of magnitude greater than that of Hittman et al. However, it is difficult to directly compare these cumulative energy demands because pyrolysis conditions of Hittman et al. are unreported. Similarly, energy demands of Notter et al. [166] and Rydh et al. [175] do not isolate synthesis impacts from cell fabrication impacts, further challenging objective comparisons. It is suggested that cumulative energy demands of these previous studies would be significantly greater and directly comparable if the significant influence of atmosphere maintenance was considered.

Carbon microsheets produced from used starch packing peanuts are superior to current battery-grade graphite at fast charging rates. The inert gas synthesis process relies heavily on energy-intensive practices, principally argon gas production. Synthesis of carbon microsheets under vacuum atmosphere can potentially reduce environmental strain with minimal loss in gravimetric capacity. This work demonstrates the influence of synthesis method to overall environmental impact, with little influence on gravimetric capacity. In the vacuum process, environmental impact is highly sensitive to the context of energy: for example, replacing the conventional mixed energy source by wind technology decreases impact in all TRACI categories.

Utilization of waste packing peanuts in this process prevents their introduction into the solid waste stream. The potential to transform waste "zero" value materials into high value products for energy storage is only beginning to be investigated from a life cycle perspective: further research is encouraged to understand possible influence upon introduction to consumer battery and other markets.

Acknowledgments

The authors declare no conflict of interest in this work. AH would like to acknowledge the role of startup funding from the University of Wisconsin-Madison in the completion of this work. VP and AD gratefully acknowledge the Assistant Secretary for Energy Efficiency and Renewable Energy, Office of Vehicle Technologies of the U.S. Department of Energy under Contract No. DE-EE0006832 under the Advanced Battery Materials Research (BMR) Program.

PART III
ANODES FOR SULFUR BATTERIES

Unless you expect the unexpected you will
never find truth, for it is hard to discover
and hard to attain.

— P. Wheelwright, 1959, *Heraclitus*

CHAPTER 8: AMORPHOUS SUBMICRON CARBON SPHERE ANODES

Anode materials are a significant consideration in lithium sulfur battery performance, particularly for eventual commercial applications. Carbon materials are viable candidates due to dual versatility as an inert conductive cathode substrate and electrochemically-active anode material. Furthermore, carbonaceous and lithium anodes exhibit a small ca. 0.3 V vs. $Li^{0/+}$ difference in lithiation voltage [49]. To explore electrochemical feasibility of synthesized carbons for anode applications, submicron carbon spheres were produced via two step sonochemical-pyrolysis process as a function of synthesis temperature.

The original publication of this work appears in Environmental Science: Nano (2018), volume 5, 1237 – 1250. Isothermal nitrogen sorption and high temperature synthesis was performed by Lok Kumar Shrestha and Katsuhiko Ariga. Low temperature synthesis, material characterization, electrochemical testing, data analysis, and manuscript preparation were performed by Arthur D. Dysart and Xin Li Phuah.

Abstract

Lithium-ion storage in monodisperse submicron carbon spheres (SCS) depends on the inert atmosphere thermal treatment of sonochemically formed polymeric precursors. Battery electrodes of SCS present great initial capacity up to 861 and 1,111 Ah kg^{-1} at ambient temperatures 27 and 50 °C, respectively, when cycled at specific current 25 Ah kg^{-1}. Beyond initial formation cycles, interestingly, the gravimetric capacity of SCS increases by up to 58% after cycle 50 if cycled up to 3.0 V. Furthermore, capacity change becomes more intense until failure when cycled at 50 °C due to enhanced lithium kinetics. During the first 30 cycles, in situ electrochemi-

cal impedance spectroscopy illustrates capacity evolution is coincident with changing capacitive behavior. Subsequently, a model is proposed to relate evolving specific capacity to morphological changes before and during galvanostatic cycling. Further mechanistic support is provided by quantitative characterization of nano-crystallites and phase disorder by X-ray powder diffraction (Scherrer equation) and Raman spectroscopy (peak fitting), elemental composition by organic elemental analysis, and textural properties by isothermal nitrogen sorption. This work provides valuable insight on pertinent ex situ and in situ factors influencing extended voltage applications of synthetic carbons in rechargeable lithium-ion batteries.

8.1 Submicron Carbon Spheres

Applications in portable devices and electric vehicles elevate the lithium-ion battery (LIB) as the centerpiece of energy storage technology. Since conception and market introduction in the 1990s [192], commercial rechargeable batteries have operated according to reversible insertion, or intercalation, of lithium ions within lithium metal-oxide cathodes and graphite anodes. In this potential-driven mechanism, the charging process forces lithium from the lithium metal oxide structure into the interlayer space between graphite sheets. This causes coordination with aromatic carbon to form graphite intercalation compounds (GIC) [52,192]. In the discharging process, lithium separates from graphite and returns to stable configuration within the cathode material. This reversible process enables storage and supply of cordless energy.

For over two decades [54, 187, 192–202], graphite anodes have been extensively studied to understand their material properties and electrochemical behavior. Graphite is prevalent because of its ability to reversibly intercalate lithium ions, providing theoretical gravimetric capacity 372 Ah kg^{-1} [203]. However, in practice (i.e., combined with conventional cathode lithium cobalt oxide [49]), graphite performs with reversible gravimetric capacity ca. 140 Ah kg^{-1} and gravimetric energy ca. 130 Wh kg^{-1}. These low performance values are insufficient for demanding applications in

emerging technologies, particularly longer-lasting portable electronics and long range electric vehicles.

While many reports have demonstrated exceptional electrochemical performance from carbonaceous anodes [204–210], few have targeted the stability of electrochemical behaviorparticularly at non-ambient temperature. There has been recent, resurgent interest in electrochemical applications of disordered carbons [211, 212] for three reasons: (1) synthetic simplicity, typically requiring only single step pyrolytic heat treatment; (2) abundant precursor availability, enabling use of virtually any carbon-rich precursor; and (3) controllable material properties, modified by adjustment of synthesis parameters. Unlike its ordered graphite counterpart, disordered carbon is capable of capacitive lithium interaction. This mode of lithium storage enables adsorptive lithium storage or release from micro and mesopores [213]. The successful 10 year lifetime of the Rosetta space probe has been linked to electrochemical performance of its synthetic carbon anode, a harbinger of future successes [214].

In context, this work describes the correlation between material properties and electrochemical performance for synthetic carbons at ambient and elevated temperatures (viz., 27 and 50 °C, respectively). The carbon morphology studied in this work is the submicron carbon sphere (SCS), first reported with sonochemical synthesis by Pol et al. [215, 216] The sub-micron carbon sphere demonstrates an amorphous organization, smooth surface, reproducible mono-dispersity, and uniform particle size; features appealing for LIB applications. Inspired by the Strber procedure [217], the sonolytic synthesis for submicron polymer spheres produces spherical particles using cost-effective, sustainable precursors in an environmentally-friendly and industrially-scalable manner. The application of ultrasound enables great energy transfer within a local transient state, characterized by over 5000 K temperature, 1800 atm pressure, and 108K s^{-1} thermal transfer rate [218], which influence reaction rate and morphology. Pyrolytic heat treatment transforms polymer spheres into carbonaeous analogues. Recent work has revealed the significance of ultrasonic cavitation to the synthesis of SCSs [219], and the exceptional tribological performance of SCSs as lu-

bricant additives [220, 221]. To further understand the influence of SCS material properties for practical applications, this work explores the galvanostatic cycling behavior of submicron carbon spheres synthesized at various pyrolysis temperatures against lithium metal at working potential 3.0 V.

Experimental Methods

Preparation of spherical polymer resins

The previously reported synthesis by Pol et al. [215] for polymeric resorcinol-formaldehyde resins was modified for this study. Ultrasonic radiation generated by a piezoelectric ultrasonic probe (VCX 750, Sonics & Materials Inc.) was applied to a mixture of 40 mL ethanol (200 proof, Decon Labs Inc.) and 100 mL Type 1 water (Barnstead, Thermo-Fisher Scientific Corp.). After homogenization, further ultrasonic radiation was applied to encourage dissolution of 500 mg resorcinol (Sigma-Aldrich Corp.) and dispersion of 0.7 mL formaldehyde solution (37 %-vol., Sigma-Aldrich) into the aqueous ethanol mixture. Under continuous ultrasound application, 0.4 mL ammonium hydroxide solution (25 %-wt., Sigma-Aldrich) was added dropwise to the solution for up to 7 min until the transparent, colorless liquid adopted an opaque white color [215]. An ice bath was implemented to maintain the reaction temperature between 28 and 35 °C to prevent ammonia vaporization from heat generated by acoustic cavitation [222]. The solid precipitate was separated by centrifuge-assisted (Thermo-Fisher Scientific) separation with water and ethanol. The polymeric product was obtained after drying the precipitate at 50 °C in vacuo (MTI Corp.).

Pyrolytic carbonization of polymer resins

Pyrolysis of the spherical polymer resin was performed in rectangular alumina crucibles (MTI) heated inside a horizontal quartz tube furnace (MTI). Covered alumina crucibles were filled with 500 mg of polymer resin and placed within the furnace tube. After sealing the furnace chamber with enclosing flanges, the chamber volume

was flushed with argon gas (99.997%, Indiana Oxygen Co.) for approximately 20 min. Under continuous argon flow, the furnace chamber was heated at constant temperature rate 10 C° min^1 to the specified dwell temperature for 4 h, then cooled to room temperature at rate ca. -10 C° min^{-1}. The dwell temperatures studied include 600, 900, 1500, and 1800 °C. The final carbon product was gently pulverized using a mortar and pestle to encourage particle separation. The collected product, termed submicron carbon spheres, was utilized in the following procedures without further treatment.

Battery Fabrication & Assembly

A viscous mixture of 80 %-wt. submicron carbon spheres, 10 %-wt. carbon black (Super P Li, Timcal Graphite Co.), and 10 %-wt. polyvinylidene fluoride (Kynar HSV 900, Arkema Corp.) was prepared with N-methylpyrrolidone solvent (Sigma Aldrich). Homogenization was performed in closed polypropylene cups (Flacktec Inc.) with alumina mixing balls (MTI) agitated using a planetary mixer (Thinky Corp.). The mixture was laminated onto copper foil (9m-thick, battery grade, MTI) using a bladed film applicator (Gardco Inc.) and automatic film coater unit (MTI). The resulting thin film lamination was dried at temperature 80 °C in vacuo for at least 12 h. Electrodes were cut from the dried laminate using an arch punch (0.25 in. dia., General Tools Co.) and installed into stainless steel CR2032 (MTI) coin cells. All cells contained electrolyte 1.0 M $LiPF_6$ in solution of dimethyl carbonate (DMC), diethyl carbonate (DEC), and ethylene carbonate (EC) (1:2:1 in volume, MTI). All cells were fabricated using a lithium metal counter electrode (viz., counter and reference; MTI) and porous polypropylene separator (Celgard 2500, Celgard LLC). Battery cells were hermetically sealed at hydraulic pressure ca. 1000 lb in^{-2} (MTI). All battery assembly & crimping was performed within a high purity glovebox (Vacuum Atmospheres Co.) filled with 99.997% argon gas (Indiana Oxygen Co.).

Electrochemical Characterization

Definitions of charge and discharge processes are taken with respect to the counter electrode: discharge is defined as lithiation of carbon spheres (viz., potential approaches 0.0 V), while charge is defined as delithiation of intercalated carbon (viz., potential approaches 3.0 V). All reported intensive properties (e.g., specific capacity, specific current) are calculated with reference to mass of carbon spheres. All voltages or potential differences are reported relative to the ionization potential of lithium metal (viz., versus $Li^{0/+}$).

Following fabrication, LIB cells were tested galvanostatically using a multi-channel battery cycler (Arbin Instruments Inc.). Prior to galvanostatic cycling, fabricated LIB cells were left at rest for ca. 12 hr (viz. open circuit configuration). All cells were tested in cutoff voltage domain 0.01 - 3.00 V without additional conditioning. This potential domain was chosen to probe high voltage material changes. High temperature galvanostatic cycling was performed in a benchtop temperature chamber (Espec Inc.) with temperature tolerance $\pm 0.5°C$.

Electrochemical impedance spectroscopy (EIS) was performed using a potentiostat with direct digital synthesis circuitry (Reference 600, Gamry Instruments). Following cycling, LIB cells were loaded into the potentiostat and cycled in voltage range 0.01 - 3.0 V. At conditioned voltage, potentiostatic impedance spectroscopy was performed in the frequency range of 0.01 - 20,000 Hz.

Characterization of SCSs

X-ray diffraction (XRD) experiments were performed using an X-ray diffractometer (Smartlab III, Rigaku Corp.) with a cross-beam optic system. Approximately 2 mg of sample was loaded into the cavity of borosilicate sample holders mounted into the theta-theta goniometer (Rigaku). Monochromatic Cu-Kα radiation was produced with a 9 kW rotating anode X-ray source, and collected with a sodium iodide scintillation detector (Rigaku). Spectral patterns were produced in 2θ scattering range

2 - 150 ° at scanning rate 0.5 ° min^{-1}. Reported spectral patterns are smoothed for clarity of interpretation but are not reduced for background.

Scanning Electron Microscopy (SEM) was performed using a scanning electron microscope (Nova 200 DualBeam, FEI Co.). Double-sided carbon tape (3M Corp.) was used to adhere carbon nano-sphere samples to an aluminum sample stage. Approximately 5 mg of sample were evenly dispersed onto the exposed surface of the carbon tape. The microscope chamber was loaded with the sample stage and then evacuated to high vacuum (i.e., < 2.6 nbar). Micrographs were recorded at various magnifications after thorough optimization of electron beam alignment, stigmation, focus, brightness, and contrast.

Transmission Electron Microscopy (TEM) was performed using an environmental transmission electron microscope (Titan, FEI). To prepare the sample, approximately 5 mg of sample was dispersed in anhydrous ethanol (Decon Labs). In the presence of a 200-mesh carbon TEM grid (Pelco, Ted Pella Inc.), the ethanol solvent was allowed to vaporize at temperature 150 °C in vacuo. The specimen chamber was then loaded with the sample-loaded grid and evacuated to high vacuum (i.e., < 2.6 nbar). Micrographs were recorded at various magnifications after thorough optimization. Electron beam alignment, stigmation, focus, brightness, and contrast were optimized for each magnification.

Raman Spectroscopy was performed using a Raman microscope (DXR, Thermo-Fisher Scientific). The apparatus was calibrated using a polystyrene calibration standard (Thermo-Fisher). Carbon nano-spheres were evenly dispersed across a borosilicate microscope slide (Fisher), and then loaded into the microscope chamber. Spectral patterns were produced using an aperatured green laser with wavelength 532 nm, beam diameter 25 μm, and power 8 mW. A single spectral pattern is the average of at least 3 exposures, with collection time 20 s per exposure.

Nitrogen adsorption and desorption isotherms were measured using an isothermal nitrogen physisorption analyzer (Nova 2200e, Quantachrome). Approximately 20 mg of submicron carbon spheres were loaded into a dehydrated quartz sample tube cell.

The loaded cell was placed into a heating mantle and outgassed at temperature 300 °C for 24 h in vacuo. Isothermal sorption measurements were performed at temperature -196 °C using a liquid nitrogen bath. Measurements were recorded in relative pressure range 0.005 - 0.999 with minimum equilibration time 60 s. Specific surface area was calculated according to the multi-point Brunauer-Emmett-Teller (BET) method, while pore size distribution is calculated according to the non-linear density functional theory (NLDFT) method.

Organic elemental analysis (OEA) was performed using an autosampling combustion-pyrolysis furnace with a tungsten conductivity sensor (CE440, Exeter Analytical Inc.). A sample of ca. 20 mg was placed within a nickel combustion capsule (Exeter Analytical) and loaded into the combustion chamber. Dynamic flash combustion was facilitated by controlled oxygen (99.997%, Praxair Inc.) injection within a continuous high purity helium atmosphere (99.997%, Indiana Oxygen). Carbon, hydrogen, and nitrogen content were determined by dynamic flash combustion, while oxygen content was determined by difference from unity.

Quantitative analysis of characterization data

X-ray powder diffraction measures the diffraction intensity from the crystalline phase of SCSs. Specifically, crystallite dimensions of submicron carbon spheres are quantified from X-ray diffraction spectrograms. The observed intensity spectrum was resolved into constituent crystallite contributions using pseudo-Voigt functions, with baseline determined using cubic spline interpolation [223].

The crystallite regions formed within amorphous carbons during pyrolysis are described by three characteristic lengths. The intraplane characteristic length L_a is determined from the spectrum broadening of the 002 intensity peak, while the interplane characteristic length L_c is determined from the spectrum broadening of the 100 intensity peak. Determined from the Scherrer equation, these dimensions are

a function of the Bragg angle θ, reduced spectrum broadening β_i (viz., full with at half maximum), X-ray wavelength λ, and shape factor K_i:

$$L_i = \frac{K_i \lambda}{\beta_i \cos\theta_i} \tag{8.1}$$

For the intraplane characteristic length L_a, the shape factor $K_a = 1.84$. For the interplane characteristic length L_c, the shape factor $K_c = 0.91$ [72].

The interplanar spacing of graphite planes within the crystallites is determined from the measured X-ray scattering of the 002 peak. Determined from the Bragg equation, interlayer spacing is a function of Bragg angle θ, and X-ray wavelength λ:

$$d_i = \frac{\lambda}{\sin\theta_i} \tag{8.2}$$

From Raman spectroscopy, the quality of the formed crystallite regions is quantified by the calculated ratio of intensities from the ordered and disordered carbon regions. The D-G ratio is calculated as the intensity ratio of the D band to the G band:

$$R_{Raman} = \frac{I_D}{I_G} \tag{8.3}$$

In this work, intensity ratio is defined as the ratio of areal intensities rather than band intensities (viz., heights). Due to asymmetrical convolution of the D and G peaks in amorphous carbon, the area and height ratios diverge as fitted peaks become less symmetric [224]; conversely, calculated values converge as fitted peaks become more symmetric and less diffuse.

8.2 Material & Electrochemical Properties of Carbon Spheres

The material and chemical properties of SCSs depend on the applied synthesis procedure (Fig. 8.1). In the first step, a pre-polymer mixture is exposed to intense mechanical sonication [215]. The pre-polymer mixture is comprised of resorcinol, formaldehyde, and ammonium hydroxide in aqueous ethanol. The aqueous ethanol solvent serves as a dual-phase solvent to induce a type III phase inversion [225]. Application of ultrasonic vibrations induces acoustic cavitation, enabling the sonolysis

of water to produce ionic radicals. Free radical attack accelerates reactions to form cross-linked resin particles [219, 226, 227]. In the second step, the submicron polymer spheres are slowly heated to pyrolytic temperature within inert atmosphere. Carbonaceous materials, derived from pyrolysis of organic compounds, have properties sensitive to heating parameters. In particular, high temperature pyrolysis encourages nucleation of graphitic nano-crystallites, small ordered regions comprised of layered aromatic carbons [71]. The influence of pyrolysis temperature (i.e., 600, 900, 1500, and 1800 °C) on material properties and resulting electrochemical performance is the focus of this work.

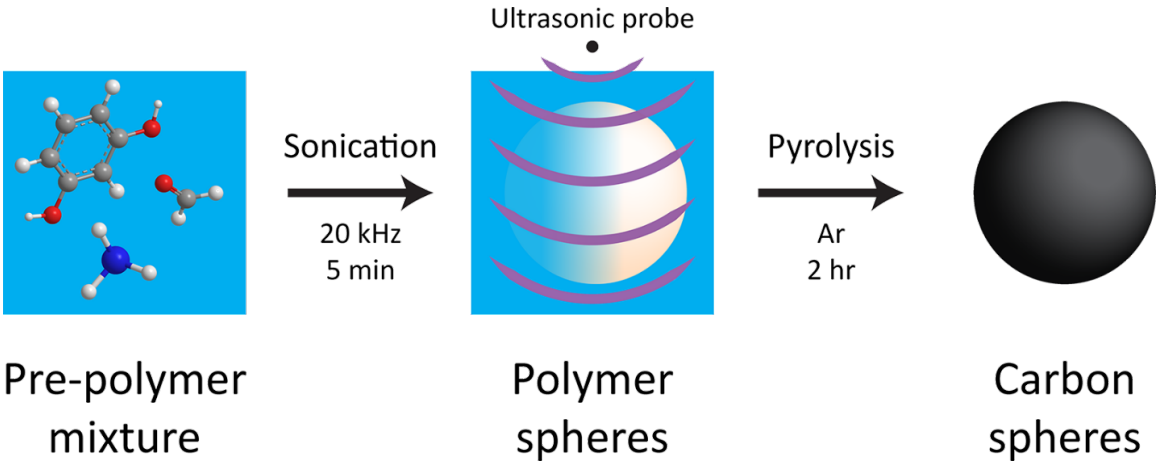

Figure 8.1. *Synthesis of amorphous carbon spheres.* Submicron carbon spheres are synthesized by carbonization of a spherical polymer produced via rapid sonication. Submicron polymer spheres are produced by the application of high intensity ultrasonic energy to a pre-polymer mixture of resorcinol, formaldehyde, and ammonia in aqueous ethanol. Pyrolysis of this product under inert atmosphere creates amorphous submicron carbon spheres.

Surface morphology and internal organization of SCSs are independent of synthesis temperature. Scanning electron micrographs (Fig. 8.2) show that carbon spheres are exceptionally spherical and resolute; that is, not conjoined. Across the shown area, the average particle diameter is ca. 500 nm. Transmission electron micrographs (Fig.

8.2b) show carbon microspheres are comprised of disordered carbon planes, whose erratic orientations delineate long range-disorder. These constituent carbon planes demonstrate short mean diameter ca. 1.5 nm. However, regions of layered planes appear occasionally throughout the bulk phase, defining a small degree of short-range order. These observations are consistent for submicron carbon spheres at all studied synthesis temperatures.

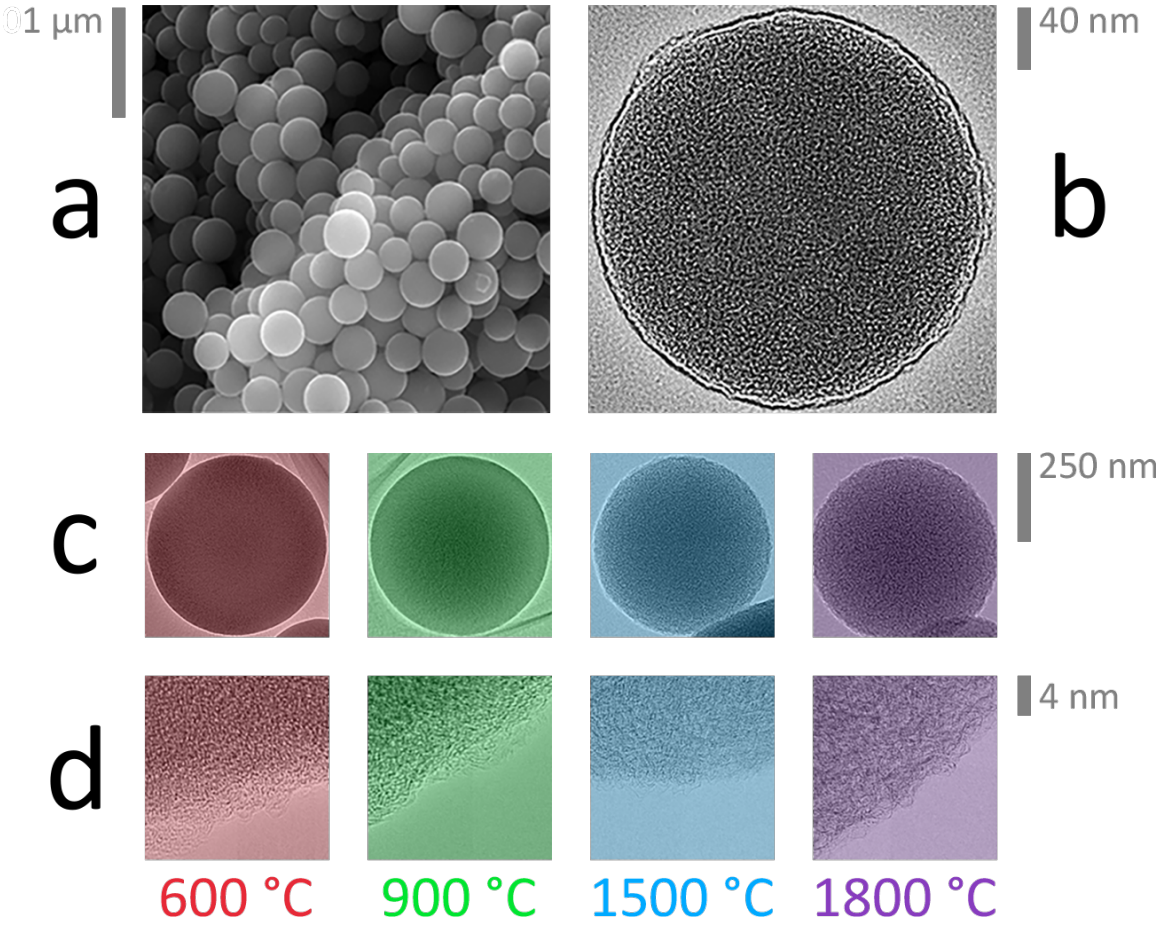

Figure 8.2. *Electron micrographs of submicron carbon spheres.* Across all pyrolysis temperatures, submicron carbon spheres are uniform in particle size, dispersity, and sphericity. (a) Scanning electron and (b) transmission electron micrographs show resolute particles with diameter ca. 50 μm. Transmission electron micrographs also show great phase disorder in both (c) bulk and (d) surface regions irrespective of synthesis temperature.

Carbon content of SCSs increases with synthesis temperature. Organic elemental analysis (Fig. 8.3) measures the composition of primary elements: carbon, hydrogen, nitrogen, and oxygen. These four elements originate from the sonolytic polymer precursor. As synthesis temperature increases, elemental percentage of carbon approaches unity, while those of heteroatoms (i.e., hydrogen, nitrogen, and oxygen) approach zero. These trends are directly due to micro-scale thermodynamics: heteroatoms disproportionate only when sufficient energy is supplied to overcome energy or diffusion-related activation barriers. Greater applied heat enables greater local disproportion of heteroatom-rich regions into vapors (e.g., H_2O, N_2, NO_2, and CO_2) and volatile species (e.g., CH_4) that are transported away by the surrounding inert gas stream [131, 153, 228–230].

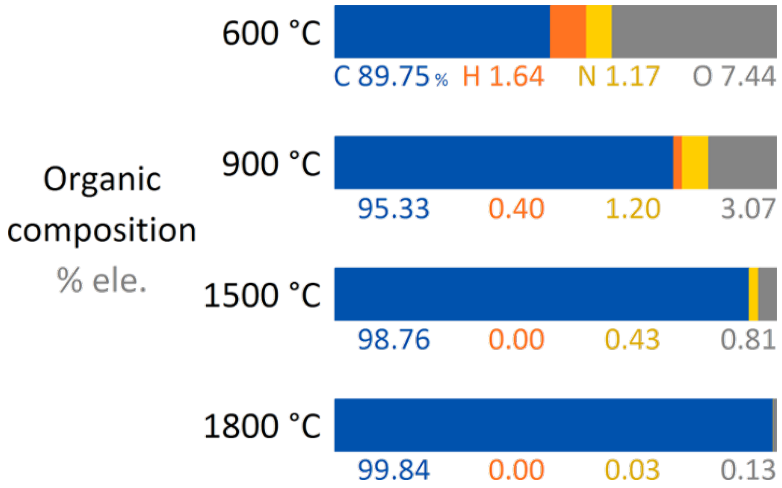

Figure 8.3. *Organic composition of submicron carbon spheres.* As pyrolysis temperature increases, carbon content increases at the expense of nitrogen, hydrogen, and oxygen content. Oxygen content is determined by difference of the measured carbon, hydrogen, and nitrogen content from unity.

The crystallinity of SCSs is directly proportional to synthesis temperature. Diffraction patterns of submicron carbon spheres (Fig. 8.4a) demonstrate irregular background with three principle intensity bands in scattering range (viz., 2θ) 10 - 100 °. The first intensity band in the scattering range of 15 - 35 ° corresponds to principle

reflection of the 002 carbon lattice facet (L_a), the mean diameter of the ordered carbon plane [72, 231, 232]. The corresponding scattering angle at maximum diffraction intensity represents interlayer separation of adjacent aromatic planes (d_{002}); that is, the effective spatial separation between constituent graphitic sheets. The second intensity band in scattering range 40 - 50 ° corresponds to principle reflection of the 10 facet (L_c), the characteristic length within the crystallite perpendicular to ordered carbon planes. The third intensity band in scattering range 70 - 90 ° corresponds to principle reflection of the 11 facet, a second in-plane characteristic length [233]. As synthesis temperature increases, background intensity decreases. Additionally, each band becomes more Gaussian with increasing synthesis temperature; that is, bands become more discernable and defined with decreasing breadth [223] (viz., full width at half maximum).

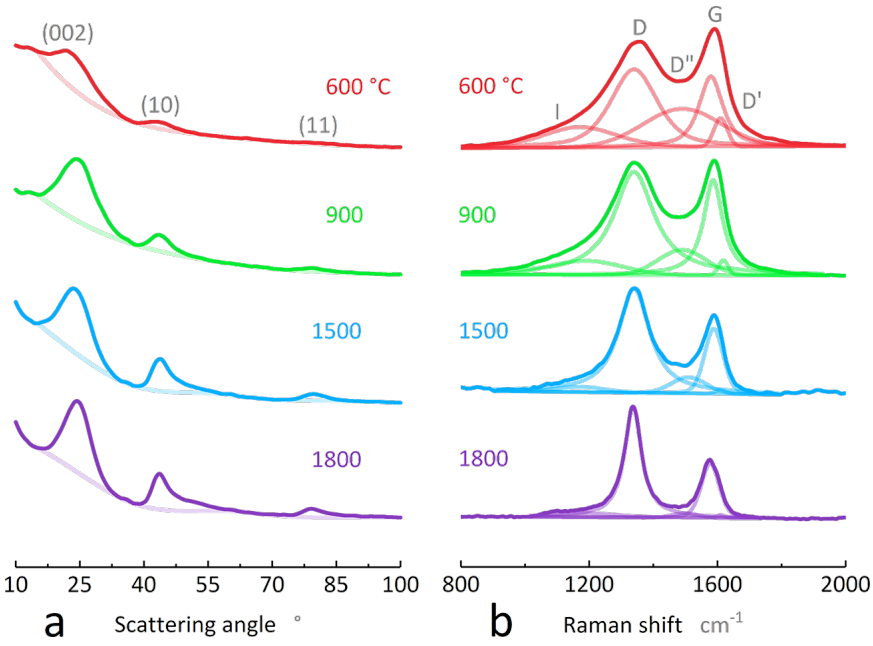

Figure 8.4. *X-ray diffraction and Raman spectroscopy of submicron carbon spheres.* Phase crystallinity increases as synthesis temperature increases. (a) All diffraction features become sharper and more intense with increasing synthesis temperature. (b) The I, D", and D' Raman features become less intense with increasing synthesis temperature.

The X-ray diffraction features of SCSs are due to incoherent scattering from short range order in the form of graphitic nano-crystallites, isolated regions of stacked carbon planes. Crystallites are defined by four parameters: height, diameter, interlayer separation, and number of constituent layers (Fig. 48.5a). The effective crystallite diameter and height, estimated using the Scherrer equation [223], increase with increasing synthesis temperature (Fig. 8.5b). This trend is inversely linear, suggesting crystallite height grows faster than diameter at low synthesis temperature (viz., below ca. 900 °C) but diameter grows faster than height at greater temperature (viz., below ca. 1500 °C). The interlayer separation, estimated using the Bragg equation [234], decreases with increasing synthesis temperature and crystallite size (Fig. 8.5c). The trend is weakly linear with crystallite diameter, showing a stable value of 0.371 nm between synthesis temperatures 900 and 1500 °C. The determined interlayer separation for all synthesis temperatures is greater than 0.335 nm, the theoretical separation in ordered graphite [235], which implies interlayer separation approaches this limit as crystallinity increases. Finally, the number of crystallite layers increases with synthesis temperature or crystallite size (Fig. 8.5d). The trend follows the same inverse linear shape of crystallite diameter relative to crystallite height.

The disorder of SCSs is directly proportional to synthesis temperature. Submicron carbon spheres demonstrate convoluted Raman spectra in the wavenumber range 800 - 2000 cm^1 (Fig. 8.4b). Each spectrum is comprised of 5 independent excitation bands [184, 223, 236, 237]: I (wavenumber ca. 1180cm^{-1}), D (1330), D' (1500), G (1580), and D" (1580). The G band is due to symmetric excitations from the ordered carbon phase, specifically the in-plane bond vibrations between sp2 hybridized carbons [185]. The D, D', D" and I bands are due to asymmetric excitations from the disordered carbon phase, particularly carbon vibrations at crystallite boundaries and sp^3 hybridized carbon bonds [185]. The I band encloses the T band, a less intense vibration characteristic of bonds containing nitrogen [238]. As synthesis temperature increases, the areal intensity of the primary excitation bands (viz., G and D) decrease.

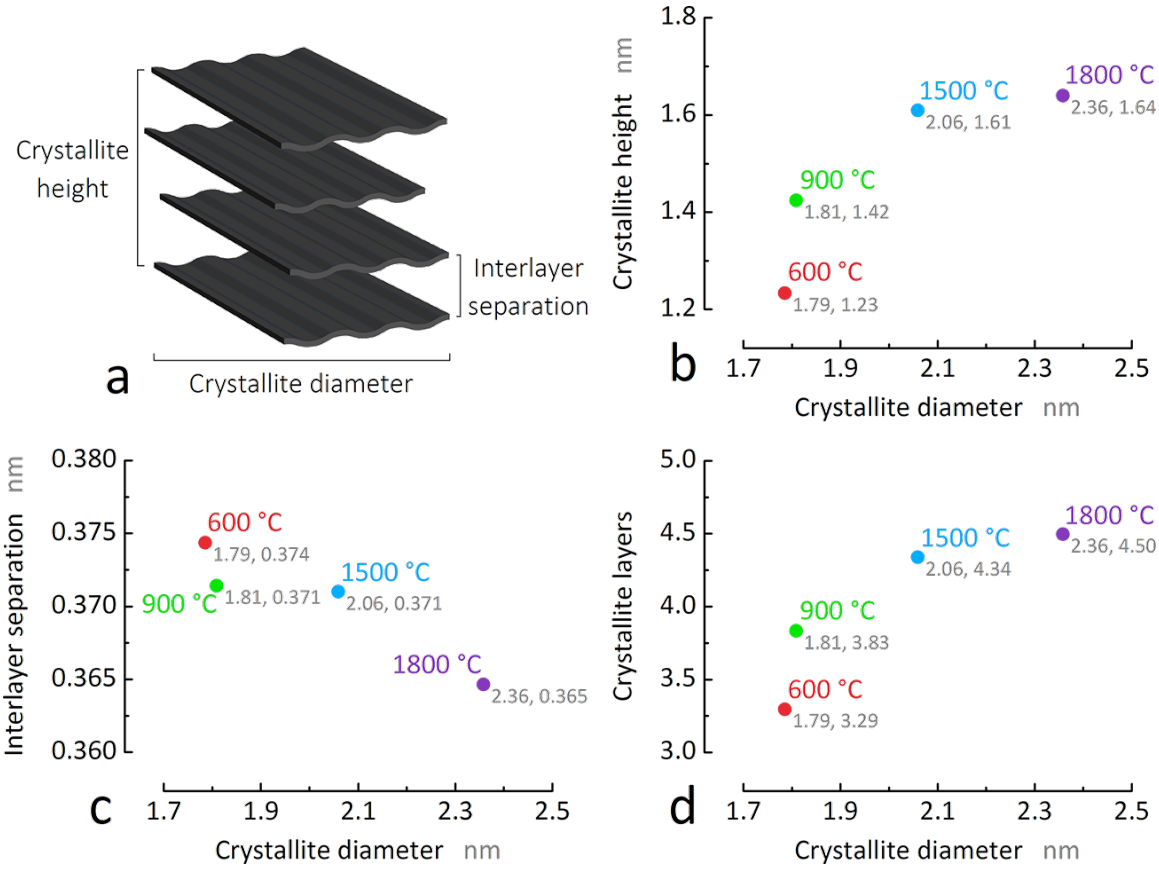

Figure 8.5. *Crystallite features of submicron carbon spheres.* Submicron carbon spheres grow more crystalline with pyrolysis temperature. (a) Graphitic nano-crystallites are defined by three dimensions: height, diameter, and interlayer separation. As synthesis temperature increases, (b) spacing between carbon layers decreases, (c) crystallite volume increases, and (d) effective number of constituent layers increases.

Similarly, the areal intensity of the secondary excitation bands (viz., D', D", and I) diminish to zero.

The Raman spectral features of SCSs are due to relative distributions of symmetric bonds (viz., between sp^2 carbons) and asymmetric bonds. This is quantified by areal intensity ratio of the D and G bands, the primary excitations of the disordered and ordered phases. Areal intensity ratio for SCSs increases as synthesis tempera-

ture or crystallite size increases (Fig. 8.6). This trend is weakly linear and results from the specific size regime of carbon crystallites: below critical length ca. 5 nm, asymmetric vibrations (from carbons at the crystallite boundary and bonds in the disordered phase) dominate symmetric ones (from smaller crystallite volumes relative to crystallite perimeter) [184, 223, 237]. Therefore, disorder is considerably more dominant in SCSs with greater synthesis temperature.

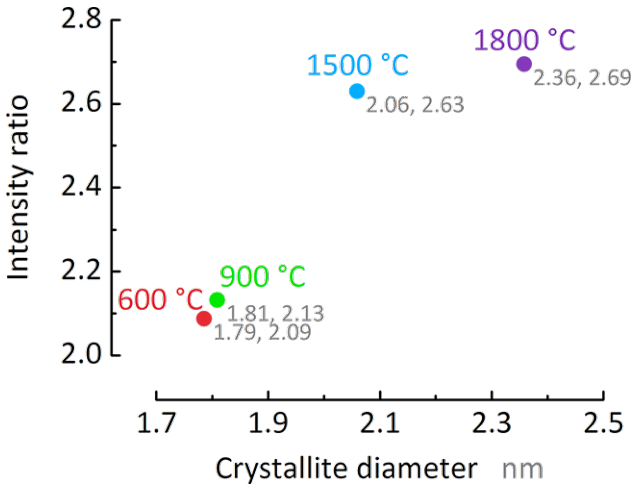

Figure 8.6. *Raman intensity ratio of submicron carbon spheres.* The D–G intensity ratio increases as synthesis temperature increases. With increasing crystallite diameter, asymmetric vibrations from disordered carbon increases relative to symmetric ones from sp^2 hybridized carbon.

Pore size distribution and specific surface area of SCSs are non-monotonic and non-linear with synthesis temperature (Fig. 8.7). These textural properties are determined from isothermal nitrogen adsorption and desorption. All isotherms measured from submicron carbon spheres belong to the Type II class (Fig. S2a) identified by: (1) pore distributions dominated by a single modal length [77] and (2) rapid adsorption and desorption as relative pressure approaches both unity and zero, respectively. From the BET equation [77], maximum specific surface area occurs with synthesis temperature 900 °C, and minimum value with 1800 °C. From simulation using non-linear density functional theory, maximum modal pore radius occurs with

synthesis temperature 1500 °C, and minimum value with 600 °C (Fig. 8.8). These observations suggest non-linear correlation between modal pore size and surface area which depends on crystallite formation. The amorphous carbon phase dominates, with increasing surface area and widening pores, as synthesis temperature increases up to ca. 900 °C. Conversely, the ordered carbon phase dominates, with decreasing surface area and contracting pores, as synthesis temperature increases above ca. 1500 °C.

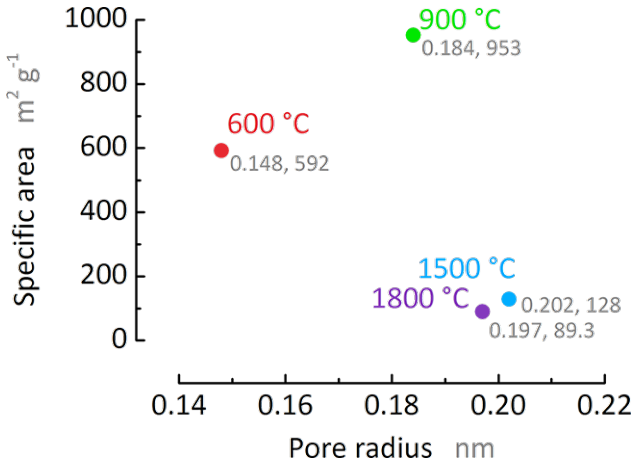

Figure 8.7. *Specific surface area and porosity of submicron carbon spheres.* Gravimetric surface area and modal pore radius are non-linearly related. Maximum gravimetric surface area is measured at synthesis temperature 900 °C. The maximum modal pore radius is observed at synthesis temperature 1500 °C.

Overall, observed SCS material properties are largely dependent on synthesis temperature. As synthesis temperature increases, carbon content increases while heteroatom content decreases because of increasing local disproportionation. Diameter, height, and constituent carbon layers of nano-crystallites increase while interlayer separation decreases due to greater extent of thermal realignment. Disorder increases with synthesis temperature due to waning significance of nano-crystallite volume relative to perimeter. Finally, pore radius and specific surface area are sensitive to synthesis temperature, influencing the extent of pore formation during pyrolysis. In

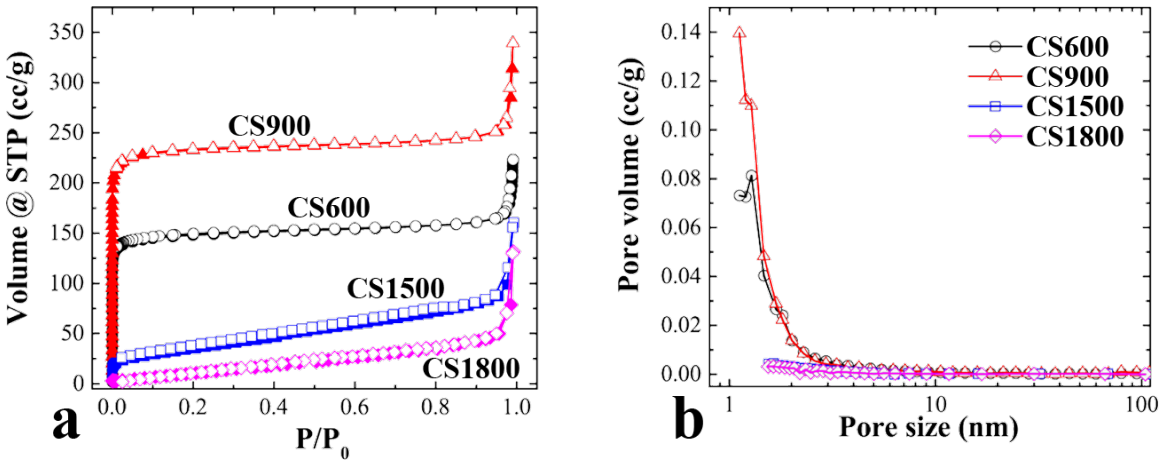

Figure 8.8. *Nitrogen sorption isotherms and simulated porosity distribution for submicron carbon spheres.* (a) Total adsorbate volume at relative pressure 1.0 decreases as synthesis temperature increases. (b) Similarly, pore radius distributions become less intense as synthesis temperature increases.

contrast to prior characterization, the morphology of submicron carbon spheres remains highly spherical and mono-disperse across the studied synthesis temperatures.

Electrochemical performance of SCSs

Much like their material properties, submicron carbon spheres demonstrate electrochemical performance with strong thermal dependence — here, both on synthesis temperature and ambient cycling temperature. Galvanostatic behavior of amorphous carbons is classified into two regimes: formation cycles (ca. 1 - 5), in which passivation phenomena dominate capacity measurements; and post-formation cycles, in which passivation rates diminish. Within both regimes, gravimetric capacity and Coulombic efficiency are functions of synthesis temperature. However, greater ambient temperature causes more turbulent and less stable changes in gravimetric capacity and Coulombic efficiency. Additionally, reversible charge storage decreases after a critical cycle between cycles 30 - 50. These trends, described using direct and differ-

ential capacity analysis, are related to material character prior to and during battery cycling.

During formation cycles, gravimetric capacity decreases while Coulombic efficiency increases at both 27 and 50 °C ambient temperature. At each cycle, synthesis temperature directly correlates to gravimetric discharge capacity (Figs. 8.9b and 8.10d) and inverse to Coulombic efficiency (Figs. 8.9a and 8.9c). In cycle 1, all synthesis temperatures demonstrate greatest gravimetric capacity and lowest Coulombic efficiency. Approaching cycle 5 at each synthesis temperature, gravimetric capacity and Coulombic efficiency decelerate to lower and greater values, respectively. These observations are consistent for the formation cycles at both 27 and 50 °C ambient temperature. An exception occurs between synthesis temperatures 600 and 900 °C: cycle 1 Coulombic efficiency is lower at 27 °C, and cycle 3 - 5 gravimetric capacity is greater at 50 °C because of enhanced lithiation kinetics.

After cycle 5 at elevated cycling temperature, capacity and Coulombic efficiency changes are more drastic. For each cycle at 27 °C, synthesis temperature directly correlates with gravimetric capacity (Fig. 8.10c) and inverse to Coulombic efficiency (Fig. 8.10a). In fact, gravimetric capacity and Coulombic efficiency continue deceleration throughout cycles 1 - 50. At 50 °C, however, this behavior grows erratic: the magnitude of change explicitly depends on synthesis temperature. Coulombic efficiency at 600 and 900 °C synthesis temperature in cycles 5 - 50 is less stable than in cycles 1 - 5. Conversely, Coulombic efficiency is more stable with 1500 and 1800 °C synthesis temperature – though stabilizing at ca. 95%, a lower efficiency than observed at room temperature. Similarly, gravimetric capacity at high temperature decreases with 600 and 900 °C synthesis temperature but increases with 1500 and 1800 °C. The direction of absolute capacity is conserved, but the magnitude of its change at 50 °C is greater than that at 27 °C. At high temperature, all materials experience failure between cycles ca. 30 - 50, attributed to enhanced dendrite phenomena.

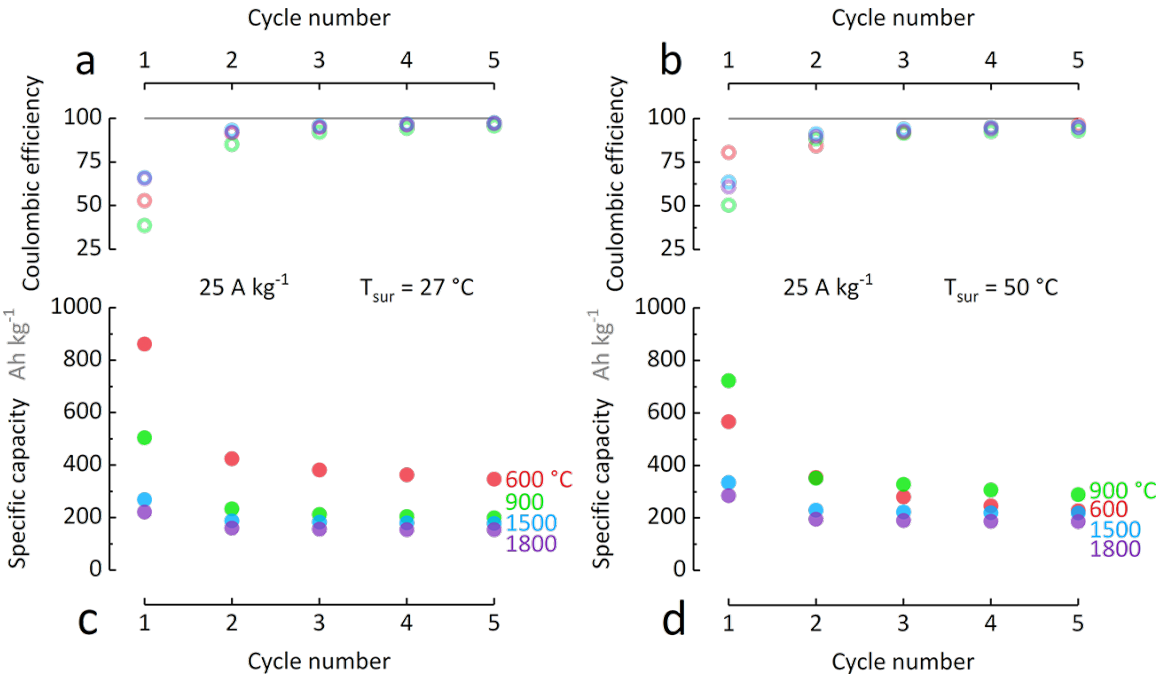

Figure 8.9. *Formation cycles of submicron carbon spheres at 27 and 50 ° C.* By cycle 5, formation phenomena negligibly influence electrochemical performance across all synthesis temperatures. At (c) 27 and (d) 50 ° C, gravimetric discharge capacity decreases from cycle 1 - 5. At (a) 27 and (b) 50 ° C, Coulombic efficiency approaches unity between cycle 1 - 5.

These temperature–dependent trends are conserved in differential chronopotentiograms for submicron carbon spheres (Fig. 8.11). Each potentiogram contains three overlapping capacity contributions. Two reversible discharge contributions result from lithium storage by capacitance or adsorption (viz., diffuse and shallow band between ca. 0.0 - 2.0 V) and intercalation (viz., sharp band between ca. 0.0 - 0.3 V); analogous charge contributions result from lithium release by desorption and deintercalation, respectively. In both processes, a third irreversible contribution results from electrolyte breakdown (viz., diffuse band between ca. 0.0 - 1.4 V), forming a solid electrolyte interphase (SEI) at the electrolyte-electrode interface. By cycle 30, artificial SEI capacity is no longer observed as chronopotentiogram inflections weaken or

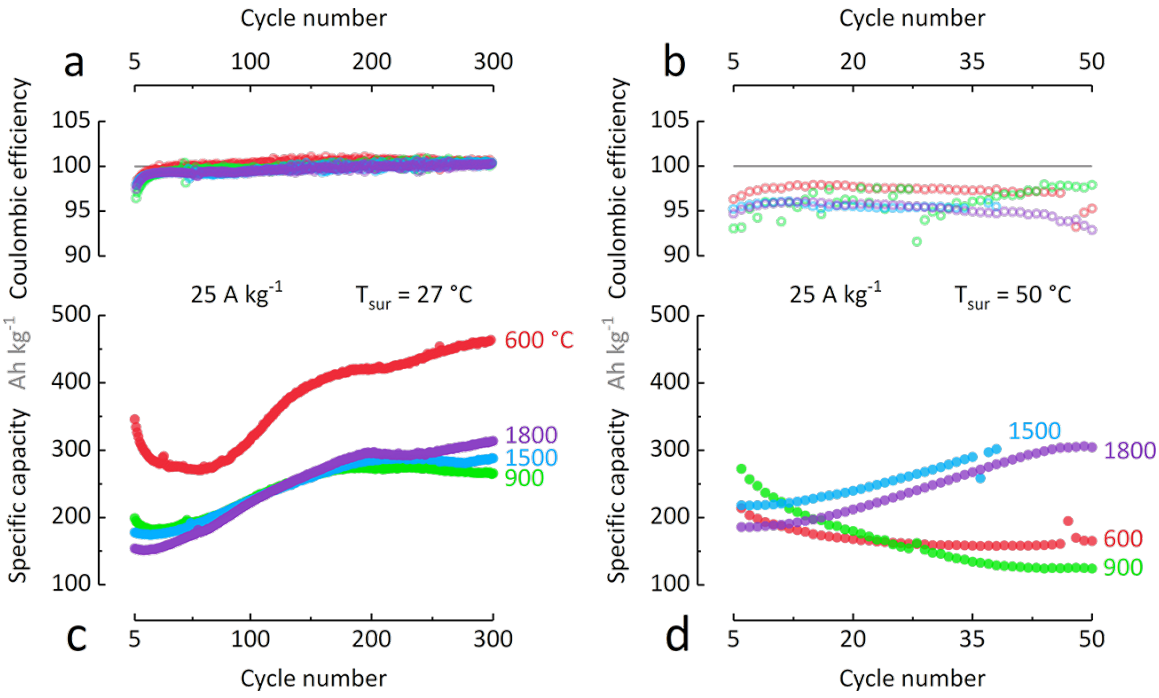

Figure 8.10. *Extended galvanostatic cycling of carbon spheres at 27 and 50 °C.* Between cycles 5 – 30, discharge capacity change is positive for high synthesis temperatures while it is negative for low synthesis temperatures. Capacity changes are negligible at (b) 27 °C but are significant at (d) 50 °C. Coulombic efficiency approaches unity for all materials at (a) 27 °C and is more stable with higher synthesis temperature at (c) 27 °C.

altogether disappear. For cycle 30 at 50 °C, the capacity attributed to lithium storage and release is proportional to synthesis temperature (Fig. 8.11d). For both cycle 1 and 30, charge-discharge hysteresis, as the disparity between charge and discharge chronopotentiograms, is inverse to synthesis temperature. At room temperature, all materials show rapid capacity increase between cycles ca. 30 - 300 (Fig. 8.10c). In fact, the gravimetric capacity of each material increases radically: in the case of synthesis at 600 °C, resulting capacity increases up to 58% corresponding to maximum value 463.6 Ah kg^{-1}. This drastic capacity rise is attributed to gradual morphological changes within the material due to applied overpotential at 3.0 V.

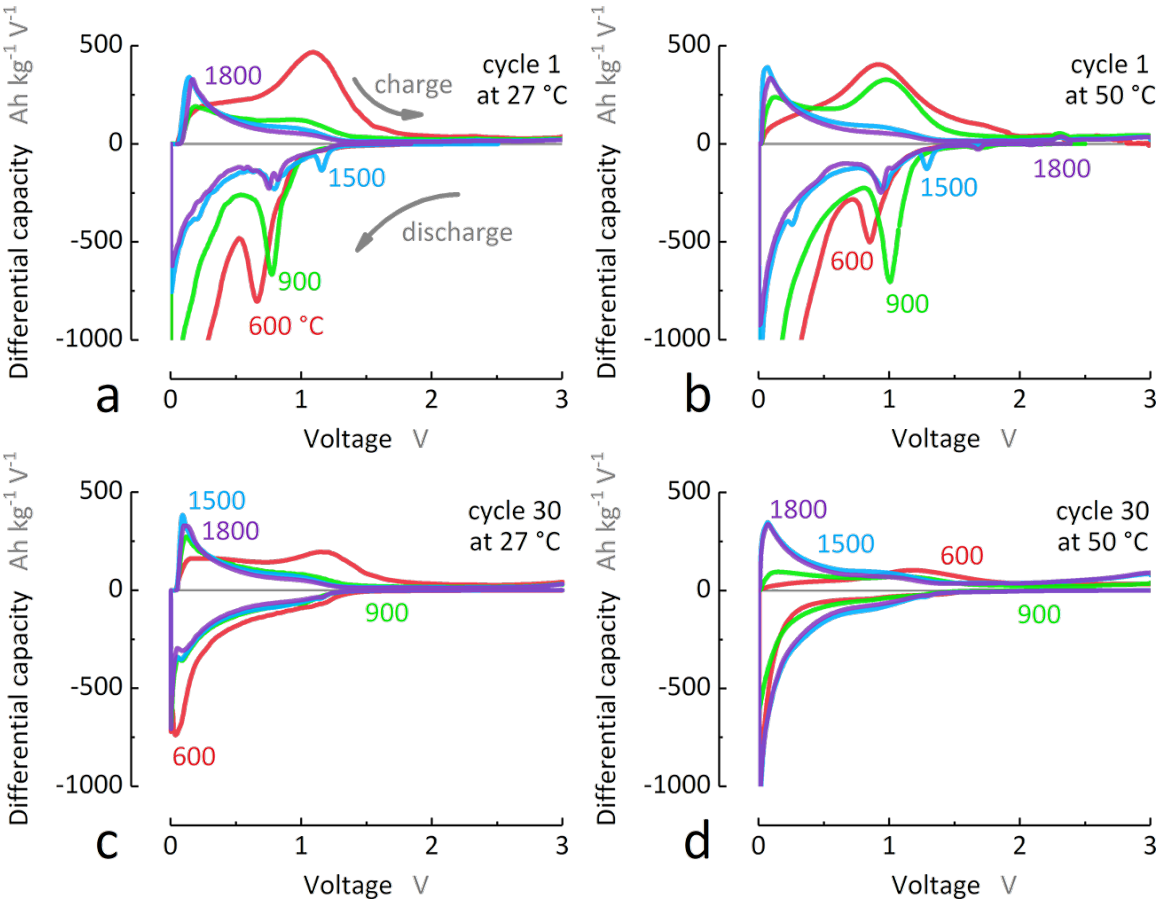

Figure 8.11. *Differential chonopotentiograms of submicron carbon spheres at 27 and 50 °C.* Differential capacity analysis shows charge and discharge features are proportional to synthesis temperature. During cycle 1 at both (a) 27 and (c) 50 °C, the charging features at ca. 1 and 0.1 V are proportional to synthesis temperature, while the discharge feature at 0 V is inversely correlated to synthesis temperature. During cycle 30 at (b) 27 and (d) 50 °C, these trends are conserved with lower intensity.

Generally, capacity evolution of SCSs follows a similar trend: capacity decreases during formation cycles, then steadily increases to greater value after ca. cycle 100. At either 27 or 50 °C ambient temperature, low synthesis temperature SCSs (i.e., 600 and 900 °C) evolve capacity differently from high temperature SCSs (i.e., 1500 and 1800 °C). Differences in capacity evolution suggest morphological change dur-

ing cycling is a function of synthesis temperature (Fig. 8.12). When modeled as an ideal Randles impedance element, the high frequency arc exhibits a characteristic frequency inversely proportional to interfacial capacitance. In discharge at voltage 0.01 V, the characteristic frequency represents extent of lithium storage through adsorption (though, not adequately quantifiable due to non-ideal capacitive behavior and staged Faradaic intercalation mechanisms). At cycle 30, the greatest characteristic frequency is shown by the 1500 °C synthesized material, while the lowest is shown by its 900 °C counterpart. In addition, the materials with synthesis temperature 600 and 1800 °C show increasing characteristic frequency, while the materials with synthesis temperature 1500 and 900 °C show stable or decreasing characteristic frequency. Decreasing characteristic frequency illustrates increasing capacitive behavior, suggesting continual diffusion of lithium-ions through the bulk phase improves lithium intercalation site accessibility in crystallites. Accessibility can be increased by expansion of the crystallite spacing by lithium-ion insertion, enabling the central interaction sites to become accessible; or "tunneling" through the disordered phase. The larger crystallite size of the 1800 and 1500 °C synthesized SCSs are seen to be ineffectively accessible, as indicated by the low capacity in cycle 1 - 5 (Fig. 8.9b). By cycle 30 at high temperature, however, the capacity increases past those of the 900 and 600 °C synthesized SCSs. This behavior is best observed at high temperatures, due to the lowered energy barriers enabled by heat transfer into the cell; though, the trends still apply at room temperature.

Correlation between Material and Electrochemical Properties

Material character is the critical link between synthesis temperature and electrochemical performance. In unique combination, material properties govern salient aspects of electrochemical behavior: overall capacity, Coulombic efficiency, chronopotentiogram shape and hysteresis, and extended capacity stability. While some tends correlate well to a single material property, others are not so well defined; electrochemical performance likely results from delicate interplay of several dimensions.

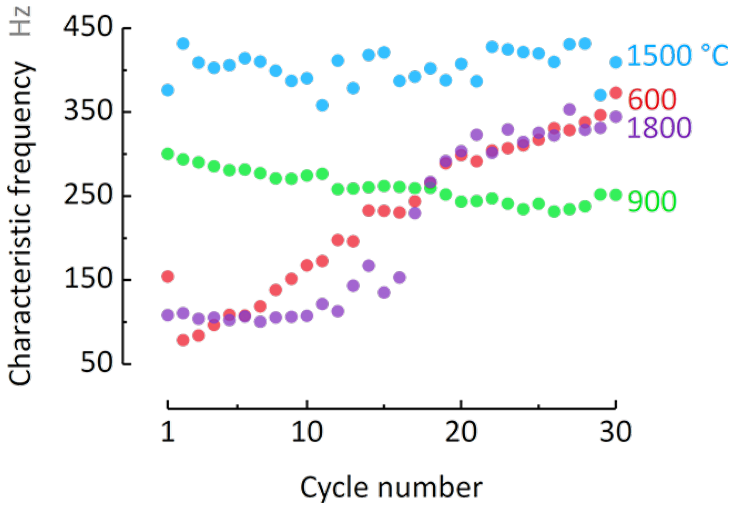

Figure 8.12. *Characteristic frequency of submicron carbon spheres.* Characteristic frequency, inverse to effective capacitance, evolves with synthesis temperature at 0.01 V. Materials with synthesis temperature 600 and 1800 °C show increasing characteristic frequency, while the materials with synthesis temperature 1500 and 900 °C show stable or decreasing characteristic frequency.

Hysteresis and charge behavior are related to elemental composition resulting from synthesis temperature. Lithium intercalation and de-intercalation depend upon the quality of the carbon phase: both occur through staged mechanisms near 0.1 V in pyrolytic graphite, but can occur at several voltages in low purity carbons. Dahn et al. have shown that potential barrier ca. 1.5 V appears during lithium de-intercalation because of greater activation barriers from terminal hydrogen [203, 208, 239, 240]. In this work, SCSs synthesized at low temperature yield greater heteroatom content, while those at high temperature yield less (Fig. 8.3). The 600 °C material contains greatest hydrogen, directly correlating to the differential capacity band magnitude in all charge steps (Fig. 8.11). In contrast, the 900 °C material shows less hydrogen; this justifies the appropriately-sized capacity bands (Fig. 8.11a, b) observed at 50 °C ambient temperature. The 1500 and 1800 °C materials do not contain appreciable hydrogen, permitting de-intercalation near 0.1 V (Fig. 8.11).

In both direct and differential chronopotentiograms, the size of capacity bands quantify intercalative or capacitive behavior (Fig. 8.11); this correlates to crystallinity and synthesis temperature (Fig. 8.5). At low synthesis temperature 600 °C, the primary capacity band occurs near 1.0 V (Fig. 8.11a, b). At high synthesis temperatures 1500 and 1800 °C, the primary capacity band occurs near 0.0 V. With moderate synthesis temperature 900 °C by cycle 30, the capacity band near 0.0 V is dominant at 27 °C cycling temperature (Fig. 8.11a, b), while both capacity bands at 0.1 and 1.0 V are similar at 50 °C cycling temperature (Fig. 8.11c, d). This trend correlates well with increasing crystallite size (i.e., number of crystallite layers, crystallite height, and crystallite diameter).

Trends in coulombic efficiency relate to textural properties. During formation cycles, low coulombic efficiency is attributed to SEI formation (Fig. 8.9a, c), in which electron transfer between thermodynamically unstable GICs and surrounding electrolyte causes electrolyte breakdown [241]. After initial cycling, the SEI stabilizes as its effective thickness impedes electron transfer by diffusion. The formation cycles exhibit low Coulombic efficiency because the implied reactions involve irreversible lithium consumption, rendering participating charges inactive in subsequent cycles. Assuming constant effective thickness, the extent of SEI increases with increasing electrode-electrolyte interfacial area. The order of increasing cycle 1 Coulombic efficiency (Fig. 8.9a) correlates well to the order of decreasing specific surface area (Fig. 8.7). An inconsistency in the cycle 1 Coulombic efficiency for the 900 °C material suggests influence from additional factors, particularly porosity.

Overall, material character summarizes the electrochemical behavior of SCSs synthesized up to 1800 °C (Fig. 8.13). The observed evolution in gravimetric capacity is subject to crystalline parameters and available sites for lithium storage via intercalation or surface storage in micro-pores. Furthermore, the prevalence of heteroatoms increases the observed gravimetric capacity – though only artificially, as observed from increased voltage-capacity hysteresis. In summary, specific capacity correlates with synthesis temperature, though this is not its only dependence. Electrochemical

performance is a complex function of intercalation sites (i.e., available crystallites) and interfacial surface sites (i.e., micropore area) available to incoming lithium species and SEI formation.

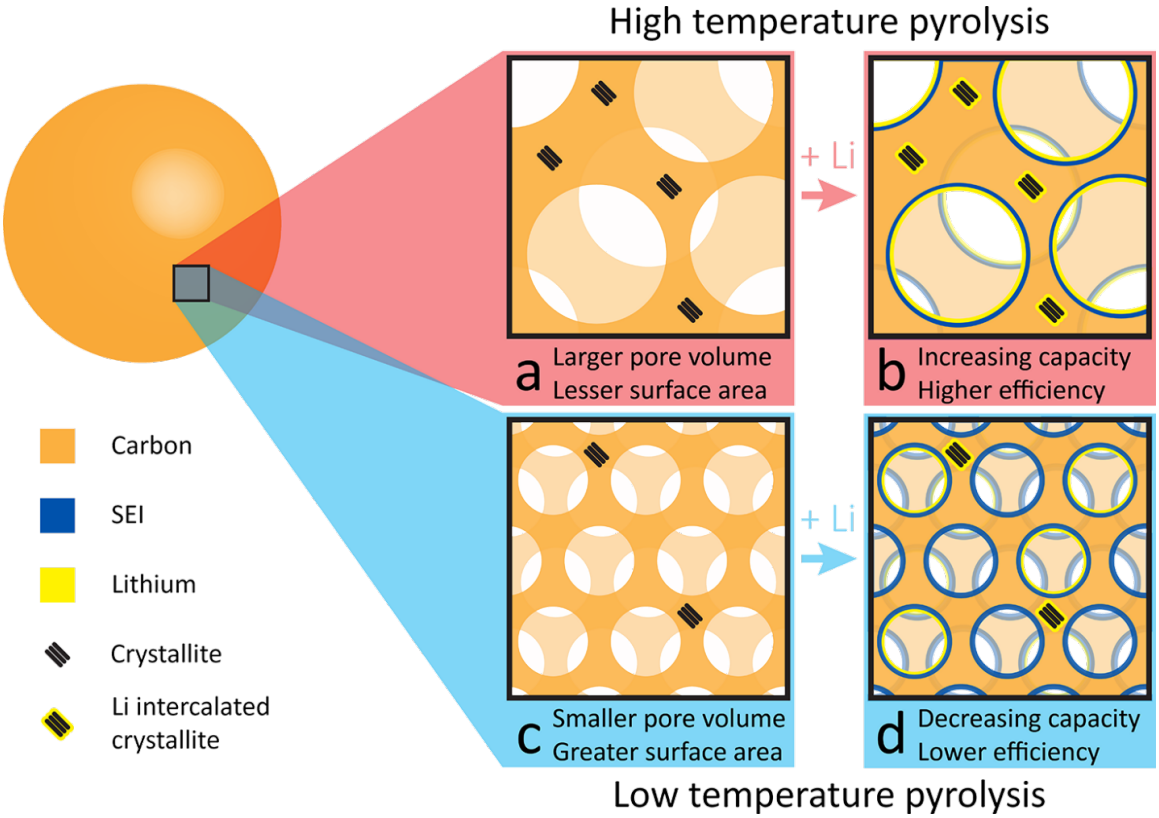

Figure 8.13. *Model of lithium storage in submicron carbon spheres.* Due to material differences, electrochemical storage of lithium is more prominent in high temperature materials and improves with cycling due to microscale restructuring. At high synthesis temperatures, SCSs feature larger pores, lower specific surface area, larger crystallites, and higher disorder. At low synthesis temperatures, SCSs feature smaller pores, lower specific surface area, smaller crystallites, and lower disorder.

8.3 Submicron Carbon Spheres as Battery Anodes

Due to appealing applications of synthetic carbons for lithium-ion batteries, understanding their electrochemical behavior is critical. Submicron carbon spheres, synthesized under varying pyrolysis temperatures with all other parameters held constant, show electrochemical performance representative of various synthetic carbons in high voltage galvanostatic applications. Disordered carbons are found to be sensitive to electrochemically-induced morphology change as a result of synthesis temperature and ambient cycling temperature. These morphology changes result from material properties of SCSs in their initial state. It was found that increasing synthesis temperature up to 1800 °C results in larger crystallite volume, greater number of constituent layers, and lower interlayer spacing; greater phase disorder; greater carbon content, and lower heteroatom content. These quantitative findings were summarized to qualify the influence of pyrolysis temperature on electrochemical performance. Finally, in situ electrochemical impedance spectroscopy demonstrates a strong correlation between effective capacitance and gravimetric capacity of SCSs, suggesting the significance of capacitive mechanisms for lithium storage and release with synthetic carbons.

Acknowledgments

This work was supported by the Assistant Secretary for Energy Efficiency and Renewable Energy, Office of Vehicle Technologies of the U.S. Department of Energy under Contract No. DE-EE0006832 under the Advanced Battery Materials Research (BMR) Program. Prof. Vilas Pol would like to thank Purdue University and the School of Chemical Engineering for generous start-up funding. Arthur Dysart acknowledges Joseph Kubal for his rewarding discussion. The authors acknowledge Dr. Paul Brockman and Exceter Analytical, Inc. for assistance in performing organic elemental analysis experiments.

CHAPTER 9: LITHIUM METAL ANODE CHARACTERIZATION WITH SYNCHROTRON TOMOGRAPHY

Sulfur cathodes realize their maximum performance when combined with the lithium metal anode. The low lithiation potential and great gravimetric capacity of lithium metal gives rise to great cell energy; however, the technical and safety challenges arising from non–uniform surface plating limit commercial use. Research progress in lithium metal anodes is hindered by difficulties in lithium metal characterization. In this context, a combined experimental and digital X–ray micro–tomography technique has been developed for the Advanced Photon Source at Argonne National Laboratory. Using high energy polychromatic Synchrotron X–rays at the Advanced Photon Source, the designed experimental apparatus can collect in situ three-dimensional tomographic scans of lithium metal anodes; that is, without deconstruction of sample cells. While this exploratory work successfully demonstrates Synchrotron X–ray micro–tomography and model reconstruction of lithium metal anodes, preliminary results suggest the interactions among hard X–rays, lithium metal, and organic electrolytes should be critically evaluated to qualify accuracy for future in situ experiments.

Experimental design and apparatus drafting performed by Arthur D. Dysart, Pierre Yao, and William Chin. Synchrotron tomography experiments were performed by Arthur D. Dysart, Pierre Yao, Andrew Chuang, and John Okasinski. Digital image processing and manuscript preparation were performed by Arthur D. Dysart.

Abstract

Hard X–ray micro–tomography experiments illustrate dendritic lithium can be successfully imaged using unfiltered polychromatic Synchrotron radiation. In situ micro–tomography of the lithium interface in lithium sulfur electrolytes demonstrate stability of fluorinated 1,1,2,2-tetrafluoroethyl 2,2,3,3-tetrafluoropropyl ether (TTE) solvent at the lithium interface. En route, a new experimental apparatus and digital image processing method are applied to reconstruct three-dimensional models of tomography data. The applicability of Hard X–ray micro–tomography is dependent on electrolyte: high vapor pressure electrolytes demonstrate bubble evolution during tomographic scanning, suggesting absorptive or thermal interaction even far from the adsorption edge. Yet, hard X–ray micro–tomography seems to demonstrate great benefit to its soft X–ray counterpart for in situ imaging of the lithium metal–liquid electrolyte interface. Improvements in scanning rate should overcome thermal or absorption rates of X–ray energy to produce a truly inert technique.

9.1 Visualizing Lithium with Hard X rays

Next generation battery technologies promise greater energy density, longer lifetimes, and smaller form factors. For instance, the lithium sulfur battery asserts high specific capacity (1672 Ah kg^{-1}) and specific energy (2600 Wh kg^{-1}), values ca. 5 times those of commercial systems [50, 56]. Lithium metal anodes can realize this performance, but stability and safety issues must be explicitly addressed. These issues (Fig. 9.1) stem from the continual evolution of dendrites, long filament–shaped growths due to uneven lithium deposition [242–246]. Prolonged cycling of lithium metal anodes results in uneven distribution of dendrite formation across the electrode surface, introducing significant stability and safety issues to the metal–electrolyte interface [242–247]. Despite this, lithium metal is the leading anode candidate for lithium sulfur batteries. Continual evolution of dendrites results in electronically–isolated lithium and, in extreme cases, explosive internal shorting [8].

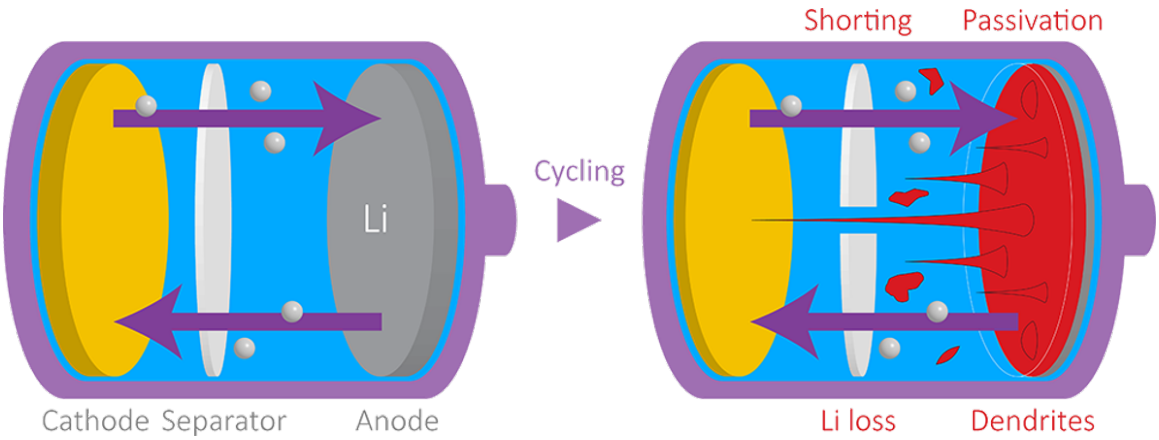

Figure 9.1. *Challenges of lithium metal anodes.* The challenges of lithium metal anodes include lithium deactivation or isolation and continuous surface passivation which cause severe stability and safety issues.

Despite the inherent dendrite issue, lithum metal is the leading anode candidate for lithium sulfur batteries. But, sparingly solvating electrolytes, the community encouraged approach to mitigate symptoms of the parasitic polysulfide shuttle, can control the composition, strength, and conductivity of passivating solid electrolyte interphases (SEI) in a viable and practical fashion. Ex situ characterization [248] shows that conventional glmye electrolytes with lithium nitrate [56] suppress dendrites by dampening lithium deposits into rounded dunes. However, this approach and others present challenges for long–range utilization: poor SEI stability, outgassing, and oxidation susceptibility comprise serious safety concerns [61,248]. This deficiency invites alternative approaches for high-performance electrolytes – particularly methods free of additives. In 2013, Weng et al. [89] demonstrated fluorinated ethers for controlled polysulfide–solubility in lithium sulfur batteries. Following this discovery, in and ex situ efforts [61] have shown that fluorinated solvents offer rigid lithium fluoride–rich SEI, low polysulfide solubility, and effective dendrite mitigation on the lithium metal surface.

In this context, this work employs in situ techniques to study how dendrite phenomena is suppressed in fluorinated electrolytes as a function of co–solvent and electrolyte properties. Unfortunately, lithium metal is difficult to study due to its high reactivity and low atomic mass, precluding conventional imaging techniques including electron microscopy [242, 247, 249]. In situ and operando imaging have greatly progressed understanding of dendrite phenomena, suggesting the inevitable subsurface formation depends on rate and SEI stability. However, in situ tomography studies appear rarely in the literature for lithium metal batteries, particularly those in liquid electrolytes. This is because lithium metal exhibits poor X–ray attenuation, in proportion to its small atomic number, suggesting difficulties with attenuation–based contrast imaging techniques. Recent work has shown that lithium dendrite growth can be tracked and imaged via X–ray tomography techniques based on phase contrast imaging [247, 249]. X–ray characterization techniques are generally considered non–destructive and feature high spatial resolution and great penetration.

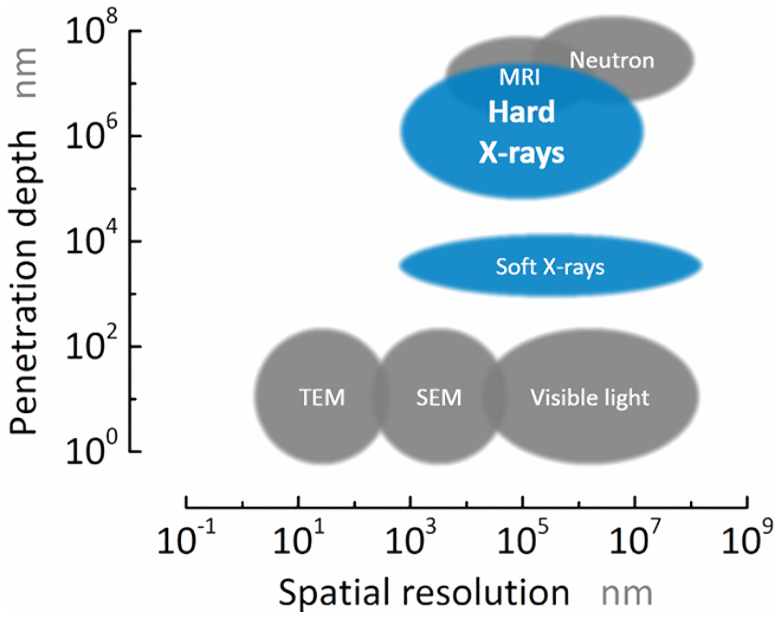

Figure 9.2. *Applications of X–rays and similar probes for small scale imaging.* Micro-tomography, using high–energy X–rays, features great spatial resolution and penetration depth compared to similar imaging techniques. Adapted from Glazer et al. [250]

Utilizing the cutting–edge facilities and broad expertise of Argonne National Laboratory, this work studies the growth of lithium metal dendrites in conventional glyme electrolyte using in situ Synchrotron micro–tomography. Low energy X–ray imaging in liquids and high energy X–ray imaging with solid electrolytes have been previously reported [242, 251], but this work is the first to combine high energy X–rays and liquid electrolytes. The results of this work demonstrate prolonged X–ray exposure can induce dendritic growth in glyme–based electrolytes. Using digital image processing techniques, tomographic reconstruction of the electrochemical cell produces 3D models of electrode structure during the in situ experiment [247]. En route, an in operando analytical tool for micro–tomography has been demonstrated, able to monitor structural and composition changes at the lithium electrode–glyme electrolyte interface. This work reveals the efficacy of X–ray tomography techniques to study lithium metal anodes: in situ techniques are capable of studying dendritic growth. Optimal scanning parameters enable phase contrast separation of deposited lithium phase during digital image processing, permitting non–destructive visual characterization of lithium dendrite growth.

Experimental Methods

Micro-tomography Battery Cell Preparation

A custom in situ cell was fabricated at the Advanced Photon Source Machine Shop. The custom cell is radially symmetric and consists of an electrochemical cell volume containing two custom stainless steel current collectors (High grade steel, McMaster–Carr) and isolating plastic body (Fig. 9.3). The custom cell body is constructed from high purity polyether ether ketone (PEEK, Mcmaster–Carr) with wall thickness 0.25 mm. The separation between steel–to–steel surfaces is 4.0 mm. Vitron torus-shaped gaskets are used to hermetically seal the stainless steel current leads.

Figure 9.3. *Custom cell for Synchrotron Micro–Tomography.* The custom cell features a symmetric active volume with PEEK walls that weakly interact with high energy X–rays. Chemically-inert sealing gaskets enable a hermetic seal to isolate the active volume.

Cell construction is performed in an inert atmosphere glovebox with less than 1.0 ppm oxygen and moisture. Lithium chips (MTI Corp) of diameter 2.0 mm are punched and adhered to the exposed steel current collector leads. The leads are inserted into the cell body and held shut with stainless steel screws. The electrochemical volume is flooded with electrolyte prior to hermetic closure.

Synchrotron X-ray Tomography Experiment

Traditional X–ray contrast imaging techniques identify phase boundaries using differences in attenuation or phase contrast [247]. X–ray attenuation is the reduction in X–ray strength due to absorption by the passing phase. It is measured as the change

in extinction coefficient, the imaginary component of material refractive index [247]. X–ray phase contrast techniques trace changes in X-ray wavelength during passage. Since X–ray attenuation is weaker in lithium metal than in most materials, phase contrast techniques are employed in conjunction or in place of attenuation imaging techniques.

In situ micro–tomography was performed at beamline 6–BM–A at the Advance Photon Source (APS), Argonne National Laboratory (ANL). Micro–tomographic scans were captured using polychromatic unfiltered Synchrotron X–rays (ca. 2 - 200 keV). The prepared in situ cell was secured onto 360 degree rotation programmable stage (Fig. 9.4). A proprietary command line interface was utilized to control rotation. The prepared cell was galvanostatically cycled using a MACCOR battery cycler at specific current 10 mA cm^{-2} for predetermined periods. For each tomography experiment, a set of ca. 1200 radiographs were collected at scan rate 0.5 ° min^{-1}. Filtered back projection (FBP) reconstruction techniques were used to create tomographic data sets.

Micro-tomographic 3D Model Reconstruction

Microtomography data sets were analyzed and processed into 3D models using digital image processing techniques 9.5 implemented in ImageJ [252] and custom python script. All tomographic slices were stabilized and contrast-corrected. Image segmentation was performed using classification machine learning algorithm. Tomographic models were created in the 3D slicer computer-assisted tomography software.

9.2 Computed Tomography of Lithium Metal Anodes

Custom Micro-Tomography Techniques at the Advanced Photon Source

Due to its weak X–ray interactions relative to most materials, lithium metal is difficult to observe in routine X–ray tomography experiments. The design of the custom battery cell addresses three principle concerns for in situ lithium characteri-

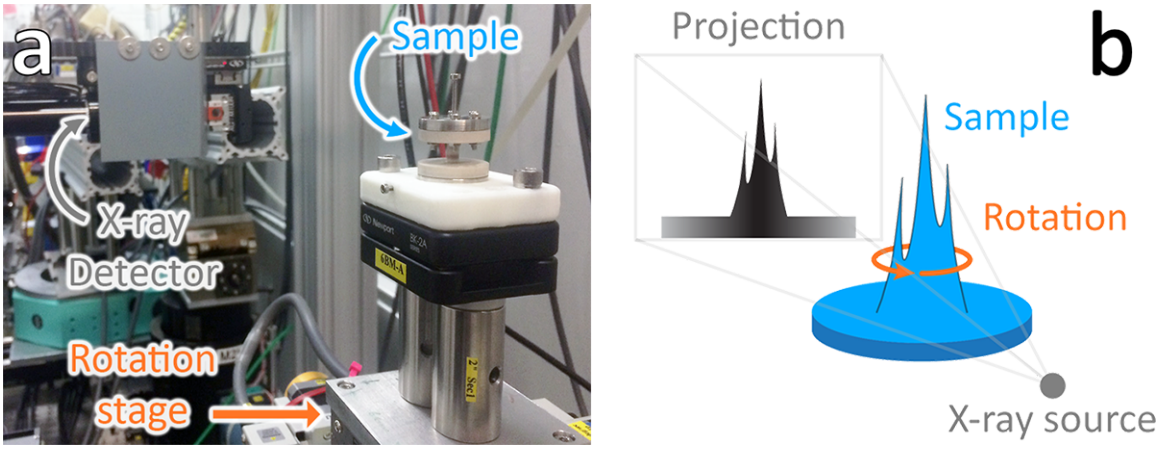

Figure 9.4. *Beamline setup for Synchrotron micro–tomography.* The experimental setup at Advanced Photon Source Beamline 6–BM–A features a rotating stage which securely holds the battery cell during 360 ° rotation. X–rays, focused onto the battery cell active volume, are attenuated as they pass through the battery cell active volume and are collected at the X-ray detector.

zation [247]: (1) experimental apparatus artifacts, (2) ambient air contamination, and (3) stray current pathways. To reduce tomography artifacts and enhance the signal–to–noise ratio of lithium metal electrodes, the custom cell walls were constructed from PEEK plastic with thickness ca. 0.25 mm. To prevent oxygen or moisture contamination, the custom cell was designed with hermetic gasket seals made using chemically-inert Vitron and industry-standard design specifications [253]. To prevent unintended current distribution, the custom cell was isolated from the rotating stage using a plastic securing base. The final battery cell design (Fig. 9.3) was fabricated to meet the specified design criteria, including compatibility with Advanced Photon Source Beamline 6–BM–A (Fig. 9.6). As the stage rotates, the custom insulating base translates rotation to the axial–symmetric custom cell. X–rays are collected at the X–ray detector after passing through the custom cell active volume.

Two-dimensional radiographs, collected from each tomography experiment, were digitally transformed into three-dimensional models using custom image processing

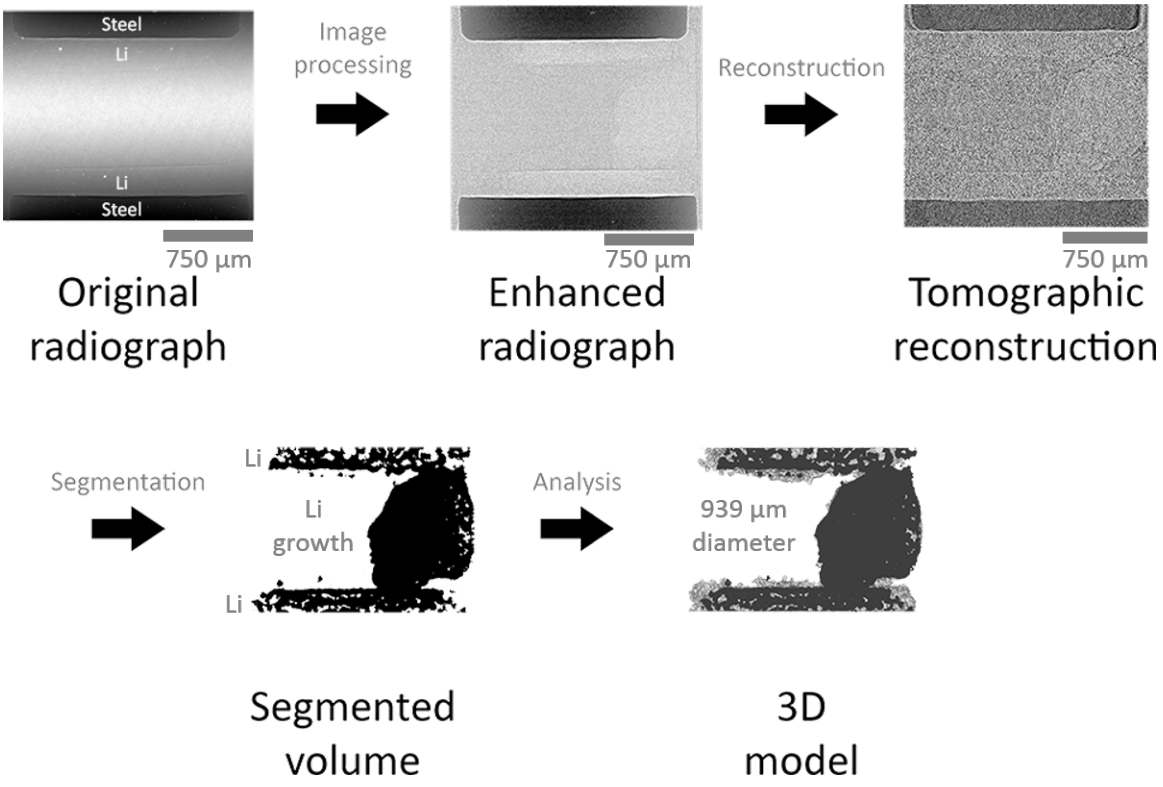

Figure 9.5. *Digital image processing method for lithium micro–tomography.* Radiographs, collected from tomography scanning, enhances feature contrast and reduces experimental noise. Reconstruction algorithms combine two–dimensional radiographs into a three–dimensional image. Image segmentation using machine learning algorithms identifies lithium features throughout the reconstruction. Finally, three–dimensional models are constructed from segmentation data.

procedure (Fig. 9.5). Each micro–tomography experiment produced a collection of radiographs representing phase contrast differences as a function of rotation angle. Several histogram and filtering techniques [252] were employed to reduce experimental artifacts and ehance signal–to–noise ratio. Processed radiographs were united into a single three–dimensional reconstruction using the Filtered Back Projection algorithm implemented in custom Python script [254]. Motivated by recent tomography progress in the biological and biomedical sciences [252,255–259], trained machine learning algo-

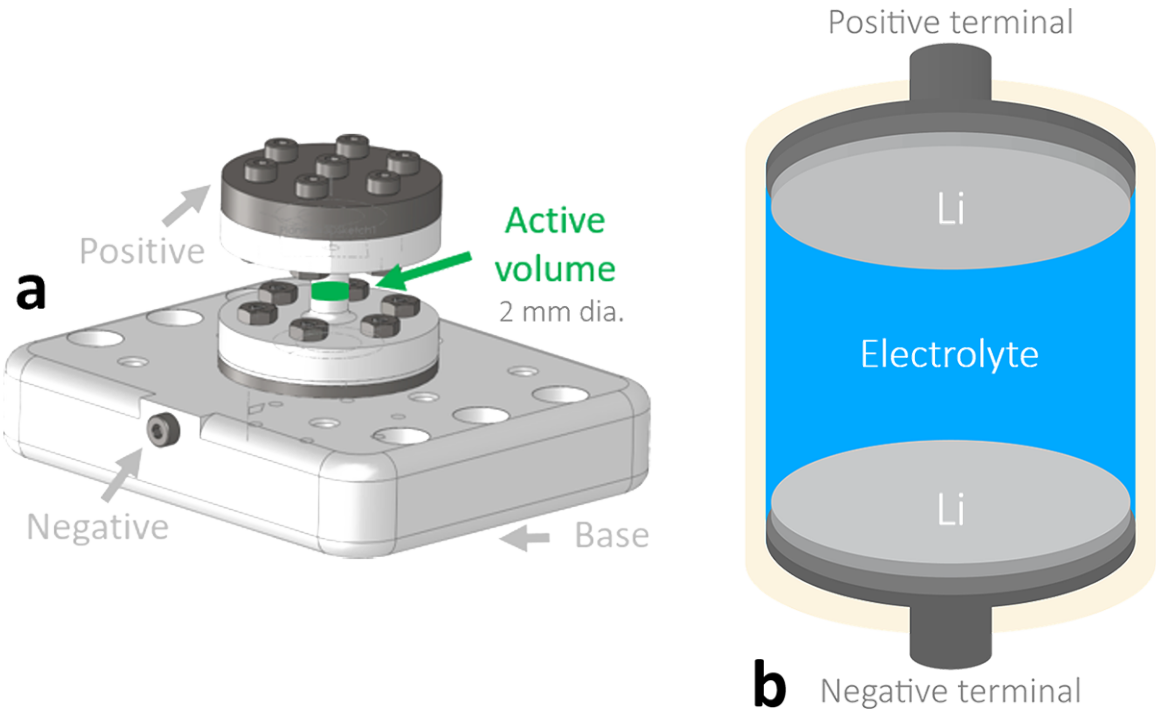

Figure 9.6. *Custom in situ battery cell for Synchrotron micro–tomography.* (a) The custom battery cell features two stainless steel leads which connect interior electrodes to the external battery cycler. The plastic base secures cell position during rotation. (b) The active volume of the custom battery cell has internal diameter 2.0 m.

rithms were used to identify and segment lithium features in the tomographic reconstruction. Segmented reconstructions were used to render three–dimensional models of the electrochemically active volume [254]. The developed procedure, encompassing noise reduction to model rendering, demonstrates significant reduction in noise compared to tomographic reconstruction alone 9.7.

Lithium Metal in Conventional Lithium Sulfur Electrolytes

In traditional glyme electrolytes, the symmetric lithium metal electrode couple demonstrates growth of a bulbous growth connecting lithium electrodes (Fig. 9.8). The appearance of this growth appears only after concentration depletion at the

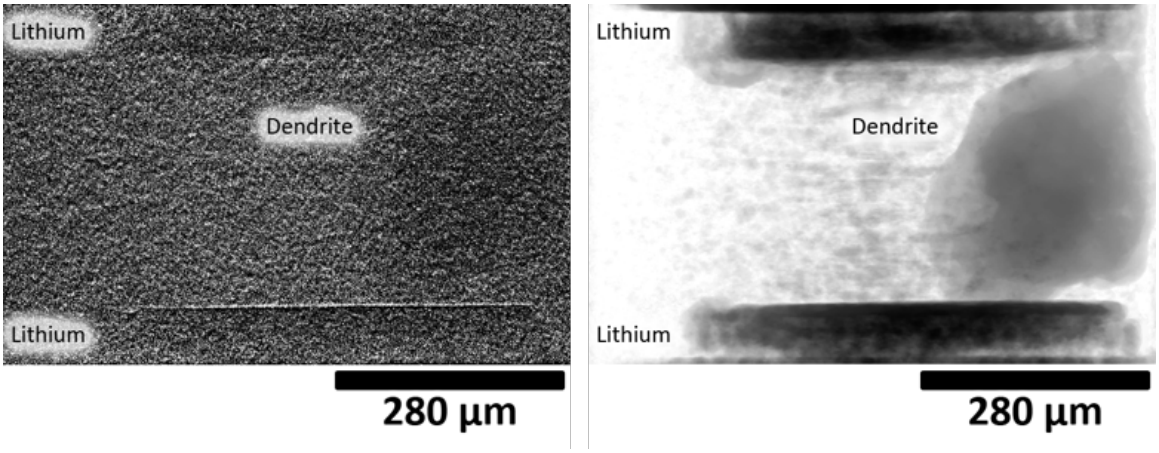

Figure 9.7. *Segmentation enhancement using digital image processing.* Compared to (a) reconstruction alone, segmentation of digital image enhancement produces images with (b) better clarity and contrast.

lithium metal surface, in turn, indicated by the rising overpotential at the lithium metal surface (Fig 9.8a). Interestingly, after current application for 85 minutes, spheroids evolve during the course of the tomographic scan. Strong edge contrast suggest these features are bubbles evolving from vaporization of electrolyte under high energy X–ray exposure. After 170 minutes, a large bulbous growth appears connecting the two electrodes. It is hypothesized that preferential lithium deposition — a result of local concentrated electric fields around evolved bubbles during the second tomography scan — caused initial nucleation of dendrites, and continued current application caused growth of the feature diameter to 939 μm.

In comparison, the symmetric lithium metal electrode couple demonstrates no appreciable surface growth (Fig. 9.9). At specific currents 0.5 and 1.0 mA cm^{-2}, the lithium metal surface does not demonstrate appreciable surface evolution. It is hypothesized that lithium fluoride species that form during electrolyte decomposition introduce mechanical strength to prevent excessive dendrite growth. Unlike conventional electrolyte, fluorinated electrolyte does not show bubble evolution during X–ray exposure.

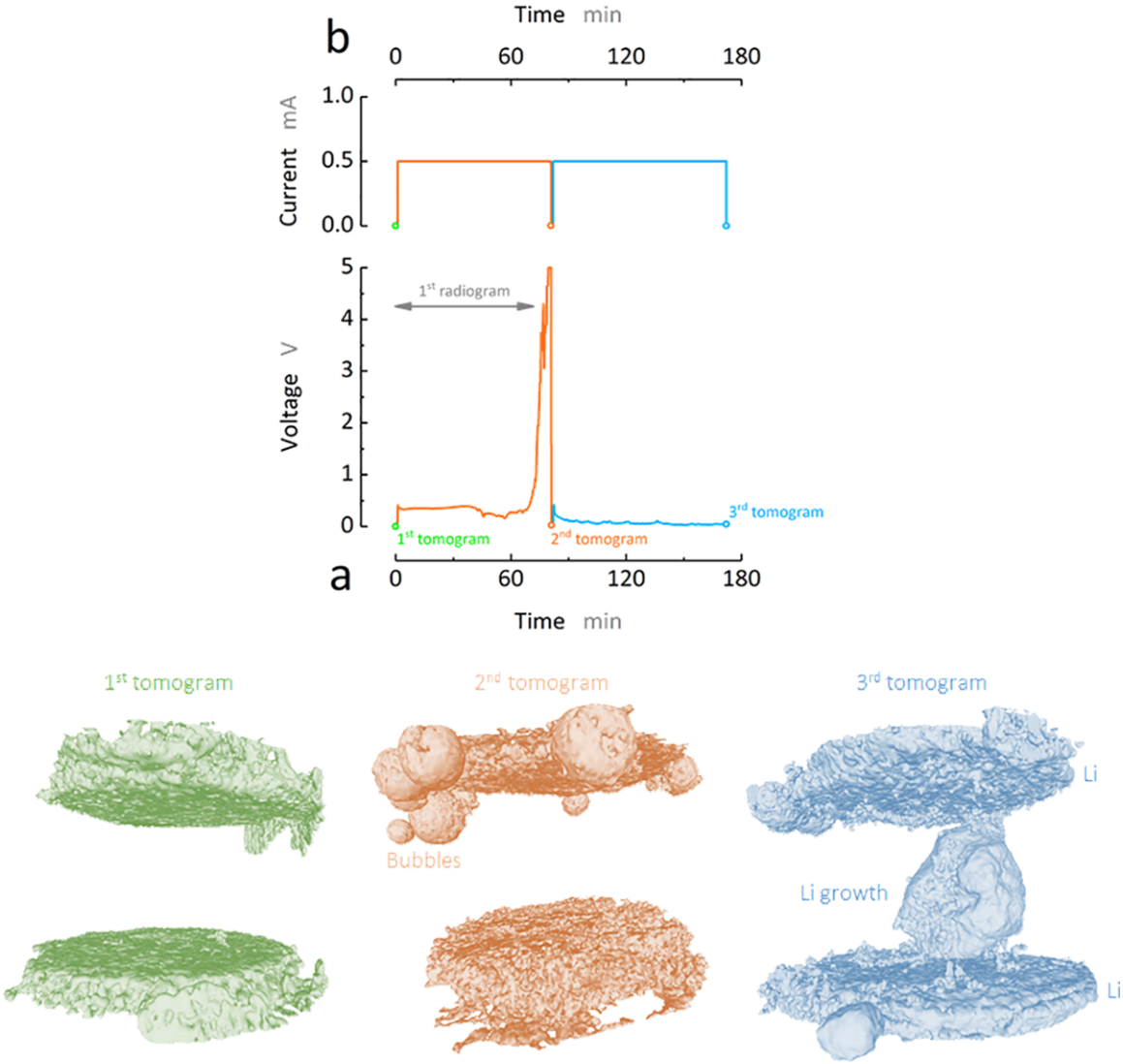

Figure 9.8. *In situ tomography of lithium metal in conventional electrolyte.* (a) The chronopotentiogram of lithium metal anodes shows unstable lithium plating near ca. 0.4 V under (b) constant specific current 0.5 mA cm^{-2}. Lithium metal tomographic reconstructions show a connecting dendritic growth after 170 minutes, following plating near ca. 0.0 V.

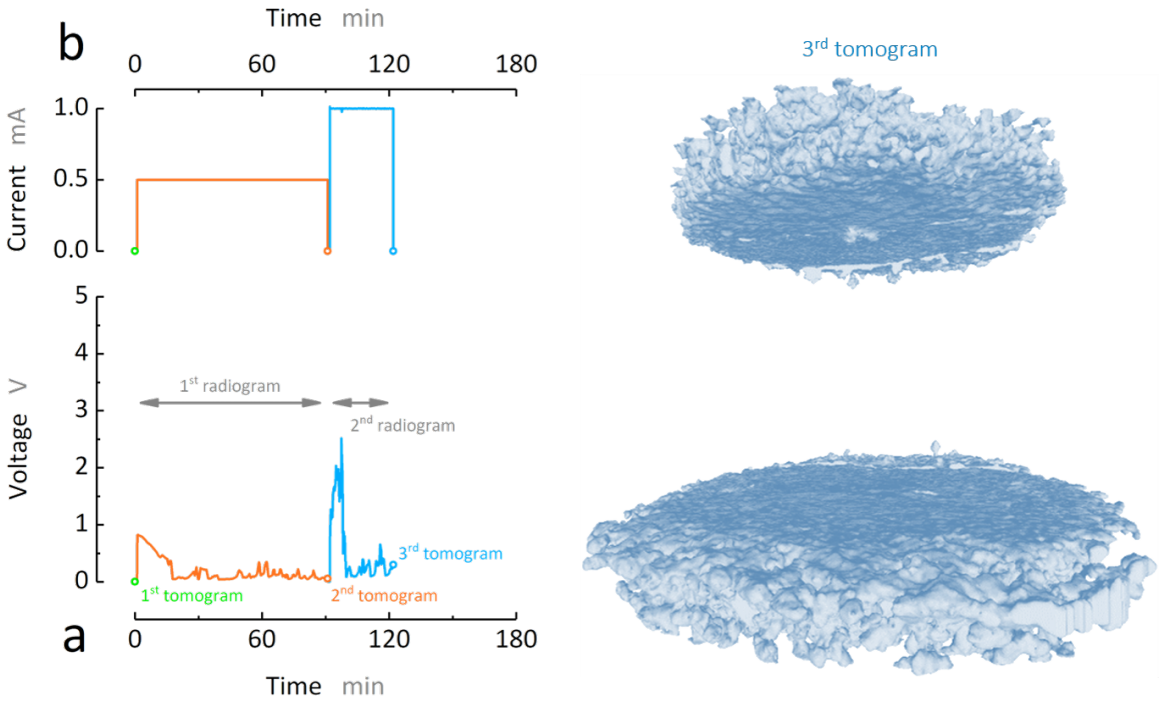

Figure 9.9. *In situ tomography of lithium metal in fluorinated electrolyte.* Under constant (a) specific currents 0.5 and 1.0 mA cm^{-2}, lithium metal anodes do not show appreciable dendrite growth.

9.3 Polysulfides Affect Dendrite Growth

This work successfully demonstrates lithium dendrite imaging using high energy Synchrotron X–ray radiation at Advanced Photon Source beamline 6–BM–A. The custom micro–tomography setup reveals three-dimensional lithium growth after extended galvanostatic current 0.5 mA cm^{-2}. Digital image processing enables isolation and ramification of the lithium growth from experimental artifacts and background intensity.

The preliminary results of this project comprise critical evidence that lithium metal imaging using micro-tomography is viable using high energy Synchrotron radiation. Tomography imaging in both glyme and fluorinated electrolytes indicates electrochemical cell stability is a function of electrolyte. In conventional glyme electrolyte, extended exposure to high energy X–ray radiation evolves organic vapor bubbles. Evolved vapor appears as spheroid features with high contrast which occupy the top of the electrochemical cell. Subsequent current application and X–ray exposure produces a bulbous lithium growth between lithium electrodes. In contrast, fluorinated electrolytes show no vapor evolution during X–ray exposure and cycling at great applied current (up to 1.0 mA cm^{-2}), providing in situ evidence for micro-tomography techniques and the possible lithium fluoride-mediated stabilization of lithium metal [61, 80].

FINAL WORDS ON POLYSULFIDES

It is the great beauty of our science, chemistry,
that advancement in it, whether in a degree
great or small, instead of exhausting the subjects
of research, opens the doors to further and more
abundant knowledge, overflowing with beauty
and utility.

— M. Faraday, 1839, *Experimental Researches in Electricity*

CHAPTER 10: SUMMARY OF EXPERIMENTS

Sulfur cathodes only comprise a single dimension of the lithium sulfur batteries. Broader considerations including practicality, sustainability, and reciprocal materials (i.e., anodes, electrolytes) must be addressed if the lithium sulfur battery will one day reach commercial maturity. The research presented through this dissertation demonstrates synthesis processes and resulting composite cathodes for lithium sulfur batteries with greater than 500 Ah kg^{-1} gravimetric capacity at nominal applied currents. Complementary research explores the often overlooked elements of process sustainability, electrolyte, and anode materials. Pyrolysis, the conventional synthesis route for various manufactured carbons [178, 260], is characterized for its health and environmental impacts with respect to synthesis pathway. Fluorinated electrolyte is tested, in combination with demonstrated carbon–sulfur composites, for its influence on electrochemical performance during extended cycling. Submicron carbon spheres and lithium metal are studied as anode materials.

At its conclusion, this dissertation reviews the broader significance of its presented research in context of ongoing research today.

10.1 Polysulfide Mitigation at the Electrode–Electrolyte Interface

Conventionally, electrochemistry is an interfacial science at the electrode–electrolyte interface. Exemplary electrochemical cells feature reduction or oxidation reactions which occur at the boundary between solid electrode and ionically-conductive electrolyte [12]. Commercial rechargeable lithium-ion batteries, whose reversible intercalation mechanisms are well understood [8, 41, 49], fall reasonably under this archetype: electrochemical charge transfer reactions facilitate lithium passage across the electrode–electrolyte interface (and distribute throughout intersticial crystal space

by diffusion mechanisms). Resting on the frontier of energy storage technology, rechargeable lithium sulfur batteries are *not* archetypal due to precipitation and dissolution of intermediate polysulfides [56]. Yet, rechargeable batteries involving precipitation and dissolution of the active material are commercially available [80] (e.g., lead–acid, sodium iron chloride, and cadmium–cadmium hydroxide systems).

Chapters 1 and 2 address electrochemistry at the electrode–electrolyte interface with carbon sulfur composite cathodes. Both chapters present synthesis of carbon sulfur composite cathodes (viz., autogenic and sonochemical synthesis) and resulting electrochemical performance. Density functional theory and molecular simulations reveal the significance of material character — particularly defect sites and microstructure of synthesized carbon substrates — to charge transfer mechanisms.

At the cathode–electrolyte interface, fluorinated electrolyte inhibits polysulfide solvation, increasing Coulombic efficiency across extended cycling. In compliment, fluorinated electrolyte decomposition at the opposing anode–electrolyte interface results in solid electrolyte interphases rich in lithium fluoride LiF [61, 80]. Chapter 9 does not explicitly study polysulfide and lithium metal anode interactions. Instead, the developed Synchrotron micro–tomography experiments provide in situ evidence that dendrites appreciably develop in glyme electrolyes but not fluorinated ones. The author recommends further research, using the developed micro–tomography technique, concerning lithium dendrite evolution in the presence of polysulfides [248, 261, 262].

10.2 Remark on Discovery

Chapters 1 and 2 study synthesis and material aspects of lithium sulfur cathode behavior. Impedance spectroscopy experiments with autogenic carbon sulfur composites illustrate that synthesis pathway influences cathode impedance. Synthesis pathway directly controls sulfur distribution in the composite product: techniques which feature homogeneous distribution of sulfur precursors correlate well to gravimetric capacity at great applied current. Fluorinated electrolytes in combination with sonochemical carbon sulfur composites improve Coulombic efficiency across various

applied currents. Computational modeling, performed in collaboration with Texas A&M University, reveals that evolution of cathode microstructure significantly influences interfacial charge transport mechanisms during extended cycling.

To supplement material and electrochemical characterization, chapters 3 and 4 explore the sustainability of synthesized carbons and their synthesis process. Pyrolysis was studied as the typical synthesis route for artificial carbons, evaluated along dimensions of health and environment impact. With respect to health effects, small scale by–products were characterized as carbon–rich micro and nano–sized spheres susceptible to agglomeration. An open surface water trap, downstream of the pyrolysis process, can collect aerosol particulates but cannot retain them over extended periods. More stringent mitigation techniques (e.g., fine particle filtration system) are recommended to health risks. With respect to environment effects, synthesis pathway controls energy consumption and environmental impact. Along dimensions of TRACI impact categories, the mode of oxygen deficient atmosphere — that is, whether pyrolysis is enabled by vacuum or continuous inert gas stream — influences energy consumption and environmental risk profiles. Life cycle analysis suggests vacuum techniques have slightly less adverse effects overall compared to inert gas techniques; yet specific advantages and disadvantages differ according to impact category.

Chapters 5 and 6 trace the electrochemical evolution of synthesized carbon and lithium metal anodes during extended cycling. Submicron carbon spheres are synthesized by two–step sonochemical and pyrolysis procedure. Synthesis pathway (i.e., pyrolysis temperature) controls the gravimetric capacity of submicron carbon spheres. As synthesis temperature increases up to 1800 °C, submicron carbon spheres exhibit larger crystallite volume, greater number of constituent layers, and lower interlayer spacing; greater phase disorder; greater carbon content; and lower heteroatom content. The specific combination of these properties control lithiation voltage, gravimetric capacity, and capacity stability during galvanostatic cycling. In parallel, surface evolution of lithium metal anodes was characterized in both glyme and fluorinated electrolyte. The designed in situ tomography technique for Beamline 6–BM–A at the

Advanced Photon Source provides evidence that fluorinated electrolytes inhibit appreciable dendrite growth under great applied current. In conjunction with enhanced cathode performance, fluorinated electrolytes could be a promising electrolyte to realize high energy lithium sulfur batteries in the near future.

10.3 The Future of Lithium Sulfur Batteries

Entering its 3rd decade, lithium sulfur battery research has not yet resolved the technical challenges that prohibit commercialization. But the difficult progress of lithium sulfur batteries invites metamorphosis in research direction and methodology. Among the wider electrochemical sector, emerging battery research calls for a return to fundamental form: methodical investigation of chemical mechanisms [263, 264] and in situ characterization [242, 265] feature heavily now more than ever in the electrochemical research community.

This dissertation presents a strong case for fluorinated electrolytes as mediator for polysulfide and dendrite suppression. Fluorinated electrolytes are adaptable; its dual functionality extends performance lifetime of sulfur carbon composite cathodes (i.e., extended Coulombic efficiency)and lithium metal anodes (i.e., negligible surface pitting or deposition). In addition, the developed in situ micro–tomography technique is expected to be a useful tool for in situ characterization of lithium sulfur cathodes, lithium metal anodes, and other electrochemical materials.

REFERENCES

REFERENCES

[1] J. A. Caton, "A Review of Investigations Using the Second Law of Thermodynamics to Study Internal-Combustion Engines," in *SAE Tech. Pap. Ser.*, no. 724, mar 2000. [Online]. Available: http://papers.sae.org/2000-01-1081/

[2] J. Smith, M. Abbott, and H. C. V. Ness, *Introduction to Chemical Engineering Thermodynamics*. McGraw-Hill Education, 2004.

[3] A. Einstein, "Über die von der molekularkinetischen Theorie der Wärme geforderte Bewegung von in ruhenden Flüssigkeiten suspendierten Teilchen," *Ann. Phys.*, vol. 322, no. 8, pp. 549–560, 1905. [Online]. Available: http://doi.wiley.com/10.1002/andp.19053220806

[4] A. M. Taylor, "Science review of internal combustion engines," *Energy Policy*, vol. 36, no. 12, pp. 4657–4667, dec 2008. [Online]. Available: http://linkinghub.elsevier.com/retrieve/pii/S0301421508005016

[5] W. Shen, H. Huang, Y. Pang, and X. Su, "Review of the Energy Saving Hydraulic System Based on Common Pressure Rail," *IEEE Access*, vol. 5, pp. 655–669, 2017. [Online]. Available: http://ieeexplore.ieee.org/document/7820153/

[6] D. C. Giancoli, *Physics: Principles with Applications*. Addison-Wesley, 2010.

[7] S. Riffat and X. Ma, "Thermoelectrics: a review of present and potential applications," *Appl. Therm. Eng.*, vol. 23, no. 8, pp. 913–935, jun 2003. [Online]. Available: http://linkinghub.elsevier.com/retrieve/pii/S1359431103000127

[8] V. Etacheri, R. Marom, R. Elazari, G. Salitra, and D. Aurbach, "Challenges in the development of advanced Li-ion batteries: a review," *Energy Environ. Sci.*, vol. 4, no. 9, p. 3243, 2011. [Online]. Available: http://xlink.rsc.org/?DOI=c1ee01598b

[9] J. W. Gibbs, *Elementary Principles in Statistical Mechanics*. Dover Publications, 2014.

[10] J. Gibbs, "A Method of Geometrical Representation of the Thermodynamic Properties of Substances by Means of Surfaces," *Trans. Connect. Acad. Arts Sci.*, pp. 382–404, 1873.

[11] H. von Helmholtz, *Physical memoirs selected and translated from foreign sources, under the direction of the Physical society of London. Vol. 1.* Taylor and Francis, 1890.

[12] A. J. Bard and L. R. Faulkner, *Electrochemical Methods: Fundamentals and Applications*. Wiley, 2000.

[13] P. Bai and M. Z. Bazant, "Charge transfer kinetics at the solid-solid interface in porous electrodes," *Nat. Commun.*, vol. 5, pp. 1–7, apr 2014. [Online]. Available: http://dx.doi.org/10.1038/ncomms4585 http://www.nature.com/doifinder/10.1038/ncomms4585

[14] M. S. Kilic, M. Z. Bazant, and A. Ajdari, "Steric effects in the dynamics of electrolytes at large applied voltages. I. Double-layer charging," *Phys. Rev. E*, vol. 75, no. 2, p. 021502, feb 2007. [Online]. Available: https://link.aps.org/doi/10.1103/PhysRevE.75.021502

[15] Q. Zheng and G.-W. Wei, "PoissonBoltzmannNernstPlanck model," *J. Chem. Phys.*, vol. 134, no. 19, p. 194101, may 2011. [Online]. Available: http://aip.scitation.org/doi/10.1063/1.3581031

[16] M. von Smoluchowski, "Zur kinetischen Theorie der Brownschen Molekularbewegung und der Suspensionen," *Ann. Phys.*, vol. 326, no. 14, pp. 756–780, 1906. [Online]. Available: http://doi.wiley.com/10.1002/andp.19063261405

[17] R. Burt, G. Birkett, and X. S. Zhao, "A review of molecular modelling of electric double layer capacitors," *Phys. Chem. Chem. Phys.*, vol. 16, no. 14, p. 6519, 2014. [Online]. Available: http://xlink.rsc.org/?DOI=c3cp55186e

[18] R. Kant and M. B. Singh, "Generalization of the Gouy-Chapman-Stern model of an electric double layer for a morphologically complex electrode: Deterministic and stochastic morphologies," *Phys. Rev. E - Stat. Nonlinear, Soft Matter Phys.*, vol. 88, no. 5, pp. 1–16, 2013.

[19] O. Stern, "Zur Theorie der Elektrolytischen Doppelschicht," *Zeitschrift fur Elektrochemie*, vol. 30, pp. 508–516, 1924.

[20] D. L. Chapman, "A contribution to the theory of electrocapillarity," *Philos. Mag. Ser. 6*, vol. 25, no. 148, pp. 475–481, 1913. [Online]. Available: http://www.tandfonline.com/doi/abs/10.1080/14786440408634187

[21] M. Gouy, "Sur la constitution de la charge électrique à la surface d'un électrolyte," *J. Phys. Théorique Appliquée*, vol. 9, no. 1, pp. 457–468, 1910. [Online]. Available: http://www.edpsciences.org/10.1051/jphystap:019100090045700

[22] P. Debye and E. Hückel, "De la théorie des électrolytes. i. abaissement du point de congélation et phénomènes associés," *Phys. Zeitschrift*, vol. 24, no. 9, pp. 185–206, 1923.

[23] A. M. Smith, A. A. Lee, and S. Perkin, "The Electrostatic Screening Length in Concentrated Electrolytes Increases with Concentration," *J. Phys. Chem. Lett.*, vol. 7, no. 12, pp. 2157–2163, jun 2016. [Online]. Available: http://pubs.acs.org/doi/10.1021/acs.jpclett.6b00867

[24] M. van Soestbergen, "Frumkin-Butler-Volmer theory and mass transfer in electrochemical cells," *Russ. J. Electrochem.*, vol. 48, no. 6, pp. 570–579, 2012. [Online]. Available: http://link.springer.com/10.1134/S1023193512060110

[25] H. Chang and G. Jaffé, "Polarization in Electrolytic Solutions. Part I. Theory," *J. Chem. Phys.*, vol. 20, no. 7, pp. 1071–1077, jul 1952. [Online]. Available: http://aip.scitation.org/doi/10.1063/1.1700669

[26] J. R. MacDonald, "Effects of various boundary conditions on the response of Poisson - Nernst - Planck impedance spectroscopy analysis models and comparison with a continuous-time random-walk model," *J. Phys. Chem. A*, vol. 115, no. 46, pp. 13 370–13 380, 2011.

[27] P. M. Biesheuvel, Y. Fu, and M. Z. Bazant, "Diffuse charge and Faradaic reactions in porous electrodes," *Phys. Rev. E - Stat. Nonlinear, Soft Matter Phys.*, vol. 83, no. 6, 2011.

[28] W. Dreyer, C. Guhlke, and R. Müller, "A new perspective on the electron transfer: recovering the ButlerVolmer equation in non-equilibrium thermodynamics," *Phys. Chem. Chem. Phys.*, vol. 18, no. 36, pp. 24 966–24 983, 2016. [Online]. Available: http://xlink.rsc.org/?DOI=C6CP04142F

[29] F. Ciucci and W. Lai, "Derivation of Micro/Macro Lithium Battery Models from Homogenization," *Transp. Porous Media*, vol. 88, no. 2, pp. 249–270, 2011.

[30] D. Meng, B. Zheng, G. Lin, and M. L. Sushko, "Numerical Solution of 3D Poisson-Nernst-Planck Equations Coupled with Classical Density Functional Theory for Modeling Ion and Electron Transport in a Confined Environment," *Commun. Comput. Phys.*, vol. 16, no. 05, pp. 1298–1322, nov 2014. [Online]. Available: http://www.journals.cambridge.org/abstract_S1815240600006186

[31] P. H. Barry, "Derivation of Unstirred-Layer Transport Number Equations from the Nernst-Planck Flux Equations," *Biophys. J.*, vol. 74, no. 6, pp. 2903–2905, jun 1998. [Online]. Available: http://linkinghub.elsevier.com/retrieve/pii/S0006349598779962

[32] M. Pabst, "Analytical solution of the Poisson-Nernst-Planck equations for an electrochemical system close to electroneutrality," *J. Chem. Phys.*, vol. 140, no. 22, 2014.

[33] J. P. Catchpole and G. Fulford, "Dimensionless Groups," *Ind. Eng. Chem.*, vol. 58, no. 3, pp. 46–60, mar 1966. [Online]. Available: http://pubs.acs.org/doi/abs/10.1021/ie50675a012

[34] R. B. Bird, W. E. Stewart, and E. N. Lightfoot, *Transport Phenomena*, 2nd ed. John Wiley & Sons, Inc., 2006.

[35] H. S. Fogler, *Elements of Chemical Reaction Engineering*. Prentice Hall, 2005.

[36] B. D. McCloskey, "Expanding the Ragone Plot: Pushing the Limits of Energy Storage," *J. Phys. Chem. Lett.*, vol. 6, no. 18, pp. 3592–3593, sep 2015. [Online]. Available: http://pubs.acs.org/doi/10.1021/acs.jpclett.5b01813

[37] T. Christen and M. W. Carlen, "Theory of Ragone plots," *J. Power Sources*, vol. 91, no. 2, pp. 210–216, dec 2000. [Online]. Available: http://linkinghub.elsevier.com/retrieve/pii/S0378775300004742

[38] P. G. Bruce, S. A. Freunberger, L. J. Hardwick, and J.-M. Tarascon, "LiO2 and LiS batteries with high energy storage," *Nat. Mater.*, vol. 11, no. 1, pp. 19–29, jan 2012. [Online]. Available: http://www.nature.com/articles/nmat3191

[39] R. Pena-Alzola, R. Sebastian, J. Quesada, and A. Colmenar, "Review of flywheel based energy storage systems," in *2011 Int. Conf. Power Eng. Energy Electr. Drives*, no. May. IEEE, may 2011, pp. 1–6. [Online]. Available: http://ieeexplore.ieee.org/document/6036455/

[40] R. C. Massé, C. Liu, Y. Li, L. Mai, and G. Cao, "Energy storage through intercalation reactions: electrodes for rechargeable batteries," *Natl. Sci. Rev.*, vol. 4, no. 1, p. nww093, dec 2016. [Online]. Available: https://academic.oup.com/nsr/article-lookup/doi/10.1093/nsr/nww093

[41] M. R. Palacín, "Recent advances in rechargeable battery materials: a chemist's perspective," *Chem. Soc. Rev.*, vol. 38, no. 9, p. 2565, 2009. [Online]. Available: http://xlink.rsc.org/?DOI=b820555h

[42] L. Carrette, K. A. Friedrich, and U. Stimming, "Fuel Cells - Fundamentals and Applications," *Fuel Cells*, vol. 1, no. 1, pp. 5–39, 2001. [Online]. Available: http://doi.wiley.com/10.1002/1615-6854%28200105%291%3A1%3C5%3A%3AAID-FUCE5%3E3.0.CO%3B2-G

[43] P. Sharma and T. S. Bhatti, "A review on electrochemical double-layer capacitors," *Energy Convers. Manag.*, vol. 51, no. 12, pp. 2901–2912, 2010. [Online]. Available: http://dx.doi.org/10.1016/j.enconman.2010.06.031

[44] U. S. A. B. C. LLC, "Advanced Batteries for Electric Vehicles - 2020 Commercialization Goals," U.S. A.B.C., Tech. Rep., 2015. [Online]. Available: http://www.uscar.org

[45] ——, "High Power Energy Storage System Requirements: Power Assist Hybrid Electric Vehicles at End of Life," U.S. A.B.C., Tech. Rep., 2017. [Online]. Available: http://www.uscar.org

[46] K. Xu, "Nonaqueous liquid electrolytes for lithium-based rechargeable batteries," *Chem. Rev.*, vol. 104, no. 10, pp. 4303–4417, 2004.

[47] H. Lee, M. Yanilmaz, O. Toprakci, K. Fu, and X. Zhang, "A review of recent developments in membrane separators for rechargeable lithium-ion batteries," *Energy Environ. Sci.*, vol. 7, no. 12, pp. 3857–3886, 2014. [Online]. Available: http://xlink.rsc.org/?DOI=C4EE01432D

[48] S. S. Zhang, "A review on the separators of liquid electrolyte Li-ion batteries," *J. Power Sources*, vol. 164, no. 1, pp. 351–364, jan 2007. [Online]. Available: http://linkinghub.elsevier.com/retrieve/pii/S0378775306022452

[49] M. S. Whittingham, "Lithium Batteries and Cathode Materials," *Chem. Rev.*, vol. 104, no. 10, pp. 4271–4302, oct 2004. [Online]. Available: http://pubs.acs.org/doi/abs/10.1021/cr020731c

[50] Q. Pang, X. Liang, C. Y. Kwok, and L. F. Nazar, "Advances in lithiumsulfur batteries based on multifunctional cathodes and electrolytes," *Nat. Energy*, vol. 1, no. 9, p. 16132, sep 2016. [Online]. Available: http://dx.doi.org/10.1038/nenergy.2016.132 http://www.nature.com/articles/nenergy2016132

[51] A. Grimaud, "Batteries: Beyond intercalation and conversion," *Nat. Energy*, vol. 2, no. 2, 2017.

[52] B. Scrosati and J. Garche, "Lithium batteries: Status, prospects and future," *J. Power Sources*, vol. 195, no. 9, pp. 2419–2430, may 2010. [Online]. Available: http://linkinghub.elsevier.com/retrieve/pii/S0378775309020564

[53] J. W. Fergus, "Recent developments in cathode materials for lithium ion batteries," *J. Power Sources*, vol. 195, no. 4, pp. 939–954, feb 2010. [Online]. Available: http://linkinghub.elsevier.com/retrieve/pii/S0378775309015304

[54] D. Aurbach, E. Zinigrad, Y. Cohen, and H. Teller, "A short review of failure mechanisms of lithium metal and lithiated graphite anodes in liquid electrolyte solutions," *Solid State Ionics*, vol. 148, no. 3-4, pp. 405–416, jun 2002. [Online]. Available: http://linkinghub.elsevier.com/retrieve/pii/S0167273802000802

[55] D. Aurbach, "Review of selected electrode-solution interactions which determine the performance of Li and Li ion batteries," *J. Power Sources*, vol. 89, no. 2, pp. 206–218, 2000.

[56] A. Manthiram, Y. Fu, S.-H. Chung, C. Zu, and Y.-S. Su, "Rechargeable LithiumSulfur Batteries," *Chem. Rev.*, vol. 114, no. 23, pp. 11 751–11 787, dec 2014. [Online]. Available: http://pubs.acs.org/doi/10.1021/cr500062v

[57] X. Ji, K. T. Lee, and L. F. Nazar, "A highly ordered nanostructured carbon-sulphur cathode for lithiumsulphur batteries," *Nat. Mater.*, vol. 8, no. 6, pp. 500–506, jun 2009. [Online]. Available: http://dx.doi.org/10.1038/nmat2460 http://www.nature.com/articles/nmat2460

[58] A. G. M. Ferreira and L. Q. Lobo, "The Low-Pressure Phase Diagram of Sulfur," *J. Chem. Thermodyn.*, vol. 43, no. 2, pp. 95–104, 2011. [Online]. Available: http://dx.doi.org/10.1016/j.jct.2010.07.007

[59] N. Angulakshmi and A. M. Stephan, "Efficient Electrolytes for LithiumâSulfur Batteries," *Front. Energy Res.*, vol. 3, may 2015. [Online]. Available: http://www.frontiersin.org/Energy_Storage/10.3389/fenrg.2015.00017/abstract

[60] X. Ji and L. F. Nazar, "Advances in LiS batteries," *J. Mater. Chem.*, vol. 20, no. 44, p. 9821, 2010. [Online]. Available: http://xlink.rsc.org/?DOI=b925751a

[61] C. Zu, N. Azimi, Z. Zhang, and A. Manthiram, "Insight into lithiummetal anodes in lithiumsulfur batteries with a fluorinated ether electrolyte," *J. Mater. Chem. A*, vol. 3, no. 28, pp. 14 864–14 870, 2015. [Online]. Available: http://xlink.rsc.org/?DOI=C5TA03195H

[62] A. Rosenman, E. Markevich, G. Salitra, D. Aurbach, A. Garsuch, and F. F. Chesneau, "Review on Li-Sulfur Battery Systems: An Integral Perspective," *Adv. Energy Mater.*, vol. 5, no. 16, pp. 1–21, 2015.

[63] J. Zhang, H. Ye, Y. Yin, and Y. Guo, "Core-shell meso/microporous carbon host for sulfur loading toward applications in lithium-sulfur batteries," *J. Energy Chem.*, vol. 23, no. 3, pp. 308–314, may 2014. [Online]. Available: http://dx.doi.org/10.1016/S2095-4956(14)60152-2 http://linkinghub.elsevier.com/retrieve/pii/S2095495614601522

[64] G. Li, W. Zhao, L. Liu, and L. Chen, "Effects of electrolyte concentration and synthesis methods of sulfur/carbon composites on the electrochemical performance in lithiumsulfur batteries," *RSC Adv.*, vol. 5, no. 67, pp. 54 293–54 300, 2015. [Online]. Available: http://xlink.rsc.org/?DOI=C5RA08939E

[65] S. V. Pol, V. G. Pol, and A. Gedanken, "Reactions under Autogenic Pressure at Elevated Temperature (RAPET) of Various Alkoxides: Formation of Metals/Metal Oxides-Carbon Core-Shell Structures," *Chem. - A Eur. J.*, vol. 10, no. 18, pp. 4467–4473, sep 2004. [Online]. Available: http://doi.wiley.com/10.1002/chem.200400014

[66] A. Odani, V. G. Pol, S. V. Pol, M. Koltypin, A. Gedanken, and D. Aurbach, "Testing Carbon-Coated VOx Prepared via Reaction under Autogenic Pressure at Elevated Temperature as Li-Insertion Materials," *Adv. Mater.*, vol. 18, no. 11, pp. 1431–1436, jun 2006. [Online]. Available: http://doi.wiley.com/10.1002/adma.200501611

[67] V. G. Pol and P. Thiyagarajan, "Remediating plastic waste into carbon nanotubes," *J. Environ. Monit.*, vol. 12, no. 2, pp. 455–459, 2010. [Online]. Available: http://xlink.rsc.org/?DOI=B914648B

[68] V. G. Pol, S. V. Pol, and A. Gedanken, "Novel Synthesis of High Surface Area Silicon Carbide by RAPET (Reactions under Autogenic Pressure at Elevated Temperature) of Organosilanes," *Chem. Mater.*, vol. 17, no. 7, pp. 1797–1802, apr 2005. [Online]. Available: http://pubs.acs.org/doi/abs/10.1021/cm048032z

[69] J. Manca, K. Croes, W. De Ceuninck, V. D'Haeger, J. D'Haen, P. Depauw, L. Tielemans, and L. De Schepper, "Localized monitoring of electromigration with early resistance change measurements," *Microelectron. Reliab.*, vol. 38, no. 4, pp. 641–650, apr 1998. [Online]. Available: http://linkinghub.elsevier.com/retrieve/pii/S0026271497001911

[70] P. Gustafson, "An Evaluation of the Thermodynamic Properties and the P, T Phase Diagram of Carbon," *Carbon N. Y.*, vol. 24, no. 2, pp. 169–176, 1986. [Online]. Available: http://linkinghub.elsevier.com/retrieve/pii/0008622386901132

[71] E. A. Belenkov, "Formation of Graphite structure in Carbon crystallites," *Inorg. Mater.*, vol. 37, no. 9, pp. 928–934, 2001. [Online]. Available: http://dx.doi.org/10.1023/A:1017403816006

[72] B. E. Warren, "X-Ray Diffraction in Random Layer Lattices," *Phys. Rev.*, vol. 59, no. 9, pp. 693–698, may 1941. [Online]. Available: https://link.aps.org/doi/10.1103/PhysRev.59.693

[73] H. P. Klug and L. E. Alexander, *X-ray diffraction procedures: for polycrystalline and amorphous materials*. Wiley & Sons, 1974.

[74] S. J. Van Der Gaast, "A Method to Eliminate the Background in X-ray Diffraction Patterns of Oriented Clay Mineral Samples," *Clay Miner.*, vol. 16, no. 4, pp. 383–393, 1981. [Online]. Available: http://www.minersoc.org/pages/Archive-CM/Volume_16/16-4-383.pdf

[75] R. F. Boehme and G. S. Cargill, "X-ray scattering measurements demonstrating in-plane anisotropy in Kapton polyimide films," in *Polyimides*. Springer, 1984.

[76] S. H. Lapidus, "Standards Data for Beamline-11." [Online]. Available: https://wiki-ext.aps.anl.gov/ug11bm/index.php/Standards_Data

[77] M. Thommes, K. Kaneko, A. V. Neimark, J. P. Olivier, F. Rodriguez-Reinoso, J. Rouquerol, and K. S. W. Sing, "Physisorption of gases, with special reference to the evaluation of surface area and pore size distribution (IUPAC Technical Report)," *Pure Appl. Chem.*, vol. 87, no. 9-10, pp. 1051–1069, jan 2015. [Online]. Available: http://www.degruyter.com/view/j/pac.ahead-of-print/pac-2014-1117/pac-2014-1117.xml https://www.degruyter.com/view/j/pac.2015.87.issue-9-10/pac-2014-1117/pac-2014-1117.xml

[78] Y. Yang, G. Zheng, S. Misra, J. Nelson, M. F. Toney, and Y. Cui, "High-Capacity Micrometer-Sized Li 2 S Particles as Cathode Materials for Advanced Rechargeable Lithium-Ion Batteries," *J. Am. Chem. Soc.*, vol. 134, no. 37, pp. 15 387–15 394, sep 2012. [Online]. Available: http://pubs.acs.org/doi/10.1021/ja3052206

[79] M. D. Levi and D. Aurbach, "Impedance of a Single Intercalation Particle and of Non-Homogeneous , Multilayered Porous Composite Electrodes for Li-ion Batteries," pp. 11 693–11 703, 2004.

[80] L. Cheng, L. A. Curtiss, K. R. Zavadil, A. A. Gewirth, Y. Shao, and K. G. Gallagher, "Sparingly Solvating Electrolytes for High Energy Density Lithium-Sulfur Batteries," *ACS Energy Lett.*, vol. 1, no. 3, pp. 503–509, 2016.

[81] M. Z. Jacobson, "Review of solutions to global warming, air pollution, and energy security," *Energy Environ. Sci.*, vol. 2, no. 2, pp. 148–173, 2009. [Online]. Available: http://xlink.rsc.org/?DOI=B809990C

[82] A. H. Fathima and K. Palanisamy, "Optimization in microgrids with hybrid energy systems A review," *Renew. Sustain. Energy Rev.*, vol. 45, pp. 431–446, may 2015. [Online]. Available: http://dx.doi.org/10.1016/j.rser.2015.01.059 http://linkinghub.elsevier.com/retrieve/pii/S1364032115000696

[83] A. Hepbasli, "A key review on exergetic analysis and assessment of renewable energy resources for a sustainable future," *Renew. Sustain. Energy Rev.*, vol. 12, no. 3, pp. 593–661, apr 2008. [Online]. Available: http://linkinghub.elsevier.com/retrieve/pii/S1364032106001225

[84] N.-S. Choi, Z. Chen, S. a. Freunberger, X. Ji, Y.-K. Sun, K. Amine, G. Yushin, L. F. Nazar, J. Cho, and P. G. Bruce, "Challenges Facing Lithium Batteries and Electrical Double-Layer Capacitors," *Angew. Chemie Int. Ed.*, vol. 51, no. 40, pp. 9994–10 024, oct 2012. [Online]. Available: http://doi.wiley.com/10.1002/anie.201201429

[85] M. M. Thackeray, C. Wolverton, and E. D. Isaacs, "Electrical energy storage for transportationapproaching the limits of, and going beyond, lithium-ion batteries," *Energy Environ. Sci.*, vol. 5, no. 7, p. 7854, 2012. [Online]. Available: http://xlink.rsc.org/?DOI=c2ee21892e

[86] P. G. Bruce, L. J. Hardwick, and K. M. Abraham, "Lithium-air and lithium-sulfur batteries," *MRS Bull.*, vol. 36, no. 07, pp. 506–512, jul 2011. [Online]. Available: http://www.journals.cambridge.org/abstract_S0883769411001576

[87] C. Wadia, P. Albertus, and V. Srinivasan, "Resource constraints on the battery energy storage potential for grid and transportation applications," *J. Power Sources*, vol. 196, no. 3, pp. 1593–1598, feb 2011. [Online]. Available: http://dx.doi.org/10.1016/j.jpowsour.2010.08.056 http://linkinghub.elsevier.com/retrieve/pii/S0378775310014679

[88] H. Yamin and E. Peled, "Electrochemistry of a nonaqueous lithium/sulfur cell," *J. Power Sources*, vol. 9, no. 3, pp. 281–287, jan 1983. [Online]. Available: http://linkinghub.elsevier.com/retrieve/pii/0378775383870293

[89] W. Weng, V. G. Pol, and K. Amine, "Ultrasound Assisted Design of Sulfur/Carbon Cathodes with Partially Fluorinated Ether Electrolytes for Highly Efficient Li/S Batteries," *Adv. Mater.*, vol. 25, no. 11, pp. 1608–1615, mar 2013. [Online]. Available: http://doi.wiley.com/10.1002/adma.201204051

[90] N. Azimi, Z. Xue, N. D. Rago, C. Takoudis, M. L. Gordin, J. Song, D. Wang, and Z. Zhang, "Fluorinated Electrolytes for Li-S Battery: Suppressing the Self-Discharge with an Electrolyte Containing Fluoroether Solvent," *J. Electrochem. Soc.*, vol. 162, no. 1, pp. A64—-A68, nov 2014. [Online]. Available: http://jes.ecsdl.org/cgi/doi/10.1149/2.0431501jes

[91] W. Kohn and L. J. Sham, "Self-Consistent Equations Including Exchange and Correlation Effects," *Phys. Rev.*, vol. 140, no. 4A, pp. A1133—-A1138, nov 1965. [Online]. Available: https://link.aps.org/doi/10.1103/PhysRev.140.A1133

[92] R. O. Jones and O. Gunnarsson, "The density functional formalism, its applications and prospects," *Rev. Mod. Phys.*, vol. 61, no. 3, pp. 689–746, jul 1989. [Online]. Available: https://link.aps.org/doi/10.1103/RevModPhys.61.689

[93] R. Car and M. Parrinello, "Unified Approach for Molecular Dynamics and Density-Functional Theory," *Phys. Rev. Lett.*, vol. 55, no. 22, pp. 2471–2474, nov 1985. [Online]. Available: http://link.aps.org/doi/10.1103/PhysRevLett.55.2471 https://link.aps.org/doi/10.1103/PhysRevLett.55.2471

[94] M. C. Payne, M. P. Teter, D. C. Allan, T. A. Arias, and J. D. Joannopoulos, "Iterative minimization techniques for ab initio total-energy calculations: molecular dynamics and conjugate gradients," *Rev. Mod. Phys.*, vol. 64, no. 4, pp. 1045–1097, oct 1992. [Online]. Available: https://link.aps.org/doi/10.1103/RevModPhys.64.1045

[95] G. Kresse and J. Hafner, "Ab initio molecular dynamics for open-shell transition metals," *Phys. Rev. B*, vol. 48, no. 17, pp. 13 115–13 118, nov 1993. [Online]. Available: https://link.aps.org/doi/10.1103/PhysRevB.48.13115

[96] G. Kresse and J. Furthmüller, "Efficient iterative schemes for ab initio total-energy calculations using a plane-wave basis set," *Phys. Rev. B*, vol. 54, no. 16, pp. 11 169–11 186, oct 1996. [Online]. Available: https://link.aps.org/doi/10.1103/PhysRevB.54.11169

[97] G. Kresse and D. Joubert, "From ultrasoft pseudopotentials to the projector augmented-wave method," *Phys. Rev. B*, vol. 59, no. 3, pp. 1758–1775, jan 1999. [Online]. Available: https://link.aps.org/doi/10.1103/PhysRevB.59.1758

[98] P. E. Blöchl, "Projector augmented-wave method," *Phys. Rev. B*, vol. 50, no. 24, pp. 17 953–17 979, dec 1994. [Online]. Available: https://link.aps.org/doi/10.1103/PhysRevB.50.17953

[99] J. P. Perdew, K. Burke, and M. Ernzerhof, "Generalized Gradient Approximation Made Simple," *Phys. Rev. Lett.*, vol. 77, no. 18, pp. 3865–3868, oct 1996. [Online]. Available: https://link.aps.org/doi/10.1103/PhysRevLett.77.3865

[100] J. D. Pack and H. J. Monkhorst, "Special points for Brillouin-zone integrations," *Phys. Rev. B*, vol. 16, no. 4, pp. 1748–1749, aug 1977. [Online]. Available: https://link.aps.org/doi/10.1103/PhysRevB.16.1748

[101] S. Grimme, J. Antony, S. Ehrlich, and H. Krieg, "A consistent and accurate ab initio parametrization of density functional dispersion correction (DFT-D) for the 94 elements H-Pu," *J. Chem. Phys.*, vol. 132, no. 15, p. 154104, apr 2010. [Online]. Available: http://aip.scitation.org/doi/10.1063/1.3382344

[102] S. Grimme, S. Ehrlich, and L. Goerigk, "Effect of the damping function in dispersion corrected density functional theory," *J. Comput. Chem.*, vol. 32, no. 7, pp. 1456–1465, may 2011. [Online]. Available: http://doi.wiley.com/10.1002/jcc.21759

[103] Q. Zhang, Y. Wang, Z. W. Seh, Z. Fu, R. Zhang, and Y. Cui, "Understanding the Anchoring Effect of Two-Dimensional Layered Materials for LithiumSulfur Batteries," *Nano Lett.*, vol. 15, no. 6, pp. 3780–3786, jun 2015. [Online]. Available: http://pubs.acs.org/doi/10.1021/acs.nanolett.5b00367

[104] D. Marx and J. Hutter, *Ab Initio Molecular Dynamics*. Cambridge: Cambridge University Press, 2009.

[105] M. Parrinello and A. Rahman, "Crystal Structure and Pair Potentials: A Molecular-Dynamics Study," *Phys. Rev. Lett.*, vol. 45, no. 14, pp. 1196–1199, oct 1980. [Online]. Available: http://link.aps.org/doi/10.1103/PhysRevLett.45.1196 https://link.aps.org/doi/10.1103/PhysRevLett.45.1196

[106] ——, "Polymorphic transitions in single crystals: A new molecular dynamics method," *J. Appl. Phys.*, vol. 52, no. 12, pp. 7182–7190, dec 1981. [Online]. Available: http://aip.scitation.org/doi/10.1063/1.328693

[107] M. P. Allen and D. J. Tildesley, "Computer simulation of liquids," *Oxford Univ. Press*, vol. 45, p. 121, 1989.

[108] T. Schlick, *Molecular modeling and simulation: an interdisciplinary guide: an interdisciplinary guide*. Springer Science & Business Media, 2010, vol. 21.

[109] M. Barghamadi, A. Kapoor, and C. Wen, "A Review on Li-S Batteries as a High Efficiency Rechargeable Lithium Battery," *J. Electrochem. Soc.*, vol. 160, no. 8, pp. A1256—-A1263, may 2013. [Online]. Available: http://jes.ecsdl.org/cgi/doi/10.1149/2.096308jes

[110] P. P. Mukherjee, Q. Kang, and C.-Y. Wang, "Pore-scale modeling of two-phase transport in polymer electrolyte fuel cellsprogress and perspective," *Energy Environ. Sci.*, vol. 4, no. 2, pp. 346–369, 2011. [Online]. Available: http://xlink.rsc.org/?DOI=B926077C

[111] S. Cho, C.-F. Chen, and P. P. Mukherjee, "Influence of Microstructure on Impedance Response in Intercalation Electrodes," *J. Electrochem. Soc.*, vol. 162, no. 7, pp. A1202—-A1214, apr 2015. [Online]. Available: http://jes.ecsdl.org/cgi/doi/10.1149/2.0331507jes

[112] C.-F. Chen and P. P. Mukherjee, "Probing the morphological influence on solid electrolyte interphase and impedance response in intercalation electrodes," *Phys. Chem. Chem. Phys.*, vol. 17, no. 15, pp. 9812–9827, 2015. [Online]. Available: http://xlink.rsc.org/?DOI=C4CP05758A

[113] Y.-H. Chen, C.-W. Wang, X. Zhang, and A. M. Sastry, "Porous cathode optimization for lithium cells: Ionic and electronic conductivity, capacity, and selection of materials," *J. Power Sources*, vol. 195, no. 9, pp. 2851–2862, may 2010. [Online]. Available: http://linkinghub.elsevier.com/retrieve/pii/S0378775309020527

[114] A. Gupta, J. H. Seo, X. Zhang, W. Du, A. M. Sastry, and W. Shyy, "Effective Transport Properties of LiMn2O4 Electrode via Particle-Scale Modeling," *J. Electrochem. Soc.*, vol. 158, no. 5, p. A487, 2011. [Online]. Available: http://jes.ecsdl.org/cgi/doi/10.1149/1.3560441

[115] K. S. Suslick, "Sonochemistry," *Science (80-.).*, vol. 247, no. 4949, pp. 1439–1445, 1990.

[116] H. Xu, B. W. Zeiger, and K. S. Suslick, "Sonochemical synthesis of nanomaterials," *Chem. Soc. Rev.*, vol. 42, no. 7, pp. 2555–2567, 2013. [Online]. Available: http://xlink.rsc.org/?DOI=C2CS35282F

[117] R. T. Downs and M. Hall-Wallace, "The American Mineralogist crystal structure database," *Am. Mineral.*, vol. 88, pp. 247–250, 2003. [Online]. Available: http://www.geo.arizona.edu/xtal//group/pdf/am88_247.pdf

[118] N. Azimi, Z. Xue, I. Bloom, M. L. Gordin, D. Wang, T. Daniel, C. Takoudis, and Z. Zhang, "Understanding the Effect of a Fluorinated Ether on the Performance of LithiumSulfur Batteries," *ACS Appl. Mater. Interfaces*, vol. 7, no. 17, pp. 9169–9177, may 2015. [Online]. Available: http://pubs.acs.org/doi/10.1021/acsami.5b01412

[119] S. Drvarič Talian, S. Jeschke, A. Vizintin, K. Pirnat, I. Arčon, G. Aquilanti, P. Johansson, and R. Dominko, "Fluorinated Ether Based Electrolyte for High-Energy LithiumSulfur Batteries: Li + Solvation Role Behind Reduced Polysulfide Solubility," *Chem. Mater.*, vol. 29, no. 23, pp. 10 037–10 044, dec 2017. [Online]. Available: http://pubs.acs.org/doi/10.1021/acs.chemmater.7b03654

[120] Y. Diao, K. Xie, S. Xiong, and X. Hong, "Insights into Li-S Battery Cathode Capacity Fading Mechanisms: Irreversible Oxidation of Active Mass during Cycling," *J. Electrochem. Soc.*, vol. 159, no. 11, pp. A1816—-A1821, sep 2012. [Online]. Available: http://jes.ecsdl.org/cgi/doi/10.1149/2.020211jes

[121] Z. Liu, D. Hubble, P. B. Balbuena, and P. P. Mukherjee, "Adsorption of insoluble polysulfides Li 2 S x (x = 1, 2) on Li 2 S surfaces," *Phys. Chem. Chem. Phys.*, vol. 17, no. 14, pp. 9032–9039, 2015. [Online]. Available: http://xlink.rsc.org/?DOI=C4CP06118G

[122] K. T. Chan, J. B. Neaton, and M. L. Cohen, "First-principles study of metal adatom adsorption on graphene," *Phys. Rev. B*, vol. 77, no. 23, p. 235430, jun 2008. [Online]. Available: https://link.aps.org/doi/10.1103/PhysRevB.77.235430

[123] B. Liu and H. C. Zeng, "Hydrothermal Synthesis of ZnO Nanorods in the Diameter Regime of 50 nm," *J. Am. Chem. Soc.*, vol. 125, no. 15, pp. 4430–4431, apr 2003. [Online]. Available: http://pubs.acs.org/doi/abs/10.1021/ja0299452

[124] X. Feng, K. Shankar, O. K. Varghese, M. Paulose, T. J. Latempa, and C. a. Grimes, "Vertically Aligned Single Crystal TiO 2 Nanowire Arrays Grown Directly on Transparent Conducting Oxide Coated Glass: Synthesis Details and Applications," *Nano Lett.*, vol. 8, no. 11, pp. 3781–3786, nov 2008. [Online]. Available: http://pubs.acs.org/doi/abs/10.1021/nl802096a

[125] J. Chen, "Recent Progress in Advanced Materials for Lithium Ion Batteries," *Materials (Basel).*, vol. 6, no. 1, pp. 156–183, jan 2013. [Online]. Available: http://www.mdpi.com/1996-1944/6/1/156

[126] K. Byrappa and T. Adschiri, "Hydrothermal technology for nanotechnology," *Prog. Cryst. Growth Charact. Mater.*, vol. 53, no. 2, pp. 117–166, jun 2007. [Online]. Available: http://linkinghub.elsevier.com/retrieve/pii/S0960897407000150

[127] B. L. Cushing, V. L. Kolesnichenko, and C. J. O'Connor, "Recent Advances in the Liquid-Phase Syntheses of Inorganic Nanoparticles," *Chem. Rev.*, vol. 104, no. 9, pp. 3893–3946, sep 2004. [Online]. Available: http://pubs.acs.org/doi/abs/10.1021/cr030027b

[128] C. Di Blasi, "Modeling chemical and physical processes of wood and biomass pyrolysis," *Prog. Energy Combust. Sci.*, vol. 34, no. 1, pp. 47–90, feb 2008. [Online]. Available: http://linkinghub.elsevier.com/retrieve/pii/S0360128507000214

[129] A. V. Bridgwater, "Review of fast pyrolysis of biomass and product upgrading," *Biomass and Bioenergy*, vol. 38, pp. 68–94, mar 2012. [Online]. Available: http://dx.doi.org/10.1016/j.biombioe.2011.01.048 http://linkinghub.elsevier.com/retrieve/pii/S0961953411000638

[130] H. S. Kambo and A. Dutta, "A comparative review of biochar and hydrochar in terms of production, physico-chemical properties and applications," *Renew. Sustain. Energy Rev.*, vol. 45, pp. 359–378, may 2015. [Online]. Available: http://dx.doi.org/10.1016/j.rser.2015.01.050 http://linkinghub.elsevier.com/retrieve/pii/S136403211500060X

[131] D. Mohan, C. U. Pittman, and P. H. Steele, "Pyrolysis of Wood/Biomass for Bio-oil: A Critical Review," *Energy & Fuels*, vol. 20, no. 3, pp. 848–889, may 2006. [Online]. Available: http://pubs.acs.org/doi/abs/10.1021/ef0502397

[132] S.-J. C. Tsai, E. Ada, J. A. Isaacs, and M. J. Ellenbecker, "Airborne nanoparticle exposures associated with the manual handling of nanoalumina and nanosilver in fume hoods," *J. Nanoparticle Res.*, vol. 11, no. 1, pp. 147–161, jan 2009. [Online]. Available: http://link.springer.com/10.1007/s11051-008-9459-z

[133] D. Bello, A. J. Hart, K. Ahn, M. Hallock, N. Yamamoto, E. J. Garcia, M. J. Ellenbecker, and B. L. Wardle, "Particle exposure levels during CVD growth and subsequent handling of vertically-aligned carbon nanotube films," *Carbon N. Y.*, vol. 46, no. 6, pp. 974–977, may 2008. [Online]. Available: http://linkinghub.elsevier.com/retrieve/pii/S0008622308001346

[134] M. M. Dahm, D. E. Evans, M. K. Schubauerberigan, M. E. Birch, and J. E. Fernback, "Occupational Exposure Assessment in Carbon Nanotube and Nanofiber Primary and Secondary Manufacturers," *Ann. Occup. Hyg.*, vol. 56, no. 5, pp. 542–556, jun 2012. [Online]. Available: https://academic.oup.com/annweh/article/56/5/542/159798/Occupational-Exposure-Assessment-in-Carbon

[135] S.-J. C. Tsai, M. Hofmann, M. Hallock, E. Ada, J. Kong, and M. Ellenbecker, "Characterization and Evaluation of Nanoparticle Release during the Synthesis of Single-Walled and Multiwalled Carbon Nanotubes by Chemical Vapor Deposition," *Environ. Sci. Technol.*, vol. 43, no. 15, pp. 6017–6023, aug 2009. [Online]. Available: http://pubs.acs.org/doi/abs/10.1021/es900486y

[136] J. Park, B. K. Kwak, E. Bae, J. Lee, Y. Kim, K. Choi, and J. Yi, "Characterization of exposure to silver nanoparticles in a manufacturing facility," *J. Nanoparticle Res.*, vol. 11, no. 7, pp. 1705–1712, oct 2009. [Online]. Available: http://link.springer.com/10.1007/s11051-009-9725-8

[137] C. S.-J. Tsai, "Potential inhalation exposure and containment efficiency when using hoods for handling nanoparticles," *J. Nanoparticle Res.*, vol. 15, no. 9, p. 1880, sep 2013. [Online]. Available: http://link.springer.com/10.1007/s11051-013-1880-2

[138] P. L. Drake and K. J. Hazelwood, "Exposure-Related Health Effects of Silver and Silver Compounds: A Review," *Ann. Occup. Hyg.*, vol. 49, no. 7, pp. 575–585, jun 2005. [Online]. Available: https://academic.oup.com/annweh/article/49/7/575/148203/ExposureRelated-Health-Effects-of-Silver-and

[139] A. Gojova, B. Guo, R. S. Kota, J. C. Rutledge, I. M. Kennedy, and A. I. Barakat, "Induction of Inflammation in Vascular Endothelial Cells by Metal Oxide Nanoparticles: Effect of Particle Composition," *Environ. Health Perspect.*, vol. 115, no. 3, pp. 403–409, dec 2006. [Online]. Available: http://www.ncbi.nlm.nih.gov/pmc/articles/PMC1849911/

[140] Y. Y. Tyurina, E. R. Kisin, A. Murray, V. A. Tyurin, V. I. Kapralova, L. J. Sparvero, A. A. Amoscato, A. K. Samhan-Arias, L. Swedin, R. Lahesmaa, B. Fadeel, A. A. Shvedova, and V. E. Kagan, "Global Phospholipidomics Analysis Reveals Selective Pulmonary Peroxidation Profiles upon Inhalation of Single-Walled Carbon Nanotubes," *ACS Nano*, vol. 5, no. 9, pp. 7342–7353, sep 2011. [Online]. Available: http://pubs.acs.org/doi/10.1021/nn202201j

[141] G. Jia, H. Wang, L. Yan, X. Wang, R. Pei, T. Yan, Y. Zhao, and X. Guo, "Cytotoxicity of Carbon Nanomaterials: Single-Wall Nanotube, Multi-Wall Nanotube, and Fullerene," *Environ. Sci. Technol.*, vol. 39, no. 5, pp. 1378–1383, mar 2005. [Online]. Available: http://pubs.acs.org/doi/abs/10.1021/es048729l

[142] C. L. Ursini, D. Cavallo, A. M. Fresegna, A. Ciervo, R. Maiello, G. Buresti, S. Casciardi, F. Tombolini, S. Bellucci, and S. Iavicoli, "Comparative cyto-genotoxicity assessment of functionalized and pristine multiwalled carbon nanotubes on human lung epithelial cells," *Toxicol. Vitr.*, vol. 26, no. 6, pp. 831–840, sep 2012. [Online]. Available: http://dx.doi.org/10.1016/j.tiv.2012.05.001 http://linkinghub.elsevier.com/retrieve/pii/S0887233312001348

[143] N. Singh, K. Kaur, H. Singh, and H. Singh, "Effect of starch-lipids inclusion complex formation on functional properties of flour in tandoori roti," *Food Chem.*, vol. 69, no. 2, pp. 129–133, may 2000. [Online]. Available: http://linkinghub.elsevier.com/retrieve/pii/S0308814699002290

[144] K. R. Parimala and M. L. Sudha, "Wheat-Based Traditional Flat Breads of India," *Crit. Rev. Food Sci. Nutr.*, vol. 55, no. 1, pp. 67–81, jan 2015. [Online]. Available: http://www.tandfonline.com/doi/abs/10.1080/10408398.2011.647121

[145] D. C. Saxena, P. V. Salimath, and P. H. Rao, "Indian wheat cultivars: their carbohydrate profile and its relation to tandoori roti quality," *Food Chem.*, vol. 68, no. 2, pp. 185–190, feb 2000. [Online]. Available: http://linkinghub.elsevier.com/retrieve/pii/S0308814699001740

[146] F. Zhang, H. Ma, J. Chen, G.-D. Li, Y. Zhang, and J.-S. Chen, "Preparation and gas storage of high surface area microporous carbon derived from biomass source cornstalks," *Bioresour. Technol.*, vol. 99, no. 11, pp. 4803–4808, jul 2008. [Online]. Available: http://linkinghub.elsevier.com/retrieve/pii/S0960852407007973

[147] F. Cheng, J. Liang, J. Zhao, Z. Tao, and J. Chen, "Biomass Waste-Derived Microporous Carbons with Controlled Texture and Enhanced Hydrogen Uptake," *Chem. Mater.*, vol. 20, no. 5, pp. 1889–1895, mar 2008. [Online]. Available: http://pubs.acs.org/doi/abs/10.1021/cm702816x

[148] V. Veeramani, R. Madhu, S.-M. Chen, B.-S. Lou, J. Palanisamy, and V. S. Vasantha, "Biomass-derived functional porous carbons as novel electrode material for the practical detection of biomolecules in human serum and snail hemolymph," *Sci. Rep.*, vol. 5, no. 1, p. 10141, sep 2015. [Online]. Available: http://dx.doi.org/10.1038/srep10141 http://www.nature.com/articles/srep10141

[149] Y. Zhai, Y. Dou, D. Zhao, P. F. Fulvio, R. T. Mayes, and S. Dai, "Carbon Materials for Chemical Capacitive Energy Storage," *Adv. Mater.*, vol. 23, no. 42, pp. 4828–4850, nov 2011. [Online]. Available: http://doi.wiley.com/10.1002/adma.201100984

[150] S. Cordero, I. Kornhauser, A. Domínguez, C. Felipe, J. M. Esparza, F. Rojas, R. H. López, A. M. Vidales, J. L. Riccardo, and G. Zgrablich, "Site-Bond Network Modeling of Disordered Porous Media," *Part. Part. Syst. Charact.*, vol. 21, no. 2, pp. 101–116, aug 2004. [Online]. Available: http://doi.wiley.com/10.1002/ppsc.200400926

[151] H. Wei, S. Deng, B. Hu, Z. Chen, B. Wang, J. Huang, and G. Yu, "Granular Bamboo-Derived Activated Carbon for High CO 2 Adsorption: The Dominant Role of Narrow Micropores," *ChemSusChem*, vol. 5, no. 12, pp. 2354–2360, dec 2012. [Online]. Available: http://doi.wiley.com/10.1002/cssc.201200570

[152] G. Ning and B. N. Popov, "Cycle Life Modeling of Lithium-Ion Batteries," *J. Electrochem. Soc.*, vol. 151, no. 10, p. A1584, 2004. [Online]. Available: http://jes.ecsdl.org/cgi/doi/10.1149/1.1787631

[153] P. Buryan and M. Staff, "Pyrolysis of the waste biomass," *J. Therm. Anal. Calorim.*, vol. 93, no. 2, pp. 637–640, aug 2008. [Online]. Available: http://link.springer.com/10.1007/s10973-007-8700-9

[154] T. Prasomsri, T. Nimmanwudipong, and Y. Román-Leshkov, "Effective hydrodeoxygenation of biomass-derived oxygenates into unsaturated hydrocarbons by MoO3 using low H2 pressures," *Energy Environ. Sci.*, vol. 6, no. 6, p. 1732, 2013. [Online]. Available: http://xlink.rsc.org/?DOI=c3ee24360e

[155] C. S. J. Tsai, M. E. Echevarría-Vega, G. A. Sotiriou, C. Santeufemio, D. Schmidt, P. Demokritou, and M. Ellenbecker, "Evaluation of environmental filtration control of engineered nanoparticles using the Harvard Versatile Engineered Nanomaterial Generation System (VENGES)," *J. Nanoparticle Res.*, vol. 14, no. 5, p. 812, may 2012. [Online]. Available: http://link.springer.com/10.1007/s11051-012-0812-x

[156] B. Dunn, H. Kamath, and J.-M. Tarascon, "Electrical Energy Storage for the Grid: A Battery of Choices," *Science (80-.).*, vol. 334, no. 6058, pp. 928–935, nov 2011. [Online]. Available: http://www.sciencemag.org/cgi/doi/10.1126/science.1212741

[157] H. Ibrahim, A. Ilinca, and J. Perron, "Energy storage systemsCharacteristics and comparisons," *Renew. Sustain. Energy Rev.*, vol. 12, no. 5, pp. 1221–1250, jun 2008. [Online]. Available: http://linkinghub.elsevier.com/retrieve/pii/S1364032107000238

[158] M. Beaudin, H. Zareipour, A. Schellenberglabe, and W. Rosehart, "Energy storage for mitigating the variability of renewable electricity sources: An updated review," *Energy Sustain. Dev.*, vol. 14, no. 4, pp. 302–314, dec 2010. [Online]. Available: http://www.sciencedirect.com/science/article/pii/S0973082610000566 http://linkinghub.elsevier.com/retrieve/pii/S0973082610000566

[159] P. J. Hall and E. J. Bain, "Energy-storage technologies and electricity generation," *Energy Policy*, vol. 36, no. 12, pp. 4352–4355, dec 2008. [Online]. Available: http://linkinghub.elsevier.com/retrieve/pii/S0301421508004497

[160] M. Yilmaz and P. T. Krein, "Review of charging power levels and infrastructure for plug-in electric and hybrid vehicles," in *2012 IEEE Int. Electr. Veh. Conf.*, vol. 28, no. 5. IEEE, mar 2012, pp. 1–8. [Online]. Available: http://ieeexplore.ieee.org/document/6183208/

[161] C. Capasso and O. Veneri, "Experimental analysis on the performance of lithium based batteries for road full electric and hybrid vehicles," *Appl. Energy*, vol. 136, pp. 921–930, dec 2014. [Online]. Available: http://dx.doi.org/10.1016/j.apenergy.2014.04.013 http://linkinghub.elsevier.com/retrieve/pii/S0306261914003560

[162] A. Nordelöf, M. Messagie, A.-M. Tillman, M. Ljunggren Söderman, and J. Van Mierlo, "Environmental impacts of hybrid, plug-in hybrid, and battery electric vehicleswhat can we learn from life cycle assessment?" *Int. J. Life Cycle Assess.*, vol. 19, no. 11, pp. 1866–1890, nov 2014. [Online]. Available: http://link.springer.com/10.1007/s11367-014-0788-0

[163] K. Richa, C. W. Babbitt, N. G. Nenadic, and G. Gaustad, "Environmental trade-offs across cascading lithium-ion battery life cycles," *Int. J. Life Cycle Assess.*, vol. 22, no. 1, pp. 66–81, jan 2017. [Online]. Available: http://dx.doi.org/10.1007/s11367-015-0942-3 http://link.springer.com/10.1007/s11367-015-0942-3

[164] A. Pehlken, S. Albach, and T. Vogt, "Is there a resource constraint related to lithium ion batteries in cars?" *Int. J. Life Cycle Assess.*, vol. 22, no. 1, pp. 40–53, jan 2017. [Online]. Available: http://link.springer.com/10.1007/s11367-015-0925-4

[165] L. A.-W. Ellingsen, G. Majeau-Bettez, B. Singh, A. K. Srivastava, L. O. Valøen, and A. H. Strømman, "Life Cycle Assessment of a Lithium-Ion Battery Vehicle Pack," *J. Ind. Ecol.*, vol. 18, no. 1, pp. 113–124, feb 2014. [Online]. Available: http://doi.wiley.com/10.1111/jiec.12072

[166] D. A. Notter, M. Gauch, R. Widmer, P. Wager, A. Stamp, R. Zah, and H.-J. Althaus, "Contribution of Li-Ion Batteries to the Environmental Impact of Electric Vehicles," *Environ. Sci. Technol.*, vol. 44, no. 17, pp. 6550–6556, sep 2010. [Online]. Available: http://pubs.acs.org/doi/abs/10.1021/es903729a

[167] L. Gaines and R. Cuenca, "Life-Cycle Costs of Lithium-Ion Vehicle Batteries," ANL/ESD-42, Tech. Rep., 2000.

[168] Hittman Associates, "Life-cycle energy analyses of electric vehicle storage batteries," U.S. Department of Energy, Tech. Rep., 1980.

[169] N. Arena, J. Lee, and R. Clift, "Life Cycle Assessment of activated carbon production from coconut shells," *J. Clean. Prod.*, vol. 125, pp. 68–77, jul 2016. [Online]. Available: http://dx.doi.org/10.1016/j.jclepro.2016.03.073 http://linkinghub.elsevier.com/retrieve/pii/S0959652616301421

[170] M. M. Labes, "Process for production of graphite flakes and films via low temperature pyrolysis," 1992.

[171] W. von Lensa, D. Vulpius, H. Steinmetz, A. W. Banford, D. Bradbury, J. M. Graves, A. N. N. Jones, B. Grambow, L. Petit, G. Pina, D. Vulpius, and A. W. Banford, "Treatment and Disposal of irradiated Graphite and other Carbonaceous Waste," *ATW - Int. J. Nucl. Power.*, vol. 56, p. 263, 2011.

[172] M. M. Tang and R. Bacon, "Carbonization of cellulose fibersI. Low temperature pyrolysis," *Carbon N. Y.*, vol. 2, no. 3, pp. 211–220, dec 1964. [Online]. Available: http://linkinghub.elsevier.com/retrieve/pii/0008622364900351

[173] S. A. Clyburn, T. Kantor, and C. Veillon, "Pyrolysis treatment for graphite atomization systems," *Anal. Chem.*, vol. 46, no. 14, pp. 2213–2215, dec 1974. [Online]. Available: http://pubs.acs.org/doi/abs/10.1021/ac60350a031

[174] G. Majeau-Bettez, T. R. Hawkins, and A. H. Strømman, "Life Cycle Environmental Assessment of Lithium-Ion and Nickel Metal Hydride Batteries for Plug-In Hybrid and Battery Electric Vehicles," *Environ. Sci. Technol.*, vol. 45, no. 10, pp. 4548–4554, may 2011. [Online]. Available: http://pubs.acs.org/doi/abs/10.1021/es103607c

[175] C. J. Rydh and B. A. Sandén, "Energy analysis of batteries in photovoltaic systems. Part I: Performance and energy requirements," *Energy Convers. Manag.*, vol. 46, no. 11-12, pp. 1957–1979, jul 2005. [Online]. Available: http://linkinghub.elsevier.com/retrieve/pii/S0196890404002407

[176] D. Whitford, "The Snack Food that's Packing America," 1996. [Online]. Available: http://www.inc.com/magazine/19961001/1828.html

[177] C. S. J. Tsai, A. D. Dysart, J. H. Beltz, and V. G. Pol, "Identification and Mitigation of Generated Solid By-Products during Advanced Electrode Materials Processing," *Environ. Sci. Technol.*, vol. 50, no. 5, pp. 2627–2634, mar 2016. [Online]. Available: http://pubs.acs.org/doi/10.1021/acs.est.5b03610

[178] V. Etacheri, C. N. Hong, and V. G. Pol, "Upcycling of Packing-Peanuts into Carbon Microsheet Anodes for Lithium-Ion Batteries," *Environ. Sci. Technol.*, vol. 49, no. 18, pp. 11 191–11 198, sep 2015. [Online]. Available: http://pubs.acs.org/doi/abs/10.1021/acs.est.5b01896 http://pubs.acs.org/doi/10.1021/acs.est.5b01896

[179] Robinair, "Vacuum pump operating manual, Model 15500."

[180] National Renewable Energy Laboratory, "U.S. Life cycle inventory database," 2012. [Online]. Available: https://www.lcacommons.gov/nrel/search

[181] Ecoinvent, "The Ecoinvent database." [Online]. Available: http://www.ecoinvent.org/database/database.html

[182] European Commission, "European Life Cycle Database." [Online]. Available: http://eplca.jrc.ec.europa.eu/ELCD3/

[183] Z. Q. Li, C. J. Lu, Z. P. Xia, Y. Zhou, and Z. Luo, "X-ray diffraction patterns of graphite and turbostratic carbon," *Carbon N. Y.*, vol. 45, no. 8, pp. 1686–1695, jul 2007. [Online]. Available: http://linkinghub.elsevier.com/retrieve/pii/S0008622307001467

[184] L. J. Childres, W. Park, H. Cao, and Y. Chen, "RAMAN SPECTROSCOPY OF GRAPHENE AND RELATED MATERIALS," in *New Dev. Phot. Mater. Res.* Elsevier, 2013.

[185] A. Umair, T. Z. Raza, and H. Raza, "Ultrathin pyrolytic carbon films on a magnetic substrate," *Mater. Res. Express*, vol. 3, no. 7, p. 75601, jul 2016.

[186] C. Jiang, E. Hosono, and H. Zhou, "Nanomaterials for lithium ion batteries," *Nano Today*, vol. 1, no. 4, pp. 28–33, 2006.

[187] K. Persson, V. A. Sethuraman, L. J. Hardwick, Y. Hinuma, Y. S. Meng, A. Van Der Ven, V. Srinivasan, R. Kostecki, and G. Ceder, "Lithium diffusion in graphitic carbon," *J. Phys. Chem. Lett.*, vol. 1, no. 8, pp. 1176–1180, 2010.

[188] K. Kim, R. A. Adams, P. J. Kim, A. Arora, E. Martinez, J. P. Youngblood, and V. G. Pol, "Li-ion storage in an amorphous, solid, spheroidal carbon anode produced by dry-autoclaving of coffee oil," *Carbon N. Y.*, vol. 133, pp. 62–68, 2018. [Online]. Available: http://linkinghub.elsevier.com/retrieve/pii/S0008622318302562 https://doi.org/10.1016/j.carbon.2018.03.013

[189] S. Zhao, Y. Fan, K. Zhu, D. Zhang, W. Zhang, S. Chen, R. Liu, M. Yao, and B. Liu, "The effect of hydrogenation on the growth of carbon nanospheres and their performance as anode materials for rechargeable lithium-ion batteries," *Nanoscale*, vol. 7, no. 5, pp. 1984–1993, 2015. [Online]. Available: http://xlink.rsc.org/?DOI=C4NR05339G http://www.scopus.com/inward/record.url?eid=2-s2.0-84921727639&partnerID=40&md5=164b0a8a39cd8475784d46d94118c0af

[190] S. Wang, R. Wang, Y. Zhang, and L. Zhang, "Highly porous carbon with large electrochemical ion absorption capability for high-performance supercapacitors and ion capacitors," *Nanotechnology*, vol. 28, no. 44, p. 445406, nov 2017. [Online]. Available: http://stacks.iop.org/0957-4484/28/i=44/a=445406?key=crossref.9488de5e96c3fdc0d644d67bbdf398fe

[191] Q. Huang, S. Wang, Y. Zhang, B. Yu, L. Hou, G. Su, S. Ma, J. Zou, and H. Huang, "Hollow Carbon Nanospheres with Extremely Small Size as Anode Material in Lithium-Ion Batteries with Outstanding Cycling Stability," *J. Phys. Chem. C*, vol. 120, no. 6, pp. 3139–3144, feb 2016. [Online]. Available: http://pubs.acs.org/doi/10.1021/acs.jpcc.5b10455

[192] Y. P. Wu, E. Rahm, and R. Holze, "Carbon anode materials for lithium ion batteries," *J. Power Sources*, vol. 114, no. 2, pp. 228–236, mar 2003. [Online]. Available: http://linkinghub.elsevier.com/retrieve/pii/S0378775302005967

[193] M. Yoshio, H. Wang, K. Fukuda, T. Umeno, T. Abe, and Z. Ogumi, "Improvement of natural graphite as a lithium-ion battery anode material, from raw flake to carbon-coated sphere," *J. Mater. Chem.*, vol. 14, no. 11, p. 1754, 2004. [Online]. Available: http://xlink.rsc.org/?DOI=b316702j

[194] C. S. Wang, G. T. Wu, and W. Z. Li, "Lithium insertion in ball-milled graphite," *J. Power Sources*, vol. 76, no. 1, pp. 1–10, nov 1998. [Online]. Available: http://linkinghub.elsevier.com/retrieve/pii/S0378775398001141

[195] M. Winter, "Graphites for Lithium-Ion Cells: The Correlation of the First-Cycle Charge Loss with the Brunauer-Emmett-Teller Surface Area," *J. Electrochem. Soc.*, vol. 145, no. 2, p. 428, 1998. [Online]. Available: http://jes.ecsdl.org/cgi/doi/10.1149/1.1838281

[196] S. E. Trask, Y. Li, J. J. Kubal, M. Bettge, B. J. Polzin, Y. Zhu, A. N. Jansen, and D. P. Abraham, "From coin cells to 400 mAh pouch cells: Enhancing performance of high-capacity lithium-ion cells via modifications in electrode constitution and fabrication," *J. Power Sources*, vol. 259, pp. 233–244, aug 2014. [Online]. Available: http://dx.doi.org/10.1016/j.jpowsour.2014.02.077 http://linkinghub.elsevier.com/retrieve/pii/S0378775314002705

[197] T. Ohzuku, "Formation of Lithium-Graphite Intercalation Compounds in Nonaqueous Electrolytes and Their Application as a Negative Electrode for a Lithium Ion (Shuttlecock) Cell," *J. Electrochem. Soc.*, vol. 140, no. 9, p. 2490, 1993. [Online]. Available: http://jes.ecsdl.org/cgi/doi/10.1149/1.2220849

[198] T. Abe, H. Fukuda, Y. Iriyama, and Z. Ogumi, "Solvated Li-Ion Transfer at Interface Between Graphite and Electrolyte," *J. Electrochem. Soc.*, vol. 151, no. 8, p. A1120, 2004. [Online]. Available: http://jes.ecsdl.org/cgi/doi/10.1149/1.1763141

[199] J. S. Gnanaraj, R. W. Thompson, J. F. DiCarlo, and K. M. Abraham, "The Role of Carbonate Solvents on Lithium Intercalation into Graphite," *J. Electrochem. Soc.*, vol. 154, no. 3, p. A185, 2007. [Online]. Available: http://jes.ecsdl.org/cgi/doi/10.1149/1.2424419

[200] V. Manev, I. Naidenov, B. Puresheva, and G. Pistoia, "Effect of electrode porosity on the performance of natural Brazilian graphite electrodes," *J. Power Sources*, vol. 57, no. 1-2, pp. 133–136, sep 1995. [Online]. Available: http://linkinghub.elsevier.com/retrieve/pii/0378775395022686

[201] S. Flandrois and B. Simon, "Carbon materials for lithium-ion rechargeable batteries," *Carbon N. Y.*, vol. 37, no. 2, pp. 165–180, feb 1999. [Online]. Available: http://linkinghub.elsevier.com/retrieve/pii/S0008622398002905

[202] C. Birkenmaier, B. Bitzer, M. Harzheim, A. Hintennach, and T. Schleid, "Lithium Plating on Graphite Negative Electrodes: Innovative Qualitative and Quantitative Investigation Methods," *J. Electrochem. Soc.*, vol. 162, no. 14, pp. A2646—-A2650, oct 2015. [Online]. Available: http://jes.ecsdl.org/lookup/doi/10.1149/2.0451514jes

[203] J. R. Dahn, T. Zheng, Y. Liu, and J. S. Xue, "Mechanisms for Lithium Insertion in Carbonaceous Materials," *Science (80-.).*, vol. 270, no. 5236, pp. 590 LP —- 593, oct 1995. [Online]. Available: http://science.sciencemag.org/content/270/5236/590.abstract

[204] J. Zhu, C. Chen, Y. Lu, Y. Ge, H. Jiang, K. Fu, and X. Zhang, "Nitrogen-doped carbon nanofibers derived from polyacrylonitrile for use as anode material in sodium-ion batteries," *Carbon N. Y.*, vol. 94, pp. 189–195, nov 2015. [Online]. Available: http://dx.doi.org/10.1016/j.carbon.2015.06.076 http://linkinghub.elsevier.com/retrieve/pii/S0008622315300245

[205] H. Fujimoto, K. Tokumitsu, A. Mabuchi, N. Chinnasamy, and T. Kasuh, "The anode performance of the hard carbon for the lithium ion battery derived from the oxygen-containing aromatic precursors," *J. Power Sources*, vol. 195, no. 21, pp. 7452–7456, nov 2010. [Online]. Available: http://dx.doi.org/10.1016/j.jpowsour.2010.05.041 http://linkinghub.elsevier.com/retrieve/pii/S0378775310009092

[206] Z. Yi, Y. Liang, X. Lei, C. Wang, and J. Sun, "Low-temperature synthesis of nanosized disordered carbon spheres as an anode material for lithium ion batteries," *Mater. Lett.*, vol. 61, no. 19-20, pp. 4199–4203, aug 2007. [Online]. Available: http://linkinghub.elsevier.com/retrieve/pii/S0167577X07000882

[207] X. Li, X. Zhu, Y. Zhu, Z. Yuan, L. Si, and Y. Qian, "Porous nitrogen-doped carbon vegetable-sponges with enhanced lithium storage performance," *Carbon N. Y.*, vol. 69, pp. 515–524, apr 2014. [Online]. Available: http://dx.doi.org/10.1016/j.carbon.2013.12.059 http://linkinghub.elsevier.com/retrieve/pii/S0008622313012141

[208] E. Buiel, "Reduction of the Irreversible Capacity in Hard-Carbon Anode Materials Prepared from Sucrose for Li-Ion Batteries," *J. Electrochem. Soc.*, vol. 145, no. 6, p. 1977, 1998. [Online]. Available: http://jes.ecsdl.org/content/145/6/1977.abstract http://jes.ecsdl.org/cgi/doi/10.1149/1.1838585

[209] L. G. Bulusheva, A. V. Okotrub, A. G. Kurenya, H. Zhang, H. Zhang, X. Chen, and H. Song, "Electrochemical properties of nitrogen-doped carbon nanotube anode in Li-ion batteries," *Carbon N. Y.*, vol. 49, no. 12, pp. 4013–4023, oct 2011. [Online]. Available: http://dx.doi.org/10.1016/j.carbon.2011.05.043 http://linkinghub.elsevier.com/retrieve/pii/S0008622311004064

[210] P. Liu, Y. Li, Y.-S. Hu, H. Li, L. Chen, and X. Huang, "A waste biomass derived hard carbon as a high-performance anode material for sodium-ion batteries," *J. Mater. Chem. A*, vol. 4, no. 34, pp. 13 046–13 052, 2016. [Online]. Available: http://xlink.rsc.org/?DOI=C6TA04877C

[211] E. M. Lotfabad, J. Ding, K. Cui, A. Kohandehghan, W. P. Kalisvaart, M. Hazelton, and D. Mitlin, "High-Density Sodium and Lithium Ion Battery Anodes from Banana Peels," *ACS Nano*, vol. 8, no. 7, pp. 7115–7129, jul 2014. [Online]. Available: http://pubs.acs.org/doi/10.1021/nn502045y

[212] Y. J. Hwang, S. K. Jeong, J. S. Shin, K. S. Nahm, and A. M. Stephan, "High capacity disordered carbons obtained from coconut shells as anode materials for lithium batteries," *J. Alloys Compd.*, vol. 448, no. 1-2, pp. 141–147, jan 2008. [Online]. Available: http://linkinghub.elsevier.com/retrieve/pii/S0925838806016264

[213] J. R. Dahn, W. Xing, and Y. Gao, "The falling cards model for the structure of microporous carbons," *Carbon N. Y.*, vol. 35, no. 6, pp. 825–830, 1997. [Online]. Available: http://linkinghub.elsevier.com/retrieve/pii/S0008622397000377

[214] T. Dawn and L. Batteries, "The Dawn of Lithium-ion Batteries," pp. 71–74, 2016.

[215] V. G. Pol, J. Wen, K. C. Lau, S. Callear, D. T. Bowron, C.-K. Lin, S. a. Deshmukh, S. Sankaranarayanan, L. a. Curtiss, W. I. F. David, D. J. Miller, and M. M. Thackeray, "Probing the evolution and morphology of hard carbon spheres," *Carbon N. Y.*, vol. 68, pp. 104–111, mar 2014. [Online]. Available: http://dx.doi.org/10.1016/j.carbon.2013.10.059 http://linkinghub.elsevier.com/retrieve/pii/S000862231301021X

[216] V. G. Pol, L. K. Shrestha, and K. Ariga, "Tunable, Functional Carbon Spheres Derived from Rapid Synthesis of Resorcinol-Formaldehyde Resins," *ACS Appl. Mater. Interfaces*, vol. 6, no. 13, pp. 10 649–10 655, jul 2014. [Online]. Available: http://pubs.acs.org/doi/10.1021/am502324m

[217] I. A. M. Ibrahim, A. A. F. Zikry, and M. A. Sharaf, "Preparation of spherical silica nanoparticles: Stober silica," *J. Am. Sci.*, vol. 6, no. 11, pp. 985–989, 2010.

[218] V. G. Pol, R. Reisfeld, and A. Gedanken, "Sonochemical Synthesis and Optical Properties of Europium Oxide Nanolayer Coated on Titania," *Chem. Mater.*, vol. 14, no. 9, pp. 3920–3924, sep 2002. [Online]. Available: http://pubs.acs.org/doi/abs/10.1021/cm0203464

[219] B. Narayanan, S. A. Deshmukh, L. K. Shrestha, K. Ariga, V. G. Pol, and S. K. R. S. Sankaranarayanan, "Cavitation and radicals drive the sonochemical synthesis of functional polymer spheres," *Appl. Phys. Lett.*, vol. 109, no. 4, p. 41901, jul 2016. [Online]. Available: http://aip.scitation.org/doi/10.1063/1.4959885

[220] A. A. Alazemi, A. D. Dysart, X. L. Phuah, V. G. Pol, and F. Sadeghi, "MoS 2 nanolayer coated carbon spheres as an oil additive for enhanced tribological performance," *Carbon N. Y.*, vol. 110, pp. 367–377, dec 2016.

[221] A. A. Alazemi, V. Etacheri, A. D. Dysart, L.-E. E. Stacke, V. G. Pol, and F. Sadeghi, "Ultrasmooth Submicrometer Carbon Spheres as Lubricant Additives for Friction and Wear Reduction," *ACS Appl. Mater. Interfaces*, vol. 7, no. 9, pp. 5514–5521, mar 2015. [Online]. Available: http://pubs.acs.org/doi/10.1021/acsami.5b00099

[222] K. S. Suslick, "The sonochemical hot spot," *J. Acoust. Soc. Am.*, vol. 89, no. 4B, pp. 1885–1886, apr 1991. [Online]. Available: http://asa.scitation.org/doi/10.1121/1.2029381

[223] G. A. Zickler, B. Smarsly, N. Gierlinger, H. Peterlik, and O. Paris, "A reconsideration of the relationship between the crystallite size La of carbons determined by X-ray diffraction and Raman spectroscopy," *Carbon N. Y.*, vol. 44, no. 15, pp. 3239–3246, dec 2006. [Online]. Available: http://linkinghub.elsevier.com/retrieve/pii/S0008622306003587

[224] A. C. Ferrari and J. Robertson, "Interpretation of Raman spectra of disordered and amorphous carbon," *Phys. Rev. B*, vol. 61, no. 20, pp. 14 095–14 107, may 2000. [Online]. Available: https://link.aps.org/doi/10.1103/PhysRevB.61.14095

[225] A. Perazzo, V. Preziosi, and S. Guido, "Phase inversion emulsification: Current understanding and applications," *Adv. Colloid Interface Sci.*, vol. 222, pp. 581–599, aug 2015. [Online]. Available: http://dx.doi.org/10.1016/j.cis.2015.01.001 http://linkinghub.elsevier.com/retrieve/pii/S0001868615000020

[226] A.-H. Lu, G.-P. Hao, and Q. Sun, "Can Carbon Spheres Be Created through the Stöber Method?" *Angew. Chemie Int. Ed.*, vol. 50, no. 39, pp. 9023–9025, sep 2011. [Online]. Available: http://doi.wiley.com/10.1002/anie.201103514

[227] G. Van Gils and G. E. Van Gils, "Study of the Reaction of Resorcinol,Formaldehyde, and Ammonia," *J. Appl. Polym. Sci.*, vol. 13, no. 5, pp. 835–849, may 1969. [Online]. Available: http://doi.wiley.com/10.1002/app.1969.070130503

[228] P. Parthasarathy, H. S. Choi, H. C. Park, J. G. Hwang, H. S. Yoo, B.-K. Lee, and M. Upadhyay, "Influence of process conditions on product yield of waste tyre pyrolysis- A review," *Korean J. Chem. Eng.*, vol. 33, no. 8, pp. 2268–2286, aug 2016. [Online]. Available: http://link.springer.com/10.1007/s11814-016-0126-2

[229] M. Tripathi, J. N. Sahu, and P. Ganesan, "Effect of process parameters on production of biochar from biomass waste through pyrolysis: A review," *Renew. Sustain. Energy Rev.*, vol. 55, pp. 467–481, mar 2016. [Online]. Available: http://dx.doi.org/10.1016/j.rser.2015.10.122 http://linkinghub.elsevier.com/retrieve/pii/S1364032115012010

[230] J. J. Manyà, "Pyrolysis for Biochar Purposes: A Review to Establish Current Knowledge Gaps and Research Needs," *Environ. Sci. Technol.*, vol. 46, no. 15, pp. 7939–7954, aug 2012. [Online]. Available: http://pubs.acs.org/doi/10.1021/es301029g

[231] P. L. Walker, H. A. McKinstry, and C. C. Wright, "X-Ray Diffraction Studies of a Graphitized Carbon - Changes in Interlayer Spacing and Binding Energy with Temperature." *Ind. Eng. Chem.*, vol. 45, no. 8, pp. 1711–1715, aug 1953. [Online]. Available: http://pubs.acs.org/doi/abs/10.1021/ie50524a033

[232] N. S. Saenko, "The X-ray diffraction study of three-dimensional disordered network of nanographites: Experiment and theory," *Phys. Procedia*, vol. 23, no. 2011, pp. 102–105, 2012. [Online]. Available: http://dx.doi.org/10.1016/j.phpro.2012.01.026 http://linkinghub.elsevier.com/retrieve/pii/S1875389212000272

[233] K. Guerin, A. Fevrier-Bouvier, S. Flandrois, B. Simon, and P. Biensan, "On the irreversible capacities of disordered carbons in lithium-ion rechargeable batteries," *Electrochim. Acta*, vol. 45, no. 10, pp. 1607–1615, jan 2000. [Online]. Available: http://linkinghub.elsevier.com/retrieve/pii/S0013468699003217

[234] J. Lachter, L. G. Henry, and R. H. Bragg, "Indirect determination of the incoherent scattering in disordered carbon materials," *J. Appl. Crystallogr.*, vol. 21, no. 2, pp. 92–96, apr 1988. [Online]. Available: http://scripts.iucr.org/cgi-bin/paper?S0021889887009427

[235] L. Lu, V. Sahajwalla, C. Kong, and D. Harris, "Quantative X-ray diffraction analysis and its application to various coals," *Carbon N. Y.*, vol. 39, pp. 1821–1833, jul 2001. [Online]. Available: http://linkinghub.elsevier.com/retrieve/pii/S0140670102860544

[236] A. C. Ferrari, "A Model to Interpret the Raman Spectra of Disordered, Amorphous and Nanostructured Carbons," *MRS Proc.*, vol. 675, p. W11.5.1, jan 2001. [Online]. Available: http://journals.cambridge.org/abstract_S1946427400626441

[237] M. S. Dresselhaus, A. Jorio, A. G. Souza Filho, and R. Saito, "Defect characterization in graphene and carbon nanotubes using Raman spectroscopy," *Philos. Trans. R. Soc. A Math. Phys. Eng. Sci.*, vol. 368, no. 1932, pp. 5355–5377, dec 2010. [Online]. Available: http://rsta.royalsocietypublishing.org/cgi/doi/10.1098/rsta.2010.0213

[238] H.-L. Liu, H. Guo, T. Yang, Z. Zhang, Y. Kumamoto, C.-C. Shen, Y.-T. Hsu, L.-J. Li, R. Saito, and S. Kawata, "Anomalous lattice vibrations of monolayer MoS 2 probed by ultraviolet Raman scattering," *Phys. Chem. Chem. Phys.*, vol. 17, no. 22, pp. 14 561–14 568, 2015. [Online]. Available: http://xlink.rsc.org/?DOI=C5CP01347J

[239] T. Zheng, "Hysteresis during Lithium Insertion in Hydrogen-Containing Carbons," *J. Electrochem. Soc.*, vol. 143, no. 7, p. 2137, 1996. [Online]. Available: http://jes.ecsdl.org/cgi/doi/10.1149/1.1836972

[240] T. Zheng, J. S. Xue, and J. R. Dahn, "Lithium Insertion in Hydrogen-Containing Carbonaceous Materials," *Chem. Mater.*, vol. 8, no. 2, pp. 389–393, jan 1996. [Online]. Available: http://pubs.acs.org/doi/abs/10.1021/cm950304y

[241] E. Peled, "The Electrochemical Behavior of Alkali and Alkaline Earth Metals in Nonaqueous Battery SystemsThe Solid Electrolyte Interphase Model," *J. Electrochem. Soc.*, vol. 126, no. 12, p. 2047, 1979. [Online]. Available: http://jes.ecsdl.org/cgi/doi/10.1149/1.2128859

[242] K. J. Harry, D. T. Hallinan, D. Y. Parkinson, A. A. MacDowell, and N. P. Balsara, "Detection of subsurface structures underneath dendrites formed on cycled lithium metal electrodes," *Nat. Mater.*, vol. 13, no. 1, pp. 69–73, jan 2014. [Online]. Available: http://www.nature.com/articles/nmat3793

[243] F. Sun, R. Moroni, K. Dong, H. Markötter, D. Zhou, A. Hilger, L. Zielke, R. Zengerle, S. Thiele, J. Banhart, and I. Manke, "Study of the Mechanisms of Internal Short Circuit in a Li/Li Cell by Synchrotron X-ray Phase Contrast Tomography," *ACS Energy Lett.*, vol. 2, no. 1, pp. 94–104, jan 2017. [Online]. Available: http://pubs.acs.org/doi/10.1021/acsenergylett.6b00589

[244] S. R. Stock, J. S. Okasinski, J. D. Almer, R. Woods, A. Miceli, D. P. Siddons, J. Baldwin, T. Madden, A. Rumaiz, T. Kuczewski, J. Mead, T. Krings, and O. Quaranta, "Tomography with energy dispersive diffraction," in *Dev. X-Ray Tomogr. XI*, B. Müller and G. Wang, Eds. SPIE, sep 2017, p. 9. [Online]. Available: https://www.spiedigitallibrary.org/conference-proceedings-of-spie/10391/2274567/Tomography-with-energy-dispersive-diffraction/10.1117/12.2274567.full

[245] F. Sun, L. Zielke, H. Markötter, A. Hilger, D. Zhou, R. Moroni, R. Zengerle, S. Thiele, J. Banhart, and I. Manke, "Morphological Evolution of Electrochemically Plated/Stripped Lithium Microstructures Investigated by Synchrotron X-ray Phase Contrast Tomography," *ACS Nano*, vol. 10, no. 8, pp. 7990–7997, aug 2016. [Online]. Available: http://pubs.acs.org/doi/10.1021/acsnano.6b03939

[246] O. O. Taiwo, D. P. Finegan, J. M. Paz-Garcia, D. S. Eastwood, A. J. Bodey, C. Rau, S. A. Hall, D. J. L. Brett, P. D. Lee, and P. R. Shearing, "Investigating the evolving microstructure of lithium metal electrodes in 3D using X-ray computed tomography," *Phys. Chem. Chem. Phys.*, vol. 19, no. 33, pp. 22 111–22 120, 2017. [Online]. Available: http://xlink.rsc.org/?DOI=C7CP02872E

[247] P. Pietsch and V. Wood, "X-Ray Tomography for Lithium Ion Battery Research: A Practical Guide," *Annu. Rev. Mater. Res.*, vol. 47, no. 1, pp. 451–479, jul 2017. [Online]. Available: http://www.annualreviews.org/doi/10.1146/annurev-matsci-070616-123957

[248] W. Li, H. Yao, K. Yan, G. Zheng, Z. Liang, Y.-M. Chiang, and Y. Cui, "The synergetic effect of lithium polysulfide and lithium nitrate to prevent lithium dendrite growth," *Nat. Commun.*, vol. 6, no. 1, p. 7436, dec 2015. [Online]. Available: http://www.nature.com/articles/ncomms8436

[249] J. Nelson, S. Misra, Y. Yang, A. Jackson, Y. Liu, H. Wang, H. Dai, J. C. Andrews, Y. Cui, and M. F. Toney, "In Operando X-ray Diffraction and Transmission X-ray Microscopy of Lithium Sulfur Batteries," *J. Am. Chem. Soc.*, vol. 134, no. 14, pp. 6337–6343, apr 2012. [Online]. Available: http://pubs.acs.org/doi/10.1021/ja2121926

[250] M. P. Glazer, J. S. Okasinski, J. D. Almer, and Y. Ren, "High-energy x-ray scattering studies of battery materials," *MRS Bull.*, vol. 41, no. 06, pp. 460–465, jun 2016. [Online]. Available: http://www.journals.cambridge.org/abstract_S0883769416000968

[251] Y.-S. Yu, M. Farmand, C. Kim, Y. Liu, C. P. Grey, F. C. Strobridge, T. Tyliszczak, R. Celestre, P. Denes, J. Joseph, H. Krishnan, F. R. N. C. Maia, A. L. D. Kilcoyne, S. Marchesini, T. P. C. Leite, T. Warwick, H. Padmore, J. Cabana, and D. A. Shapiro, "Three-dimensional localization of nanoscale battery reactions using soft X-ray tomography," *Nat. Commun.*, vol. 9, no. 1, p. 921, dec 2018. [Online]. Available: http://www.nature.com/articles/s41467-018-03401-x

[252] S. M. Hartig, "Basic Image Analysis and Manipulation in ImageJ," in *Curr. Protoc. Mol. Biol.* Hoboken, NJ, USA: John Wiley & Sons, Inc., apr 2013. [Online]. Available: http://doi.wiley.com/10.1002/0471142727.mb1415s102

[253] P. H. Corporation, "Parker O-Ring Handbook," Tech. Rep., 2007.

[254] R. C. Gonzalez and R. E. Woods, *Digital Image Processing*, 3rd ed. Pearson, 2007.

[255] S. Luo, X. Li, and J. Li, "Review on the Methods of Automatic Liver Segmentation from Abdominal Images," *J. Comput. Commun.*, vol. 02, no. 02, pp. 1–7, 2014. [Online]. Available: http://www.scirp.org/journal/doi.aspx?DOI=10.4236/jcc.2014.22001

[256] A. Kerhet, C. Small, H. Quon, T. Riauka, R. Greiner, A. McEwan, and W. Roa, "Segmentation of Lung Tumours in Positron Emission Tomography Scans: A Machine Learning Approach," 2009, pp. 146–155. [Online]. Available: http://link.springer.com/10.1007/978-3-642-02976-9_19

[257] F. A. Gonzalez, *Biomedical Image Analysis and Machine Learning Technologies: Applications and Techniques.* IGI Global, 2009.

[258] Yuanzhong Li, S. Hara, and K. Shimura, "A Machine Learning Approach for Locating Boundaries of Liver Tumors in CT Images," in *18th Int. Conf. Pattern Recognit.* IEEE, 2006, pp. 400–403. [Online]. Available: http://ieeexplore.ieee.org/document/1698917/

[259] J. Hsieh, *Computed Tomography Principles, Design, Artifacts, and Recent Advances*, 2nd ed., Wiley, Ed., 2009.

[260] A. D. Dysart, X. L. Phuah, L. K. Shrestha, K. Ariga, and V. G. Pol, "Room and elevated temperature lithium-ion storage in structurally submicron carbon spheres with mechanistic," *Carbon N. Y.*, vol. 134, pp. 334–344, aug 2018. [Online]. Available: http://linkinghub.elsevier.com/retrieve/pii/S0008622318300241

[261] C. Zu and A. Manthiram, "Stabilized LithiumMetal Surface in a Polysulfide-Rich Environment of LithiumSulfur Batteries," *J. Phys. Chem. Lett.*, vol. 5, no. 15, pp. 2522–2527, aug 2014. [Online]. Available: http://pubs.acs.org/doi/10.1021/jz501352e

[262] K. N. Wood, E. Kazyak, A. F. Chadwick, K.-H. Chen, J.-G. Zhang, K. Thornton, and N. P. Dasgupta, "Dendrites and Pits: Untangling the Complex Behavior of Lithium Metal Anodes through Operando Video Microscopy," *ACS Cent. Sci.*, vol. 2, no. 11, pp. 790–801, nov 2016. [Online]. Available: http://pubs.acs.org/doi/10.1021/acscentsci.6b00260

[263] H.-J. Peng, J.-Q. Huang, X.-B. Cheng, and Q. Zhang, "Review on High-Loading and High-Energy Lithium-Sulfur Batteries," *Adv. Energy Mater.*, vol. 7, no. 24, p. 1700260, dec 2017. [Online]. Available: http://doi.wiley.com/10.1002/aenm.201700260

[264] P. Bai, J. Li, F. R. Brushett, and M. Z. Bazant, "Transition of lithium growth mechanisms in liquid electrolytes," *Energy Environ. Sci.*, vol. 9, no. 10, pp. 3221–3229, 2016. [Online]. Available: http://xlink.rsc.org/?DOI=C6EE01674J

[265] A. J. Ilott, M. Mohammadi, H. J. Chang, C. P. Grey, and A. Jerschow, "Real-time 3D imaging of microstructure growth in battery cells using indirect MRI," *Proc. Natl. Acad. Sci.*, vol. 113, no. 39, pp. 10 779–10 784, sep 2016. [Online]. Available: http://www.pnas.org/lookup/doi/10.1073/pnas.1607903113

VITA

VITA

Arthur D. Dysart was born in Long Island, New York, United States of America. Upon completing secondary education with honors at Baldwin Senior High School (Baldwin, New York), Dysart attended the Engineering Honors College of the Polytechnic Institute of New York University (Brooklyn, New York). In 2013, Dysart graduated *Summa Cum Laude* with a Bachelors of Science in Chemical & Biomolecular Engineering, and enrolled in graduate education at the Davidson School of Chemical Engineering of Purdue University (West Lafayette, Indiana).

In 2011, Dysart began his research career at Polytechnic Institute under the careful guidance of Professors B. A. Garetz & J. E. Aber in Non-Photochemical Laser Induced Nucleation. Upon graduation, Dysart continued as a graduate research assistant at Purdue under the influential leadership of Professor V. G. Pol. Between 2013 – 2018, Dysart performed graduate research in the areas of rechargeable energy systems, material synthesis, tribology, health sciences, and life cycle analysis. In 2017, as a Department of Energy Office of Science Graduate Research (DOESCGR) Fellow of Argonne National Laboratory (Lemont, Illinois), Dysart developed procedures for in situ synchrotron tomography imaging under the supervision of Senior Materials Scientist D. P. Abraham.

In 2018, Dysart received a Doctorate of Philosophy in Chemical Engineering for his dissertation "Polysulfide Mitigation at the Electrode-Electrolyte Interface: Experimental Approaches for Rechargeable Lithium Sulfur Batteries."